Université de Liège
Vibrations et Identification des Structures
Département d'Aérospatiale et Mécanique

Stochastic Finite Element Method for the Modeling of Thermoelastic Damping in Micro-Resonators

Thèse de doctorat présentée en vue
de l'obtention du grade de
Docteur en Sciences Appliquées

par

Séverine LEPAGE
Ingénieur Civil Electro-Mécanicien (Aérospatiale)
M.Sc., Astronautics and Space Engineering, Cranfield University, UK
Aspirant FNRS

Décembre 2006

Abstract

Micro-electromechanical systems (MEMS) are subject to inevitable and inherent uncertainties in their dimensional and material parameters, that lead to variability in their performance and reliability. Manufacturing processes leave substantial variability in the shape and geometry of the device due to its small dimensions and high feature complexity, while the material properties of a component are inherently subject to scattering. The effects of these variations have to be considered and a modeling methodology is needed in order to ensure required MEMS performance under uncertainties.

In the design of high-Q micro-resonators, dissipation mechanisms may have detrimental effects on the quality factor (Q). One of the major dissipation phenomena to consider is thermoelastic damping, so that performances are directly related to the thermoelastic quality factor, which has to be predicted accurately. The purpose of this research is to develop a numerical method to analyze the effects of geometric and material property random variations on the thermoelastic quality factor of micro-resonators.

This work is divided into two main research tasks: the development of a computational framework to determine the thermoelastic quality factor, and the modeling of uncertainties. A thermopiezoelectric finite element formulation is first derived to carry out modal analyses of MEMS. The application of this method makes possible the determination of the thermoelastic quality factor of piezoelectrically actuated structures, and allows a better understanding of the phenomena occurring in thermopiezoelectric vibrations. Once the deterministic finite element problem is well defined and characterized, uncertainties can be added into the model. The present work focuses on second moment approaches, in which the first two statistical moments, i.e. the mean and the variance, are estimated. The perturbation Stochastic Finite Element Method (SFEM) is used to determine the mean and the variance of the thermoelastic quality factor and is compared to direct Monte-Carlo simulations. The perturbation SFEM consists in a deterministic analysis complemented by a sensitivity analysis with respect to the random parameters, which are modeled as random variables as well as random fields.

The originality of this work is the extension of SFEM to the analysis of strongly coupled multiphysic phenomena. Therefore, using the proposed SFEM, a numerical method is available to quantify the influence of uncertain geometric and material property variations on the thermoelastic quality factor of micro-resonators, making available a new efficient numerical tool to MEMS designers.

Acknowledgements

I wish to acknowledge the Belgian National Fund for Scientific Research (FNRS) for its financial support to this research. This work was also supported by DGA/ STTC 03.34.049 convention between the Direction Générale pour l'Armement (DGA), ONERA and Open-Engineering. The support from the Communauté Française de Belgique - Direction Générale de la Recherche Scientifique in the framework Actions de Recherche Concertées (convention ARC 03/08-298), is also acknowledged.

I would like to thank my advisor Professor Jean-Claude Golinval for his precious help and support during the course of this research. I appreciated his advices and his confidence in me.

During my stays at the University of Illinois at Urbana-Champaign, I had the opportunity to interact with several researchers and faculty members. I would like to thank Professor Lawrence Bergman, from the Department of Aerospace Engineering, for hosting my visits and introducing me to the world of stochastization. I appreciated discussing about the feasibility of a stochastic micro-meso-macro approach with Professor Martin Ostoja-Starzewski, from the Department of Mechanical Science and Engineering. It was a pleasure to share my opinion about efficient modeling techniques for MEMS design with Professor Narayana Aluru affiliated to Beckman Institute.

I express my gratitude to the members of the Physics, Instrumentation and Sensing Department (DMPH) at ONERA for their warm welcome. Olivier Le Traon and Stève Masson were always available to answer my questions and discuss the VIA modeling issues. They helped me identifying the modeling needs in micro-resonator design.

Thanks must also go to the community of Oofelie developers who everyday enhance the capability of the software. I acknowledge the members of Open-Engineering for their help and assistance with the software implementation of my developments. I would like to thank Igor Klapka and Christophe Louis who contributed to my involvement in this challenging research project.

Many thanks also go to Professors Pierre Beckers, Jean-Pierre Coyette, Gerhart Schueller and Doctors Gaetan Kerschen and Jean-Philippe Ponthot who accepted to participate in the examination committee of this doctoral thesis.

I am also grateful to my colleagues and friends of the Structural Vibrations and Identification group and especially, to my office fellows, who supported me in everyday work. I am more than thankful to Doctors Olivier Bruls and Guillaume Serandour for their comments and suggestions throughout the writing of this dissertation.

In conformity with my motto "Mens sana in corpore sano", I thanks my former and current mountain biking teams, namely Houffa Bike Team and Cuestas Biking Team, for supporting me and discharging me of so many obligations to help me to reach both my academic and biking goals. I'm also grateful to the bikers (Illinois Bicycle Racing Club, 9.2 bikers, Generations and Liege BMB) who have shared the trails with me.

Finally and foremost, my thoughts go to my parents who have always supported me in the choices I have made.

Table of Contents

Chapter 1

Introduction

1.1 Background and Motivation

Microelectromechanical systems (MEMS) technology has been rapidly growing since its beginnings in the early 1980's. Deriving from the semiconductor industry, MEMS industry can take advantage of the existing semiconductor manufacturing techniques and infrastructures, leading to a low cost and large volume production which makes MEMS commercialization attractive. Moreover, as MEMS are light, small and consume few energy, they are used in a wide spectrum of areas of engineering such as aerospace, medical, automotive or information technology. Ink jet printer heads, micropumps, projection display arrays and airbag accelerometers can be cited as a few examples of everyday live devices where MEMS have successfully replaced more conventional systems. Amongst MEMS community, there are increasing demands in developing reliable micro-structures with very high quality factors. These micro-structures constitute the essential active part of applications such as resonant sensors and RF-MEMS filters, where increasing the sensitivity and resolution of devices is a critical issue.

In order to design high-Q micro-resonators, all dissipation mechanisms that contribute to decreasing the quality factor have to be identified. The majority of these are extrinsic (e.g. air damping), which means that they can be minimized by a proper design and operating conditions. Intrinsic losses, on the other hand, can not be controlled as easily as extrinsic ones. Thermoelastic damping has been identified as an important loss mechanism in numerous high-Q micro-resonators [1, 44, 45, 67, 68]. The ability to accurately model and predict energy loss due to

the thermoelastic effects is therefore a key requirement in order to improve the performance of high-Q resonators. However most studies of thermoelastic quality factor till date have been based on analytical models, which are subject to very restrictive assumptions so that they are not sufficiently accurate to predict the behavior of complex 3-D structures.

Another important issue in MEMS design is that micro-electromechanical systems are subject to inevitable and inherent uncertainties in dimensional and material parameters, that lead to variability in their performance and reliability. Manufacturing processes leave substantial variability in the shape and geometry of the device due to its small dimensions and high feature complexity, while the material properties of a component are inherently subject to scattering. The effects of these variations have to be considered and a modeling methodology is needed in order to ensure required MEMS performance under uncertainties.

1.2 Research Objectives

Due to the importance of the interaction between several physical fields in micro-structures, the interest in numerical multi-physics simulations is growing for the design of accurate micro-sensors. Numerical simulations are advantageous as they are less demanding in terms of both time and costs than experiments. They also allow a better understanding of the interactions between the different physical fields. Hence, numerical multi-physics simulations are useful in order to improve the design of high precision micro-structures.

The purpose of this thesis is to develop a numerical method to analyze the effects of geometric and material property random variations on the quality factor of micro-resonators. The objectives can be divided into two main tasks:

- First, a computational framework has to be developed in order to determine the thermoelastic quality factor of micro-resonators. The proposed approach is to derive a strongly coupled thermopiezoelectric finite element formulation from a variational analysis considering mechanical, thermal and electric fields. The electric contributions are introduced into the formulation in order to determine the thermoelastic quality factor of micro-resonators using piezoelectricity as transduction mechanism. Two different kinds of analysis allow to obtain the thermoelastic quality factor. On the one hand,

the quality factor can be calculated from the complex eigenvalues obtained by a modal analysis. On the other hand, an harmonic analysis gives the frequency response function from which the quality factor can be derived. The developed finite element method has to be validated and its validity has to be investigated through numerical examples from analytically tractable test cases to complex 3-D structures.

- Once the deterministic problem is well defined and characterized, uncertainties can be added into the model. A stochastic finite element method can be applied to the thermoelastic problem. Firstly, the most adequate method should be selected to handle uncertainties in non-symmetric damped problems. In classical mechanics, finite element models use symmetric damping matrix assumption and till date, all stochastic finite element methods have been developed for this kind of applications. Secondly, the method being selected, it has to be adapted to thermoelastic problems. The final development of this research work is to understand how variability propagates through the thermoelastic model. Indeed, in order to model uncertainties, mathematical tools such as probabilistic distributions or random fields are used introducing new parameters for which no experimental data are available for their determination and the sensitivity of the response variability to these mathematical data has to be investigated.

All the developments of this doctoral thesis are implemented in a software called `Oofelie` ("Object Oriented Finite Element Led by Interactive Executer"). It is written in C++ language which using modern object oriented programming concepts, is favorable for an open architecture and well-suited for the addition of new features. Its kernel has been designed to deal with strongly coupled multiphysic problems [77, 78] so that the new thermopiezoelectric elements are easily implemented. A new tool kit is incorporated into `Oofelie` in order to model global or spatially variable material properties as well as geometric uncertainties and hence, to provide their effects on the variability of the behavior of thermoelastic resonators.

1.3 Dissertation Outline

In order to present the work carried out, the dissertation is divided into the following chapters:

- Chapter 1, **Introduction**, has briefly introduced the context of the research and describes the work objectives and strategy.

- Chapter 2, **Micro-Resonators**, reviews the different energy losses that occur in MEMS. From this review, it is shown that thermoelastic damping is the most important energy loss mechanism that has to be considered in high quality factor micro-resonator design. This chapter also presents the geometric and material property variability that is inherent to MEMS due to micro-fabrication.

- Chapter 3, **Fundamentals of Thermoelastic Damping**, concerns the thermoelastic fundamentals and gives the state of the art in the prediction of thermoelastic effects on the behavior of micro-resonators.

- Chapter 4, **Thermopiezoelectric Finite Element Formulation**, derives the thermopiezoelectric finite element formulation from the variational principle. The finite element method is validated on 1-D simple test cases that are analytically tractable.

- Chapter 5, **Numerical Applications**, exposes the thermoelastic analysis of clamped-clamped silicon beams. In particular, the effects of the beam aspect ratio, anchor configuration and residual stress are investigated. It also presents the thermopiezoelectric analysis of the Vibrating Inertial Accelerometer, which is a vibrating beam accelerometer developed by ONERA. It is shown that the finite element results are in good agreement with the experimental ones and the finite element method allows to take into account features which cannot be considered in analytical models. This chapter ends the deterministic study of the thermoelastic quality factor.

- Chapter 6, **Uncertainty Treatment in Finite Element Analysis**, provides a state of the art presentation of the finite element methods allowing to handle stochastic problems. The random field discretization techniques are

also introduced. From this review, knowing the advantages and drawbacks of different methods, it is shown that the perturbation stochastic finite element method is the most adequate method in order to handle uncertainties in analyses of thermoelastic quality factor of micro-resonators.

- Chapter 7, **Perturbation Stochastic Finite Element Method**, presents the extension of the perturbation stochastic finite element method (PSFEM) to the thermoelastic problem. This includes the determination of the first and second order sensitivities of the eigenpairs of non-symmetrically damped problems.

- Chapter 8, **Application of the PSFEM on Quality Factor Analyses** provides numerical examples, where material as well as geometric uncertainties are handled.

- Chapter 9, **Introduction to a Stochastic Micro-meso-macro Approach**, gives a general overview of the feasibility of a stochastic micro-meso-macro approach to derive the correlation characteristics of a random heterogenous material.

- **Conclusion** finally concludes the project and presents further recommendations.

Chapter 2

Micro-Resonators

This chapter reviews the different energy losses that occur in MEMS. From this review, it is shown that thermoelastic damping is the most important energy loss mechanism that has to be considered in high quality factor micro-resonator design. This chapter also presents the geometric and material property variability that is inherent to MEMS due to micro-fabrication processes. Finally, the VIA, i.e. the Vibrating Inertial Accelerometer developed at ONERA is presented. This accelerometer is an example of a micro-resonator whose quality factor is limited by thermoelastic damping and will constitute the application case of this dissertation.

2.1 Damping in MEMS

Resonators are critical components in a wide variety of MEMS applications, such as in accelerometers [89, 138], gyrometers [16, 45, 47], sensors [7], charge detectors [35], radio-frequency filters [11, 108, 109], magnetic resonance force microscopes [162], torque magnetometers [19], ... For these applications, it is important to fabricate resonators with high quality factors Q, where Q is defined by the ratio of the stored energy in the resonator W and the total dissipated energy per cycle of vibration ΔW:

$$Q = 2\pi \frac{W}{\Delta W}. \tag{2.1}$$

Understanding the energy dissipation mechanisms in these high-Q resonators is an important issue to optimize their design and performance. The loss mechanisms

can be classified into two categories [33, 140, 154, 155, 156]:

- the extrinsic losses, which can be altered by changing the design or the operating conditions of the MEMS. Air damping and support losses are the main contributing extrinsic losses.

- the intrinsic losses, which impose an upper limit to the reachable quality factors. Thermoelastic damping and internal losses such as the intergranular losses can be listed as common intrinsic losses.

The global quality factor Q_{total} can be expressed as [33, 85, 154, 155, 156]

$$Q_{total}^{-1} = \sum_i Q_i^{-1} = Q_{air}^{-1} + Q_{support}^{-1} + Q_{TED}^{-1} + Q_{int}^{-1} + Q_{other}^{-1}, \tag{2.2}$$

where Q_{air} represents the quality factor associated with air damping, $Q_{support}$ reflects the energy losses due to the fixation to the support, Q_{TED} is the effect of thermoelastic damping, Q_{int} corresponds to internal losses other than thermoelastic damping, e.g. intergranular losses and Q_{other} represents any residual losses, e.g. surface losses. It is obvious that Q_{total} can not exceed the smallest Q_i. The following discussion focusses successively on each isolated contribution.

2.1.1 Air Damping

Air damping also called gas damping is one of the most important energy loss in MEMS. Depending on the pressure level, three different air damping regions can be identified [22]:

- intrinsic damping region: in this region, the pressure is near vacuum and air damping is negligible;

- molecular region: damping is caused by independent collisions of noninteracting air molecules with the vibrating surface of the resonator;

- viscous region: air acts as a viscous fluid.

Figure 2.1 shows the variation of the quality factor of a Tang resonator with the pressure. The three regions appear clearly. Below 0.02 mbar, the quality factor reaches an upper limit of 10000 and is not influenced by air damping, it is the intrinsic damping region. Above 200 mbar, the quality factor reaches its

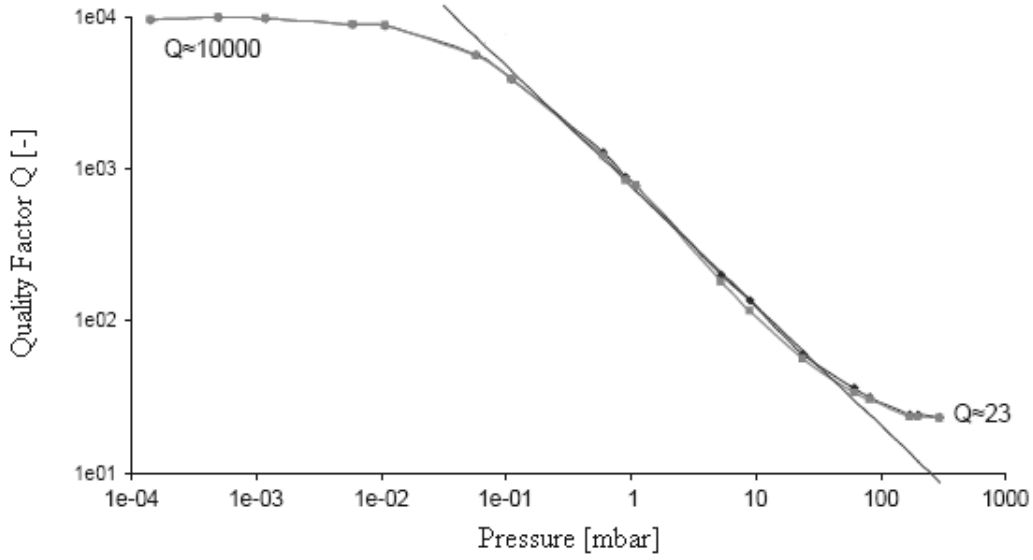

Figure 2.1: Variation of the quality factor of a Tang resonator with pressure [119].

lower limit of 23. It is the viscous region. Between these two limits, the quality factor varies with the pressure, it is the molecular region.

Analytical models are able to quantify the quality factor in the molecular region. For example, for a cantilever beam, Q is given by [22]

$$Q = \frac{2\pi f_n H \rho}{k_m P} = \frac{k_n^2}{k_m P}\left(\frac{H}{L}\right)^2 \sqrt{\left(\frac{E\rho}{12}\right)}, \tag{2.3}$$

where

$$k_m = \sqrt{\frac{32M}{9\pi RT}}, \tag{2.4}$$

f_n is the resonant frequency of the nth mode, ρ is the mass density of the cantilever, P is the pressure, k_n is the constant of the nth natural mode (e.g. $k_n = 1.875$ for the first bending mode of a cantilever beam), H and L are the thickness and length of the cantilever, respectively, the gas constant $R = 8.314\,10^3$ J/K, T is the temperature (in K) and M is the molecular mass of gas.

For simple geometries, analytical models exist in order to quantify the viscous damping. Two different types of viscous damping can be usually identified in MEMS:

- In the Couette flow case, the damping force appears between two plates

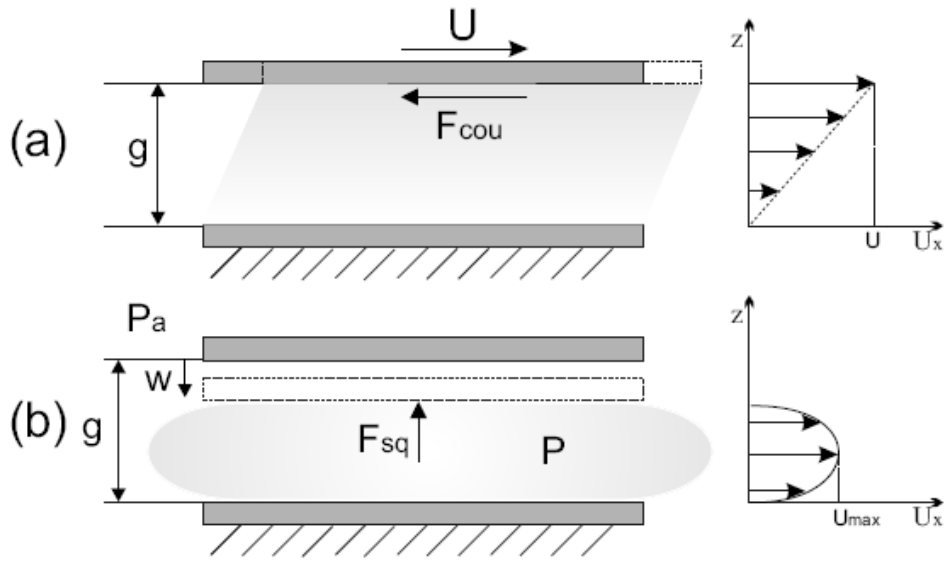

Figure 2.2: (a) Couette flow damping between two plates that move parallel one to the other; (b) Squeeze film damping between two plates that move one against the other.

that move parallel to each other and are separated by a Newtonian fluid (Figure 2.2a) [30].

- In the squeeze-film case, a moving plate moves downwards and upwards from a fixed plate (Figure 2.2b). Due to the plate motion, the pressure inside the gas increases, and the gas is squeezed out from the edges of the plates. When the plates separate, the situation reverses: the pressure drops between the plates and the gas is sucked back. The viscous drag of the air during the flow creates a dissipative mechanical force on the plate, opposing the motion [14].

In many MEMS devices, viscous damping is dominated by squeeze-film damping. In order to model squeeze-film damping, the most popular approach is based on the compressible Reynolds equation, which is modified by correction factors to extend its validity over the operating range of MEMS [156]. For example, Reynolds equation can be modified in order to model perforated plates [18]. Another approach is to numerically solve the Navier-Stokes equations [66, 141].

Air damping is extrinsic and can be avoided by operating the device in vacuum in order to enter the intrinsic damping region.

2.1.2 Support Loss

Support loss also called anchor loss or clamping loss is the second dominant dissipation mechanism in MEMS. Support loss concerns the mechanical energy that is dissipated via the coupling to the support structure. During its vibrating motion, a resonator exerts both vibrating shear force and moment on its clamped ends. Acting as excitation sources, these vibrating shear force and moment generate elastic waves propagating into the support. Therefore, the support structure absorbs some of the vibration energy of the resonator.

Support loss mechanism has been investigated experimentally on cantilever resonators [154, 155] and analytical models have been derived in [63] considering the support as a semi-infinite thin-plate and in [74] considering the support as a semi-infinite solid. Both models give a similar expression for the quality factor:

$$Q \approx k_s \left(\frac{L}{H}\right)^3, \tag{2.5}$$

where H and L are the beam thickness and length, respectively and k_s ranges between 2 and 3 depending on the flexural mode. Although these models due to their inherent assumptions can not be successfully applied in some cases for which they overestimate the support losses [85].

Numerical simulations have also been carried out on this topic, see for example the PML (Perfectly Matched Layer) simulations in [20].

Support loss can be considered as an extrinsic loss since it can be altered by changing the design and especially the mounting mechanisms. For example, designing nonintrusive supports reduces support loss [148].

2.1.3 Thermoelastic Damping

In the 1930's, Zener [157] was the first to realize that thermoelastic damping may be a significant dissipation mechanism in flexural resonators. More recently, thermoelastic damping has been identified as an important loss mechanism in numerous high-Q micro-resonators, especially in those using flexural vibration modes [1, 44, 45, 67, 68, 85, 154, 155]. Thermoelastic damping is an intrinsic loss mechanism that occurs through heat conduction. In a thermoelastic solid, a strong coupling exists between the thermal and mechanical fields through the

coefficient of thermal expansion. When the thermal and mechanical response-times are of the same order of magnitude, thermoelastic damping occurs. The dissipation mechanism is achieved through an irreversible heat flow which allows the solid to relax to equilibrium. Analytical models have been derived to quantify the thermoelastic damping in very simple structures [91, 158]. Chapter 3 provides a more detailed presentation of the study of thermoelastic damping in micro-resonators.

2.1.4 Internal Losses

The internal losses, which are due to internal friction other than thermoelastic damping, are dependent on the purity and dislocations of the material used. This internal friction is difficult to quantify, since it depends on the imperfections in the structure of the material and also on the fabrication method. Internal friction is the dissipation in the form of heat occurring when chemical bonds are made and broken. In a single-crystal beam, point defects and dislocations are the cause of internal friction. The energy loss due to a single defect or dislocation can be modeled and a number of each can be estimated using probabilities to compute the overall internal friction [94]. In a polycrystalline material, the dominant cause of internal friction is grain boundaries [136]. In an amorphous material, the friction is a bulk property. Composite materials also have energy loss at the boundary between layers.

2.1.5 Surface Losses

Scaling down MEMS increases the surface-to-volume ratio so that the surface losses become important. This phenomenon has been observed for submicrometer thick cantilevers [154, 155]. Surface losses are mostly caused by surface stress, which can significantly be modified by absorbates on the surface, or surface defects. To model the surface dissipation, a complex Young's modulus E_c is considered in the surface layer: $E_c = E + iE_d$, where E_d is the dissipation part of Young's modulus. The quality factor of structures dominated by surface losses can be modified through heat or surface treatments.

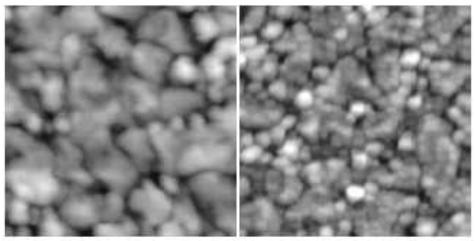

Figure 2.3: Two AFM images from two different MUMPS runs indicating the significant variation of grain sizes of polysilicon [164].

2.2 Uncertainties in MEMS

The performance of a micro-electromechanical system is affected by uncertainties. Manufacturing processes may leave substantial uncertainties in the shape and geometry of the device while the material properties of a component are inherently subject to scattering. Moreover, microscale properties are extremely sensitive to process variations. Accuracy and precision of standard processes are difficult to control so that properties vary by recipe, fabrication run, wafer-to-wafer and across the wafer. The design of accurate MEMS has to take into account the influence of these uncertainties.

2.2.1 Material Uncertainties

The materials making up MEMS are deposited as thin films. Although the electric characterization of thin films is well established, the mechanical characterization of the same films is difficult. Moreover, the material properties are dependent on the fabrication process and therefore are not the same as the bulk material ones. The material properties can even be different between runs of the same fabrication process. Figure 2.3 illustrates two AFM (Atomic Force Microscope) images for the polysilicon films from MUMPS (Multi-User MEMS Processes) process at different runs.

Although polysilicon shows a lower intrinsic quality factor than single crystal silicon, it is also used in high-Q resonators [1, 7, 148]. Polysilicon is the most common material used in MEMS and a large number of experimental characterizations of its mechanical properties are available in the literature [41, 42, 73, 132]. Figure 2.4 shows the variation of the experimental results obtained for Young's

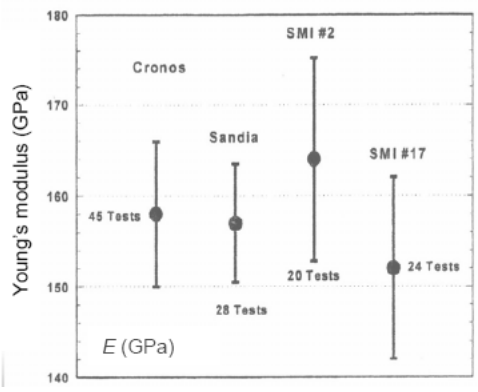

Figure 2.4: Variation of Young's modulus for polysilicon [132].

modulus in different laboratories. There are several sources for the large scatter of the results. There is of course the inherent experimental measurement errors but there may also be some material differences in polysilicon from one fabrication facility to another. A difference in crystalline orientation from [1 0 0] to [1 1 1] can account for a change from 130 GPa to 188 GPa. The film density and average orientation are affected by film deposition and annealing parameters, changing Young's modulus by up to 10 percents. In [73], the experimental results show really good agreement with the expected value derived via Voigt and Reuss models from the grain texture using the Electron Backscatter Kikuchi Pattern technique. Polysilicon as every polycrystalline material is non-homogeneous and shows spatial variation in its material properties.

Single-crystal materials have excellent resonating properties in terms of very high intrinsic Q-factors. The high Q-factor together with other properties make crystalline silicon and quartz the best candidates for the resonator material. These single-crystal materials have material properties which are characterized with high precision. However, the uncertainty on the material properties can be indirect. Indeed, the material properties depend on the temperature so that uncertainty on the operation temperature of the resonators induces an uncertainty on the material properties. Another source of uncertainty arises when doped silicon is used. Although mechanical properties are not dependent on doping level [160], thermal properties are directly dependent on the doping level [24, 126]. Due to the non-uniformity of the doping [131], the thermal properties show spatial variations.

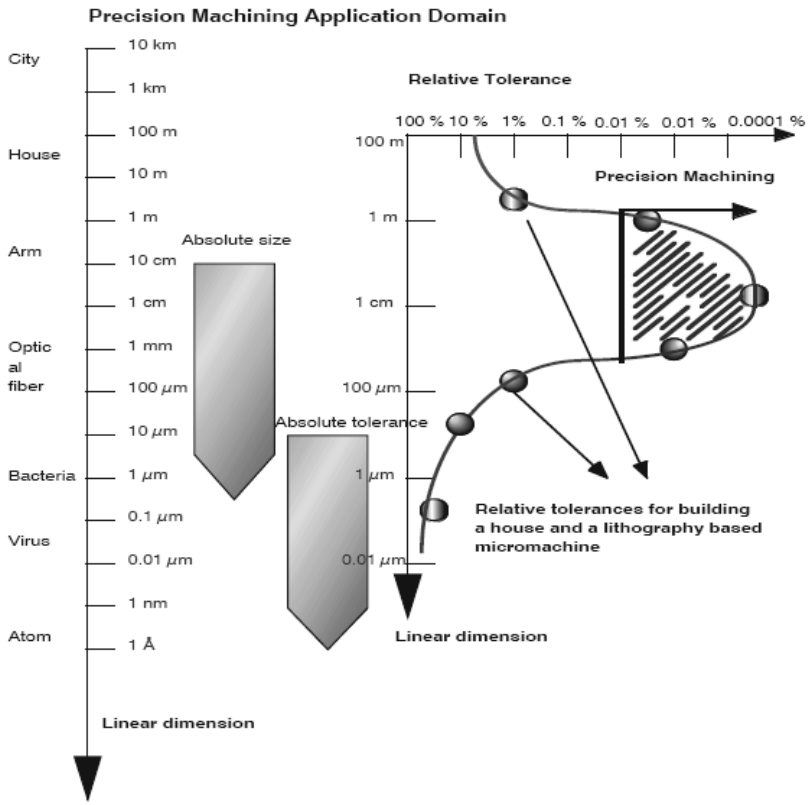

Figure 2.5: Application field for precision machining in terms of absolute sizes and absolute and relative tolerances [96].

2.2.2 Geometric Uncertainties

Figure 2.5 shows the increasing loss of relative manufacturing tolerance with decreasing structure size [96]. While MEMS micromachining, which originates from the integrated circuit technology, can achieve excellent absolute tolerances, relative tolerances are rather poor compared with those achieved by more traditional techniques in macroscale applications. For example, the relative tolerances achieved for a lithography based micromachining are the same as for building a house.

Micromachining processes yield shapes that are not geometrically perfect. Figure 2.6 shows an example of geometric imprecisions induced by MUMPS fabrication process. This shows that the process yields rounded corners instead of sharp 90° corners and a beam that is narrower by 20 % than the layout width. Another common geometric imperfection is the trapezoidal cross-sections that

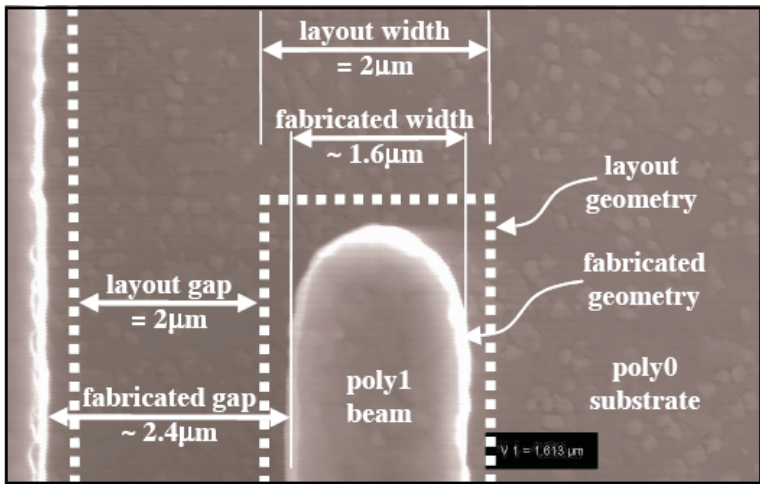

Figure 2.6: Geometric errors induced by MUMPS fabrication process [34].

result from anisotropic wet etching. Figure 2.7 shows the profiles obtained by an anisotropic wet etching in a <100> silicon wafer. It is obvious that such a fabrication process does not allow manufacturing rectangular cross-sections.

2.2.3 Residual Stress

The residual stress is another source for imprecision in microfabrication. The residual stress is setup in a microstructure and deforms it, especially when the microstructure has a small thickness. Causes for residual stresses include gas entrapment or impurity inclusions, microvoids created by gases that are generated during deposition and escape, thermal and lattice mismatches between the film and the substrate, and doping [96]. Moreover, the residual stresses combine with thermal stresses that are generated through different thermal expansion coefficients of the substrate and deposited film. Eliminating or reducing the levels of residual stresses is generally attempted by post-deposition thermal treatment processes, such as annealing. The residual stresses, which appear during and after deposition, can be either tensile or compressive.

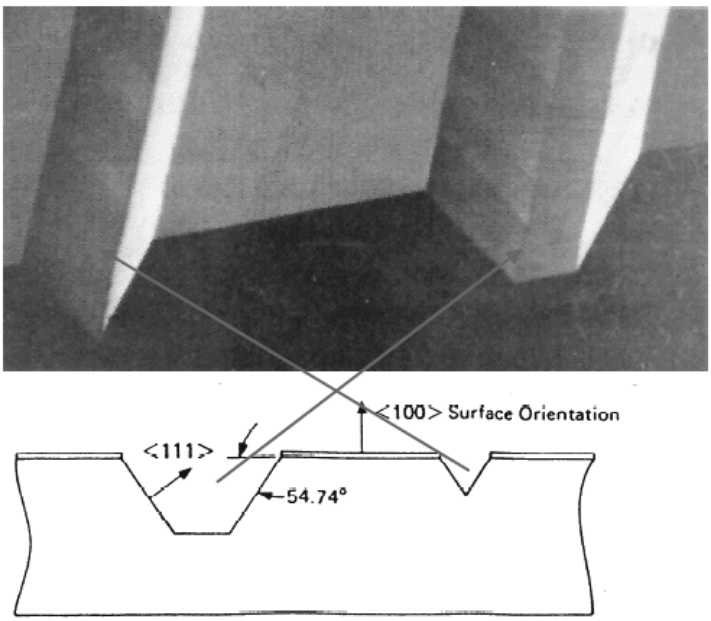

Figure 2.7: Anisotropic wet etched profiles in a <100> silicon wafer [96].

2.3 The Vibrating Inertial Accelerometer

The resonator devices used in this work are accelerometers fabricated at ONERA. In order to respond to the demand of accurate miniature inertial navigation systems, ONERA has been working on the design of a vibrating beam accelerometer called the Vibrating Inertial Accelerometer (VIA) [87]. The present applications of this device are the guidance and the attitude control of vehicles as well as navigation applications when coupled with other positioning systems such as GPS. The accuracy of the VIA is directly related to the quality factor of its sensitive element, which is a beam made of quartz.

2.3.1 VIA Principle and Performance

The Vibrating Inertial Accelerometer (VIA) [86, 87, 98] is a Vibrating Beam Accelerometer (VBA) made of monocrystalline quartz. Its concept is based on the resonance frequency shift of a beam when submitted to axial stresses induced by acceleration. More precisely, in the VIA design, a micrometric beam (cross section 30 μm x 60 μm, length 2.26 mm) is clamped at one of its ends and is

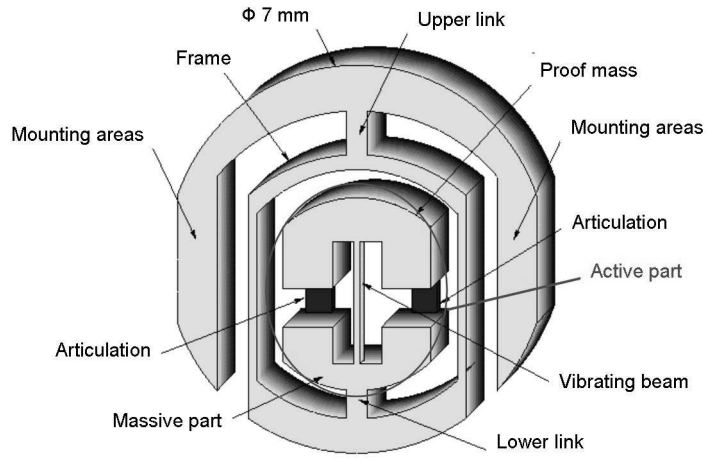

Figure 2.8: VIA transducer design with the decoupling frame.

connected to the proof mass at the other one (Figure 2.8). When an acceleration is applied along the sensitive axis of the sensor, the proof mass generates an axial stress in the beam, which modifies its bending resonant frequency. The working frequency is around 60 kHz and the sensitivity is 24 Hz/g. Upon a measuring range of 100 g, the scale factor error is about 10 ppm and the bias error is a few hundreds of μg for a long term stability (10 years).

As quartz is a piezoelectric material, it is possible to actuate and detect the oscillations of the beam by metallic electrodes which are deposited on it. An electronic oscillator, with gain and phase control, is used to excite the beam at its resonance. The output of VIA is thus the frequency of the oscillator signal, and its variations represent the applied acceleration. Bias stability, i.e. beam frequency without acceleration, requires a resonator with high quality factor, in order to reduce the sensitivity of electronic phase drift.

In the VIA, extrinsic losses have been decreased as much as possible. Indeed, air damping is avoided by operating under vacuum (p= 0.1 mbar), and a specific insulation frame has been developed in order to reduce the losses out of the quartz structure. Finite element analyses show that, due to this frame, less than 10^{-8} of the whole energy is dissipated into the support, and very high quality factors are allowed. Lastly, due to the quality of quartz crystal, viscosity losses can be neglected.

Thus, intrinsic losses, and especially thermoelastic damping, are the main

contribution to energy losses and limit the VIA quality factor : $Q_{total} = Q_{TED}$. The experimental quality factor Q_{total} is about 13 000, whereas Zener's analytical thermoelastic model [157] evaluates Q_{TED} around 17 000. This difference can be explained by the strong assumptions of the analytical model (such as rectangular beam, isotropic solid,...) which are not satisfied in the case of the VIA beam. Therefore, a finite element approach has to be developed for the purpose of better understanding the thermoelastic damping, and hence, improving the design of future accelerometers.

2.3.2 VIA Fabrication

The VIA is made of two quartz transducers and two electronic oscillator circuits which actuate the two beams at their resonant frequency by piezoelectricity. Transducers, i.e. monolithic quartz structures (Figure 2.8), operate in differential mode, in order to reduce common parasitic sensitivities, e.g. temperature, pressure, aging,... The opposite variations of these frequencies provide a direct measurement of the applied acceleration.

VIA transducers are manufactured by wet etching of quartz in hydrofluoric acid-based solution. This anisotropic wet etching does not allow the fabrication of rectangular cross-sections but only trapezoidal ones. The initial quartz wafer has a chromium-gold metallization on both sides. This Cr/Au metallization is obtained via a classical double-side photolithography process and is utilized as a mask for the chemical etching. The substrate is etched in a fluorine-based solution until the desired beam thickness is reached. Finally, the actuation and detection electrodes are made by a Cr/Au metallization. Figure 2.9 shows a quartz wafer on which 16 VIA transducers have been machined.

After micromachining, the quartz transducer is glued to a standard TO8 base as shown on the left hand side of Figure 2.10. In order to realize the differential system, two transducers are mounted into a copper case, under a local vacuum (p=0.1 mbar). A standard Surface Mount Technology is used for the realization of the electronic oscillator circuits. The right hand side of Figure 2.10 shows an example of a complete VIA including the electronic circuit.

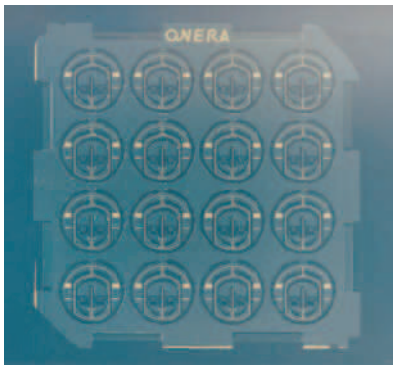

Figure 2.9: Quartz wafer comprising 16 VIA transducers.

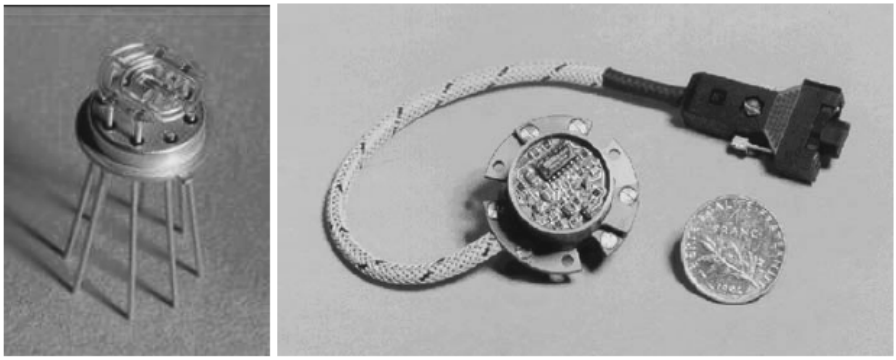

Figure 2.10: VIA transducer mounted on a TO8 base (left) and complete VIA with electronic circuit (right).

2.3.3 Thermopiezoelectricity

Quartz crystal is used for the VIA, which leads to several advantages. Firstly, its piezoelectric properties can be easily used to actuate the oscillations of the vibrating elements and to detect the vibrations. Secondly, the mechanical properties of quartz are highly stable and quartz sensors generally show low temperature sensitivity and low aging. Moreover, intrinsic quality of quartz allows high-Q resonators to be achieved. Finally, chemical etching of quartz permits collective micromachining of sensors.

Piezoelectricity is a fundamental process of electromechanical interaction, which results from the coupling between the electric and mechanical fields. The direct piezoelectric effect refers to the electric polarization produced by mechanical stress. In other terms, when a piezoelectric material is squeezed, an electric

charge collects on its surface. Closely related to the direct effect is the converse effect; whereby a crystal becomes strained when an electric field is applied. In other words, when a piezoelectric material is subjected to an electric field, it mechanically deforms. Piezoelectricity influences the resonant frequency [71] and the quality factor of the VIA beam.

From an engineering or modeling point of view, the constitutive equations of a piezoelectric material involve coupled mechanical and electric contributions. Moreover, since ONERA has identified the thermoelastic damping as the principal dissipation source in the VIA, the thermal field has also to be taken into account. Therefore, the generalized thermopiezoelectric constitutive equations have to be considered in order to precisely quantify the quality factor of VIA beam.

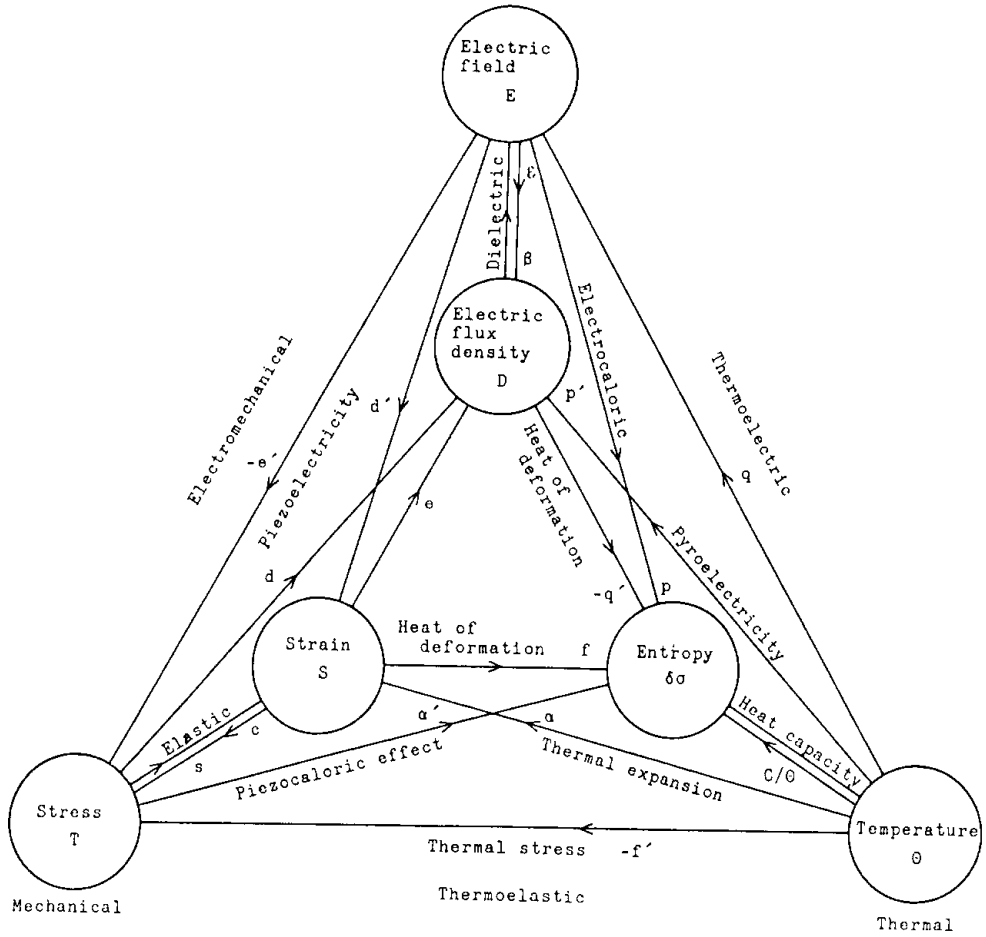

Figure 2.11: Interaction processes between the electric, mechanical and thermal fields [71].

Interaction processes between any two of the three physical fields - electric, mechanical and thermal - are represented in Figure 2.11. In addition to piezoelectricity, pyroelectricity and thermoelasticity have to be considered. In simplest terms, pyroelectricity is characterized by the fact that the temperature changes when an electric field is applied and conversely, an electric potential is induced when the material is heated or cooled. Pyroelectricity does not occur in the VIA as quartz is not pyroelectric. Thermoelasticity results from the coupling between the thermal and mechanical fields: when the material is heated or cooled, it expands or contracts and conversely, when the material is contracted or stretched, its temperature changes. The linear thermopiezoelectric constitutive equations are the following [71]

$$\boldsymbol{\sigma} = \mathbf{Q}\boldsymbol{\varepsilon} - \mathbf{P}\mathbf{E} - \mathbf{k}\theta, \tag{2.6}$$

$$\mathbf{D} = \mathbf{P}^{\mathbf{T}}\boldsymbol{\varepsilon} + \mathbf{B}\mathbf{E} + \mathbf{d}\theta, \tag{2.7}$$

$$S = \mathbf{k}^{\mathbf{T}}\boldsymbol{\varepsilon} + \mathbf{d}^{\mathbf{T}}\mathbf{E} + a_T\theta, \tag{2.8}$$

where $\boldsymbol{\sigma}$, $\mathbf{D}$ and S are respectively the stress vector, the electric displacement vector and the entropy and $\boldsymbol{\varepsilon}$, $\mathbf{E}$ and θ are respectively the strain vector, the electric field vector and the temperature increment from the reference temperature. Matrices $\mathbf{Q}$, $\mathbf{B}$, $\mathbf{P}$, $\mathbf{k}$ and $\mathbf{d}$ respectively denote the matrix forms of elastic constant, dielectric permittivity, piezoelectric constant, thermal-mechanical coupling constant and pyroelectric constant. a_T is defined as C_E/T_o where C_E is the heat capacity and T_o is the reference temperature. These equations can be derived from the thermodynamic function as explained in Chapter 4.

2.4 Concluding Remarks

The main dissipation mechanisms that occur in MEMS and consequently, limit the quality factor of micro-resonators have been presented. From this review, thermoelastic damping can be considered as the most important loss source in high-Q micro-resonators using flexural vibration modes. Indeed, since high-Q micro-resonators are designed to avoid extrinsic losses and their material is chosen to have a good intrinsic quality, their quality factor is limited by thermoelastic damping which is the main intrinsic loss source unless the surface-to-volume becomes really high.

With present micromachining techniques, fabrication process variations in MEMS are inevitable and especially, when devices are miniaturized to the point of process limitations. In the literature, different works were carried out to quantify the effect of the uncertainties on electrostatically actuated MEMS [8, 81, 100, 124]. These studies considered the material and geometric parameters as random variables and used Monte-Carlo methods as well as first and second order reliability methods. Another approach to avoid the detrimental effect of these uncertainties is to design MEMS whose performances are not sensitive to the uncertain design parameters [92, 101, 102]. In Part II of this dissertation, a stochastic finite element method is investigated in order to take into account the effects of the uncertainties on the quality factor of micro-resonators.

Finally, the VIA, i.e. the Vibrating Inertial Accelerometer developed at ONERA is presented. This accelerometer is an example of a micro-resonator whose quality factor is limited by thermoelastic damping and will constitute the application case of this dissertation. Thermopiezoelectric constitutive equations are used in the finite element formulation, allowing the determination of the thermoelastic quality factor of piezoelectrically actuated micro-resonators such as VIA (Chapter 4).

Part I

Deterministic Analyses

Chapter 3

Fundamentals of Thermoelastic Damping

In this chapter, thermoelastic damping is analyzed analytically. Firstly, the process of thermoelastic damping is explained. Two basic analytical models are then presented. On the one hand, Zener's well known model [157] is exposed. On the other hand, based on Lifshitz and Roukes work [91], the equations of linear thermoelasticity are used to derive the natural frequencies of a thermoelastic beam as well as its quality factor. Finally, the relevant literature based on these two models is reviewed.

3.1 The Process of Thermoelastic Damping

The basic notions of thermoelasticity are well known [110]. The term "thermoelastic damping" represents the loss in energy from an entropy rise caused by the coupling between heat transfer and strain rate. Indeed, in isotropic solids with a positive thermal expansion coefficient, an increase of temperature induces a dilatation and inversely, a decrease of temperature produces a compression. Similarly, a dilatation lowers the temperature and a compression raises it. Therefore, when a thermoelastic solid is set in motion, it is taken out of equilibrium, having an excess of kinetic and potential energy. The coupling between the strain and the temperature fields provides an energy dissipation mechanism which allows the system to relax back to the static equilibrium. Relaxation of the thermoelastic

solid is achieved through the irreversible flow of heat driven by local temperature gradients that are generated by the strain field through the coupling.

MEMS resonators generally contain elements which vibrate in flexural modes. In first approximation, this sensitive part can be considered as a simple beam in flexion and it is shown that thermoelastic dissipation may become an important loss mechanism. In a vibrating beam, the two opposite sides undergo opposite deformations. When the upper side is compressed (and consequently, its temperature increases), the lower side is stretched (its temperature decreases), and inversely. Thus, temperature gradients are generated and a relaxation mechanism occurs. However, this dissipation has not always a measurable influence. Indeed, when the vibration frequency is much lower than the relaxation rate, the solid is always in thermal equilibrium and the vibrations are isothermal. On the other hand, when the vibration frequency is much larger than the relaxation rate, the system has no time to relax and the vibrations are adiabatic. Hence, it is only when the vibration frequency is of the order of the relaxation rate that the energy loss becomes appreciable. In MEMS, due to the small dimensions, the response time of both the mechanical and thermal fields have similar order of magnitude and hence, thermoelastic damping has to be taken into account.

3.2 Zener's Standard Model

Zener [158] developed expressions to approximate thermoelastic damping for flexural vibrations of thin rectangular beams. His theory is based on an extension of Hooke's law involving stress σ, strain ε as well as their first time derivatives $\dot{\sigma}$ and $\dot{\varepsilon}$ [158]:

$$\sigma + \tau_\varepsilon \dot{\sigma} = E_R(\varepsilon + \tau_\sigma \dot{\varepsilon}). \tag{3.1}$$

This model is also called the "Standard Anelastic Solid" model. Figure 3.1 represents the mechanical model corresponding to Equation (3.1). This model consists of a spring in parallel with another spring and a dashpot in series. Parameters $k1$, $k2$ and c are related to the three parameters τ_ε, τ_σ and E_R as follows

$$E_R = k_1, \tag{3.2}$$

$$\tau_\varepsilon = \frac{c}{k_2} \tag{3.3}$$

and

$$\tau_\sigma = \frac{k_1 + k_2}{k_1 k_2} c. \tag{3.4}$$

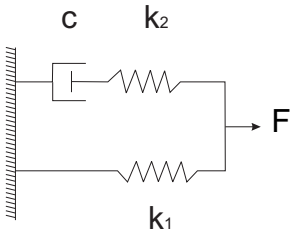

Figure 3.1: Equivalent mechanical model of the standard anelastic solid.

The three parameters τ_ε, τ_σ and E_R have the following physical interpretation:

- τ_ε is the relaxation time associated with the exponential stress relaxation at constant strain,

- τ_σ is the relaxation time associated with the exponential strain relaxation at constant stress,

- E_R is elastic modulus after all relaxations have occurred.

The unrelaxed value of the elastic modulus E_U is defined using the three previous parameters as

$$E_U = E_R \frac{\tau_\sigma}{\tau_\varepsilon}. \tag{3.5}$$

In order to analyze the vibration characteristics of the solid, the stress and the strain are considered to vary harmonically:

$$\sigma = \sigma_o e^{i\omega t}, \tag{3.6}$$

$$\varepsilon = \varepsilon_o e^{i\omega t}. \tag{3.7}$$

Hence, under periodic dynamical conditions, the extended Hooke's law becomes

$$\sigma_o(1 + i\omega\tau_\varepsilon) = \varepsilon_o E_R(1 + i\omega\tau_\sigma). \tag{3.8}$$

The stress and strain amplitudes are related by a frequency-dependent complex elastic modulus:

$$E_o(\omega) = E_R \frac{\sigma_o}{\varepsilon_o} = \frac{1 + i\omega\tau_\sigma}{1 + i\omega\tau_\varepsilon} \tag{3.9}$$

$$= E_R \frac{(1 + i\omega\tau_\sigma)(1 - i\omega\tau_\varepsilon)}{1 + \omega^2\tau_\varepsilon^2} \tag{3.10}$$

$$= E_R \frac{1 + \omega^2\tau_\sigma\tau_\varepsilon + i\omega(\tau_\sigma - \tau_\varepsilon)}{1 + \omega^2\tau_\varepsilon^2}. \tag{3.11}$$

With this complex modulus, the strain is out-of-phase with the applied sinusoidal stress, which leads to an hysteresis.

The dissipation in the solid can be measured by Q^{-1}, the inverse of the quality factor of the resonating beam, which is defined as the fraction of energy lost per cycle. The dissipation associated to the nth mode is equal to the ratio of the imaginary and real parts of the complex modulus at the nth natural pulsation ω_n [75], giving

$$Q^{-1} = \frac{\Im(E_o(\omega_n))}{\Re(E_o(\omega_n))} = \frac{\omega_n(\tau_\sigma - \tau_\varepsilon)}{1 + \omega_n^2\tau_\sigma\tau_\varepsilon} \tag{3.12}$$

$$= \frac{\omega_n\sqrt{\tau_\sigma\tau_\varepsilon}}{1 + \omega_n^2\tau_\sigma\tau_\varepsilon}\left(\sqrt{\frac{\tau_\sigma}{\tau_\varepsilon}} - \sqrt{\frac{\tau_\varepsilon}{\tau_\sigma}}\right) \tag{3.13}$$

$$= \Delta_E \frac{\omega_n\tau}{1 + (\omega_n\tau)^2}, \tag{3.14}$$

where $\tau = \sqrt{\tau_\sigma\tau_\varepsilon}$ is the effective relaxation time and $\Delta_E = \sqrt{\frac{\tau_\sigma}{\tau_\varepsilon}} - \sqrt{\frac{\tau_\varepsilon}{\tau_\sigma}} = \frac{E_U - E_R}{\sqrt{E_R E_U}}$ is the relaxation strength.

Thus, the dissipation exhibits a Lorentzian behavior as a function of $\omega_n\tau$ with a maximum value of $\Delta_E/2$ when $\omega_n\tau = 1$. This agrees with the qualitative explanation of Section 3.1. Indeed, when the frequency is small compared to the relaxation rate, i.e. $\omega_n\tau << 1$, the thermoelastic dissipation is negligible since the oscillations are isothermal. On the other hand, when the frequency is large compared to the relaxation rate, i.e. $\omega_n\tau >> 1$, the oscillations are adiabatic. Therefore, the thermoelastic dissipation only takes importance when the frequency is of the order of the relaxation rate, i.e. $\omega_n\tau \approx 1$.

In order to identify the effective relaxation time and the relaxation strength in the case of thermoelasticity, the extended Hooke's law is to be derived from

the coupled linearized equations:

$$\varepsilon = \frac{\sigma}{E} + \alpha\theta, \tag{3.15}$$

$$\frac{d\theta}{dt} = \frac{\kappa}{C_v}\nabla^2\theta - \frac{E\alpha T_o}{C_v}\frac{d\varepsilon}{dt}, \tag{3.16}$$

where E is Young's modulus, α is the heat expansion coefficient, κ is the heat conduction coefficient, C_v is the heat capacity at constant volume and T_o is the reference temperature. The first equation is Hooke's law involving the contribution of the thermal dilatation on the strain. The second equation is the heat conduction equation involving the thermoelastic coupling term [46].

Applying Fourier transform to the above equations and eliminating the temperature yield an effective transfer function for stress versus strain and the relaxation parameters can be identified. For the Fourier transform, the variables σ, ε and θ are assumed to have periodic time and spatial dependencies: $x(t,x) \Leftrightarrow X(s,k)$. Finally, the quality factor of a thermoelastic flexural beam resonator is given by

$$Q^{-1} = \frac{E\alpha^2 T_o}{C_v}\frac{\omega_n\tau}{1+(\omega_n\tau)^2}, \tag{3.17}$$

where $\tau = C_v k^2/\kappa$ is the effective relaxation time. Therefore, in the case of thermoelasticity, the relaxation strength Δ_E is expressed as follows

$$\Delta_E = \frac{E\alpha^2 T_o}{C_v}. \tag{3.18}$$

In reference [157], Zener assumes that $k = b/\pi$ where b is the vibrating thickness of the beam. This assumption is justified if the relaxation only occurs through the first transverse thermal mode of the beam as defined in [157]. In order to assess the quality factor, the thermoelastic natural frequency ω_n of the beam is needed, but, in first approximation, the isothermal frequency $\omega_{o,n}$ can be used. In order to study the influence of the different parameters on the quality factor, it is interesting to express Q^{-1} as a function of the dimensionless parameter $\zeta = b\sqrt{\frac{\omega_{o,n}}{2\chi}}$ where $\omega_{o,n}$ is the isothermal natural frequency and $\chi = \kappa/C_v$ is the thermal diffusivity . Hence, approximating the frequency by its isothermal value, Q^{-1} is written

$$Q^{-1} = \frac{E\alpha^2 T_o}{C_v}\frac{2\zeta^2/\pi^2}{1+(2\zeta^2/\pi^2)^2}. \tag{3.19}$$

This expression will be used to compare Zener's approximation to another model presented hereafter.

3.3 Thermoelastic Analysis of a Beam

Zener's theory [157], which has been exposed in the previous section, does not allow the estimation of the frequency shift induced by thermoelastic effects. For this purpose, thermoelastic equations of a vibrating beam have been developed.

Lifshitz and Roukes (LR) [91] proposed an analysis based on the same fundamental physics than Zener [157] but in which the transverse temperature profile is more accurately modeled. Their model allows the obtention of an expression for thermoelastic damping for the simple geometry of a rectangular beam. A rectangular beam of length L, width h and height b is considered. The axes are defined so that x is along the length, y is directed along the height and z is in the direction of the width. Pure transverse vibration in the y-direction is considered.

Accounting for the strain arising from both thermal expansion and mechanical stress, the strain tensor components are

$$\varepsilon_{xx} = \frac{\sigma_{xx}}{E} + \alpha\theta, \tag{3.20}$$

$$\varepsilon_{yy} = \varepsilon_{zz} = -\frac{\nu}{E}\sigma_{xx} + \alpha\theta, \tag{3.21}$$

$$\varepsilon_{xy} = \varepsilon_{yz} = \varepsilon_{zx} = 0, \tag{3.22}$$

where ν is the Poisson's ratio. The above equations only involve the stress tensor component σ_{xx}. Indeed, the beam surface is stress free, which means that all stress components but σ_{xx} vanish on the surface. Moreover, because the beam is slender, this holds in the interior.

In the absence of external force, the motion equation of a bending beam is given by

$$\rho_l \frac{\partial^2 w}{\partial t^2} + \frac{\partial^2 M}{\partial x^2} = 0, \tag{3.23}$$

where ρ_l is the linear density of the beam, M is the bending moment and w is the vertical displacement.

According to Bernoulli's beam model, the displacements u and w in the x and y directions are given by

$$u = -\frac{\partial w}{\partial x} y, \qquad w = w(x,t). \tag{3.24}$$

Therefore, the longitudinal strain component is expressed as follows

$$\varepsilon_{xx} = -y\frac{\partial^2 w}{\partial x^2}. \tag{3.25}$$

Using the expression given by Equation (3.20) for the stress σ_{xx} and substituting the longitudinal strain from Equation (3.25), the bending moment can be written as

$$M = -\int_{-b/2}^{b/2} hy\sigma_{xx}dy \tag{3.26}$$

$$= E\frac{\partial^2 w}{\partial x^2}\int_{-b/2}^{b/2} hy^2 dy - \alpha Eh\int_{-b/2}^{b/2}\theta y dy \tag{3.27}$$

$$= EI\frac{\partial^2 w}{\partial x^2} - \alpha EI_T, \tag{3.28}$$

where I and I_T denote the mechanical and thermal area moments of inertia. Finally, the equation of motion for the beam is obtained:

$$\rho_l A\frac{\partial^2 w}{\partial t^2} + \frac{\partial^2}{\partial x^2}(EI\frac{\partial^2 w}{\partial x^2} + E\alpha I_T) = 0. \tag{3.29}$$

This equation does not represent the full thermoelastic coupling, as it only accounts for the modification of the strain due to the thermal expansion. In addition, the heat conduction equation involving the thermoelastic coupling term has to be considered: [46]

$$\frac{\partial\theta}{\partial t} = \chi\nabla^2\theta - \frac{E\alpha T}{(1-2\nu)C_v}\frac{\partial}{\partial t}\sum_j \varepsilon_{jj}. \tag{3.30}$$

Two simplifications can be made to this equation:

- As the temperature increment is very small compared to the reference temperature, the temperature T can be replaced by the reference temperature T_o. This allows the elimination of unnecessary nonlinearities from the problem.

- As the thermal gradients in the plane of the cross section along the y-direction are much larger than gradients along the beam axis and as no gradient exists in the z-direction, $\nabla^2\theta$ can be replaced by $\partial^2\theta/\partial y^2$.

Substituting the value of the strain field using Equations (3.20) and (3.25) and using Equation (3.18) for the expression of the relaxation strength, the heat conduction equation (3.30) becomes

$$\left(1 + 2\Delta_E\frac{1+\nu}{1-2\nu}\right)\frac{\partial\theta}{\partial t} = \chi\frac{\partial^2\theta}{\partial y^2} + y\frac{\Delta_E}{\alpha}\frac{\partial}{\partial t}\left(\frac{\partial^2 w}{\partial x^2}\right). \tag{3.31}$$

Equations (3.29) and (3.31) constitute the coupled thermoelastic problem. They allow the calculation of the thermoelastic coupling effect on the vibration of a thin beam.

If the transverse displacement and the temperature increment are assumed to change harmonically with a pulsation ω, i.e.

$$w(x,t) = w_o(x)e^{i\omega t}, \qquad \theta(x,y,t) = \theta_o(x,y)e^{i\omega t}, \tag{3.32}$$

the temperature profile along the cross section can be first calculated using the heat equation (3.31). Then, using the equation of motion (3.29), the normal modes of vibration and their corresponding frequencies are evaluated.

The heat equation (3.31) gives

$$\frac{\partial^2\theta_o}{\partial y^2} = i\frac{\omega}{\chi}\left((1+2\Delta_E\frac{1+\nu}{1-2\nu})\theta_o - y\frac{\Delta_E}{\alpha}\frac{\partial^2 w_o}{\partial x^2}\right), \tag{3.33}$$

where the term of order Δ_E that multiplies θ_o introduces a correction of order Δ_E^2 and can thus be neglected. It should be noted that the same heat equation would have been obtained if no cross section deformation had been assumed ($\varepsilon_{xx} = \varepsilon_{yy} = 0$) and if the heat conduction equation had been the weak coupling form (3.15). The solution of this differential equation is

$$\theta_o = y\frac{\Delta_E}{\alpha}\frac{\partial^2 w_o}{\partial x^2} + A\sin(ky) + B\cos(ky), \tag{3.34}$$

where $k = \sqrt{i\frac{\omega}{\chi}}$. The coefficients A and B are determined by the thermal boundary conditions on the upper and lower surfaces. It is assumed that these surfaces are thermally insulated, i.e. $\partial\theta_o/\partial y = 0$ at $y = \pm b/2$. Thus, the temperature profile across the beam is given by

$$\theta_o(x,y) = \frac{\Delta_E}{\alpha}\frac{\partial^2 w_o}{\partial x^2}\left(y - \frac{\sin(ky)}{k\cos(\frac{bk}{2})}\right). \tag{3.35}$$

This temperature profile can be substituted in the motion equation (3.29). In fact, the temperature profile is only present in the thermal inertia:

$$I_T = \int_A y\theta dydz \tag{3.36}$$

$$= \frac{\Delta_E}{\alpha}\frac{\partial^2 w_o}{\partial x^2}h\int_{-b/2}^{b/2}(y^2 - y\frac{sin(ky)}{kcos(bk/2)})dye^{i\omega t} \tag{3.37}$$

$$= \frac{\Delta_E}{\alpha}\frac{\partial^2 w_o}{\partial x^2}\frac{hb^3}{12}(1+\frac{24}{b^3k^3}(\frac{bk}{2} - tan(\frac{bk}{2}))e^{i\omega t}. \tag{3.38}$$

Therefore, the thermal inertia can be expressed in terms of the mechanical inertia, the mechanical constants and a function of the pulsation $f(\omega)$:

$$I_T = \frac{\Delta_E}{\alpha}\frac{\partial^2 w_o}{\partial x^2} I(1 + f(\omega))e^{i\omega t}, \tag{3.39}$$

where $f(\omega) = \frac{24}{b^3k^3}(\frac{bk}{2} - \tan(\frac{bk}{2}))$.

Substituting the thermal inertia (Equation (3.39)) in the motion equation (3.29) gives

$$\omega^2 w_o = \frac{EI}{\rho_l A}\left[1 + \Delta_E\left(1 + f(\omega)\right)\right]\frac{\partial^4 w_o}{\partial x^4}, \tag{3.40}$$

which is formally identical to the equation of the isothermal beam with no thermoelastic coupling. The only yet crucial difference is that the isothermal value of Young's modulus E is replaced by a frequency dependent modulus:

$$E_\omega = E\left[1 + \Delta_E\left(1 + f(\omega)\right)\right]. \tag{3.41}$$

When ω becomes very large, $f(\omega) \to 0$ and the Young's modulus tends to its adiabatic value. On the other hand, when the pulsation vanishes to zero, $f(\omega) \to -1$ and the Young's modulus recovers its isothermal value E. For intermediate value of the pulsation, the Young's modulus is complex. The variation of the Young's modulus is represented in Figures 3.2 and 3.3 in terms of the variable $\xi = b\sqrt{\frac{\omega}{2\chi}}$ so that it is not required to fix the values of the beam height b and the thermal diffusivity χ. The relaxation strength value is arbitrarily set to 10. When ξ is smaller than 0.5, the Young's modulus is real and equal to its isothermal value, E. When ξ is greater than 20, the Young's modulus is real and equal to its adiabatic value. The phase reaches a maximum value of 56° for $\xi = 1.2$. An example can be considered to illustrate the order of magnitude of the frequency range in which the Young's modulus takes its isothermal or adiabatic value. For a beam height of 9 nm in silicon, for which the thermal diffusivity is 1.0396e+008 nm^2/s, below a frequency of 100 kHz, the Young's modulus can be considered to be isothermal and over a frequency of 160 MHz, it is adiabatic.

The normal modes of vibration of the beam are given as in the isothermal case by

$$w_o = A\sin(qx) + B\cos(qx) + C\sinh(qx) + D\cosh(qx), \tag{3.42}$$

where the values of A, B, C, D and q are determined by the mechanical boundary conditions at both ends of the beam. $a_n = q_n L$ is the nth dimensionless pulsation

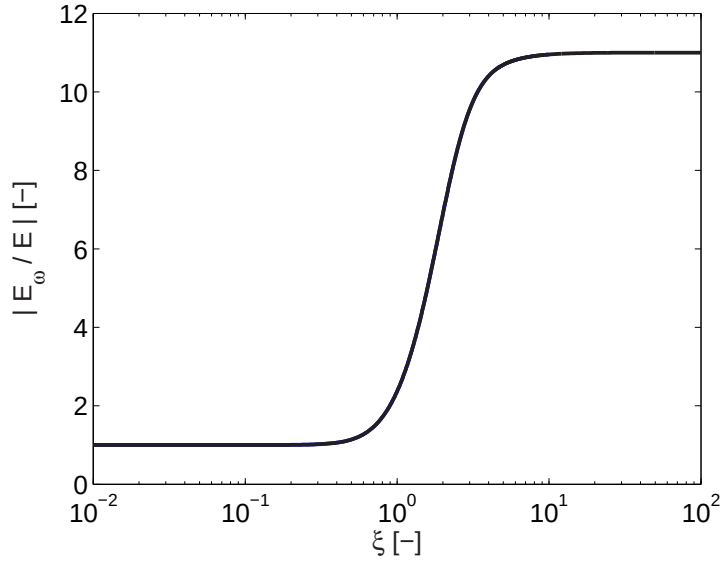

Figure 3.2: Variation of the absolute value of the frequency dependent Young's modulus ($\Delta_E = 10$).

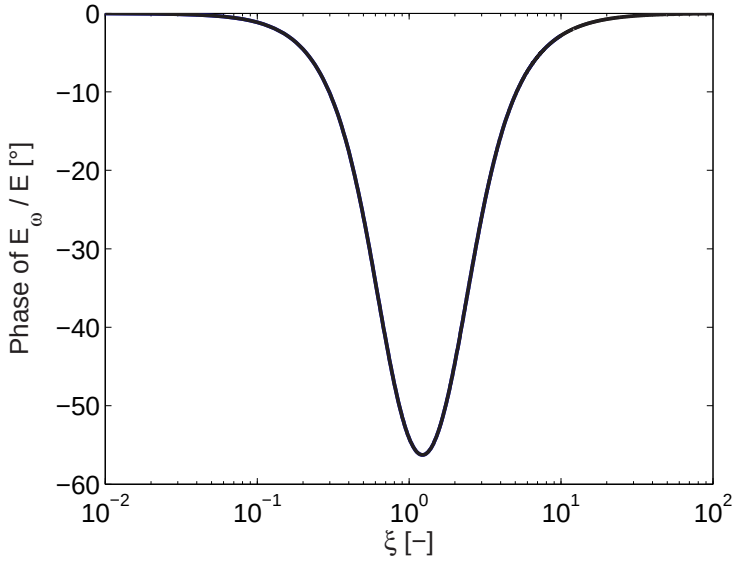

Figure 3.3: Variation of the phase of the frequency dependent Young's modulus ($\Delta_E = 10$).

of the beam whose length is denoted L and q_n is related to the natural pulsation ω_n by

$$q_n^4 = \frac{\rho_l A}{I E_\omega} \omega_n^2. \tag{3.43}$$

The natural pulsation is given by the following intrinsic equation:

$$\omega_n = \sqrt{\frac{E_\omega I}{\rho_l A}} q_n^2 = \omega_{o,n} \sqrt{1 + \Delta_E \left(1 + f(\omega_n)\right)}, \tag{3.44}$$

where $\omega_{o,n}$ is the isothermal resonant pulsation. Neglecting the terms of order Δ_E^2, the value of the thermoelastic resonant pulsation becomes

$$\omega_n = \omega_{o,n} \left[1 + \frac{\Delta_E}{2} \left(1 + f(\omega_n)\right)\right]. \tag{3.45}$$

The implicit nature of this equation is removed if $f(\omega_n)$ is approximated by $f(\omega_{o,n})$, which only introduces an error of order Δ_E^2. Hence, the real and imaginary parts of the thermoelastic pulsation can be extracted from the following equation:

$$\omega_n = \omega_{o,n} \left[1 + \frac{\Delta_E}{2} \left(1 + f(\omega_{o,n})\right)\right]. \tag{3.46}$$

The real part $\Re(\omega_n)$ represents the new resonant pulsation of the beam in the presence of thermoelastic coupling. The frequency shift can be calculated by $(\Re(\omega_n) - \omega_{o,n})/\omega_{o,n}$. The imaginary part $\Im(\omega_n)$ induces an amplitude attenuation of the vibration. It allows the thermoelastic damping to be determined.

$$\Re(\omega_n) = \omega_{o,n} \left[1 + \frac{\Delta_E}{2} \left(1 - \frac{6}{\zeta^3} \frac{\sinh\zeta - \sin\zeta}{\cosh\zeta + \cos\zeta}\right)\right], \tag{3.47}$$

$$\Im(\omega_n) = \omega_{o,n} \frac{\Delta_E}{2} \left(\frac{6}{\zeta^3} \frac{\sinh\zeta + \sin\zeta}{\cosh\zeta + \cos\zeta} - \frac{6}{\zeta^2}\right), \tag{3.48}$$

where

$$\zeta = b \sqrt{\frac{\omega_{o,n}}{2\chi}}. \tag{3.49}$$

The quality factor can be expressed in terms of the imaginary and real parts of the pulsation. The inverse of the quality factor, which is the fraction of energy lost per radian, is given by

$$Q^{-1} = \frac{2\,|\Im(\omega_n)|}{\sqrt{\Re^2(\omega_n) + \Im^2(\omega_n)}}, \tag{3.50}$$

where the factor 2 arises from the fact that the mechanical energy of the beam is proportional to the square of the amplitude of deformation. Note that this

definition of the quality factor is the same as the usual one expressed in terms of the damping ratio ξ: $Q = 1/2\xi$. This can be checked by considering that $\omega_n = \sqrt{1-\xi^2}\omega_{o,n} + i\xi\omega_{o,n}$ in Equation (3.50).

As the imaginary part of the resonant pulsation can be considered to be small compared to the real part, the inverse of the quality factor can be approximated by the following expression:

$$Q^{-1} \approx 2\left|\frac{\Im(\omega_n)}{\Re(\omega_n)}\right|. \tag{3.51}$$

Finally, substituting Equations (3.47) and (3.48) in Equation (3.51), the inverse of the quality factor is given by

$$Q^{-1} = \frac{E\alpha^2 T_o}{C_v}\left(\frac{6}{\zeta^2} - \frac{6}{\zeta^3}\frac{\sinh\zeta + \sin\zeta}{\cosh\zeta + \cos\zeta}\right). \tag{3.52}$$

It should be recalled that this theory has been developed to the first order of Δ_E and that it considers the effect of thermal deformation on the strain but neglects the relaxation in the longitudinal direction.

3.4 Model Comparison

In this section, the results obtained from Zener and LR models are compared. These models differ in the way the transverse temperature profile is approximated. Both methods allow an analytical expression of the quality factor to be obtained, but only LR model gives the expression of the complex thermoelastic natural frequencies, allowing the frequency shift as well as the attenuation due to thermoelastic effects to be quantified.

Firstly, the expressions of the inverse of the quality factor are considered (Equations (3.19) and (3.52)). In both cases, the ratio Q^{-1}/Δ_E can be expressed as a convex function of the dimensionless isothermal natural frequency ζ, which is represented in Figure 3.4. Both models give similar results and present a maximum at $\zeta \approx 2.225$. The peak value depends on the Young's modulus, the heat expansion coefficient and the heat capacity and not on the dimensions of the beam. However, the dimensions influence the dissipation by means of the

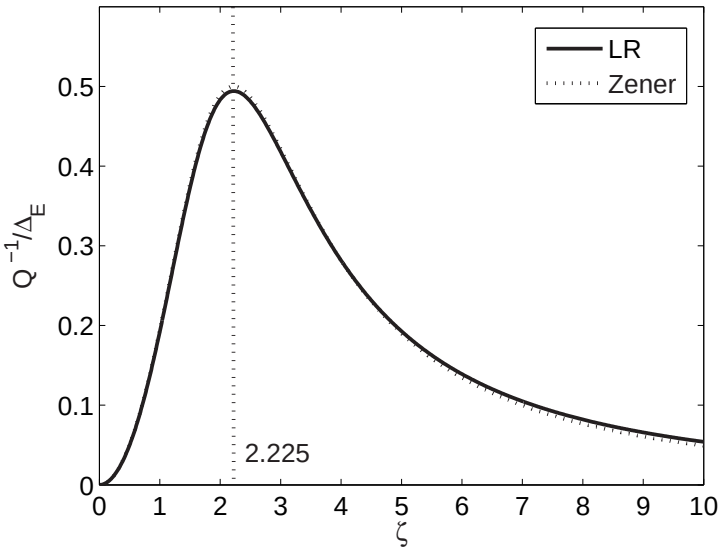

Figure 3.4: Variation of the inverse of the quality factor in units of the relaxation strength with respect to the dimensionless variable ζ.

variable ζ since

$$\zeta = b\sqrt{\frac{\omega_{o,n}}{2\chi}} \tag{3.53}$$

$$= b\left(\frac{q_n^2 b}{2\chi L^2}\sqrt{\frac{E}{12\rho}}\right)^{0.5}, \tag{3.54}$$

where ρ is the mass density. The quality factors predicted by LR model differ from Zener's ones by between 2 % and 20 % depending on the value of the dimensionless parameter ζ. Indeed, it can be shown [91] that the quality factor given by Equation (3.52) is bounded between two Lorentzians:

$$\Delta_E \frac{2\sqrt{6}}{5}\mathcal{L}\left(\frac{\zeta^2}{\sqrt{24}}\right) \leq Q^{-1} \leq \Delta_E \frac{\sqrt{6}}{2}\mathcal{L}\left(\frac{\zeta^2}{\sqrt{24}}\right), \tag{3.55}$$

where the Lorentzian $\mathcal{L}$ is defined as

$$\mathcal{L}(\eta) = \frac{\eta}{1+\eta^2}. \tag{3.56}$$

For small values of ζ, the quality factor tends to its lower Lorentzian bound, while for large values of ζ, it tends to its upper Lorentzian bound. Zener's solution

corresponds to the following Lorentzian:

$$Q^{-1} = \mathcal{L}\left(\frac{2\zeta^2}{\pi^2}\right). \tag{3.57}$$

It results from this comparison that expressions (3.19) and (3.52) differ by less than 2% on the isothermal side of the peak (low ζ), while on the adiabatic side of the peak (high ζ), the difference can reach 20 %. Hence, when considering configurations located on the adiabatic side of the peak, it is better to use LR model than Zener's approximation.

Mathematically, the difference is explained by the inherent approximations assumed in the transverse temperature profiles, which are illustrated in Figure 3.5. Assuming that the temperature conduction occurs through the first transverse thermal mode, Zener's model approximate the transverse temperature profile by a sinusoidal function:

$$\frac{\theta(y)}{\theta_{max}} = sin\left(\frac{\pi y}{y_{max}}\right), \tag{3.58}$$

whereas according to Equation (3.35), LR transverse temperature profile can be expressed as

$$\frac{\theta(y)}{\theta_{max}} = \left(y - \frac{\sin(ky)}{k\cos(y_{max}k)}\right). \tag{3.59}$$

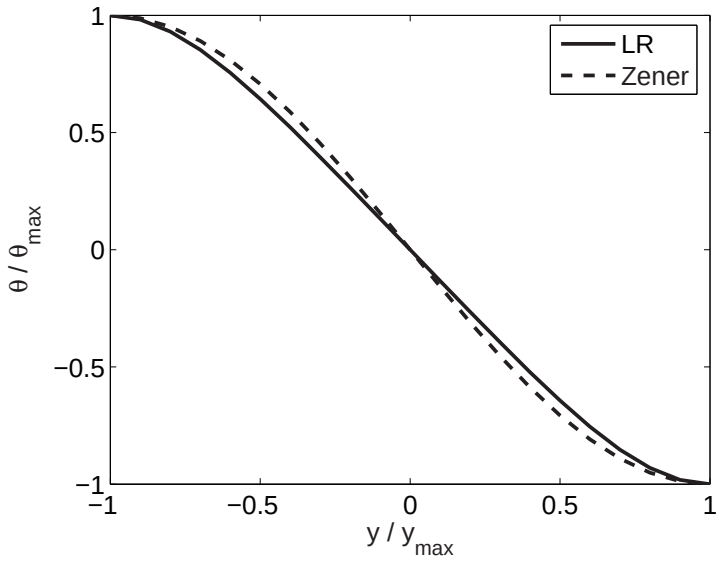

Figure 3.5: Transverse temperature profile.

The influence of the geometry on the thermoelastic dissipation can be shown by studying the variation of Q^{-1} with the beam height for a fixed beam length L. This variation is plotted in Figure 3.6. This figure shows that for a given length, there exists a height for which the thermoelastic dissipation is maximum.

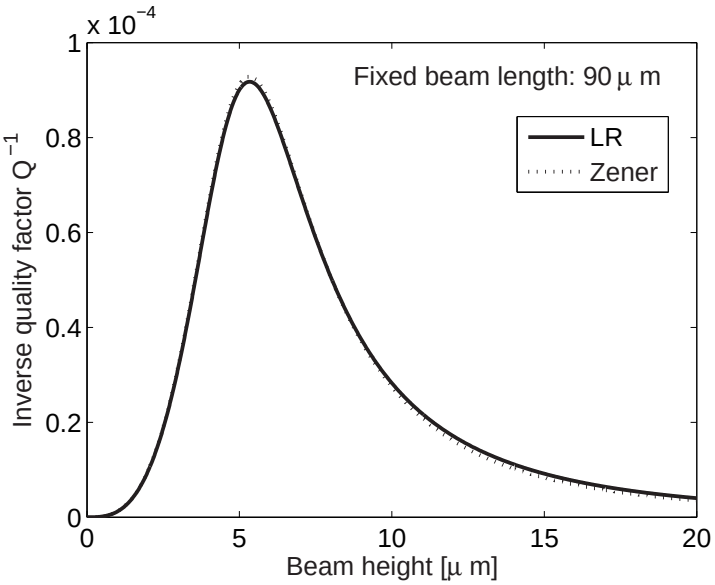

Figure 3.6: Variation of the inverse of the quality factor with the height for a fixed length of 90 μm.

From LR model, the imaginary and real parts of the thermoelastic frequency are given by Equations (3.48) and (3.47). They depend on the material property Δ_E. The frequency shift $\frac{\Re(\omega_n)-\omega_{o,n}}{\Delta_E \omega_{o,n}}$ and the imaginary attenuation $\frac{\Im(\omega_n)}{\Delta_E \omega_{o,n}}$ are plotted in Figure 3.7 as a function of ζ. The frequency shift varies from zero for small values of ζ, for which the beam can be considered isothermal, to the adiabatic threshold value for large values of ζ. The adiabatic frequency shift threshold is equal to $\Delta E/2$ while at the thermoelastic damping peak, the frequency shift reaches a value of $\Delta E/4$. The value of the frequency shift only depends on material data through the parameter ΔE. The attenuation presents a maximum for $\zeta \approx 2.225$ as the thermoelastic dissipation does. The value of the attenuation maximum is equal to $\Delta E/4$ and therefore, only depends on material data parameters. The shape of the attenuation curve is similar to the inverse of the quality factor one, which is coherent since the imaginary part of the frequency

represents the damping.

As ζ represents the dependence on the geometry, the complex frequency depends on the geometry. Figure 3.8 illustrates the variation of the frequency shift and the attenuation with respect to the height of the beam for a fixed length. For frequency-agile mechanisms, it is important to note that the geometry of the beam has an influence on the quality factor but also on the natural frequency. It also should be noted that all models assume that the upper and lower surfaces are thermally insulated. This assumption is adequate for micro-structures under vacuum since there is no heat exchange by convection and since the temperature remains low, heat radiation can be neglected.

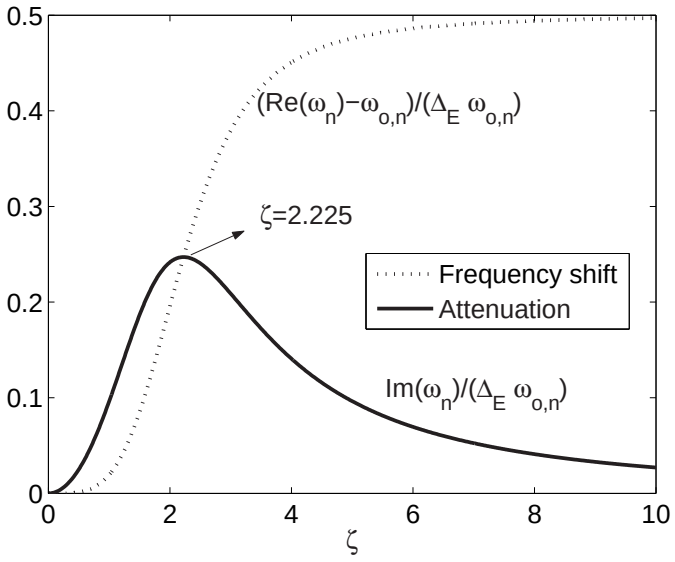

Figure 3.7: Variation of the frequency shifting and attenuation with the dimensionless variable ζ.

3.5 Extension of Classical Models

The analytical models of Zener and Lifshitz-Roukes are based on very restrictive assumptions and are only adequate for the study of thermoelastic damping

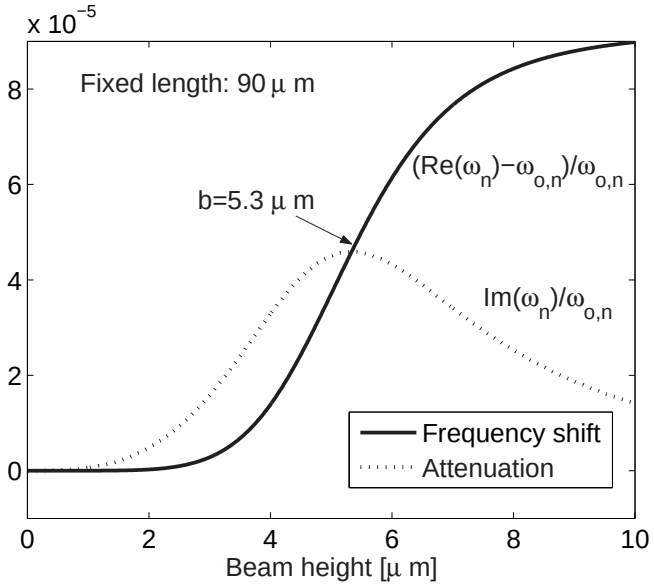

Figure 3.8: Variation of the frequency shifting and attenuation with the height for a fixed length of 90 μm.

in isotropic homogeneous flexural beams. Two different approaches are used in the literature in order to extend these analytical models to some more complex structures: an approach based on energy considerations and an approach based on the resolution of the thermoelasticity equations.

The energy approach can be viewed as an extension of Zener's model. The method consists in identifying the mode through which the energy is dissipated and especially, in quantifying the thermal path lengths that are involved in the relaxation process. Houston et al [67, 68] assume that the energy loss occurs solely via flexural motion. Therefore, defining a flexural modal participation factor, i.e. the fraction of potential energy stored in flexure, and applying this to Zener's theory, these authors quantify the thermoelastic damping occurring in a silicon double paddle oscillators. Wong et al [150] also derive the quality factor of slotted beams by studying their strain energy and the corresponding thermal path lengths. Bishop and Kinra [21] study thermoelastic damping of laminated beams. Knowing the specific thermal path length for each layer, they derive the quality factor of the laminated beam using an energy approach. Using the analytical framework developed by Bishop and Kinra, Vengallatore [147] shows that metallization of silicon and silicon carbide beams can lead to a considerable in-

crease in damping as well as coating silicon with SiC. Based on similar procedure, Srikar and Senturia [136] present a closed-form expression to estimate an upper bound of the attainable quality factors of polycrystalline beam resonators with thickness much larger than the average grain size.

The second approach is based on the resolution of thermoelasticity equations as Lifshitz-Roukes model. Wong et al [149] derive an analytical expression for the thermoelastic quality factor of the in-plane vibration of thin silicon rings. The presented methodology is exactly the same as in LR work. Moreover, the obtained results are compared with the results obtained with a modified Zener model and this comparison shows that both approaches agree to within 2 %. Younis [106, 156] presents a model to quantify the thermoelastic quality factors of microplates. He solves the heat equation for the heat flow across the microplate so that the thermal equation is decoupled from the mechanical plate equation. Then a perturbation method allows the derivation of an analytical expression for the thermoelastic quality factor of microplates. This model takes into account electrostatic loading as well as residual stresses.

In order to investigate more complex structures (i.e. non rectangular geometry, anisotropic material,...), a numerical approach is required. In order to analyze thermoelastic damping in 1-D longitudinal vibrations, Zhang et al [161] discretize the thermoelasticity equations and hence, solving the corresponding PDE's, get the value of the thermoelastic quality factor. A preliminary finite element method is developed by Gorman [59]. Due to the chosen finite element formulation, the resulting model is only suitable for isotropic problems. Moreover, this finite element formulation leads to an imaginary eigenvalue problem whose resolution is computationally expensive. This method is thus restricted to small size models, such as slotted beams [25].

3.6 Concluding Remarks

In this chapter, two classical analytical models, i.e. Zener and LR models, have been presented for a vibrating thermoelastic beam. The thermoelastic coupling has been shown to introduce an energy loss as well as a natural frequency shift in vibrating beams. The importance of the thermoelastic effects depends on the dimensions of the vibrating beam as well as on its material properties, whereas

the upper bound value of the energy loss factor only depends on the material data parameters.

Both classical models only hold for simple geometries and isotropic solids and are not applicable to structures involving a more complex geometry or made of an anisotropic material. Some extended analytical models have been reviewed, but these methods are not straightforward and are still restricted to simple problems. Hence, another method should be developed to predict the thermoelastic effects.

Some preliminary work on numerical methods have also been found in the literature. Even if these results are promising, the adopted formulations limit their applicability. The development of a more general thermoelastic finite element formulation will allow the prediction of the thermoelastic effects for complex geometries and anisotropic materials.

Chapter 4

Thermopiezoelectric Finite Element Formulation

This chapter concerns the finite element formulation of thermopiezoelectricity. The first part of this chapter is concerned with a unified variational principle describing the fundamental equations of thermopiezoelectricity. Then, the finite element matrices associated with thermopiezoelectricity are derived. A non-symmetric block Lanczos method is exposed in order to solve the thermopiezoelectric eigenproblem. Finally, the finite element formulation is validated for a one-dimensional problem for which an analytical solution is available.

4.1 Variational Principle

To describe the behavior of a thermopiezoelectric continuum, the coupled contributions of the thermal, electric and mechanical fields have to be taken into account. Indeed, the total free energy B of a thermopiezoelectric body is given by the following equation [1] [9]:

$$B(\varepsilon_{ij}, E_i, \theta) = \frac{1}{2}c_{ijkl}\varepsilon_{ij}\varepsilon_{kl} - e_{ijk}E_i\varepsilon_{jk} - \frac{1}{2}b_{ij}E_iE_j - k_{ij}\theta\varepsilon_{ij} - d_iE_i\theta - \frac{1}{2}a_T\theta^2, \quad (4.1)$$

where ε_{ij} are the components of the strain tensor, E_i are the components of the electric field vector, and θ is the temperature rise from the reference tempera-

[1] Einstein's notation is used.

ture T_0, at which the structure is unstrained and unstressed. The quantities c_{ijkl} and e_{ijk} respectively represent the elastic and piezoelectric constants and b_{ij} is the dielectric permittivity. The quantities k_{ij} and d_i respectively represent the thermo-mechanical and the thermopiezoelectric coupling constants and a_T is defined as C_E/T_0, where C_E is the heat capacity. To take into account the heat conduction, the dissipation function F has to be considered [9]:

$$F(e_i) = \frac{1}{2}\kappa_{ij}e_j e_i, \tag{4.2}$$

where κ_{ij} are the components of the conductivity tensor and e_i are the components of the thermal field vector.

Consequently, using the thermodynamic formulation, the constitutive equations can be derived from the total free energy whereas Fourier's law can be derived from the dissipation function:

$$\sigma_{ij} = \frac{\partial B}{\partial \varepsilon_{ij}} = c_{ijkl}\varepsilon_{kl} - e_{ijk}E_k - k_{ij}\theta, \tag{4.3}$$

$$D_i = -\frac{\partial B}{\partial E_i} = e_{ijk}\varepsilon_{jk} + b_{ij}E_j + d_i\theta, \tag{4.4}$$

$$S = -\frac{\partial B}{\partial \theta} = k_{ij}\varepsilon_{ij} + d_i E_i + a_T\theta, \tag{4.5}$$

$$q_i = \frac{\partial F}{\partial e_i} = \kappa_{ij}e_j, \tag{4.6}$$

where σ_{ij} are the components of the stress tensor, D_i are the components of the electric displacement vector, S is the entropy and q_i are the components of the heat flux vector.

In order to apply the variational principle, some assumptions are considered. Three assumptions, one for each physical field, give rise to the following compatibility equations:

- Based on the assumption of small displacements, the strain can be expressed in terms of the displacements u_i

$$\varepsilon_{ij} = \frac{1}{2}(u_{i,j} + u_{j,i}), \tag{4.7}$$

  where the notation $,i$ represents the partial derivative $\partial/\partial x_i$.

- Based on linear piezoelectricity, the electric field vector is derivable from a scalar potential function Φ as follows

$$E_i = -\Phi_{,i}. \tag{4.8}$$

- Based on Fourier's law, the thermal field vector can be expressed as the gradient of the temperature increment

$$e_i = -\theta_{,i}. \tag{4.9}$$

In order to obtain the dynamic equations of a thermopiezoelectric continuum, Hamilton's principle is used:

$$\delta \int_{t_1}^{t_2} (\mathcal{L} + \mathcal{W}) dt = 0, \tag{4.10}$$

in which all variations vanish at times t_1 and t_2, i.e. $\delta_{u_i}(t_1) = 0$, $\delta_{u_i}(t_2) = 0$, $\delta_\theta(t_1) = 0$, $\delta_\theta(t_2) = 0$,... The Lagrangian $\mathcal{L}$ and the virtual work $\mathcal{W}$ of external contributions have to include the thermal, electric and mechanical contributions. For a thermopiezoelectric domain Ω with an external surface S^*, the Lagrangian can be defined as follows [9]

$$\mathcal{L} = \int_\Omega (K + F - B - S\theta - ST_0\dot{\theta}) d\Omega, \tag{4.11}$$

where $K = \frac{1}{2}\rho \dot{u}_i \dot{u}_i$ is the kinetic energy density.

Using Equations (4.1) to (4.6), B and F become

$$B = \frac{1}{2}\sigma_{ij}\varepsilon_{ij} - \frac{1}{2}D_i E_i - \frac{1}{2}S\theta, \tag{4.12}$$

$$F = \frac{1}{2}q_i e_i. \tag{4.13}$$

Taking into account the three compatibility equations (4.7) to (4.9), the variation of the Lagrangian is decomposed into independent variations with respect to the displacement components u_i, the electric potential Φ and the temperature increment θ. Making use of the interchangeability of variation with differentiation or integration and integrating by parts with respect to time, the variational

equations are obtained:

$$\begin{aligned}
\delta_u\mathcal{L}+\delta_u\mathcal{W} &= -\int_{t_1}^{t_2}\int_{\Omega}\left[\rho\ddot{u}_i\delta u_i+\sigma_{ij}\delta\varepsilon_{ij}\right]d\Omega dt+\int_{t_1}^{t_2}\int_{S^*}t_i\delta u_i dS^* dt,\\
&+ \int_{\Omega}\rho\dot{u}_i\delta u_i|_{t_1}^{t_2}d\Omega\\
&= 0, \qquad (4.14)\\
\delta_\Phi\mathcal{L}+\delta_\Phi\mathcal{W} &= \int_{t_1}^{t_2}\int_{\Omega}D_i\delta E_i d\Omega dt+\int_{t_1}^{t_2}\int_{S^*}q_e\delta\Phi dS^* dt,\\
&= 0, \qquad (4.15)\\
\delta_\theta\mathcal{L}+\delta_\theta\mathcal{W} &= \int_{t_1}^{t_2}\int_{\Omega}\left[q_i\delta e_i+\dot{S}T_0\delta\theta\right]d\Omega dt+\int_{t_1}^{t_2}\int_{S^*}q_s\delta\theta dS^* dt\\
&- \int_{\Omega}ST_0\delta\theta|_{t_1}^{t_2}d\Omega\\
&= 0, \qquad (4.16)
\end{aligned}$$

where t_i, q_e and q_s respectively represent the components of the traction vector, the charge density and heat flux.

As each variation vanishes at times $t=t_1$ and $t=t_2$ and recalling Equations (4.8) and (4.9), the governing equations of the coupled thermopiezoelectricity take the final form:

$$\begin{aligned}
\delta_u\mathcal{L}+\delta_u\mathcal{W} &= -\int_{t_1}^{t_2}\int_{\Omega}\left[\rho\ddot{u}_i\delta u_i+\sigma_{ij}\delta\varepsilon_{ij}\right]d\Omega dt+\int_{t_1}^{t_2}\int_{S^*}t_i\delta u_i dS^* dt\\
&= 0, \qquad (4.17)\\
\delta_\Phi\mathcal{L}+\delta_\Phi\mathcal{W} &= -\int_{t_1}^{t_2}\int_{\Omega}D_i\delta\Phi_{,i}d\Omega dt+\int_{t_1}^{t_2}\int_{S^*}q_e\delta\Phi dS^* dt\\
&= 0, \qquad (4.18)\\
\delta_\theta\mathcal{L}+\delta_\theta\mathcal{W} &= \int_{t_1}^{t_2}\int_{\Omega}\left[-q_i\delta\theta_{,i}+\dot{S}T_0\delta\theta\right]d\Omega dt+\int_{t_1}^{t_2}\int_{S^*}q_s\delta\theta dS^* dt\\
&= 0. \qquad (4.19)
\end{aligned}$$

Equations (4.17)-(4.19) involve the coupling between temperature, electric and mechanical fields simultaneously and they are based on the assumption of no body force or heat source.

4.2 Finite Element Formulation

In the finite element formulation, the three continuous physical fields are discretized. The displacement field $\mathbf{u}$, the electric potential Φ and the temperature

increment θ are related to the corresponding node values $\mathbf{u_u}$, $\mathbf{u_\Phi}$ and $\mathbf{u}_\theta$ by means of shape function matrices $\mathbf{N_u}$, $\mathbf{N_\Phi}$ and $\mathbf{N}_\theta$:

$$\mathbf{u} = \mathbf{N_u u_u}, \tag{4.20}$$

$$\Phi = \mathbf{N_\Phi u_\Phi}, \tag{4.21}$$

$$\theta = \mathbf{N}_\theta \mathbf{u}_\theta. \tag{4.22}$$

Therefore, the strain field $\boldsymbol{\varepsilon}$, the electric field $\mathbf{E}$ and the thermal field $\mathbf{e}$ are related to the degree of freedom vector, i.e. to the nodal values, by the shape function derivative matrices $\mathbf{B_u}$, $\mathbf{B_\Phi}$ and $\mathbf{B}_\theta$:

$$\boldsymbol{\varepsilon} = \mathcal{D}\mathbf{N_u u_u} = \mathbf{B_u u_u}, \tag{4.23}$$

$$\mathbf{E} = -\nabla \mathbf{N_\Phi u_\Phi} = \mathbf{B_\Phi u_\Phi}, \tag{4.24}$$

$$\mathbf{e} = -\nabla \mathbf{N}_\theta \mathbf{u}_\theta = \mathbf{B}_\theta \mathbf{u}_\theta, \tag{4.25}$$

where ∇ is the gradient operator and $\mathcal{D}$ is the derivation operator defined so that $\varepsilon = \mathcal{D}\mathbf{u}$ according to Equation (4.7).

Equations (4.3)-(4.6) can be rewritten in vector form:

$$\boldsymbol{\sigma} = \mathbf{Q}\boldsymbol{\varepsilon} - \mathbf{P}\mathbf{E} - \mathbf{k}\theta, \tag{4.26}$$

$$\mathbf{D} = \mathbf{P^T}\boldsymbol{\varepsilon} + \mathbf{B}\mathbf{E} + \mathbf{d}\theta, \tag{4.27}$$

$$S = \mathbf{k^T}\boldsymbol{\varepsilon} + \mathbf{d^T}\mathbf{E} + a_T\theta, \tag{4.28}$$

$$\mathbf{q} = \boldsymbol{\kappa}\mathbf{e}, \tag{4.29}$$

where $\boldsymbol{\sigma}$ and $\mathbf{D}$ are respectively the stress vector and the electric displacement vector and $\boldsymbol{\varepsilon}$ and $\mathbf{E}$ are respectively the strain vector and the electric field vector. Matrices $\mathbf{Q}$, $\mathbf{B}$, $\mathbf{P}$, $\mathbf{k}$, $\mathbf{d}$ and $\boldsymbol{\kappa}$ respectively denote the matrix forms of elastic constant, dielectric permittivity, piezoelectric constant, thermo-mechanical coupling constant, thermopiezoelectric coupling constant and thermal conductivity.

The introduction of Equations (4.20)-(4.29) in Equations (4.17)-(4.19) yields

the following relations:

$$\begin{aligned}
\delta_u\mathcal{L} &= -\int_{t_1}^{t_2}\int_{\Omega}\delta\mathbf{u}^T\rho\ddot{\mathbf{u}}d\Omega dt - \int_{t_1}^{t_2}\int_{\Omega}\delta\boldsymbol{\varepsilon}^T\boldsymbol{\sigma}d\Omega dt \\
&= -\int_{t_1}^{t_2}\int_{\Omega}[\delta\mathbf{u}^T\rho\ddot{\mathbf{u}} + \delta\boldsymbol{\varepsilon}^T(\mathbf{Q}\boldsymbol{\varepsilon} - \mathbf{P}\mathbf{E} - \mathbf{k}\theta)]d\Omega dt \\
&= -\int_{t_1}^{t_2}\int_{\Omega}\delta\mathbf{u_u}^T[\mathbf{N_u}^T\rho\mathbf{N_u}\ddot{\mathbf{u}}_\mathbf{u} + \mathbf{B_u}^T(\mathbf{Q}\mathbf{B_u}\mathbf{u_u} - \mathbf{P}\mathbf{B_\Phi}\mathbf{u_\Phi} - \mathbf{k}\mathbf{N}_\theta\mathbf{u}_\theta)]d\Omega dt \\
&= -\delta\mathbf{u_u}^T\int_{t_1}^{t_2}(\mathbf{M_{uu}}\mathbf{u_u} + \mathbf{K_{uu}}\mathbf{u_u} + \mathbf{K_{u\Phi}}\mathbf{u_\Phi} + \mathbf{K_{u\theta}}\mathbf{u}_\theta)dt, \qquad (4.30)
\end{aligned}$$

$$\begin{aligned}
\delta_\Phi\mathcal{L} &= \int_{t_1}^{t_2}\int_{\Omega}\delta\mathbf{E}^T\mathbf{D}d\Omega dt \\
&= \int_{t_1}^{t_2}\int_{\Omega}\delta\mathbf{E}^T(\mathbf{P^T}\boldsymbol{\varepsilon} + \mathbf{B}\mathbf{E} + \mathbf{d}\theta)d\Omega dt \\
&= \int_{t_1}^{t_2}\int_{\Omega}\delta\mathbf{u_\Phi}^T\mathbf{B_\Phi}^T(\mathbf{P^T}\mathbf{B_u}\mathbf{u_u} + \mathbf{B}\mathbf{B_\Phi}\mathbf{u_\Phi} + \mathbf{d}\mathbf{N}_\theta\mathbf{u}_\theta)d\Omega dt \\
&= -\delta\mathbf{u_\Phi}^T\int_{t_1}^{t_2}(\mathbf{K_{\Phi u}}\mathbf{u_u} + \mathbf{K_{\Phi\Phi}}\mathbf{u_\Phi} + \mathbf{K_{\Phi\theta}}\mathbf{u}_\theta)dt, \qquad (4.31)
\end{aligned}$$

$$\begin{aligned}
\delta_\theta\mathcal{L} &= \int_{t_1}^{t_2}\int_{\Omega}(\delta\mathbf{e}^T\mathbf{q} + \dot{S}T_0\delta\theta)d\Omega dt \\
&= \int_{t_1}^{t_2}\int_{\Omega}(\delta\mathbf{e}^T\boldsymbol{\kappa}\mathbf{e} + T_0\delta\theta(\mathbf{k^T}\dot{\boldsymbol{\varepsilon}} + \mathbf{d^T}\dot{\mathbf{E}} + a_T\dot{\theta}))d\Omega dt \\
&= \int_{t_1}^{t_2}\int_{\Omega}\delta\mathbf{u}_\theta^T(\mathbf{B}_\theta^T\boldsymbol{\kappa}\mathbf{B}_\theta\mathbf{u}_\theta + T_0\mathbf{N}_\theta^T(\mathbf{k^T}\mathbf{B_u}\dot{\mathbf{u}}_\mathbf{u} + \mathbf{d^T}\mathbf{B_\Phi}\dot{\mathbf{u}}_\mathbf{\Phi} + a_T\mathbf{N}_\theta\dot{\mathbf{u}}_\theta))d\Omega dt \\
&= -\delta\mathbf{u}_\theta^T\int_{t_1}^{t_2}(\mathbf{K}_{\theta\theta}\mathbf{u}_\theta + \mathbf{C}_{\theta\mathbf{u}}\dot{\mathbf{u}}_\mathbf{u} + \mathbf{C}_{\theta\mathbf{\Phi}}\dot{\mathbf{u}}_\mathbf{\Phi} + \mathbf{C}_{\theta\theta}\dot{\mathbf{u}}_\theta)dt. \qquad (4.32)
\end{aligned}$$

The variation of the terms involving the external contributions are written as follows

$$\begin{aligned}
\delta_u\mathcal{W} &= \int_{t_1}^{t_2}\int_{S^*}\delta\mathbf{u}^T\mathbf{t}dS^*dt \\
&= \int_{t_1}^{t_2}\int_{S^*}\delta\mathbf{u_u}^T\mathbf{N_u}^T\mathbf{t}dS^*dt \\
&= \delta\mathbf{u_u}^T\int_{t_1}^{t_2}\mathbf{F_u}dt, \qquad (4.33)
\end{aligned}$$

$$\begin{aligned}\delta_{\Phi}\mathcal{W} &= \int_{t_1}^{t_2}\int_{S^*}\delta\Phi^T q_e dS^* dt \\ &= \int_{t_1}^{t_2}\int_{S^*}\delta\mathbf{u_\Phi}^T\mathbf{N_\Phi}^T q_e dS^* dt \\ &= \delta\mathbf{u_\Phi}^T\int_{t_1}^{t_2}\mathbf{F_\Phi} dt, \end{aligned} \tag{4.34}$$

$$\begin{aligned}\delta_{\theta}\mathcal{W} &= \int_{t_1}^{t_2}\int_{S^*}\delta\theta^T q_s dS^* dt \\ &= \int_{t_1}^{t_2}\int_{S^*}\delta\mathbf{u}_\theta{}^T\mathbf{N}_\theta{}^T q_s dS^* dt \\ &= \delta\mathbf{u}_\theta{}^T\int_{t_1}^{t_2}\mathbf{F}_\theta dt. \end{aligned} \tag{4.35}$$

Hence, the discretized dynamic equilibrium equation governing the thermopiezoelectric problem is obtained:

$$\begin{pmatrix}\mathbf{M_{uu}} & 0 & 0\\ 0 & 0 & 0\\ 0 & 0 & 0\end{pmatrix}\begin{pmatrix}\ddot{\mathbf{u}}_\mathbf{u}\\ \ddot{\mathbf{u}}_\mathbf{\Phi}\\ \ddot{\mathbf{u}}_\theta\end{pmatrix}+\begin{pmatrix}0 & 0 & 0\\ 0 & 0 & 0\\ \mathbf{C}_{\theta\mathbf{u}} & \mathbf{C}_{\theta\mathbf{\Phi}} & \mathbf{C}_{\theta\theta}\end{pmatrix}\begin{pmatrix}\dot{\mathbf{u}}_\mathbf{u}\\ \dot{\mathbf{u}}_\mathbf{\Phi}\\ \dot{\mathbf{u}}_\theta\end{pmatrix}+$$
$$\begin{pmatrix}\mathbf{K_{uu}} & \mathbf{K_{u\Phi}} & \mathbf{K_{u}}\theta\\ \mathbf{K_{\Phi u}} & \mathbf{K_{\Phi\Phi}} & \mathbf{K_{\Phi}}\theta\\ 0 & 0 & \mathbf{K}_{\theta\theta}\end{pmatrix}\begin{pmatrix}\mathbf{u_u}\\ \mathbf{u_\Phi}\\ \mathbf{u}_\theta\end{pmatrix}=\begin{pmatrix}\mathbf{F_u}\\ \mathbf{F_\Phi}\\ \mathbf{F}_\theta\end{pmatrix}, \tag{4.36}$$

where $\mathbf{M_{uu}}$ is the mass matrix, $\mathbf{C}_{\theta\mathbf{u}}$ and $\mathbf{C}_{\theta\mathbf{\Phi}}$ are respectively the damping matrices due to thermo-mechanical and thermo-electric coupling effect and $\mathbf{C}_{\theta\theta}$ is the damping matrix due to the thermal field. Matrices $\mathbf{K_{u\Phi}}$ and $\mathbf{K_{\Phi u}}$ are the stiffness matrices due to piezoelectric-mechanical coupling effect. $\mathbf{K_{u}}\theta$ and $\mathbf{K_{\Phi}}\theta$ are the stiffness matrices due to thermo-mechanical and thermo-electric coupling respectively. $\mathbf{K_{uu}}$, $\mathbf{K_{\Phi\Phi}}$ and $\mathbf{K}_{\theta\theta}$ are the stiffness matrices due to mechanical, electric and thermal fields, respectively. $\mathbf{F_u}$, $\mathbf{F_\Phi}$ and $\mathbf{F}_\theta$ are the force vectors due to mechanical, electric and thermal fields, respectively.

Elementary matrix expressions can be identified from Equations (4.30)-(4.32):

$$\mathbf{M_{uu}} = \int_\Omega \mathbf{N_u}{}^T\rho\mathbf{N_u}d\Omega, \tag{4.37}$$

$$\mathbf{K_{uu}} = \int_\Omega \mathbf{B_u}{}^T\mathbf{Q}\mathbf{B_u}d\Omega, \tag{4.38}$$

$$\mathbf{K_{u\Phi}} = -\int_{\Omega} \mathbf{B_u}^T \mathbf{P} \mathbf{B_\Phi} d\Omega, \tag{4.39}$$

$$\mathbf{K_{u\theta}} = -\int_{\Omega} \mathbf{B_u}^T \mathbf{k} \mathbf{N}_\theta d\Omega, \tag{4.40}$$

$$\mathbf{K_{\Phi u}} = -\int_{\Omega} \mathbf{B_\Phi}^T \mathbf{P}^T \mathbf{B_u} d\Omega, \tag{4.41}$$

$$\mathbf{K_{\Phi\Phi}} = -\int_{\Omega} \mathbf{B_\Phi}^T \mathbf{B} \mathbf{B_\Phi} d\Omega, \tag{4.42}$$

$$\mathbf{K_{\Phi\theta}} = -\int_{\Omega} \mathbf{B_\Phi}^T \mathbf{d} \mathbf{N}_\theta d\Omega, \tag{4.43}$$

$$\mathbf{K}_{\theta\theta} = -\int_{\Omega} \mathbf{B}_\theta{}^T \kappa \mathbf{B}_\theta d\Omega, \tag{4.44}$$

$$\mathbf{C_{\theta u}} = -\int_{\Omega} T_0 \mathbf{N}_\theta{}^T \mathbf{k}^T \mathbf{B_u} d\Omega, \tag{4.45}$$

$$\mathbf{C_{\theta\Phi}} = -\int_{\Omega} T_0 \mathbf{N}_\theta{}^T \mathbf{d}^T \mathbf{B_\Phi} d\Omega, \tag{4.46}$$

$$\mathbf{C}_{\theta\theta} = -\int_{\Omega} T_0 \mathbf{N}_\theta{}^T a_T \mathbf{N}_\theta d\Omega. \tag{4.47}$$

Note that those elementary matrices are not independent since following relations exist:

$$\mathbf{K_{\Phi u}} = \mathbf{K_{u\Phi}}^T, \tag{4.48}$$

$$\mathbf{C_{\theta u}} = T_0 \mathbf{K_{u\theta}}^T, \tag{4.49}$$

$$\mathbf{C_{\theta\Phi}} = T_0 \mathbf{K_{\Phi\theta}}^T. \tag{4.50}$$

Despite relations (4.48)-(4.50), the structural stiffness and damping matrices are not symmetric.

4.3 Formulation of the Thermopiezoelectric Eigenvalue Problem

As shown by Lifshitz and Roukes [91] and discussed in Section 3.4, the thermoelastic coupling induces damping and its effect can also be characterized by a resonance frequency shift. Therefore, it is necessary to compute the eigenvalues of the coupled problem and to derive the quality factor associated with each eigenvalue pair:

$$Q = \left| \frac{\omega_i}{2\omega_r} \right|, \tag{4.51}$$

where ω_i and ω_r are the real and imaginary parts of the conjugate complex eigenvalue.

The generalized quadratic eigenvalue problem to solve results from the governing differential equation (4.36) written in compact form:

$$\mathbf{M}\ddot{\mathbf{q}} + \mathbf{C}\dot{\mathbf{q}} + \mathbf{K}\mathbf{q} = \mathbf{0}, \tag{4.52}$$

where $\mathbf{C}$ and $\mathbf{K}$ are non-symmetric matrices by construction.

Therefore, the homogeneous system has a right-handed and a left-handed solutions of the form:

$$\mathbf{q}_{RHS} = e^{\lambda t}\mathbf{\Phi} \qquad \text{and} \qquad \mathbf{q}_{LHS} = e^{\lambda t}\mathbf{\Psi}, \tag{4.53}$$

where $\mathbf{\Phi}$ is the right eigenvector, $\mathbf{\Psi}$ is the left eigenvector and λ is the eigenvalue, which is the same for the left and the right eigensolutions. When these solutions are substituted into the differential equation (4.52), the right-handed and the left-handed characteristic equations are obtained:

$$(\mathbf{M}\lambda^2 + \mathbf{C}\lambda + \mathbf{K})\mathbf{\Phi} = 0 \qquad \text{and} \qquad \mathbf{\Psi}^T(\mathbf{M}\lambda^2 + \mathbf{C}\lambda + \mathbf{K}) = 0. \tag{4.54}$$

In the following, the resolution method is exposed for the right eigenvalue problem but the same procedure could be applied to the left eigenvalue problem. A linearization transformation [17] is first performed to convert the original quadratic problem of size n into a first order problem of size $2n$. Therefore, the characteristic equations are written in the state-space form using the following relation:

$$\dot{\mathbf{q}}_{RHS} = \lambda\mathbf{q}_{RHS} \tag{4.55}$$

$$= e^{\lambda t}\lambda\mathbf{\Phi}, \tag{4.56}$$

which leads to

$$\begin{bmatrix} -\mathbf{K} & 0 \\ 0 & \mathbf{I} \end{bmatrix} \begin{pmatrix} \mathbf{\Phi} \\ \dot{\mathbf{\Phi}} \end{pmatrix} = \lambda \begin{bmatrix} \mathbf{C} & \mathbf{M} \\ \mathbf{I} & 0 \end{bmatrix} \begin{pmatrix} \mathbf{\Phi} \\ \dot{\mathbf{\Phi}} \end{pmatrix}. \tag{4.57}$$

This equation has the form of a generalized linear eigenvalue problem: $\mathbf{A}\mathbf{x} = \lambda\mathbf{B}\mathbf{x}$. However, the matrix $\mathbf{B}$ is singular due to the massless degrees of freedom Φ and θ. In order to circumvent this problem, Equation (4.57) is repartitioned

between the mechanical, electric and thermal degrees of freedom leading to this eigenvalue problem formulation:

$$\left(\begin{array}{cccc|cc} -\mathbf{K}_{uu} & -\mathbf{K}_{u\Phi} & -\mathbf{K}_{u\theta} & 0 & 0 & 0 \\ -\mathbf{K}_{u\Phi}^T & -\mathbf{K}_{\Phi\Phi} & -\mathbf{K}_{\Phi\theta} & 0 & 0 & 0 \\ 0 & 0 & -\mathbf{K}_{\theta\theta} & 0 & 0 & 0 \\ 0 & 0 & 0 & \mathbf{I} & 0 & 0 \\ \hline 0 & 0 & 0 & 0 & \mathbf{I} & 0 \\ 0 & 0 & 0 & 0 & 0 & \mathbf{I} \end{array}\right) \left(\begin{array}{c} \mathbf{x}_u \\ \mathbf{x}_\Phi \\ \mathbf{x}_\theta \\ \dot{\mathbf{x}}_u \\ \hline \dot{\mathbf{x}}_\Phi \\ \dot{\mathbf{x}}_\theta \end{array}\right) =$$

$$\lambda \left(\begin{array}{cccc|cc} 0 & 0 & 0 & \mathbf{M}_{uu} & 0 & 0 \\ 0 & 0 & 0 & 0 & 0 & 0 \\ \mathbf{C}_{\theta u} & \mathbf{C}_{\theta\Phi} & \mathbf{C}_{\theta\theta} & 0 & 0 & 0 \\ \mathbf{I} & 0 & 0 & 0 & 0 & 0 \\ \hline 0 & \mathbf{I} & 0 & 0 & 0 & 0 \\ 0 & 0 & \mathbf{I} & 0 & 0 & 0 \end{array}\right) \left(\begin{array}{c} \mathbf{x}_u \\ \mathbf{x}_\Phi \\ \mathbf{x}_\theta \\ \dot{\mathbf{x}}_u \\ \hline \dot{\mathbf{x}}_\Phi \\ \dot{\mathbf{x}}_\theta \end{array}\right). \tag{4.58}$$

Due to the block triangular structure of this equation, the eigenvalues associated with the fifth and sixth matrix equations are independent of the four other ones. Indeed, the time derivatives of the electric and thermal degrees of freedom are artificial variables which can be eliminated from the problem so that the eigenvalue problem to solve is

$$\left(\begin{array}{cccc} -\mathbf{K}_{uu} & -\mathbf{K}_{u\Phi} & -\mathbf{K}_{u\theta} & 0 \\ -\mathbf{K}_{u\Phi}^T & -\mathbf{K}_{\Phi\Phi} & -\mathbf{K}_{\Phi\theta} & 0 \\ 0 & 0 & -\mathbf{K}_{\theta\theta} & 0 \\ 0 & 0 & 0 & \mathbf{I} \end{array}\right) \left(\begin{array}{c} \mathbf{x}_u \\ \mathbf{x}_\Phi \\ \mathbf{x}_\theta \\ \dot{\mathbf{x}}_u \end{array}\right) =$$

$$\lambda \left(\begin{array}{cccc} 0 & 0 & 0 & \mathbf{M}_{uu} \\ 0 & 0 & 0 & 0 \\ \mathbf{C}_{\theta u} & \mathbf{C}_{\theta\Phi} & \mathbf{C}_{\theta\theta} & 0 \\ \mathbf{I} & 0 & 0 & 0 \end{array}\right) \left(\begin{array}{c} \mathbf{x}_u \\ \mathbf{x}_\Phi \\ \mathbf{x}_\theta \\ \dot{\mathbf{x}}_u \end{array}\right). \tag{4.59}$$

If the numbers of mechanical, electric and thermal degrees of freedom are denoted n_u, n_Φ and n_θ, respectively, the eigenvalue problem (4.59) has $2n_u$ conjugate complex eigenvalues, n_Φ infinite eigenvalues and n_θ real eigenvalues. The $2n_u$ eigenvalues correspond to the mechanical eigenfrequencies and the n_θ ones to the thermal eigenfrequencies. The n_Φ infinite values correspond to the electric degrees of freedom which do not have any dynamics but respond statically.

In practice, the matrices are scaled before solving the eigenvalue problem. This operation allows to eliminate numerical errors due to the fact that the elements of the submatrices are not of the same order of magnitude. As example, for the thermoelastic beam element of the model used in the next chapter, the diagonal elements of the mechanical stiffness matrix are of the order of 10^{16}, the diagonal elements of the thermal stiffness matrix are of the order of 10^{18} and the diagonal elements of the mass matrix are of the order of 10^{-4} (the units are chosen to be adequate for a micro-problem, i.e. μm, μg and s). The scaling consists in left and right multiplying matrices $\mathbf{A}$ and $\mathbf{B}$ by a diagonal matrix whose elements are the inverse of the square root of the diagonal elements of $\mathbf{A}$, so that the diagonal elements of the scaled matrix $\mathbf{A}$ are equal to 1.

4.4 Non-symmetric Real Block Lanczos Method

The thermopiezoelectric eigenproblem (4.59) is a generalized non-symmetric right eigenproblem:

$$\mathbf{A}\mathbf{q} = \omega\mathbf{B}\mathbf{q}, \tag{4.60}$$

where the matrices $\mathbf{A}$ and $\mathbf{B}$ are non-symmetric real matrices, ω is the eigenvalue, which can be complex, and the vector $\mathbf{q}$ is the right eigenvector, which is complex if ω is complex. To this eigenvalue corresponds a left eigenvector $\mathbf{r}$ which satisfies the eigenproblem:

$$\mathbf{r}^*\mathbf{A} = \omega\mathbf{r}^*\mathbf{B}, \tag{4.61}$$

where $\mathbf{r}^*$ is the conjugate transpose vector of $\mathbf{r}$.

The generalized right eigenproblem (4.60) can be transformed to a standard eigenvalue problem:

$$\mathbf{A}^{-1}\mathbf{B}\mathbf{q} = \frac{1}{\omega}\mathbf{q}, \tag{4.62}$$

which can be directly resolved by the QZ algorithm [13]. However, this method is only adequate for small size problems. For large size problems, an iteration method such as the Lanczos method [83] is more adequate. Making use of the specificity of the eigenproblem (non-symmetric real matrices leading to complex eigenvalues), a non-symmetric real block Lanczos method is developed. This method is a two-sided iterative method based on real subspace oblique projections. It allows the approximation of the complex eigenpairs of a real non-

symmetric matrix by the complex eigensolutions of the real non-symmetric tridiagonal matrix of the Lanczos coefficients.

With two starting real block vectors $\mathbf{X_0}$ and $\mathbf{Y_0}$, the Lanczos method builds a pair of biorthogonal bases for the Krylov subspaces $\mathcal{K}^j(\mathbf{A}^{-1}\mathbf{B}, \mathbf{X_0})$ and $\mathcal{K}^j(\mathbf{A}^{-T}\mathbf{B}^T, \mathbf{Y_0})$:

$$\mathcal{K}^j(\mathbf{A}^{-1}\mathbf{B}, \mathbf{X_0}) = \left[\mathbf{X_0}, \mathbf{A}^{-1}\mathbf{B}\mathbf{X_0}, \left(\mathbf{A}^{-1}\mathbf{B}\right)^2 \mathbf{X_0}, \ldots\right], \tag{4.63}$$

$$\mathcal{K}^j(\mathbf{A}^{-T}\mathbf{B}^T, \mathbf{Y_0}) = \left[\mathbf{Y_0}, \mathbf{A}^{-T}\mathbf{B}^T\mathbf{Y_0}, \left(\mathbf{A}^{-T}\mathbf{B}^T\right)^2 \mathbf{Y_0}, \ldots\right], \tag{4.64}$$

which are biorthogonalized via a two-sided Gram-Schmidt procedure.

The two sequences of block vectors $\mathcal{K}^j(\mathbf{A}^{-1}\mathbf{B}, \mathbf{X_0})$ and $\mathcal{K}^j(\mathbf{A}^{-T}\mathbf{B}^T, \mathbf{Y_0})$ are generated using two three-term recurrences:

$$\mathbf{X_{j+1}}\mathbf{C_{j+1}} = \mathbf{A}^{-1}\mathbf{B}\mathbf{X_j} - \mathbf{X_j}\mathbf{A_j} - \mathbf{X_{j-1}}\mathbf{B_{j-1}}, \tag{4.65}$$

$$\mathbf{Y_{j+1}}\mathbf{F_{j+1}} = \mathbf{A}^{-T}\mathbf{B}^T\mathbf{Y_j} - \mathbf{Y_j}\mathbf{D_j} - \mathbf{Y_{j-1}}\mathbf{E_{j-1}}, \tag{4.66}$$

where matrices $\mathbf{C_{j+1}}$, $\mathbf{A_j}$, $\mathbf{B_{j-1}}$, $\mathbf{F_{j+1}}$, $\mathbf{D_j}$ and $\mathbf{E_{j-1}}$ are such that the bi-orthogonality relations are satisfied:

$$\mathbf{Y_{j+1}}^T\mathbf{B}\mathbf{X_i} = \mathbf{0}, \qquad \text{for} \quad i = 1, \ldots, j \tag{4.67}$$

$$\mathbf{Y_i}^T\mathbf{B}\mathbf{X_i} = \mathbf{I}, \qquad \text{for} \quad i = 1, \ldots, j+1. \tag{4.68}$$

Therefore, the matrices are given by

$$\mathbf{A_j} = \mathbf{Y_j}^T\mathbf{B}\mathbf{A}^{-1}\mathbf{B}\mathbf{X_j}, \tag{4.69}$$

$$\mathbf{B_{j-1}} = \mathbf{Y_{j-1}}^T\mathbf{B}\mathbf{A}^{-1}\mathbf{B}\mathbf{X_j}, \tag{4.70}$$

$$\mathbf{C_{j+1}} = \mathbf{Y_{j+1}}^T\mathbf{B}\mathbf{A}^{-1}\mathbf{B}\mathbf{X_j}, \tag{4.71}$$

$$\mathbf{D_j} = \mathbf{X_j}^T\mathbf{B}^T\mathbf{A}^{-T}\mathbf{B}^T\mathbf{Y_j}, \tag{4.72}$$

$$\mathbf{E_{j-1}} = \mathbf{X_{j-1}}^T\mathbf{B}^T\mathbf{A}^{-T}\mathbf{B}^T\mathbf{Y_j}, \tag{4.73}$$

$$\mathbf{F_{j+1}} = \mathbf{X_{j+1}}^T\mathbf{B}^T\mathbf{A}^{-T}\mathbf{B}^T\mathbf{Y_j}. \tag{4.74}$$

From these expressions, it can be shown that the matrices corresponding to the left and right recurrences are not independent:

$$\mathbf{A_j} = \mathbf{D_j}^T, \quad \mathbf{C_j} = \mathbf{E_{j-1}}^T \quad \text{and} \quad \mathbf{F_j} = \mathbf{B_{j-1}}^T. \tag{4.75}$$

It can be observed that the orthogonality of the new iterates with respect to the previous ones is automatically obtained by recurrence.

In matrix notation, at the jth step, the Lanczos method generates two matrices $\mathbf{X}$ and $\mathbf{Y}$:

$$\mathbf{X} = [\mathbf{X_0}, \ldots, \mathbf{X_j}], \tag{4.76}$$

$$\mathbf{Y} = [\mathbf{Y_0}, \ldots, \mathbf{Y_j}], \tag{4.77}$$

which satisfy the Lanczos factorizations:

$$\mathbf{A}^{-1}\mathbf{B}\mathbf{X} = \mathbf{X}\mathbf{T_R} + \mathbf{X_{j+1}}\mathbf{C_{j+1}}\mathbf{e_j}^T, \tag{4.78}$$

$$\mathbf{A}^{-T}\mathbf{B}^T\mathbf{X} = \mathbf{Y}\mathbf{T_L} + \mathbf{Y_{j+1}}\mathbf{F_{j+1}}\mathbf{e_j}^T, \tag{4.79}$$

where matrices $\mathbf{T_R}$ and $\mathbf{T_L}$ are tridiagonal block matrices:

$$\mathbf{T_R} = \begin{bmatrix} \mathbf{A_0} & \mathbf{B_0} & \cdots & \mathbf{0} & \mathbf{0} \\ \mathbf{C_1} & \mathbf{A_1} & \cdots & \mathbf{0} & \mathbf{0} \\ \vdots & \vdots & \ddots & \vdots & \vdots \\ \mathbf{0} & \mathbf{0} & \cdots & \mathbf{A_{j-1}} & \mathbf{B_{j-1}} \\ \mathbf{0} & \mathbf{0} & \cdots & \mathbf{C_j} & \mathbf{A_j} \end{bmatrix} \tag{4.80}$$

and

$$\mathbf{T_L} = \begin{bmatrix} \mathbf{D_0} & \mathbf{E_0} & \cdots & \mathbf{0} & \mathbf{0} \\ \mathbf{F_1} & \mathbf{D_1} & \cdots & \mathbf{0} & \mathbf{0} \\ \vdots & \vdots & \ddots & \vdots & \vdots \\ \mathbf{0} & \mathbf{0} & \cdots & \mathbf{D_{j-1}} & \mathbf{E_{j-1}} \\ \mathbf{0} & \mathbf{0} & \cdots & \mathbf{F_j} & \mathbf{D_j} \end{bmatrix}, \tag{4.81}$$

so that taking into account relations (4.75), matrices $\mathbf{T_R}$ and $\mathbf{T_L}$ are such that

$$\mathbf{T_R} = \mathbf{T_L}^T. \tag{4.82}$$

The interaction problem is obtained at step j by premultiplying Equation (4.78) by $\mathbf{Y}^T\mathbf{B}$:

$$\begin{aligned} \mathbf{Y}^T\mathbf{B}\mathbf{A}^{-1}\mathbf{B}\mathbf{X} &= \mathbf{Y}^T\mathbf{B}\mathbf{X}\mathbf{T_R} + \mathbf{Y}^T\mathbf{B}\mathbf{X_{j+1}}\mathbf{C_{j+1}}\mathbf{e_j}^T \\ &= \mathbf{T_R}, \end{aligned} \tag{4.83}$$

due to the biorthogonality relations (4.67) and (4.68). This shows that the tridiagonal block matrix $\mathbf{T_R}$ results from the oblique projection of $\mathbf{A}^{-1}\mathbf{B}$ onto the left and right real Lanczos bases. It has thus the same eigensolutions as the oblique

projection of $\mathbf{A}^{-1}\mathbf{B}$ onto the left and right real Lanczos bases. Indeed, starting from the initial inverse right eigenproblem:

$$\mathbf{A}^{-1}\mathbf{B}\mathbf{Q} = \mathbf{Q}\boldsymbol{\Omega}^{-1} \tag{4.84}$$

and writing $\mathbf{Q}$ as a linear combination of the right Lanczos vectors $\mathbf{Q} = \mathbf{X}\mathbf{Z}$, the eigenproblem is expressed as follows

$$\mathbf{A}^{-1}\mathbf{B}\mathbf{X}\mathbf{Z} = \mathbf{X}\mathbf{Z}\boldsymbol{\Omega}^{-1}, \tag{4.85}$$

which, premultiplied by $\mathbf{Y}^T\mathbf{B}$, gives

$$\mathbf{Y}^T\mathbf{B}\mathbf{A}^{-1}\mathbf{B}\mathbf{X}\mathbf{Z} = \mathbf{Y}^T\mathbf{B}\mathbf{X}\mathbf{Z}\boldsymbol{\Omega}^{-1}. \tag{4.86}$$

Using the biorthogonality relations and Equation (4.83), it comes that

$$\mathbf{T}_\mathbf{R}\mathbf{Z} = \mathbf{Z}\boldsymbol{\Omega}^{-1}. \tag{4.87}$$

Eigensolutions $\mathbf{Z}$ and $\boldsymbol{\Omega}^{-1}$ of matrices $\mathbf{T}_\mathbf{R}$ are called the right Ritz vectors and values, respectively and can be calculated via a QZ algorithm. Ritz vectors and values can be complex while $\mathbf{T}_\mathbf{R}$ is real. As the Lanczos bases become larger, the Ritz values and vectors converge to the eigenvalues and eigenvectors of the original matrix $\mathbf{A}^{-1}\mathbf{B}$. This convergence can be evaluated by comparing the norms of the complex eigenvalues to those obtained at the previous step. Hence, if the condition:

$$|\Omega_{i,j}| - |\Omega_{i,j-1}| < \epsilon, \tag{4.88}$$

where $\Omega_{i,j}$ is the ith Ritz value calculated at step j and ϵ is the required precision, is satisfied for $i = 1$ to $i = N_{val}$, the N_{val} first eigenvalues are converged and the N_{val} first right complex eigenvectors can be calculated from the right Ritz vectors:

$$\mathbf{Q} = \mathbf{X}\mathbf{Z}. \tag{4.89}$$

Analogously, the left eigenvectors can be calculated. Firstly, the solutions of the projected problem:

$$\mathbf{T}_\mathbf{L}{}^T\mathbf{T} = \mathbf{T}\boldsymbol{\Omega}^{-1} \tag{4.90}$$

are calculated. Note that the left Ritz values are the same as the right ones, while the left Ritz vectors $\mathbf{T}$ are not equal to the right ones $\mathbf{Z}$. Then, the left eigenvectors are calculated from the left Ritz vectors once convergence is satisfied:

$$\mathbf{R} = \mathbf{Y}\mathbf{T}. \tag{4.91}$$

Note that the proposed algorithm allows to determine complex eigensolutions of a non-symmetric real generalized problem via oblique projections onto real Lanczos bases. Hence, all algebraic operations deal with real vectors and matrices. The complex computational framework is only required at the stage of the convergence checking and at the final step of the calculation of the converged eigenvectors. This procedure provides a less computationally expensive algorithm than the classic non-hermitian block Lanczos method that uses complex Lanczos bases.

4.5 One-Dimensional Thermopiezoelectric Problem

In order to validate the finite element formulation, a simple test case is considered. It consists in an axially vibrating bar of length l fixed at its middle and free at both ends. The thermal boundary conditions, which are in agreement with the mechanical boundary conditions, fix the temperature at both ends. The L-effect coupling is considered for the piezoelectric coupling, which means that the electric condition is given by [71]

$$\frac{dD}{dx} = 0. \tag{4.92}$$

In the following, two-field coupling analyses are firstly carried out. Thermoelastic and piezoelectric couplings are studied via analytical models as well as finite element models. Pyroelectric coupling is not considered in this study. Finally, the three field coupling is modeled analytically and numerically. This approach allows the effects of the different couplings on the frequency and the quality factor of the bar to be identified and physically interpreted.

4.5.1 Thermoelastic Coupling

Analytical Model

The quality factor of a bar in axial vibrations can be approximated by Zener's model (Equation (3.19)). If it is assumed that the relaxation occurs only through the first longitudinal thermal mode, parameter k is given by $k = l/\pi$ where l is the bar length. Moreover, assuming that the thermoelastic frequency can be

approximated by its isothermal value, the quality factor of the bar is expressed as

$$Q^{-1} = \frac{E\alpha^2 T_o}{C_v} \frac{2\zeta^2/\pi^2}{1 + (2\zeta^2/\pi^2)^2}, \tag{4.93}$$

where $\zeta = l\sqrt{\frac{\omega_o}{2\chi}}$ with $\omega_o = \frac{\pi}{l}\sqrt{\frac{E}{\rho}}$.

The complex pulsation of an axially vibrating bar can be assessed from the linear thermoelastic equations [84] which involve:

- the equation of motion with no thermoelastic coupling but with the modified thermoelastic strain

$$-\rho\ddot{u} + E\frac{d^2u}{dx^2} - E\alpha\frac{d\theta}{dx} = 0, \tag{4.94}$$

  where u is the longitudinal displacement and θ is the temperature increment,

- the heat equation with thermoelastic coupling

$$k\frac{d^2\theta}{dx^2} = E\alpha T_0 \frac{d}{dt}\left(\frac{du}{dx}\right) + C_v\frac{d\theta}{dt}. \tag{4.95}$$

The harmonic solutions of the linear thermoelastic equations are considered:

$$u = U_0 e^{i\omega t} \quad \text{and} \quad \theta = \theta_0 e^{i\omega t}. \tag{4.96}$$

It is assumed that the mechanical and thermal mode shapes are not modified by the thermoelastic coupling, i.e. the first mechanical mode is given by

$$U_0 = A\sin\left(\frac{\pi x}{l}\right) \tag{4.97}$$

and the first thermal mode is given by

$$\theta_0 = B\cos\left(\frac{\pi x}{l}\right), \tag{4.98}$$

where the constants A and B are dependent. Indeed, substituting Equations (4.97) and (4.98) in the first linear thermoelastic equation (4.94) gives the following relation:

$$B = A\left(\frac{\pi}{l}\frac{1}{\alpha} - \omega^2\frac{l}{\pi}\frac{\rho}{E\alpha}\right). \tag{4.99}$$

Hence, substituting the mechanical and thermal harmonic solutions in the second linear thermoelastic equation (4.95) gives that the thermoelastic pulsation ω of the bar satisfies the following equation:

$$-\frac{\rho}{E}\left(\frac{l}{\pi}\right)^2 i\omega^3 - \frac{\rho}{E}\frac{k}{C_v}\omega^2 + \left(1 + \frac{T_o\alpha^2 E}{C_v}\right)i\omega + \frac{k}{C_v}\left(\frac{\pi}{l}\right)^2 = 0. \tag{4.100}$$

It should be noted that the thermal mode given by Equation (4.98) considers that the temperature is fixed at both ends, which is in agreement with the mechanical boundary conditions.

Moreover, the thermal eigenvalues can be estimated by analytical solutions in the case of 1-D conduction. Indeed, the method of separation of variables can be used to solve the transient heat conduction equation for a one-dimensional problem:

$$\frac{\partial^2\theta}{\partial x^2} = \frac{C_v}{k}\frac{\partial\theta}{\partial t}. \tag{4.101}$$

It is assumed that the spatial and temporal dependence of the temperature can be separated as follows

$$\theta(x,t) = \theta_o(x)T(t). \tag{4.102}$$

Hence, the heat conduction equation can be written as

$$\frac{1}{\theta_o}\frac{\partial^2\theta_o}{\partial x^2} = \frac{C_v}{kT}\frac{\partial T}{\partial t}. \tag{4.103}$$

This equation is of the form $f(x) = g(t) = -(\lambda)^2$ so that after integration it gives

$$\theta_o(x) = Acos(\lambda x) + Bsin(\lambda x) \tag{4.104}$$

and

$$T(t) = e^{-\frac{C_v}{k}\lambda^2 t}, \tag{4.105}$$

where A and B depend on the boundary conditions. If the temperature of both ends of the bar is fixed, the boundary conditions are expressed as follows

$$\theta_o(0) = 0, \tag{4.106}$$

$$\theta_o(l) = 0. \tag{4.107}$$

Introducing these boundary conditions in Equation (4.104) induces that $A = 0$ and $B\cos(\lambda l) = 0$ for which the non-trivial solution is $\lambda_n = n\pi/l$. Hence, the nth thermal mode can be expressed

$$\theta_{o,n} = cos(n\pi\frac{x}{l}) \tag{4.108}$$

and it temporally varies as

$$T(t) = e^{-\frac{C_v}{k}\left(\frac{n\pi}{l}\right)^2 t}. \tag{4.109}$$

Hence, the thermal eigenvalues are real negative and are given by

$$\omega_{th,n} = -\frac{C_v}{k}\left(\frac{n\pi}{l}\right)^2. \tag{4.110}$$

Finite Element Model

Based on the thermopiezoelectric finite element formulation where the electric degrees of freedom are deleted, a thermoelastic bar element can be developed. The degrees of freedom of the bar element correspond to the temperature increment and to the axial displacement at the end nodes of the element. It uses linear shape functions for the longitudinal variation of both the displacement and the temperature.

The considered material is silicon, as it is largely used in micro-technology. Its thermal and mechanical properties are: $E = 1.5810^{11}\ N/m^2$, $\rho = 2300\ kg/m^3$, $c_v = 711\ J/kgK$, $\alpha = 2.510^{-6}\ K^{-1}$ and $k = 170\ Wm^{-1}K^{-1}$ [62].

According to Equation (4.93), the influence of the thermoelastic coupling on the quality factor is maximum when $2\zeta^2/\pi^2 = 1$. Hence, the importance of the thermoelastic effects depends on the material thermal and mechanical properties as well as on the dimensions of the structure. For a bar in silicon fixed at its center and free at its ends, the thermoelastic effects are maximum when its length is $3.9\ 10^{-8}$ m. Usually, in practice, bars are largely longer than $3.9\ 10^{-8}$ m so that they are in adiabatic regime. However, in order to study the one-dimensional thermoelastic coupling, hypothetical bar lengths from 10^{-9} m to 10^{-6} m are considered.

In order to determine the number of elements that are required to model accurately the thermoelastic effects in the bar, a convergence analysis is carried out for a bar of $3.9\ 10^{-8}$ m. Figure 4.1 shows the variation of the calculated quality factor with respect to the number of elements. Models with more than 20 elements are fine enough in order to determine the thermoelastic quality factor.

Result Discussion

Figure 4.2 shows the variation of the quality factor with the bar length. The analytical models as well as the finite element method give similar results. The quality factor reaches its minimum value of 11304 for a bar length of $3.9\ 10^{-8}$ m. For bar lengths largely lower than $3.9\ 10^{-8}$ m, the thermoelastic damping can be neglected and the regime is isothermal. For bars largely longer than $3.9\ 10^{-8}$ m, which is usually the case in practice, the thermoelastic damping is negligible and the bars are in adiabatic regime.

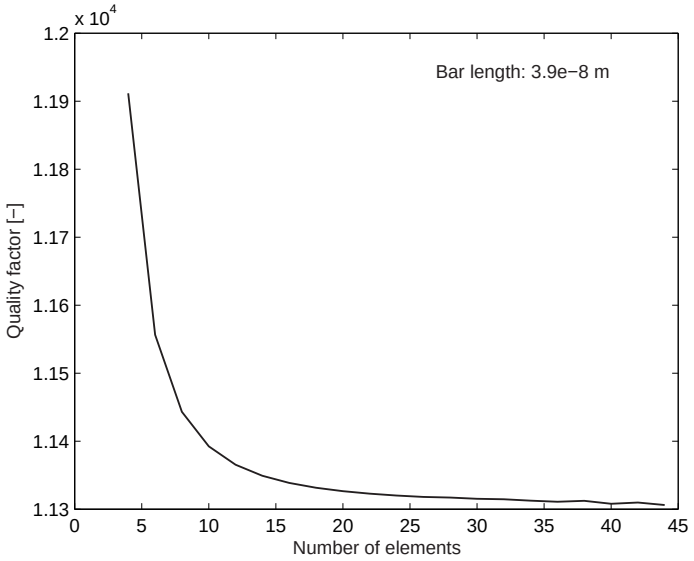

Figure 4.1: Quality factor variation with the number of elements of the finite element model.

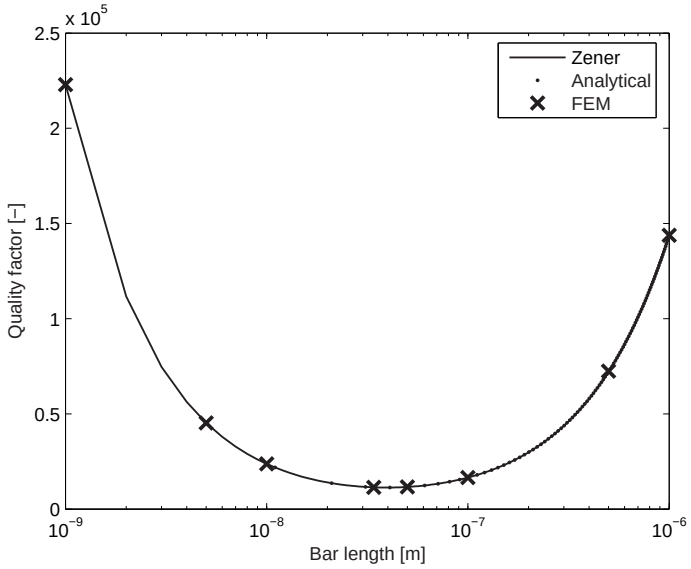

Figure 4.2: Quality factor variation with the bar length.

Figures 4.3 and 4.4 represent the variation of the frequency shift, $\Re(\omega)/\omega_0 - 1$, and the amplitude attenuation, $\Im(\omega)/\omega_0$, with the bar length. Due to the thermoelastic effects, the frequency becomes larger than the isothermal frequency.

The frequency shift increases with the length of the bar and reaches an upper limit of 8.9 10^{-5} for bar lengths larger than 0.5 μm, which corresponds to the adiabatic regime. The attenuation exhibits a maximum value of 4.42 10^{-5} for the bar length of 3.9 10^{-8}, which also corresponds to the minimum of the quality factor. Both the analytical and finite element methods give similar results.

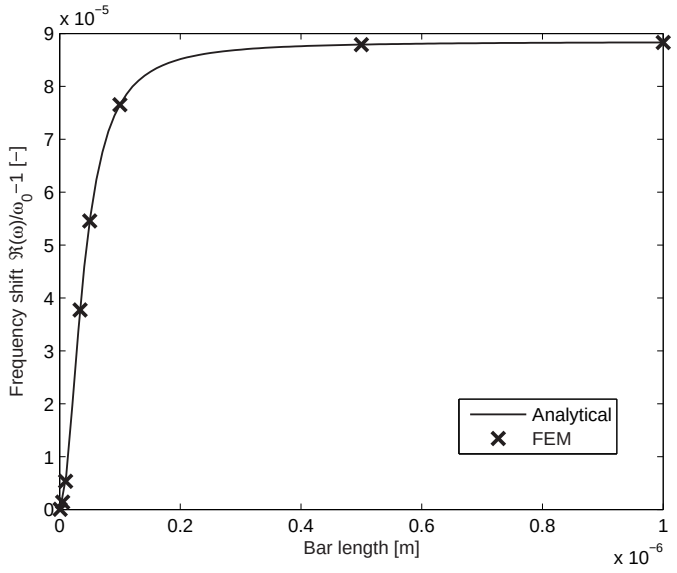

Figure 4.3: Variation of the frequency shift with the bar length.

Thermoelastic effects introduce complex natural frequencies and complex thermoelastic natural modes. The thermal and mechanical degrees of freedom are out of phase, so that the maximum of the temperature increment does not occur when the deformation is maximum. This is due to the relaxation which occurs through conduction. The difference of phase between the thermal and mechanical degrees of freedom depends on the importance of the thermoelastic effects.

The phase lag between the thermal and mechanical degrees of freedom can be quantified by plotting the components of the mode in the complex plane. Figure 4.5 shows that for a bar length of 3.9 10^{-8} m, the difference of phase between the mechanical and thermal degrees of freedom is equal to 45°. Figure 4.6 gives the variation of the difference of phase with the bar length. As the bar length increases, the difference of phase decreases. The difference of phase is of 45° when the bar length is equal to 3.9 10^{-8} m, i.e. when the thermoelastic

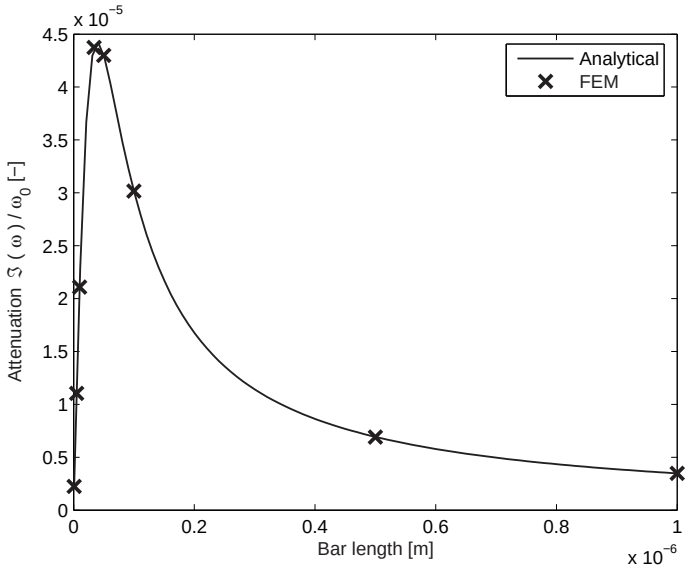

Figure 4.4: Variation of the amplitude attenuation with the bar length.

coupling has the greatest influence. For long bars, the thermal and mechanical degrees of freedom tend to be in phase. Indeed, as the bar length increases, the natural frequencies decrease but the thermal frequencies (Equation (4.110)) decrease faster so that the relaxation does not have the time to occur through conduction. When a bar part is extended, it is cooled and this temperature variation is not transmitted to the neighbor parts. The oscillations are adiabatic. On the other hand, when the length is small, the thermal and mechanical degrees of freedom tend to be in quadrature of phase since the longitudinal conduction plays an important role. Indeed, as the natural frequency increases slower than the thermal frequency when the length decreases, the longitudinal conduction occurs and the temperature difference along the bar vanishes. Hence, for a small bar length, the oscillations can be considered as isothermal.

Figures 4.7 and 4.8 represent the shape of the mechanical and thermal modes, respectively, for a bar of 3.9 10^{-8} m. These figures show clearly that the assumptions made in analytical model are adequate. Indeed, the thermoelastic coupling does not affect the shape of the thermal and mechanical modes.

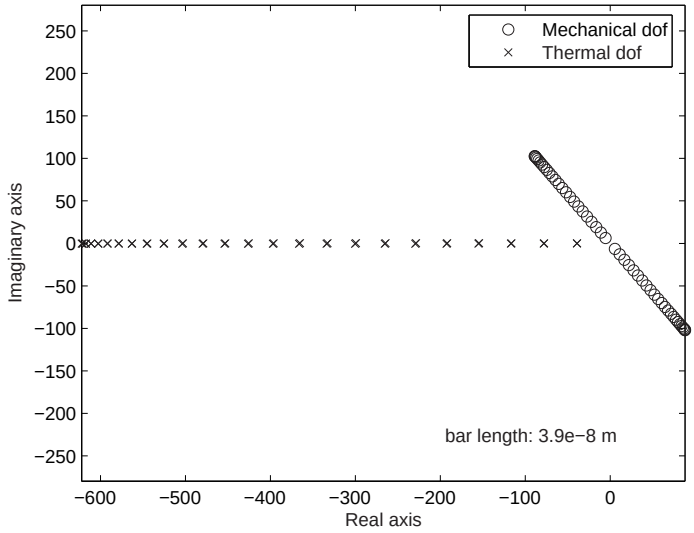

Figure 4.5: Complex representation of the thermoelastic extension mode of a bar.

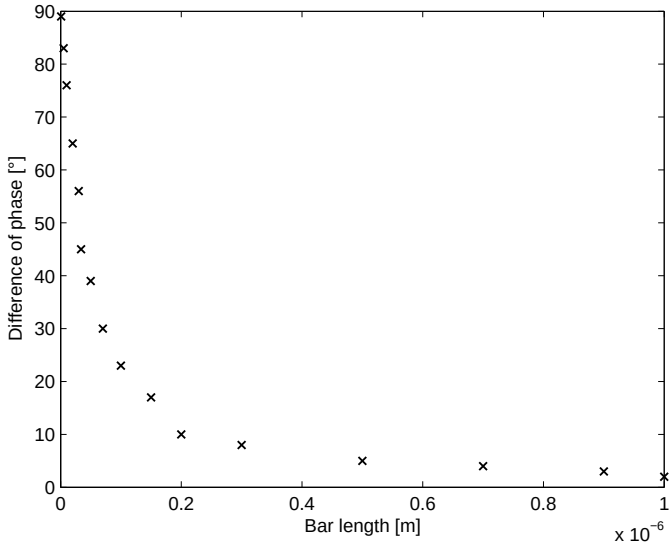

Figure 4.6: Variation of the difference of phase between the thermal and mechanical degrees of freedom with the bar length.

4.5.2 Piezoelectric Coupling

Analytical Model

The equation of motion of the bar is

$$\rho \frac{d^2u}{dt^2} = \frac{d\sigma}{dx}, \tag{4.111}$$

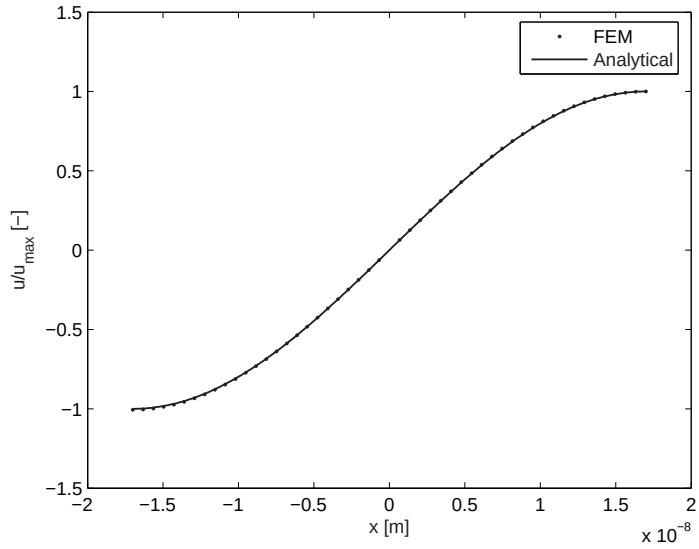

Figure 4.7: Mechanical mode shape.

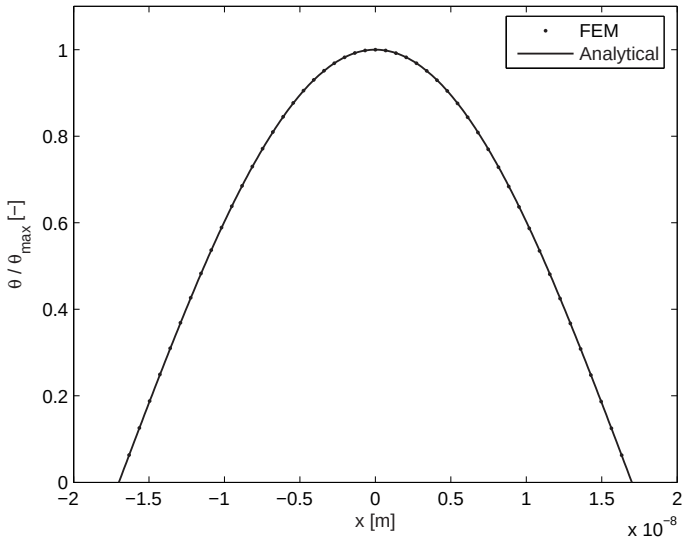

Figure 4.8: Thermal mode shape.

where σ takes into account the piezoelectric coupling. The linear piezoelectric constitutive equations (4.3) and (4.4) are

$$\sigma = E\epsilon - eE_x, \tag{4.112}$$

$$D = e\epsilon + bE_x. \tag{4.113}$$

Eliminating E_x gives

$$\sigma = (E + \frac{e^2}{b})\epsilon - \frac{e}{b}D. \tag{4.114}$$

The equation of motion leads to

$$\rho\frac{d^2u}{dt^2} = (E + \frac{e^2}{b})\frac{d^2u}{dx^2} \tag{4.115}$$

since the electric condition (4.92) imposes $dD/dx = 0$. Hence, due to the piezoelectric coupling, the bar behaves as if its Young's modulus were changed from E to $E + \frac{e^2}{b}$.

Finite Element Model

Based on the thermopiezoelectric finite element formulation, a piezoelectric bar element can be developed by deleting the thermal degrees of freedom. The degrees of freedom of the bar element are the electric potential and the axial displacement at the end nodes of the element. It uses linear shape functions for the longitudinal variation of both the displacement and the electric potential.

A hypothetical material is considered in order to illustrate the method. Its mechanical properties are equal to those of silicon: $E = 1.5810^{11}\ N/m^2$, $\rho = 2300\ kg/m^3$, whereas its piezoelectric constant is $e = 0.1711\ Cm^{-2}$ and its dielectric modulus is $b = 3.992\ 10^{-11}\ Fm^{-1}$. The bar length is set to $3.9\ 10^{-8}$ m. The model consists of 40 elements.

Result Discussion

According to the analytical model, the natural pulsation varies from its mechanical value $6.6765\ 10^{11}$ rad/s to its piezoelectric value $6.6923\ 10^{11}$ rad/s. The finite element model gives a similar variation, i.e. from $6.6768\ 10^{11}$ rad/s without the piezoelectric coupling to $6.6925\ 10^{11}$ rad/s with the piezoelectric coupling. Clearly, the piezoelectric effects induce an hardening of the bar, and the frequency shift due to the piezoelectric coupling is equal to $2.36\ 10^{-3}$.

4.5.3 Thermopiezoelectric Coupling

Analytical Model

The equation of motion of the bar is

$$\rho \frac{d^2u}{dt^2} = \frac{d\sigma}{dx}, \tag{4.116}$$

where σ takes into account the piezoelectric coupling:

$$\sigma = (E + \frac{e^2}{b})\epsilon - \frac{e}{b}D - \alpha E\theta. \tag{4.117}$$

Substituting the stress by its expression and taking into account the electric condition, the equation of motion becomes

$$\rho \frac{d^2u}{dt^2} = (E + \frac{e^2}{b})\frac{d^2u}{dx^2} - \alpha E\frac{d\theta}{dx}. \tag{4.118}$$

As the pyroelectric coupling is neglected, the heat equation with thermopiezoelectric coupling is the same as the thermoelastic one (Equation (4.95)):

$$k\frac{d^2\theta}{dx^2} = E\alpha T_0 \frac{d}{dt}\left(\frac{du}{dx}\right) + C_v\frac{d\theta}{dt}. \tag{4.119}$$

In order to obtain an expression of the complex pulsation, it is proceeded as for the thermoelastic coupling. The harmonic solutions of the linear thermopiezoelectric equations are considered:

$$u = U_0 e^{i\omega t} \quad \text{and} \quad \theta = \theta_0 e^{i\omega t}. \tag{4.120}$$

It is assumed that the mechanical and thermal mode shapes are not modified by the thermopiezoelectric coupling, i.e. the first mechanical mode is given by

$$U_0 = A\sin\left(\frac{\pi x}{l}\right), \tag{4.121}$$

and the first thermal mode is given by

$$\theta_0 = B\cos\left(\frac{\pi x}{l}\right), \tag{4.122}$$

where the constants A and B are dependent. Indeed, substituting Equations (4.121) and (4.122) in the first linear thermopiezoelectric equation (4.118) gives the following relation:

$$B = A\left(\frac{\pi}{l}\frac{1}{\alpha}\left(1 + \frac{e^2}{Eb}\right) - \omega^2\frac{l}{\pi}\frac{\rho}{E\alpha}\right). \tag{4.123}$$

Hence, substituting the mechanical and thermal harmonic solutions in the second linear thermopiezoelectric equation (4.119) gives that the thermopiezoelectric pulsation ω of the bar satisfies the following equation:

$$-\frac{\rho}{E}\left(\frac{l}{\pi}\right)^2 i\omega^3 - \frac{\rho}{E}\frac{k}{C_v}\omega^2 + \left(1+\frac{e^2}{bE}+\frac{T_o\alpha^2 E}{C_v}\right) i\omega + \frac{k}{C_v}\left(\frac{\pi}{l}\right)^2\left(1+\frac{e^2}{bE}\right) = 0. \tag{4.124}$$

Finite Element Model

Based on the thermopiezoelectric finite element formulation, a thermopiezoelectric bar element is developed. The degrees of freedom of the bar element correspond to the temperature increment, the electric potential and the axial displacement at the end nodes of the element. It uses linear shape functions for the longitudinal variations of the displacement, the temperature increment and the electric potential.

A hypothetical material is considered in order to illustrate the method. Its mechanical properties are equal to those of silicon: $E = 1.5810^{11}\ N/m^2$, $\rho = 2300\ kg/m^3$, whereas its piezoelectric constant is $e = 0.1711\ Cm^{-2}$ and its dielectric modulus is $b = 3.992\ 10^{-11}\ Fm^{-1}$. The model consists of 40 elements when the bar length is set to 3.9 10^{-8} m.

Note that as pyroelectricity is disregarded, the corresponding matrices $\mathbf{K}_{\phi\theta}$ and $\mathbf{C}_{\theta\phi}$ are equal to zero.

Result Discussion

Figure 4.9 shows the variation of the quality factor with the bar length. The analytical model as well as the finite element method give similar results. The quality factor reaches its minimum value of 11362 for a bar length of 3.9 10^{-8} m. For bar lengths largely lower than 3.9 10^{-8} m, the thermoelastic damping can be neglected and the regime is isothermal. For bars largely longer than 3.9 10^{-8} m, which is usually the case in practice, the thermoelastic damping is negligible and the bars are in adiabatic regime.

Figure 4.10 compares the variation of the thermoelastic and thermopiezoelectric quality factor. The thermopiezoelectric analyses give the same kind of variation of the quality factor with the bar length as the thermoelastic ones.

The thermopiezoelectric values of the quality factor are slightly larger than the thermoelastic ones and the quality factor is minimum at the same bar length.

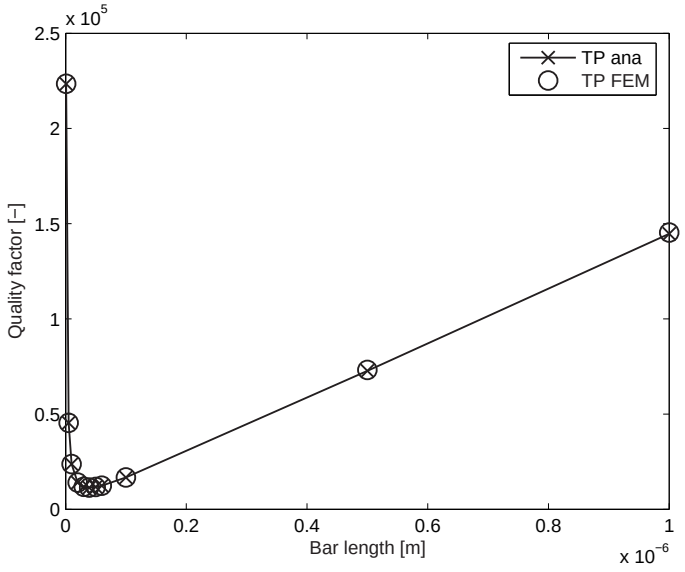

Figure 4.9: Quality factor variation with the bar length (Analytical and FEM thermopiezoelectric results).

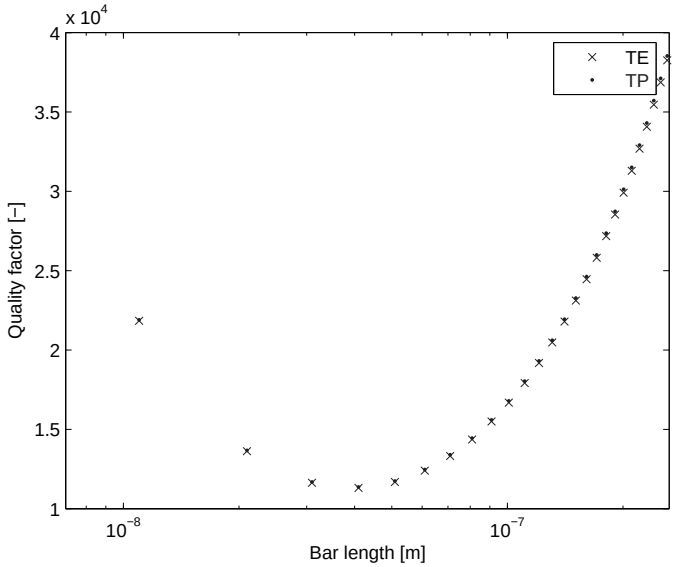

Figure 4.10: Comparison of the thermoelastic and thermopiezoelectric quality factor variation.

In order to understand the effect of thermopiezoelectricity on the quality factor, the frequency shift and the amplitude attenuation are studied. Figure 4.11 represents the variation of the frequency shift, $\Re(\omega)/\omega_0 - 1$, with the bar length. The thermopiezoelectric frequency shift increases with the length of the bar and reaches an upper limit of 2.445 10^{-3} for bars longer than 0.5 μm. Compared to the thermoelastic problem (Figure 4.3), the shape of the curve is similar but the order of magnitude of the upper limit is strongly different, i.e. 2.445 10^{-3} for the thermopiezoelectric problem and 4.42 10^{-5} for the thermoelastic problem. As explained previously, piezoelectricity induces an hardening effect, leading to a frequency shift of 2.36 10^{-3}. The piezoelectric shift is the same whatever the bar length, it only depends on the material data. If the effects of piezoelectricity and thermoelasticity were decoupled, the thermopiezoelectric frequency shift would be equal to the sum of the piezoelectric and thermoelastic frequency shifts. A zoom (Figure 4.12) shows that the thermopiezoelectric frequency shift is lower than the sum of the piezoelectric and thermoelastic frequency shifts so that the effects of thermoelasticity and piezoelectricity on the frequency shift are coupled.

Figure 4.13 represents the variation of the amplitude attenuation, $\Im(\omega)/\omega_0$, with the bar length. The attenuation exhibits a maximum value of 4.42 10^{-5} for the bar length of 3.9 10^{-8} m, to which also corresponds the minimum of the quality factor. Piezoelectricity by itself does not induce damping but as piezoelectric and thermoelastic effects are coupled, the thermopiezoelectric attenuation curve is not exactly the same as the thermoelastic one. The thermopiezoelectric attenuation is lower than the thermoelastic one.

The difference between the thermoelastic and thermopiezoelectric analytical models comes from the factor e^2/b between the amplitude of the thermal and mechanical modes (Equations (4.99) and (4.123)). Hence, the piezoelectric constant e directly influences the thermopiezoelectric quality factor. Table 4.1 presents the thermopiezoelectric quality factor and complex frequency for different values of the piezoelectric constant e. The quality factor increases with the piezoelectric constant. This quality factor augmentation is due to two contributions: the increase in the frequency shift (mainly due to the piezoelectric frequency shift) and the decrease in the attenuation.

The thermopiezoelectric complex modes are also influenced by the value of the piezoelectric constant. The thermal and mechanical degrees of freedom are out

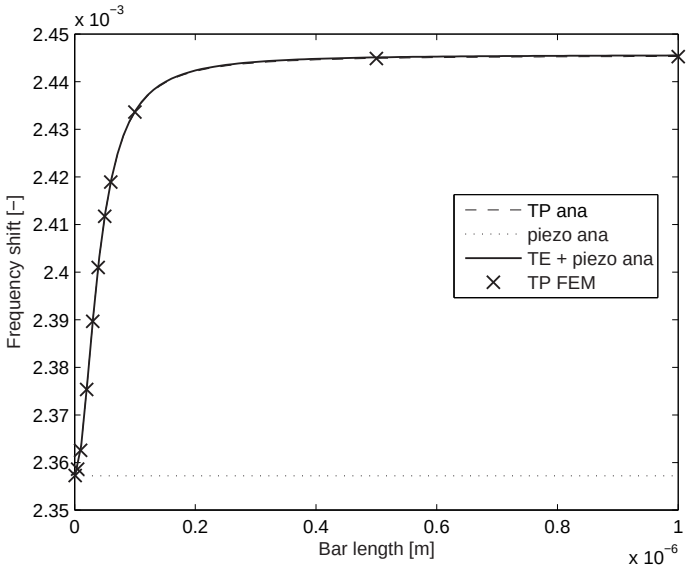

Figure 4.11: Variation of the thermopiezoelectric frequency shift with the bar length.

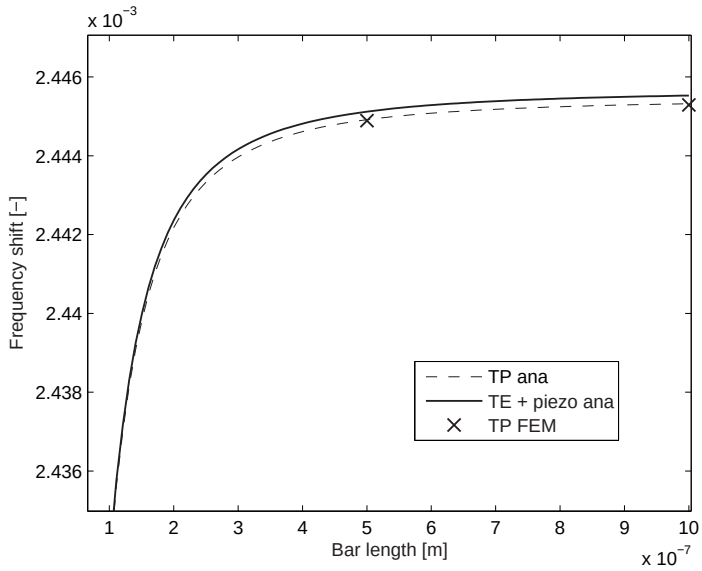

Figure 4.12: Variation of the thermopiezoelectric frequency shift with the bar length (Zoom).

of phase. Figure 4.15 shows the complex representation of the thermopiezoelectric mode for the values of e listed in Table 4.1 for a bar length of 3.9 10^{-8} m. The

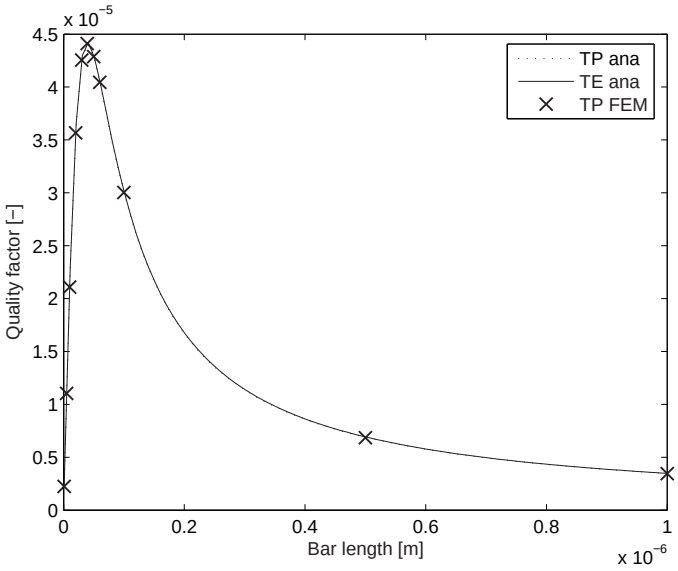

Figure 4.13: Variation of the amplitude attenuation with the bar length.

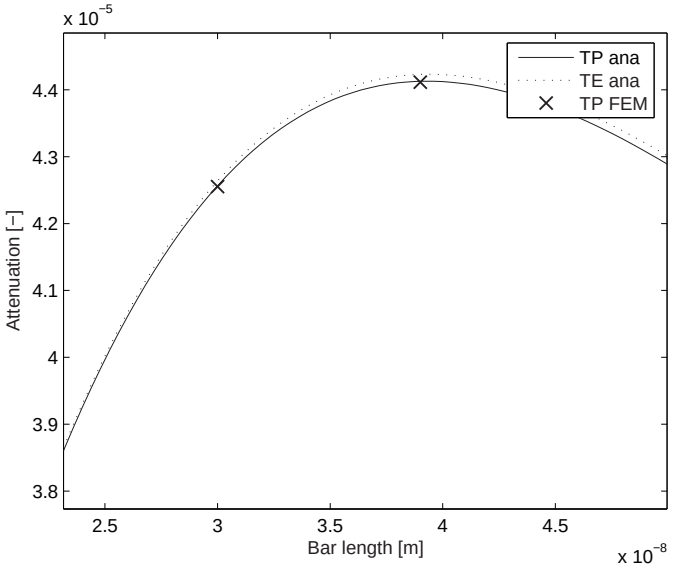

Figure 4.14: Variation of the amplitude attenuation with the bar length.

mechanical degrees of freedom have the same amplitude whatever the value of e, while the thermal degrees of freedom are modified. Figure 4.16 shows that as e increases, the relative amplitude of the thermal mode with respect to the mechanical one increases while the difference of phase decreases.

Table 4.1: Effect of the piezoelectric constant.

e $[Cm^{-2}]$	Q [-]	ω [rad/s]
0	11305	$6.6768\ 10^{11} + 2.9531\ 10^{7}i$
0.172	11358	$6.6925\ 10^{11} + 2.9462\ 10^{7}i$
0.3	11469	$6.7251\ 10^{11} + 2.9320\ 10^{7}i$

Physically, piezoelectricity modifies the stress and consequently the strain, so that the induced temperature changes are also modified and hence, the relaxation process is different leading to a different quality factor. In particular, for a bar in extension, piezoelectricity increases the relative temperature increment and decreases the phase lag between the thermal and mechanical degrees of freedom leading to a higher quality factor.

4.6 Concluding Remarks

In this chapter, the thermopiezoelectric finite element formulation has been derived from a unified variational principle taking into account the mechanical, thermal and electric fields. In order to solve the thermopiezoelectric eigenproblem, an iteration method has been selected and a real non-symmetric block Lanczos method has been developed.

In order to validate the finite element formulation, a simplistic one-dimensional thermopiezoelectric problem has been investigated. This problem, which consists in the longitudinal vibrations of a bar, has been studied analytically and numerically, taking into account successively the thermoelastic, piezoelectric and thermopiezoelectric couplings. This procedure has allowed to understand the influence of the different couplings on the quality factor. It has shown that the thermopiezoelectric coupling leads to a higher quality factor than the thermoelastic one in the case of a vibrating bar. This increase is not only due to the piezoelectric hardening resulting in a higher resonant frequency but also to the decrease in damping induced by the effect of piezoelectricity on the temperature gradients.

As the thermopiezoelectric finite element formulation and the method of resolution have been validated on a simple analytically tractable case, real 3-D problems can now be numerically studied using the developed thermopiezoelectric finite element method.

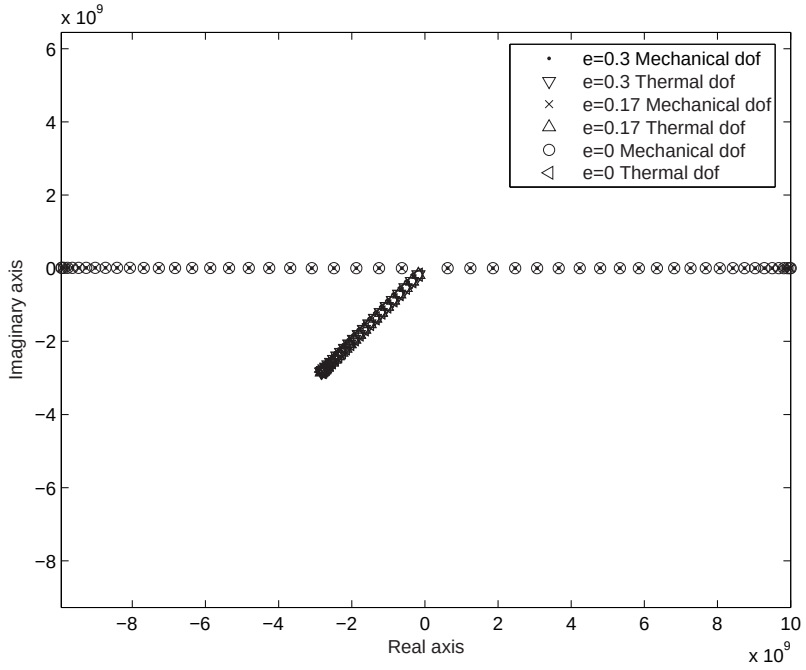

Figure 4.15: Complex representation of the thermopiezoelectric extension mode of a bar (3.9 10^{-8} m).

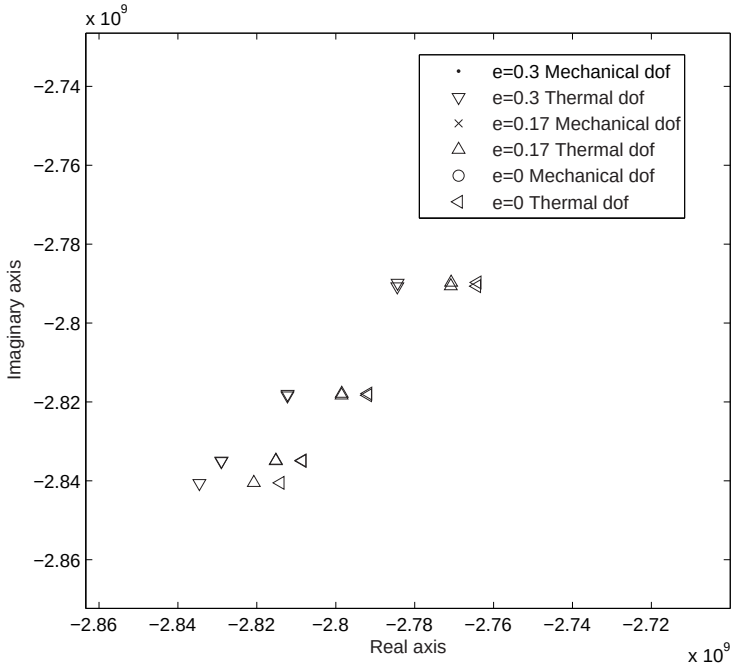

Figure 4.16: Complex representation of the thermopiezoelectric extension mode of a bar (3.9 10^{-8} m) (zoom on the thermal dof).

Chapter 5

Numerical Applications

The thermopiezoelectric finite element formulation developed in the previous chapter is used in order to quantify the quality factor of two structures. Firstly, a clamped-clamped silicon beam is modeled with various kinds of thermoelastic finite elements. The effects of the anchor and the residual stress are studied on this test case. Secondly, the vibrating beam of the VIA presented in Chapter 2 is analyzed. In particular, the influences of thermopiezoelectricity, the trapezoidal cross-section and the electrodes on the quality factor are highlighted.

5.1 Clamped-clamped Silicon Beam

In numerous micro-resonators, the vibrating part consists in a clamped-clamped silicon beam. In this section, the test case beam has the following dimensions: a length L of 90 μm, a height h of 4.5 μm and a width w of 4.5 μm (Figure 5.1). The thermal and mechanical properties of silicon at $T_o = 298\ K$ are: $E = 1.58\ 10^{11}\ N/m^2$, $\rho = 2300\ kg/m^3$, $\nu = 0.2$, $c_v = 711\ J/kgK$, $\alpha = 2.510^{-6}\ K^{-1}$ and $k = 170\ Wm^{-1}K^{-1}$. The contribution of the piezoelectric effect is not considered for this example and the thermoelastic quality factor is determined for the first bending mode in plane OYZ.

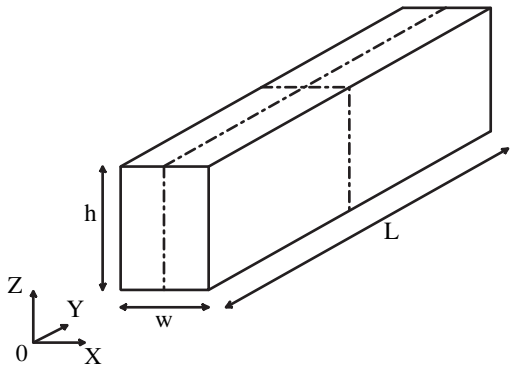

Figure 5.1: Beam geometry.

5.1.1 Hexahedral Finite Element Model

Based on the thermopiezoelectric finite element formulation developed in Chapter 4, thermoelastic quadratic 3-D elements are derived by disregarding the electric degrees of freedom. In this analysis, 20-node hexahedral elements are used. Each node i has three mechanical degrees of freedom (u_i, v_i, w_i), the displacements of node i along the three directions (X, Y, Z). At each node, a thermal degree of freedom represents the temperature increment θ_i. The displacement field and the thermal field use tri-quadratic interpolation functions as shape functions.

Making use of the symmetry planes of the problem (dashed lines in Figure 5.1), only one quarter of the beam is modeled. The mesh comprises 40 elements along the half length, 4 elements along the vibrating height and 2 elements along the half width. The boundary conditions are such that one of the extremity is clamped and the symmetry conditions are imposed on the symmetry planes. The temperature increment of the central node of the clamped extremity is fixed to zero.

Figure 5.2 represents the thermoelastic mode. The temperature increment field is coherent with the strain field:

- The temperature does not vary along the width which does not undergo any deformation except those induced by the Poisson effect.

- The lowest and highest temperature increments are observed at the clamped extremity where the strain maxima are located.

- The temperature of the neutral fiber does not vary.

- The middle of the beam shows local extrema of temperature increments.

The corresponding quality factor is equal to 12 767. The frequency shift due to the thermoelastic damping is equal to 2.2203e-5 and the attenuation is equal to 3.9162e-5.

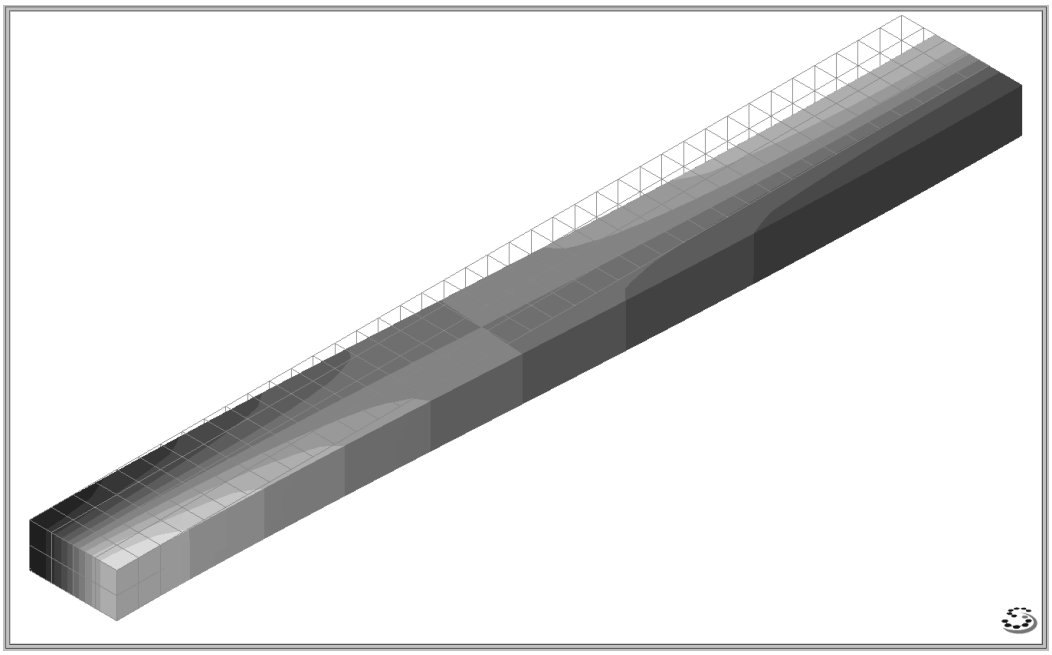

Figure 5.2: Thermoelastic mode of the hexahedral finite element model (White: temperature increase, Black: temperature decrease).

5.1.2 Quadrilateral Finite Element Model

Based on the thermopiezoelectric finite element formulation developed in Chapter 4, thermoelastic quadratic 2-D elements are derived by disregarding the electric degrees of freedom. In this analysis, 8-node quadrilateral plane stress elements are used. Each node i has two mechanical degrees of freedom (v_i, w_i), the displacements of node i along the two directions (Y, Z). At each node, a thermal degree of freedom represents the temperature increment θ_i. The displacement field and the thermal field use bi-quadratic interpolation functions as shape functions.

Making use of the symmetry of the problem, only one half of the beam is modeled. The mesh comprises 80 elements along the half length and 8 elements

along the vibrating height. The boundary conditions are such that one of the extremity is clamped and the symmetry conditions are imposed on the symmetry plane. The temperature increment of the central node of the clamped extremity is fixed to zero.

Figure 5.3 represents the thermoelastic mode. The temperature increment field is coherent with the strain field:

- The maxima of the temperature decrease and increase are located at the clamped extremity where the strain maxima are located.

- The temperature of the neutral fiber does not vary.

- The middle of the beam shows local maxima of the temperature decrease and increase.

The corresponding quality factor is equal to 13 258. The frequency shift due to the thermoelastic damping is equal to 2.2169e-5 and the attenuation is equal to 3.7713e-5.

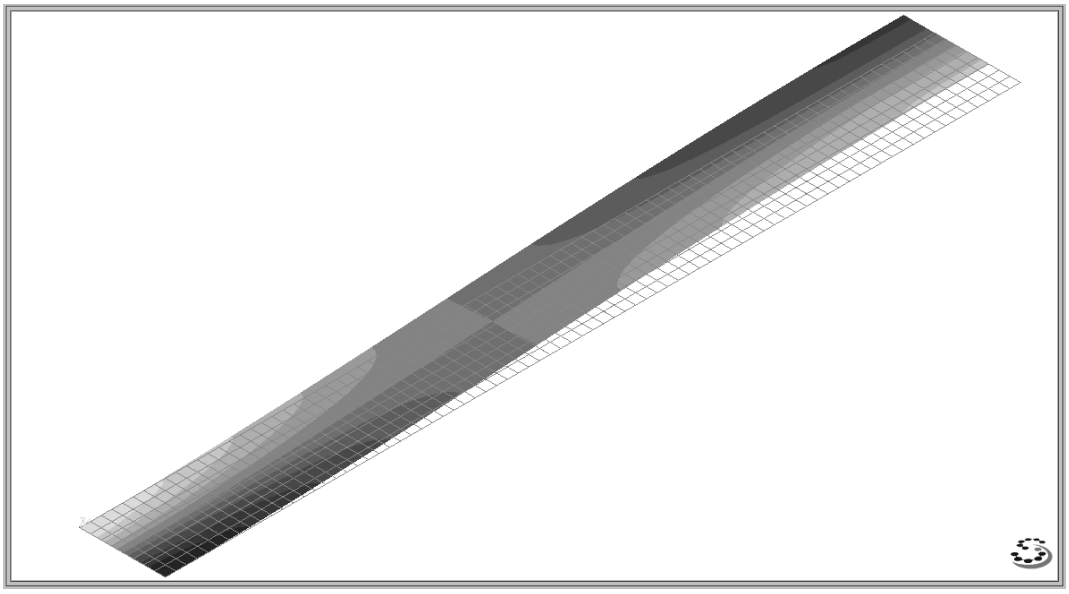

Figure 5.3: Thermoelastic mode of the quadrilateral finite element model (White: temperature increase, Black: temperature decrease).

5.1.3 Beam Finite Element Model

Based on the thermoelastic finite element formulation, a specific beam element may be developed in order to simulate the thermoelastic behavior of vibrating beams. For the displacement field, a classical Bernoulli-Euler beam model is assumed. For the sake of simplicity, a plane beam element is considered here although the following developments may be extended to a more general 3-D beam element. The motion of a beam in the $(x,\ y)$ plane is described by the axial $u(x,y)$ and transverse $v(x,y)$ displacement components. The motion in z-direction, which is primarily due to Poisson's ratio effects, can be neglected. The classical Bernoulli-Euler beam model assumes that

$$u(x,y) = -y\frac{\partial v(x)}{\partial x} = -y\vartheta, \tag{5.1}$$

$$v(x,y) = v(x). \tag{5.2}$$

A Bernoulli-Euler plane beam element has two end nodes, i and j, and four degrees of freedom collected in the node displacement vector $\mathbf{u_u}$:

$$\mathbf{u_u} = [\ v_i \quad \vartheta_i \quad v_j \quad \vartheta_j\ ]^T. \tag{5.3}$$

Figure 5.4 shows the degrees of freedom of a node j of a Bernoulli-Euler plane beam element.

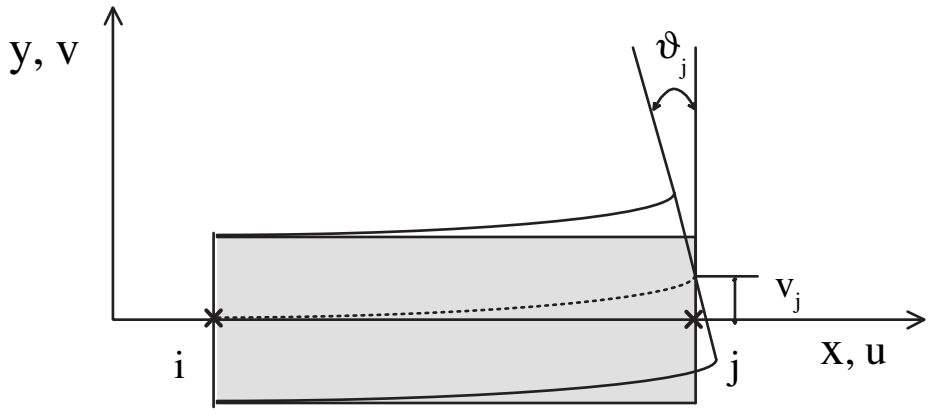

Figure 5.4: Bernoulli-Euler plane beam element.

Using Hermitian cubic shape functions, the transverse displacement is expressed

as follows

$$v = [\ N_{v_i} \quad N_{\vartheta_i} \quad N_{v_j} \quad N_{\vartheta_j}\ ][\ v_i \quad \vartheta_i \quad v_j \quad \vartheta_j\ ]^T = \mathbf{N_u u_u}. \tag{5.4}$$

The shape functions are conveniently expressed in terms of the dimensionless coordinate:

$$\xi = \frac{2x}{\ell} - 1 \quad (-1 \leq \xi \leq 1), \tag{5.5}$$

where ℓ is the element length. The shape functions are explicitly given by

$$N_{v_i} = \frac{1}{4}(1-\xi)^2(2+\xi), \tag{5.6}$$

$$N_{\vartheta_i} = \frac{1}{8}\ell(1-\xi)^2(1+\xi), \tag{5.7}$$

$$N_{v_j} = \frac{1}{4}(1+\xi)^2(2-\xi), \tag{5.8}$$

$$N_{\vartheta_j} = -\frac{1}{8}\ell(1+\xi)^2(1-\xi). \tag{5.9}$$

Knowing the expression of the shape functions, the strain can be calculated:

$$\varepsilon = \frac{\partial u}{\partial x} = -y\frac{\partial^2 v}{\partial x^2} = \mathbf{B_u u_u}, \tag{5.10}$$

where

$$\mathbf{B_u} = -y\mathbf{N_u''} = -\frac{y}{\ell}[\ 6\tfrac{\xi}{l} \quad 3\xi - 1 \quad -6\tfrac{\xi}{l} \quad 3\xi + 1\ ]. \tag{5.11}$$

As the transverse variation of the temperature plays a key role in the thermoelastic behavior of vibrating beams, the temperature has to be modeled by at least two values at each node. It is important to note that although a linear temperature field, with only θ_0 as degree of freedom, can address the axial temperature distribution, it cannot satisfy the top and bottom surface thermal boundary conditions:

$$-\kappa_{yy}\frac{\partial \theta}{\partial y} = 0, \quad y = \pm b/2, \tag{5.12}$$

where κ_{yy} is the heat conduction coefficient in y-direction and b is the height of the beam. Therefore, temperature variations through the height, which produce the most important bending deformation, cannot be modeled accurately by the linear temperature field. Therefore, for each beam element, the two nodes have two thermal degrees of freedom: θ_0 and θ_1. θ_0 represents the neutral fiber temperature and θ_1, the temperature variation on the height of the beam. In particular, the temperature field:

$$\theta(x, y, z, t) = \theta_0(x, t) + g(y)\theta_1(x, t), \tag{5.13}$$

where the function $g(y)$ takes the following form:

$$g(y) = y - \frac{4}{3b^2}y^3, \tag{5.14}$$

automatically satisfies the thermal boundary conditions. θ_0 and θ_1 are approximated using linear interpolation functions:

$$\begin{pmatrix} \theta_0 \\ \theta_1 \end{pmatrix} = \begin{pmatrix} N_1 & 0 & N_2 & 0 \\ 0 & N_1 & 0 & N_2 \end{pmatrix} \begin{pmatrix} \theta_0^i \\ \theta_1^i \\ \theta_0^j \\ \theta_1^j \end{pmatrix}, \tag{5.15}$$

where

$$N_1 = 1 - \frac{x}{\ell}, \tag{5.16}$$

$$N_2 = \frac{x}{\ell}. \tag{5.17}$$

Therefore, the temperature increment θ is expressed in term of the node value vector $\mathbf{u}_\theta$:

$$\theta = \begin{pmatrix} 1 & g(y) \end{pmatrix} \begin{pmatrix} \theta_0 \\ \theta_1 \end{pmatrix} \tag{5.18}$$

$$= \begin{pmatrix} 1 & g(y) \end{pmatrix} \begin{pmatrix} N_1 & 0 & N_2 & 0 \\ 0 & N_1 & 0 & N_2 \end{pmatrix} \begin{pmatrix} \theta_0^i \\ \theta_1^i \\ \theta_0^j \\ \theta_1^j \end{pmatrix} \tag{5.19}$$

$$= \begin{pmatrix} N_1 & g(y)N_1 & N_2 & g(y)N_2 \end{pmatrix} \begin{pmatrix} \theta_0^i \\ \theta_1^i \\ \theta_0^j \\ \theta_1^j \end{pmatrix} \tag{5.20}$$

$$= \mathbf{N}_\theta \mathbf{u}_\theta. \tag{5.21}$$

In order to determine the thermal field, the shape function derivative matrix $\mathbf{B}_\theta$ has to be defined:

$$\mathbf{B}_\theta = -\nabla \mathbf{N}_\theta \tag{5.22}$$

$$= -\begin{pmatrix} -1/\ell & -g(y)/\ell & 1/\ell & g(y)/\ell \\ 0 & g'(y)(1-x/\ell) & 0 & g'(y)x/\ell \end{pmatrix}, \tag{5.23}$$

where

$$g'(y) = y - \frac{4}{b^2}y^2. \tag{5.24}$$

The beam is modeled using 50 thermoelastic beam finite elements. Both ends are clamped and the temperature increment at both extremities is fixed to zero. Figure 5.5 represents the first thermoelastic bending mode of a clamped-clamped beam. The variation of temperature is given for a maximum displacement of the neutral fiber of 1 μm. The mechanical deformation is similar to the usual isothermal natural mode. As expected from the transverse temperature profile, the upper and lower surfaces exhibit opposite temperature increments: when a point located on the upper side is heated, the corresponding lower point is cooled, and conversely. Moreover, along the longitudinal direction, the middle part is heated when both ends are cooled, and conversely. The neutral fiber does not experience any change of temperature. All these observations are in agreement with the mechanical deformation of the mode. Indeed, when the upper part of the beam is compressed, the corresponding lower part is stretched, and conversely, but the neutral fiber remains unstrained. When the middle part of a longitudinal surface is compressed, both ends are stretched, and conversely. The resulting quality factor is equal to 12 967. The frequency shift due to the thermoelastic damping is equal to 1.8827e-5 and the attenuation is equal to 3.6326e-5.

5.1.4 Result Discussion

Table 5.1 compares the quality factor and the real and imaginary parts of the frequency for the different models, i.e. the analytical models of Zener and Lifshitz-Roukes explained in Chapter 3 and the finite element models exposed above. The maximum relative difference in the quality factor between all the models is about 4 %. As explained in details in Chapter 3, the difference between Zener and LR models resides in the different approximation for the transverse temperature profile. Beam finite elements use a cubic approximation for the transverse temperature profile. As showed in Figure 5.6, the BFEM (Beam Finite Element Model) profile is comprised between Zener and LR ones as well as does the quality factor.

The difference between the hexahedral and quadrilateral models comes from

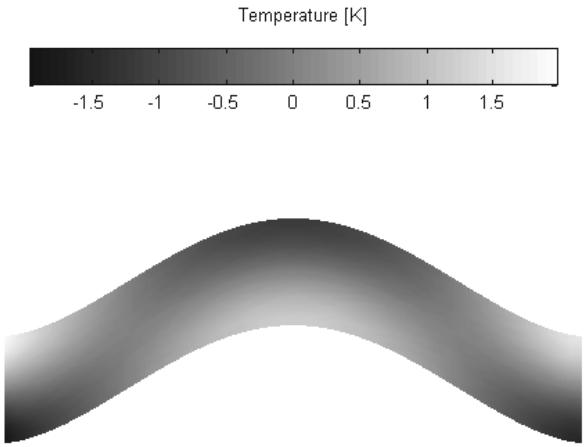

Figure 5.5: Mechanical deformation and temperature variation of the first thermoelastic bending mode.

Table 5.1: Quality factor of a 4.5 x 4.5 x 90 [μm] silicon C-C beam.

Model	Quality factor [-]	ω_r [rad/s]	ω_i [rad/s]
Zener	12729	N/A	N/A
LR	13112	1134	2.974e7
Hexa20	12767	1149	2.934e7
Quad8	13258	1104	2.929e7
Beam	12967	1146	2.974e7

Poisson's effects in the direction orthogonal to the vibration direction, which are only considered in the hexahedral model. A priori, these Poisson's effects could be considered negligible referring to the thermoelastic mode (Figure 5.2), where it seems that no deformation or temperature variation occurs along the width . Table 5.2 shows that if Poisson's effects are completely disregarded ($\nu = 0$), the hexahedral and quadrilateral models gives exactly the same values for the quality factor and the complex frequency. Taking into account Poisson's effects decreases the quality factor from 13351 to 12767, i.e. 4.6 %. Poisson's effects in

the vibration plane induces a variation from 13351 to 13258 while adding Poisson's effect in the width direction implies another decrease from 13258 to 12767.

Table 5.2: Variation of the quality factor of a 4.5 x 4.5 x 90 [μm] silicon C-C beam with Poisson's ratio.

Model	Poisson's ratio	Quality factor [-]	ω_r [rad/s]	ω_i [rad/s]
Hexa20	0.2	12767	1149	2.934e7
Hexa20	0	13351	1098	2.934e7
Quad8	0.2	13258	1104	2.929e7
Quad8	0	13351	1098	2.934e7

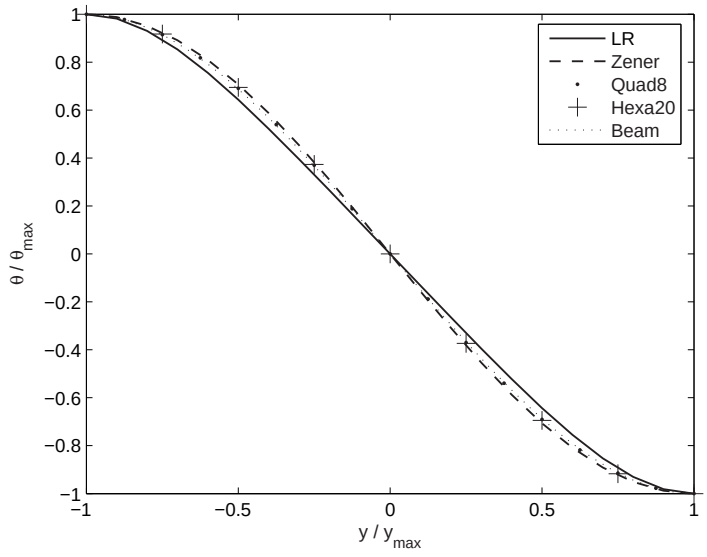

Figure 5.6: Transverse temperature profile at the clamped extremity of a C-C beam for different models.

The difference between the beam and the two other finite element models has three main causes. Firstly, the models are not exactly the same mechanically. A difference of 1 % is observed between the mechanical frequencies of the beam and the two other models. This leads to slight differences in the strain field, which influence the temperature distribution and hence, the quality factor. Secondly,

due to the choice of the thermal degrees of freedom in the thermoelastic beam element, when the temperature increment is fixed at one end of the neutral fiber, the beam model does not take into account the longitudinal conduction and consequently, neglects the longitudinal thermal relaxation. In order to study the effect of the longitudinal thermal relaxation, the thermal conductivity is decreased in the direction of the length in the quadrilateral model ($\nu = 0$). Figure 5.7 shows that if the longitudinal thermal conductivity (k_l) is decreased with respect to the transverse one (k_t), the quality factor decreases. Note that k_l can not be decreased indefinitely because the eigenvalue problem becomes badly conditioned and some spurious thermal rigid modes appear. Thirdly, in the beam finite element model, the transverse temperature profile is imposed to be the same along the length, while a slight variation is observed in hexahedral and quadrilateral finite element models.

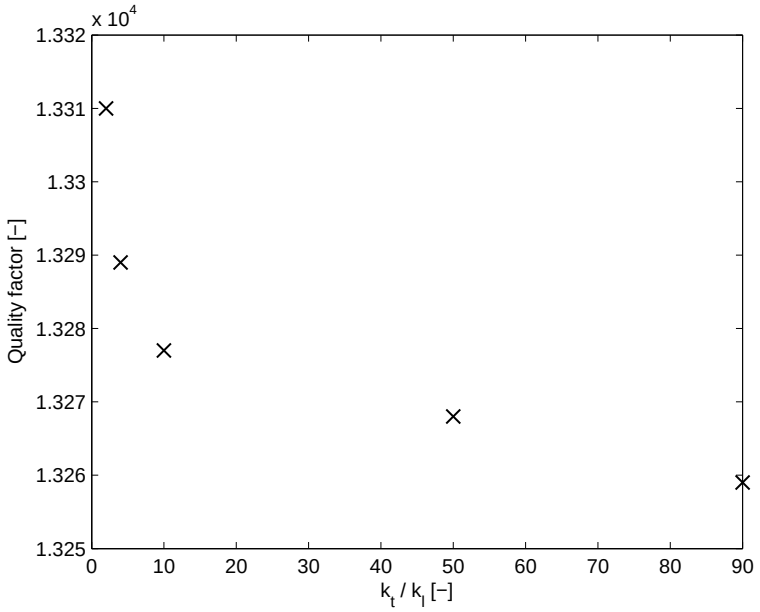

Figure 5.7: Variation of the quality factor when the longitudinal thermal conductivity (k_l) is decreased with respect to the transverse one (k_t).

5.1.5 Effect of Beam Height

As predicted by the analytical models, the thermoelastic effects on the behavior of an oscillating beam depend on the aspect ratio of the beam. For a beam of a fixed length of 90 μm, the first natural frequency is calculated using the thermoelastic models as a function of its height. Figure 5.8 represents the frequency shift, which is given by $\Re(\omega_n)/\omega_{o,n} - 1$, and the attenuation, $\Im(\omega_n)/\omega_{o,n}$, where $\omega_{o,n}$ is the isothermal natural frequency. The frequency shift increases with the height of the beam, but the slope decreases so that the frequency shift tends to reach an upper limit. The attenuation exhibits a maximum for a beam height of 5.3 μm. The analytical and finite element models give similar results. As the beam height to length ratio increases, Poisson's effect is reinforced, leading to larger errors in the beam finite element model and LR models. Indeed, when the beam is not slender enough, Euler-Bernoulli assumption becomes too restrictive. Figure 5.9 shows the variation of the quality factor with the height of the beam. The quality factor reaches its minimum for a beam height of 5.3 μm.

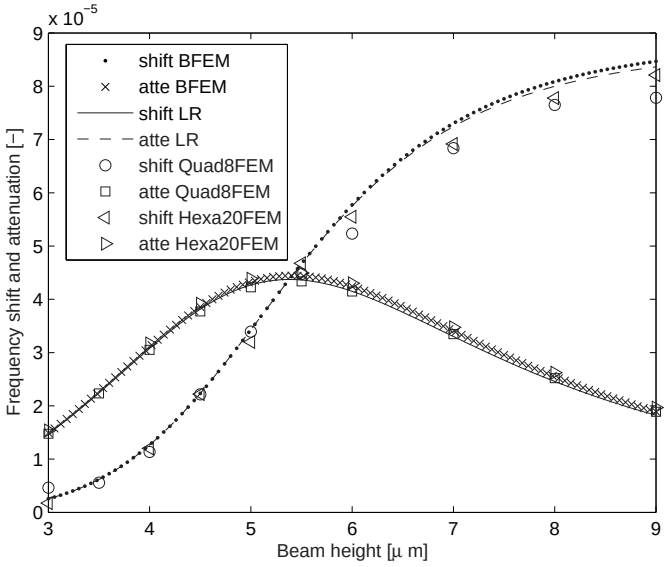

Figure 5.8: Variation of the frequency shift and attenuation versus the beam height (beam length: 90 μm).

Thermoelastic effects introduce complex natural frequencies and the corresponding thermoelastic natural modes are also complex. Due to the relaxation

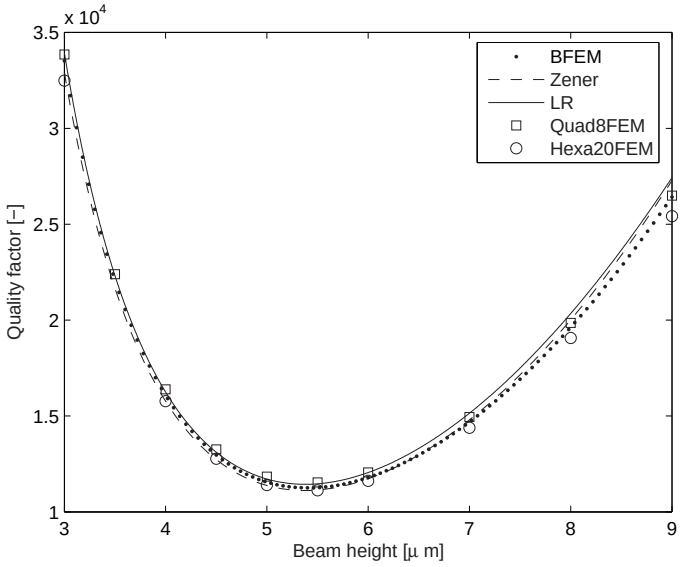

Figure 5.9: Variation of the quality factor versus the beam height (beam length: 90 μm).

through conduction, the thermal and mechanical degrees of freedom are out of phase. Hence, the maximum of the temperature increment does not occur when the deformation is maximum. The difference of phase between the thermal and mechanical responses depends on the importance of the thermoelastic effects.

The phase lag between the thermal and mechanical degrees of freedom can be quantified by plotting the components of the mode in the complex plane. This is done for the modes obtained by the beam finite element models. Figure 5.10 shows that for a beam height of 4.5 μm the difference of phase between the mechanical and thermal degrees of freedom is equal to 60°. Figure 5.11 gives the variation of the difference of phase for different beam heights. As the beam height increases, the difference of phase decreases. The difference of phase is of 45° when the beam height is equal to 5.3 μm, i.e. when the thermoelastic coupling has the greatest influence. For a large beam height, the thermal and mechanical degrees of freedom tend to be in phase. Indeed, as the beam height increases, the natural frequencies increase and the relaxation does not have the time to occur through conduction. When a fiber is extended, it is cooled and this temperature variation is not transmitted to the neighbor fibers. The oscillations are adiabatic. On the other hand, when the height is small, the thermal and

mechanical degrees of freedom tend to be in quadrature of phase. The transverse conduction plays an important role. Indeed, as the natural frequency is relatively small, the transverse conduction occurs and the oscillations can be considered as isothermal.

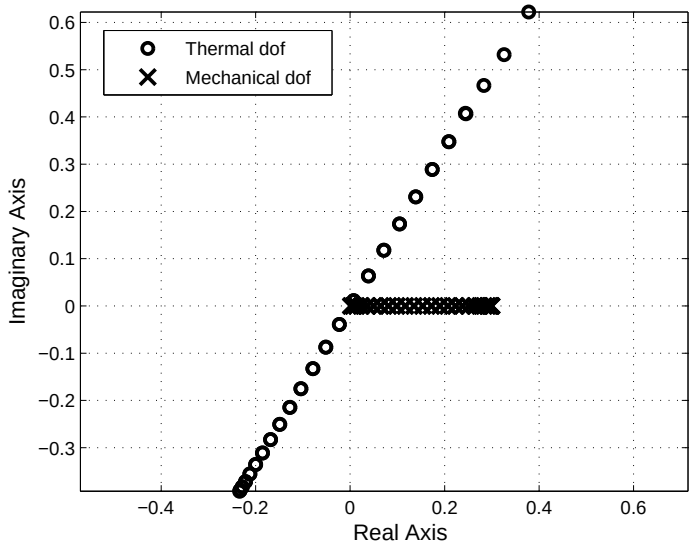

Figure 5.10: Complex representation of the first thermoelastic bending mode.

5.1.6 Influence of Anchor

Anchors are added to the clamped-clamped beam in order to understand their influence on the thermal and mechanical fields. The anchor dimensions are such that they include most of the stress and temperature distribution that extend into the anchor structure [59]. The width w of the anchor is the same as the beam one, its height is equal to three times the height h of the beam and its length is equal to two beam heights (Figure 5.12). The three sides of the anchor rectangle which are not attached to the beam (delimited by bold lines in Figure 5.12) are clamped. Due to the symmetry plane (represented by dotted lines in Figure 5.12), one half of the structure is modeled using quadrilateral finite elements.

The effects of anchor are studied on two test cases. One is located on the isothermal side of the quality factor curve. The beam height is set to 4.5 μm. The other one is located on the adiabatic side of the quality factor curve. The

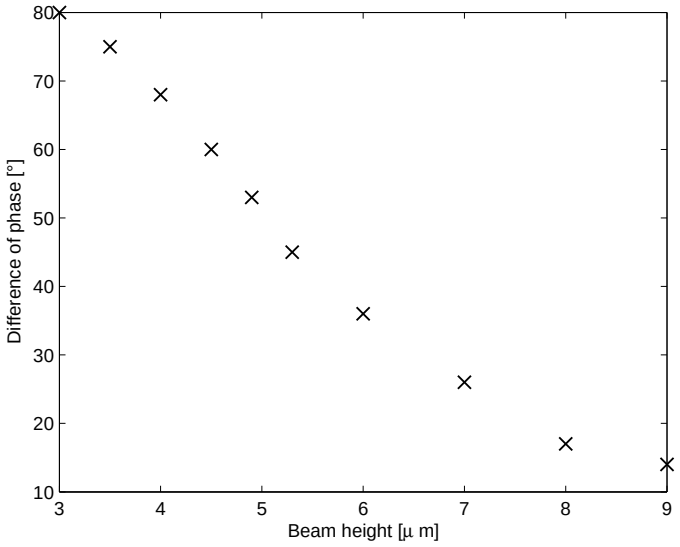

Figure 5.11: Variation of the difference of phase between the thermal and mechanical degrees of freedom.

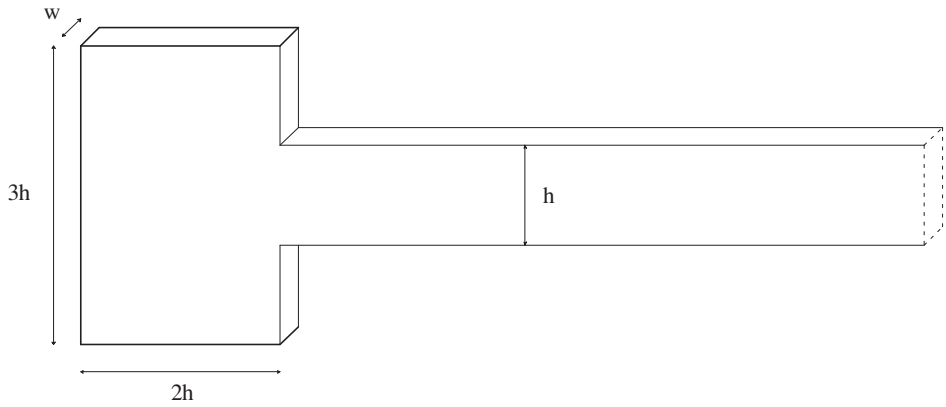

Figure 5.12: Geometry of the half beam with anchor.

beam height is equal to 7 μm. For both cases, the beam width is set to 4.5 μm and the beam length is equal to 90 μm. Table 5.3 compares the quality factor, the damping and the resonant frequency with and without anchor for both cases. In both cases, the addition of the anchor decreases the resonant frequency due to an effective lengthening of the beam and decreases the damping due to the reduction of strain and temperature gradients near the anchor to beam interface. Relaxing the strain near the ends of the beam increases the performance of the

resonator. In the isothermal case, the decrease in damping is more important than the decrease in resonant frequency, ultimately raising the quality factor. On the other hand, the decrease in damping does not overcome the decrease in the resonant frequency for the adiabatic case, leading to a smaller quality factor.

Table 5.3: Effect of anchor on the quality factor of C-C silicon beams.

Height [μm]	Anchor	Q [-]	ω_r [rad/s]	ω_i [rad/s]
4.5	Yes	14553	939	2.7317e7
4.5	No	13258	1104	2.9296e7
7	Yes	14296	1406	4.0210e7
7	No	14942	1493	4.4629e7

Fillets are added to the geometry to smooth out the intersection between the beam and the anchors. To study their effect on thermoelastic damping, the quality factor is calculated for two fillet sizes; the radius is successively set to 10 % and 20 % of the beam height. Figures 5.13 and 5.14 compare the temperature distribution for the isothermal configuration with a fillet of 0.45 μm and 0.9 μm. The configuration with the larger fillet presents higher temperature gradient at the beam to anchor junction. Table 5.4 shows the influence of the fillet radius on the quality factor, damping and resonant frequency for both the isothermal and adiabatic cases. A larger fillet induces an increase in the resonant frequency as the beam becomes effectively shorter. As the effective beam height increases near the beam to anchor junction, the effective relaxation time for damping in that region increases. In the isothermal case, the increase in the damping outpaces the increase in the resonant frequency, decreasing the quality factor. Conversely, in the adiabatic case, the increase in the resonant frequency outpaces the increase in the damping, giving a higher quality factor. Globally, increasing the fillet has similar consequences than increasing the effective height of the beam. In the adiabatic side, an increase in the height yields a larger quality factor, whereas in the isothermal side, it yields a lower quality factor.

Table 5.4: Effect of fillet on the quality factor of C-C silicon beams.

Height [μm]	Fillet radius [μm]	Q [-]	ω_r [rad/s]	ω_i [rad/s]
4.5	0	14553	939	2.7317e7
4.5	0.45	14351	960	2.7569e7
4.5	0.9	14166	984	2.7879e7
7	0	14296	1406	4.0210e7
7	0.7	14312	1425	4.0786e7
7	1.4	14417	1438	4.1463e7

5.1.7 Effect of Residual Stress

The effect of residual stress on the quality factor is studied. In order to take into account the effect of an initial stress field σ_{ij}^0, the following term has to be added to the total free energy B (Equation (4.1)) [52]:

$$B_g = \sigma_{ij}^0 \epsilon_{ij}^{(2)}, \tag{5.25}$$

where $\epsilon_{ij}^{(2)}$ is the quadratic part of the strain tensor:

$$\epsilon_{ij}^{(2)} = \frac{1}{2} \frac{\partial u_k}{\partial x_i} \frac{\partial u_k}{\partial x_j}. \tag{5.26}$$

Therefore, the mechanical stiffness matrix becomes

$$\mathbf{K_{uu}}^* = \mathbf{K_{uu}} + \mathbf{K_g}, \tag{5.27}$$

where $\mathbf{K_g}$ is the geometric stiffness matrix which satisfies

$$\int_\Omega B_g d\Omega = \frac{1}{2} \mathbf{u_u}^T \mathbf{K_g} \mathbf{u_u}. \tag{5.28}$$

For a beam element of length ℓ and cross-section area A, the geometric stiffness matrix is expressed as follows

$$\mathbf{K_g} = \frac{\sigma_0 A}{30\ell} \begin{pmatrix} 36 & 3\ell & -36 & 3\ell \\ 3l & 4\ell^2 & -3\ell & -\ell^2 \\ -36 & -3\ell & 36 & -3\ell \\ 3\ell & -\ell^2 & -3\ell & 4\ell^2 \end{pmatrix}, \tag{5.29}$$

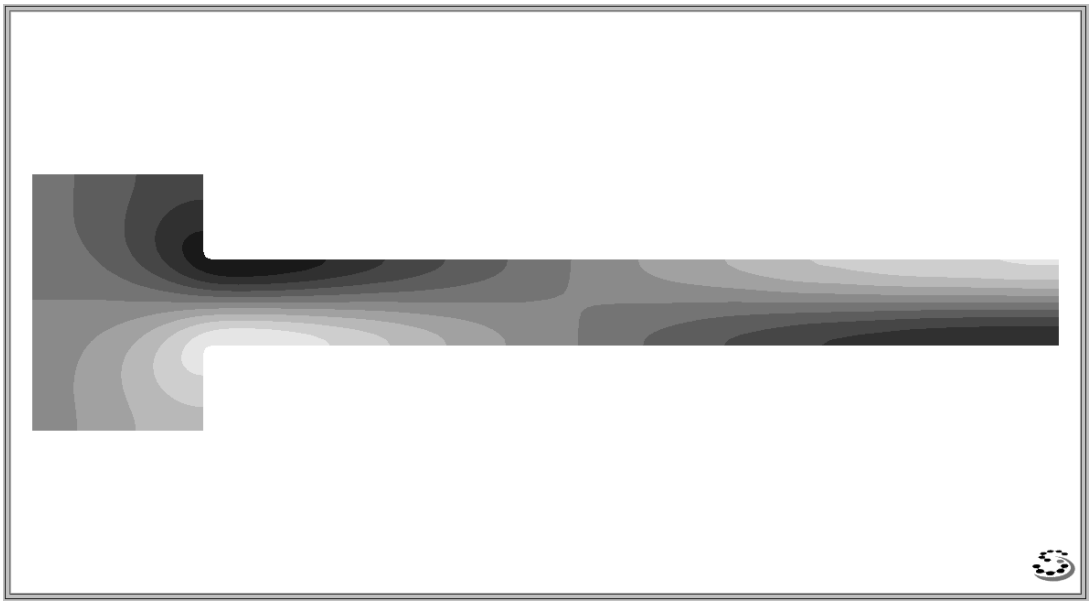

Figure 5.13: Temperature distribution for the isothermal case with the anchor and fillet (radius=0.45 μm).

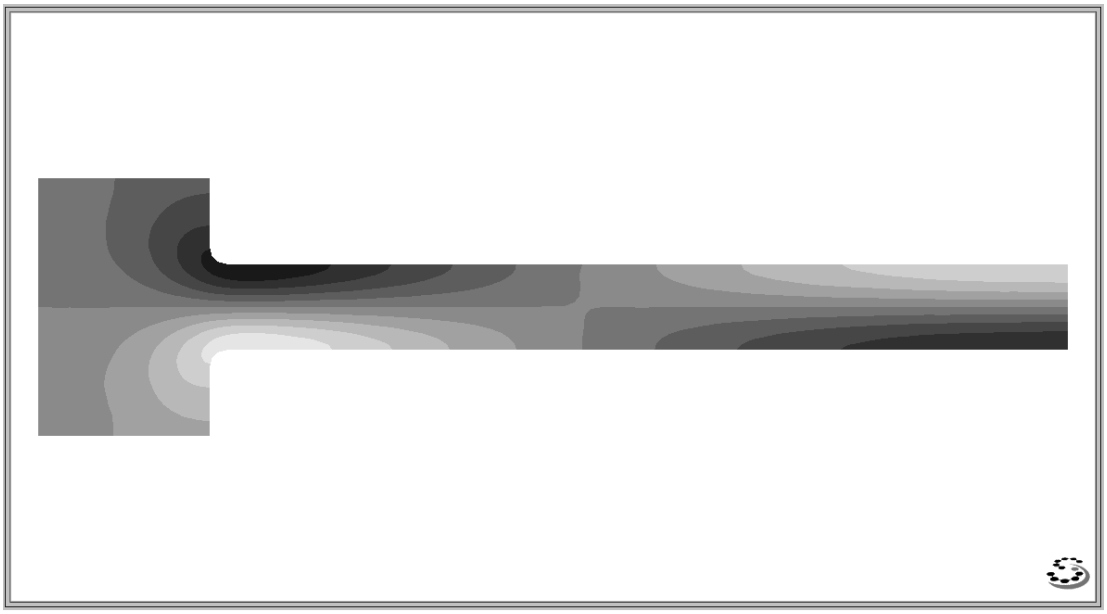

Figure 5.14: Temperature distribution for the isothermal case with the anchor and fillet (radius=0.9 μm).

where σ_0 is a constant axial initial stress.

The effect of residual stress is studied on a beam of length 90 μm, height 4.5 μm and width 4.5 μm. Figure 5.15 represents the variation of the quality factor with the residual stress (solid line). It shows that the quality factor grows linearly with the residual stress. This influence is not only explained by the increase in the resonant frequency (this effect is represented by the dotted line in Figure 5.15), but also by the decrease in the damping as shown in Figure 5.16.

Figure 5.17 compares the temperature increment distribution near the clamped end for the unstressed configuration and the configuration with a residual stress of 200 MPa. The temperature gradient in the longitudinal direction is larger in the unstressed configuration than in the the stressed one. The tensile residual stress reduces the strain concentration at the clamping and hence, the quality factor is improved.

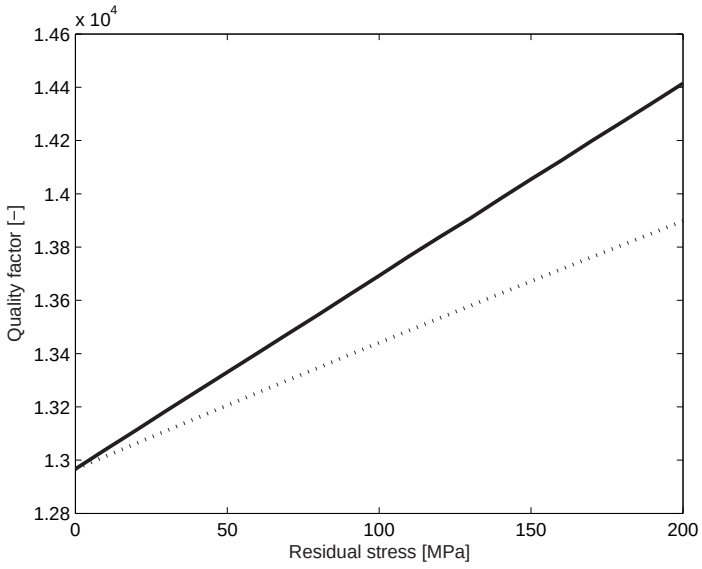

Figure 5.15: Variation of the quality factor with the residual stress (solid line: actual variation, dotted line: variation due to the variation of the resonant frequency).

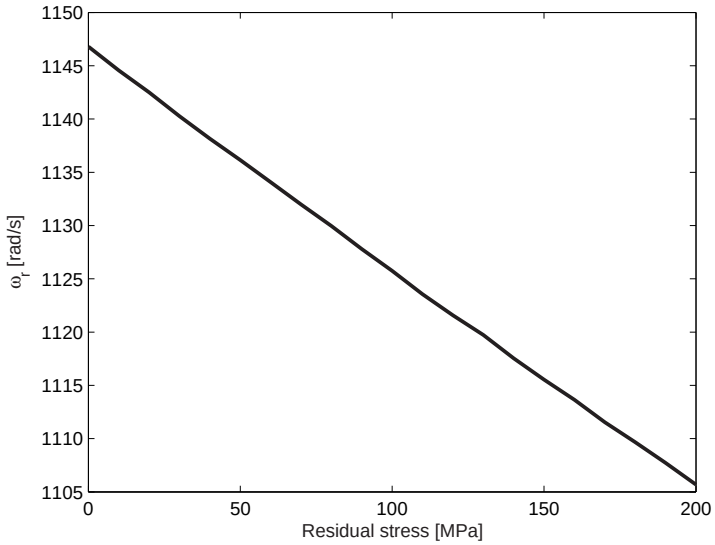

Figure 5.16: Variation of the damping with the residual stress.

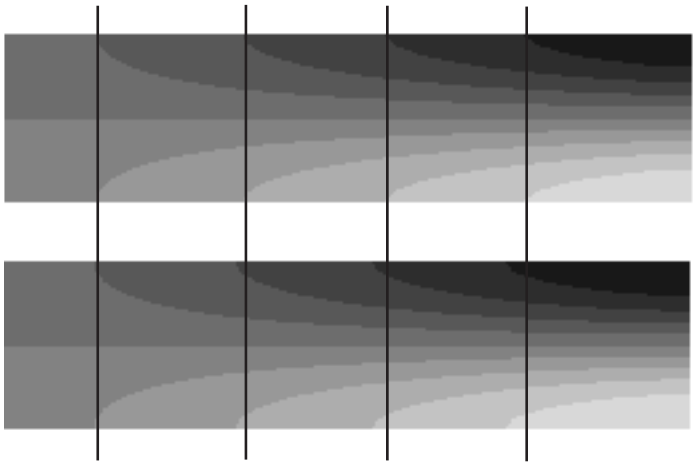

Figure 5.17: Effect of residual stress on the temperature distribution near the clamped end (above: $\sigma_0 = 0$ MPa, below: $\sigma_0 = 200$ MPa).

5.2 Vibrating Inertial Accelerometer Beam

In order to quantify the performance of the VIA (presented in Chapter 2), the thermoelastic quality factor of its sensitive part, a clamped-clamped beam, has to be determined. The beam is made of quartz, which is anisotropic and moreover, piezoelectric. Figure 5.18 shows the geometry of the beam. In this figure, the

scale in the direction of the beam length is ten times smaller than the one in the other two directions. The cross-section of the beam is a right trapezoid. Due to chemical anisotropic etching of quartz during the manufacturing of transducers, some crystalline planes appear and modify the beam geometry, so that the real cross-section of VIA beams is trapezoidal. The beam vibrates along the direction of the largest sides of the trapezoid. The dimensions are given in Table 5.5. Figure 5.18 also illustrates the configuration of the electrodes, which are made of a 200 nm thick layer of gold.

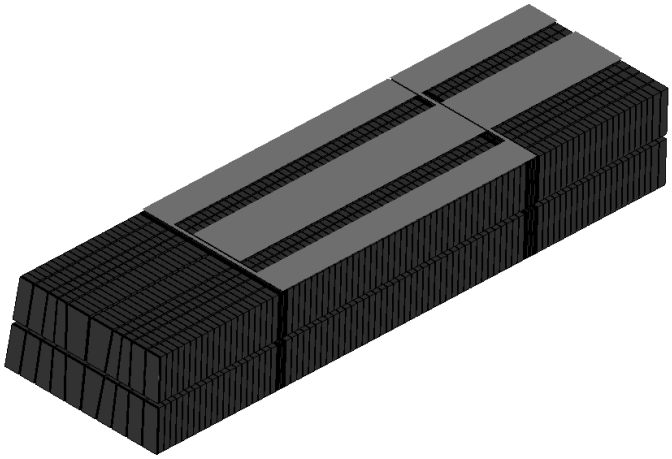

Figure 5.18: VIA beam geometry with electrode position.

Table 5.5: Dimensions of VIA vibrating beam.

Data	Dimension $[\mu m]$
Height	33
Large base	59
Small base	54
Length	2260

Experiments show that the quality factor of the VIA is around 13000 at a resonant frequency of about 62 kHz [98]. However, using equivalent isotropic material data and a resonant frequency of 62 kHz, Zener's model (Equation (3.19))

gives a quality factor of 16576, which is nearly 30 % higher than the experimental value. LR model (Equation 3.52) gives 14763, which is 12 % different from Zener's quality factor. The difference between the two analytical models, which has been explained in Chapter 3, is large when the dimensionless frequency is high. In order to check the influence of the dimensionless frequency, the cantilever configuration, for which the beam is clamped at one end and free at the other one, is considered. In terms of parameters involved in the analytical models, the cantilever configuration differs from the clamped-clamped one only in its frequency, which is lower. For the cantilever configuration, Zener's quality factor is 2712 while LR model gives 2620, and as expected, the difference between the two values is smaller.

Mathematically, the difference is explained by the inherent approximations assumed for the transverse temperature profile. In the finite element method, no approximation is made about the transverse temperature profile, so that the finite element results can be considered as a reference solution. Finite element analyses of both configurations are carried out using exactly the same rectangular geometry and material data as in the analytical models. The finite element quality factors differ from a few percents from LR results, i.e. the finite element quality factor is equal to 2640 for the cantilever configuration and 14111 for the clamped-clamped configuration. Figure 5.19 represents the transverse temperature profile assumed in the two analytical models as well as the finite element profiles. For both configurations (cantilever and clamped-clamped), LR curve gives a better approximation than Zener's curve. As expected, the two finite element curves are different. Indeed, the deformations induced by the bending mode are different in the two cases, so that the thermo-mechanical coupling leads to different distributions of the induced temperature variation.

Even if LR model gives a better approximation than Zener's one, LR quality factor is still more than 10 % higher than the experimental value. This overestimation can be due to the inability of LR model to take into account the real geometry and material behavior of the VIA beam, in particular the trapezoidal cross-section and the anisotropic material. Moreover, piezoelectricity as well as the electrodes can also influence the quality factor. In order to study these additional factors, different finite element analyses are carried out.

Firstly, the effect of anisotropy is taking into account. Tables 5.6 and 5.7

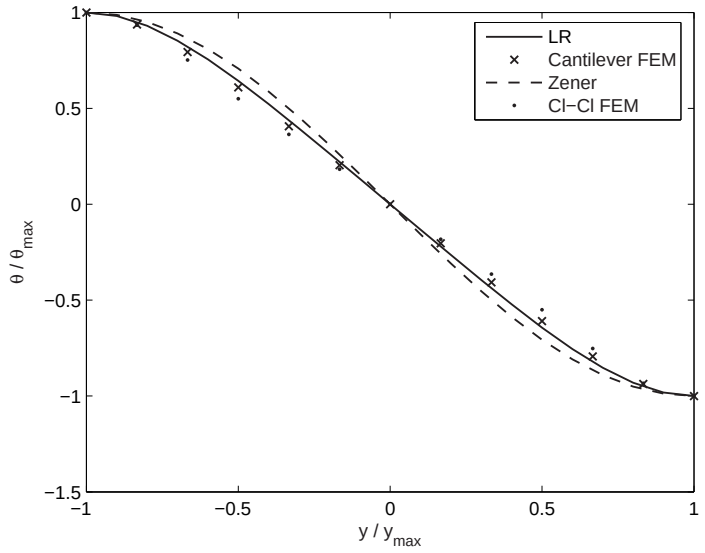

Figure 5.19: Transverse temperature profile.

Table 5.6: Rectangular cross-section configuration resonant frequency.

Configuration	FEM Fr. [Hz]	Ana. Fr. [Hz]
Iso cantilever	9751	9682
Ani cantilever	9724	9682
Iso clamped-clamped	61871	61949
Ani clamped-clamped	61607	61949

Table 5.7: Rectangular cross-section configuration quality factor.

Configuration	FEM Q	LR Q	Z Q
Iso cantilever	2640	2620	2712
Ani cantilever	2649	2620	2712
Iso clamped-clamped	14 111	14763	16576
Ani clamped-clamped	14 157	14763	16576

summarize the results for the clamped-clamped and cantilever configurations. They show that anisotropy slightly increases the quality factor while it lowers the resonant frequency. However, the anisotropy effect cannot explain the difference from the experimental results.

Trapezoidal cross-section finite element models are investigated. Table 5.8 lists the results for trapezoidal cross-section configurations. As before, anisotropy decreases the resonant frequency while it increases the quality factor. However, as for rectangular cross-section configurations, quality factors are still 10 % larger than the experimental results.

Table 5.8: Trapezoidal cross-section configuration results.

Configuration	FEM Fr. [Hz]	FEM Q	LR Q	Z Q
Isotropic	61992	14236	14763	16576
Anisotropic	61626	14644	14763	16576

Table 5.9: VIA structure results.

Configuration	FEM Fr. [Hz]	FEM Q
TE w/o elec	61830	15125
TP w/o elec	62117	14363
TE w/ elec	60815	13700
TP w/ elec	61111	13090

Two effects are still to be investigated: piezoelectricity and the influence of the electrodes. Piezoelectricity is known to increase the resonant frequency, what could also affect the quality factor. The electrodes made of gold, which is a really good thermal conductor compared to quartz, will perturb the thermal field and hence, modify the quality factor. Table 5.9 gives the quality factor of the VIA for four different models: thermoelastic analysis without the electrodes, thermopiezoelectric analysis without the electrodes, thermoelastic analysis with the

electrodes and thermopiezoelectric analysis with the electrodes. It can be seen that the electrodes decrease the quality factor but also the resonant frequency. Figures 5.20 and 5.21 show the temperature increment magnitude distributions corresponding to the bending mode of the VIA beam with and without the electrodes, respectively. The electrodes modify the temperature distribution on the surface of the beam creating a temperature gradient through the height of the beam so that the quality factor decreases significantly. Piezoelectricity increases the resonant frequency as well as it also slightly lowers the quality factor.

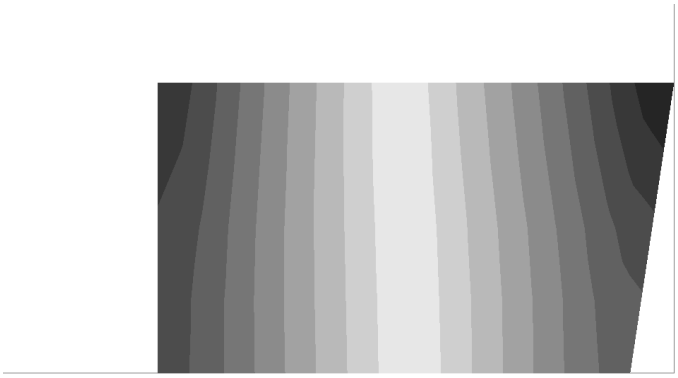

Figure 5.20: Temperature increment magnitude distribution of the VIA beam bending mode without the electrodes.

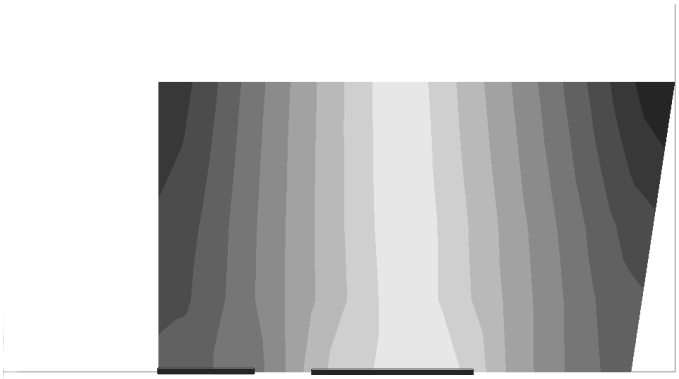

Figure 5.21: Temperature increment magnitude distribution of the VIA beam bending mode with the electrodes.

Therefore, when taking piezoelectricity into account, the quality factor as well as the resonant frequency correspond to the experimental values. These analyses show that the electrodes play an important role in the quality factor, so that this effect is further investigated in the next section.

5.2.1 Effect of Electrodes

Among all the specificities of the VIA beam, the presence of the electrodes implies the most important change in the quality factor. In order to study their effects in more details, a purely thermoelastic test case is considered. It consists in a clamped-clamped beam with a length of 2.26 mm, a vibrating thickness of 56.5 μm and a height of 30 μm. Four 200 nm thick gold electrodes are deposited on this beam near the clampings. The length of the electrodes is equal to one quarter of the beam length and their width is equal to one half of the vibrating thickness of the beam. The electrode position is such that the structure is symmetric with respect to Y and Z axes, so that only one quarter of the structure has to be modeled. The material data are the same as those used for the isotropic quartz in the previous section. The beam is modeled using quadratic hexahedral finite elements. There are 2 elements along the half height, 8 elements along the vibrating thickness and 15 elements along the half length. The electrode is meshed using quadratic quadrilateral plane stress finite elements, which match the beam mesh. Figure 5.22 shows the model with the electrode position.

Table 5.10 compares the quality factor Q, the damping ω_r, the thermoelastic resonant frequency ω_i and the isothermal resonant frequency ω_0 of the configurations without and with electrodes. The electrodes decrease the isothermal as well as the thermoelastic resonant frequency, but they also increases the damping. Both effects lead to a reduction in the quality factor. Figure 5.23 shows the temperature increment distribution at the clamped end for the configuration with electrodes. The electrode induces a temperature gradient into the height of the beam and it also modifies the longitudinal temperature distribution.

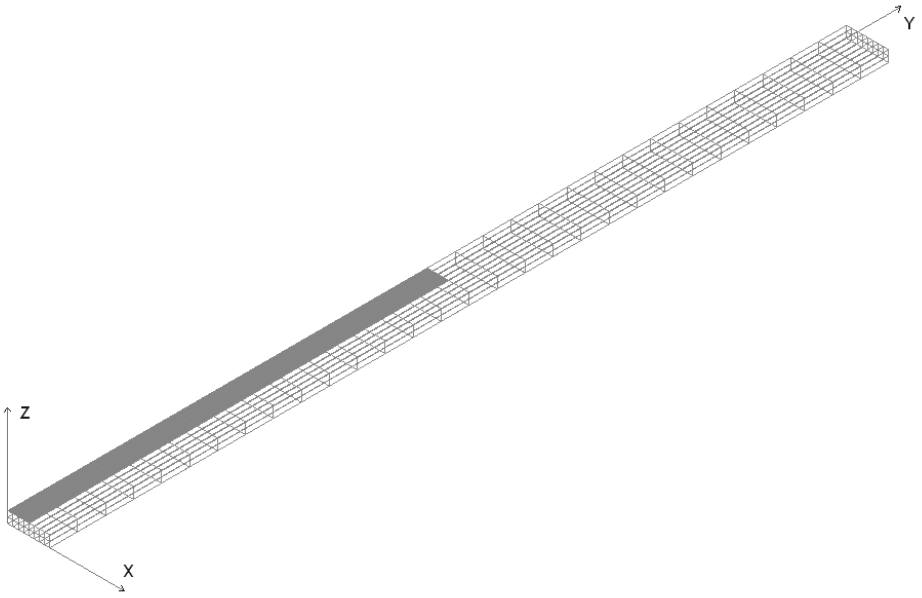

Figure 5.22: Mesh of one quarter of the beam with electrodes.

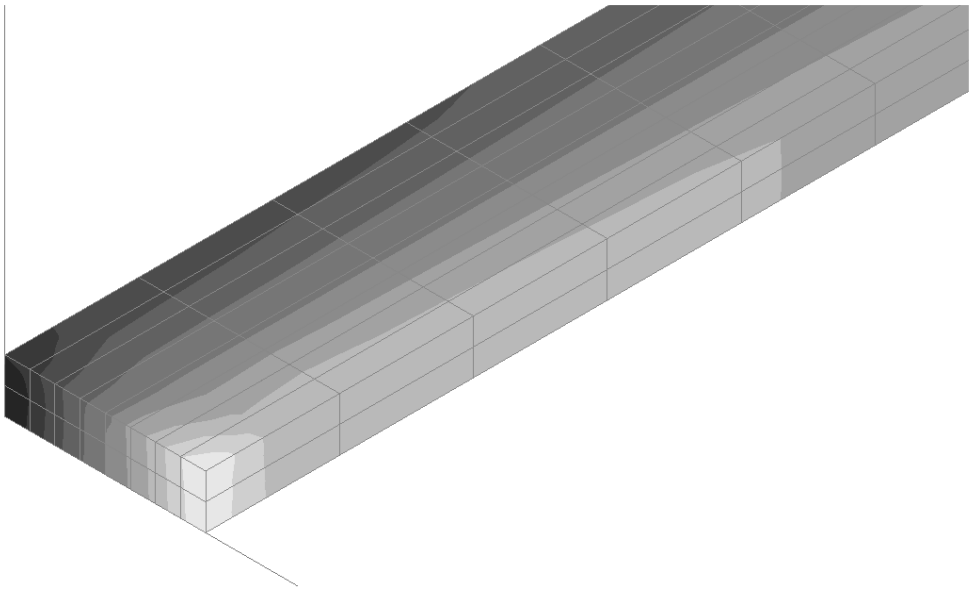

Figure 5.23: Temperature increment distribution at the clamped end for the configuration with electrodes.

Table 5.10: Influence of the electrodes.

Configuration	ω_r [rad/s]	ω_i [rad/s]	Q [-]	ω_0 [rad/s]
w/o electrodes	13.63	388554	14249	388130
w/ electrodes	15.51	388497	12521	388060

5.3 Concluding Remarks

This chapter has presented several applications of the finite element formulation for the thermoelastic and thermopiezoelectric couplings. Two test cases have been studied.

Firstly, a clamped-clamped silicon beam has been modeled. Its quality factor has been quantified using different methods: analytical methods (Zener and Lifshitz-Roukes) and finite element methods (hexahedral FE model, quadrilateral FE model and beam FE model). All these models have intrinsic assumptions and their comparison allows to highlight the influence of different phenomena (Poisson's effect, longitudinal thermal relaxation,...) on the quality factor. The influence of the length to height ratio has been investigated. The effect of anchor and fillet has also been analyzed. It is shown that a tensile residual stress increases the quality factor.

Secondly, the vibrating beam of the VIA presented in Chapter 2 has been analyzed. The specificities of VIA beams, which are not taken into account in analytical models, are the material behavior (anisotropic and piezoelectric), the trapezoidal cross-section and the presence of electrodes. Among these specificities, the electrodes have the most important influence on the quality factor and their effect has been more deeply studied. The finite element results have been compared to the experimental data. When taking into account a model actuated by piezoelectricity, the quality factor as well as the resonant frequency are in agreement with the experimental values. The analyses show that the electrodes play an important role in the quality factor and that piezoelectricity has to be considered in order to accurately determine the resonant frequency.

Part II

Stochastic Analyses

Chapter 6

Uncertainty Treatment in Finite Element Analysis

This chapter reviews the basics of stochastic finite element methods. Firstly, the uncertainty definition is clarified. The concept of random field, which allows the spatial variability modeling of parameters, is exposed as well as methods for its discretization. Second moment stochastic finite element methods are then reviewed. Finally, the most suitable stochastic finite element method and random field discretization method are selected for the modeling of multiphysic problems, and in particular, for thermopiezoelectric eigenproblems.

6.1 Uncertainty Definition

The non-deterministic finite element approaches have received an increasing attention over the last decade. Non-deterministic methods intend to assess the effect of uncertainties on the response or performance of systems. In non-deterministic finite element methods, uncertainty sources are of various types:

- When modeling a system, assumptions are made and a source of uncertainty resides in the mathematical models that are used to describe physical phenomena. One example of this kind of uncertainty is the modeling of damping in materials.

- Numerical errors introduced by the computational implementation of the

mathematical models are another source of uncertainty. In the finite element method, the discretization error is an illustration of this kind of numerical uncertainty.

- The model parameters do also show uncertainty. Many design parameters that describe the geometry, material and environmental effects on the design are subject to uncertainty. These parameters can scatter intrinsically as well as because of the uncontrollable random effects that affect the results of experimental measurements. Moreover, production inaccuracy and design tolerances introduce variability which inevitably leads to a scattering around the nominal behavior of the design.

This work focusses on the third source of uncertainty. It is assumed that the variability of the design parameters has the most important influence on the response variability and that other sources of uncertainty can be disregarded.

Uncertainty can be characterized in different ways. In the literature, uncertain parameters are modeled by probabilistic or possibilistic approaches. In this work, probabilistic uncertainty is considered and any uncertain parameter is represented by a random variable X. The probability that the value of X lies within the interval $[a, b]$ is given by

$$P(a \leq X \leq b) = \int_a^b f_X(x)dx, \tag{6.1}$$

where $f_X(x)$ is the probability density function (PDF) of X. The expectation of the function $g(X)$ is defined by

$$E[g(X)] = \int_{-\infty}^{\infty} g(X) f_X(x)dx. \tag{6.2}$$

If $g(X) = X^n$, one obtains the moments of the random variable X. The first moment ($n = 1$) is the mean or the expectation of X. The central moments of X are obtained by taking $g(X) = (X - E[X])^n$. While the first central moment is zero, the second central moment is by definition the variance of X, denoted $Var(X)$. The square root of the variance, σ, is the standard deviation of X, which is a common measure for the dispersion of the distribution about the mean value.

For multiple probabilistic variables $(X_1, X_2, \ldots, X_n)$, the concept of the probability density function is extended to dimension n using the joint probability

density function $f_{X_1,X_2,\ldots,X_n}(x_1, x_2, \ldots, x_n)$. The multivariate expectation is defined analogously to the univariate one. In order to quantify the interdependence between the variables, the covariance of two variables X_i and X_j is defined as the expectation of the product of the deviations from their respective means, m_i and m_j:

$$B_{ij} = Cov(X_i, X_j) = E[(X_i - m_i)(X_j - m_j)] = E[X_i X_j] - m_i m_j, \tag{6.3}$$

and the covariance matrix $\mathbf{B}$ containing all individual variances and covariances is constructed:

$$\mathbf{B} = \begin{pmatrix} Var(X_1) & Cov(X_1, X_2) & \cdots & Cov(X_1, X_n) \\ Cov(X_2, X_1) & Var(X_2) & \cdots & Cov(X_2, X_n) \\ \vdots & \vdots & \vdots & \vdots \\ Cov(X_n, X_1) & Cov(X_n, X_2) & \cdots & Var(X_n) \end{pmatrix}. \tag{6.4}$$

The main property of $\mathbf{B}$ is that it is positive definite.

6.2 Discretization Methods for Random Fields

Random field concept allows the continuous spatial variability of parameters to be taken into account in stochastic modeling. This means that instead of dealing with a discrete set of random variables $(X_1, X_2, \ldots, X_n)$, the random field formalism can deal with a distributed random variable $X = X(\mathbf{x})$ which takes one value for any $\mathbf{x}$ located in the parameter space. For example, Young's modulus E of a solid can be modeled as a random field in order to take into account its spatial variation and at any point $\mathbf{x}$ of the solid, the value of Young's modulus $E(\mathbf{x})$ is a random variable. Vanmarcke [144] provides extensive details on the analysis and synthesis of random fields. Random processes are analogous to random fields in the way they allow the time variability of parameters to be modeled.

The complete description of a random function is generally too complex, so that the description is usually based on just the first two moments of the probability distribution, which is a complete description for a Gaussian function. The first and second moments are also referred as the mean and covariance functions, respectively. In this work, homogeneous Gaussian random fields are considered,

meaning that probabilistic properties remain the same when the spatial coordinates are translated and a second order description is complete. The mean of the random field at location $\mathbf{x}$ is

$$E[X(\mathbf{x})] = m_X(\mathbf{x}) = m \tag{6.5}$$

and the variance of $X(\mathbf{x})$ is

$$Var[X(\mathbf{x})] = E[(X(\mathbf{x}) - m(\mathbf{x}))^2] = \sigma_X^2(\mathbf{x}) = \sigma^2, \tag{6.6}$$

where σ is the standard deviation. Note that the mean m and the variance σ^2 are constant as the random field is homogeneous. In order to characterize the random field, the covariance function, which gives the covariance of the values of the random field at two different locations $\mathbf{x}_1$ and $\mathbf{x}_2$, is to be defined:

$$\begin{aligned} B_X(\mathbf{x}_1, \mathbf{x}_2) &= Cov[X(\mathbf{x}_1), X(\mathbf{x}_2)] && (6.7)\\ &= E[X(\mathbf{x}_1)X(\mathbf{x}_2)] - m_X(\mathbf{x}_1)m_X(\mathbf{x}_2) && (6.8)\\ &= E[X(\mathbf{x}_1)X(\mathbf{x}_2)] - m^2. && (6.9) \end{aligned}$$

Likewise the correlation function can be defined as

$$\begin{aligned} \rho_X(\mathbf{x}_1, \mathbf{x}_2) &= \frac{B_X(\mathbf{x}_1, \mathbf{x}_2)}{\sigma_X(\mathbf{x}_1)\sigma_X(\mathbf{x}_2)} && (6.10)\\ &= \frac{B_X(\mathbf{x}_1, \mathbf{x}_2)}{\sigma^2}. && (6.11) \end{aligned}$$

Considering that the random field is homogeneous and isotropic, the covariance and correlation functions only depend on the distance τ between points $\mathbf{x}_1$ and $\mathbf{x}_2$: $\tau = |\mathbf{x}_1 - \mathbf{x}_2|$.

The most common correlation functions for random fields are [80, 144]:

- the triangular correlation function that decreases linearly from 1 to 0 as τ goes from 0 to a:

$$\rho(\tau) = \begin{cases} 1 - \frac{\tau}{a}, & \tau \le a, \\ 0, & \tau \ge a. \end{cases} \tag{6.12}$$

- the exponential correlation function associated with a first-order autoregressive (or Markov) field, which is one of the most commonly applied in engineering:

$$\rho(\tau) = e^{-\tau/b}, \tag{6.13}$$

- the Gaussian (squared exponential) correlation function used when the correlation decreases rapidly with τ:

$$\rho(\tau) = e^{-(\tau/d)^2}, \tag{6.14}$$

- the correlation function associated with a second-order autoregressive process:

$$\rho(\tau) = \left[1 + \frac{\tau}{c}\right] e^{-\tau/c}. \tag{6.15}$$

In Equations (6.12) to (6.15), coefficients a, b, c and d are influence lengths. In particular, b is also called the correlation length. The scale of fluctuation θ_F characterizes the decreasing behavior of the covariance with the distance independently of the character and shape of the correlation function and is related to the influence lengths as follows

$$\theta_F = a, \quad \theta_F = 2b, \quad \theta_F = 4c \text{ and } \theta_F = \sqrt{\pi}/d. \tag{6.16}$$

Figure 6.1 represents the above correlation functions against the normalized distance τ/θ_F.

Due to the lack of experimental data, some assumptions have to be made regarding the homogeneity, isotropy and Gaussianess of the random field and the expression of the correlation function. In particular, the influence of the correlation function assumption on the stochastic response has to be highlighted.

A discretization procedure is the approximation of the random field $X(.)$ by $\hat{X}(.)$ defined by means of a finite set of random variables. Some partial literature reviews are available in the following references [97, 99, 128, 137, 142]. The discretization methods can be divided into three groups:

- point discretization methods,
- average discretization methods,
- series expansion methods.

6.2.1 Point Discretization Methods

The point discretization methods consist in modeling the random field $X(.)$ by its values at some given points $\mathbf{x}_i$, so that the number of points determines the number of random variables $b_i = X(\mathbf{x}_i)$ required to represent the random field. The advantages of these methods are that:

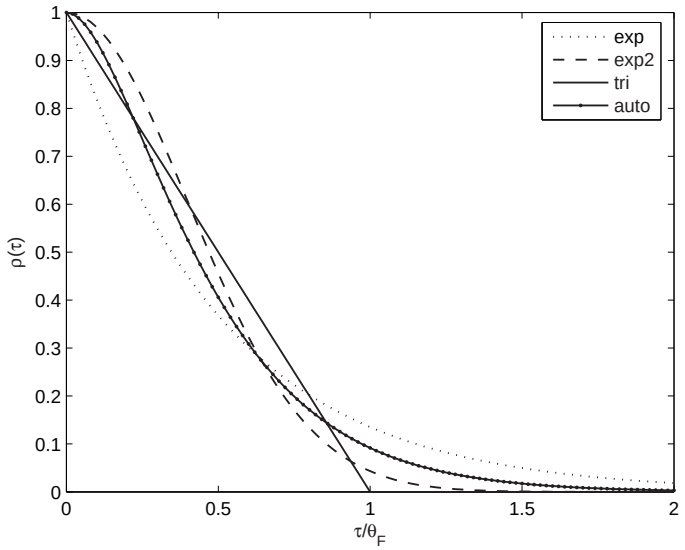

Figure 6.1: The triangular (tri), exponential (exp), squared exponential (exp2) and autoregressive (auto) correlation functions $\rho(\tau)$ plotted against the normalized distance τ/θ_F.

- the covariance matrix of the random variables can easily be computed,
- the covariance matrix is positive definite,
- the discretization of the random field has the same distribution function as the initial random field, so that these methods are not restricted to the discretization of Gaussian random fields.

The midpoint discretization method is the most widely used point discretization method. It consists in discretizing the random field on a mesh (i.e. the finite element mesh or any other one) using its values at the center points $\mathbf{x}_i^c$ of the mesh elements Ω_i:

$$\hat{X}(\mathbf{x}) = X(\mathbf{x}_i^c) = b_i, \quad \mathbf{x} \in \Omega_i. \tag{6.17}$$

The first two statistical moments of the random variables b_i are directly obtained from the first two statistical moments of the random field:

$$E[b_i] = E[\mathbf{x}_i^c] = m \tag{6.18}$$

and

$$B_{ij} = Cov(b_i, b_j) \tag{6.19}$$
$$= B_X(\mathbf{x}_i^c, \mathbf{x}_j^c). \tag{6.20}$$

The drawback of this method is that its performance is directly related to the mesh characteristics. The size of the mesh elements has to be small with respect to the correlation length, so that the modeled random properties can be considered as constant within each element. Moreover, the shape and size of all these elements should be the same in order to reduce the discretization error. In terms of computational cost, if a fine mesh is required (e.g. due to a small correlation length), the number of random variables can become excessive. Note that if the finite element mesh is used for the generation of the random field mesh and is finer than the required random field mesh, the random field elements can be blocks of several finite elements. This allows not only the reduction of the number of random variables but also numerical instability caused by near perfect correlation between variables to be avoided [40]. It is shown in [40] that the midpoint method tends to over-represent the variability of the random field within each element. This method can be used in Monte-Carlo simulations as well as in the perturbation Stochastic Finite Element Method [49].

Other less known examples of point discretization methods are the nodal point method [99], the integration point method [99], the interpolation method (or shape function method) [93] and the optimal linear estimation method (or Kriging method) [90].

6.2.2 Average Discretization Methods

In average discretization methods, the random variables are weighted integrals of $X(.)$ over a domain. The Local Average method consists in approximating the field in each element Ω_i of a mesh (e.g. finite element mesh or any other one) as a constant being computed as the average of the original field over the element [144]:

$$\hat{X}(\mathbf{x}) = \frac{\int_{\Omega_i} X(\mathbf{x}) d\Omega}{\int_{\Omega_i} d\Omega} = b_i, \quad \mathbf{x} \in \Omega_i. \tag{6.21}$$

The first two statistical moments of the random variables are expressed in terms of the statistical moments of the random field:

$$E[b_i] = E\left[\frac{\int_{\Omega_i} X(\mathbf{x})d\Omega}{\int_{\Omega_i} d\Omega}\right] \tag{6.22}$$

$$= \frac{\int_{\Omega_i} E[X(\mathbf{x})]d\Omega}{|\Omega_i|} \tag{6.23}$$

$$= m \tag{6.24}$$

and

$$B_{ij} = Cov(b_i, b_j) = Cov\left(\frac{\int_{\Omega_i} X(\mathbf{x})d\Omega}{\int_{\Omega_i} d\Omega}, \frac{\int_{\Omega_j} X(\mathbf{x})d\Omega}{\int_{\Omega_j} d\Omega}\right) \tag{6.25}$$

$$= \frac{\int_{\Omega_i}\int_{\Omega_j} B_X(\mathbf{x},\mathbf{s})d\Omega_i d\Omega_j}{|\Omega_i||\Omega_j|}. \tag{6.26}$$

Comparison of Equations (6.20) and (6.26) clearly shows that the computation of the covariance matrix is easier for the midpoint method than for the local average method. Vanmarcke [144] gives analytical expressions for 1-D and 2-D homogeneous fields discretized on a regular mesh. For example, the covariance between two elements U and U' in 1-D is given by

$$Cov(U, U') = \frac{\sigma^2}{2UU'}[U_o^2\gamma(Uo) - U_1^2\gamma(U1) + U_2^2\gamma(U2) - U_3^2\gamma(U3)], \tag{6.27}$$

where U_o, U_1, U_2 and U_3 are distances as illustrated in Figure 6.2 and $\gamma(.)$ is the variance function which measures the reduction of the point variance σ^2 under local averaging. It is defined by

$$Var(X_L) = \gamma(L)\sigma^2, \tag{6.28}$$

where X_L is the local average of the random field X over an element of size L. The variance function is related to the correlation function $\rho(\tau)$ as follows

$$\gamma(L) = \frac{2}{L}\int_0^L \left(1 - \frac{\tau}{L}\right)\rho(\tau)d\tau, \tag{6.29}$$

so that the variance function corresponding to the above expressed correlation functions (Equations (6.12)-(6.15)) are expressed as:

- the triangular variance function

$$\gamma(L) = \begin{cases} 1 - \frac{L}{3a}, & L \le a, \\ \frac{a}{L}\left(1 - \frac{a}{3L}\right), & L \ge a, \end{cases} \tag{6.30}$$

- the exponential variance function

$$\gamma(L) = 2\left(\frac{b}{L}\right)^2\left(\frac{L}{b} - 1 + e^{-L/b}\right), \tag{6.31}$$

- the squared exponential variance function

$$\gamma(L) = \left(\frac{d}{L}\right)^2\left(\sqrt{\pi}\frac{L}{d}E\left(\frac{L}{d}\right) - 1 + e^{-(L/d)^2}\right), \tag{6.32}$$

  where $E(.)$ is the widely tabulated error function,

- the autoregressive variance function

$$\gamma(L) = 2\left(\frac{c}{L}\right)^2\left(2 + e^{-L/c} - 3\frac{c}{L}(1 - e^{-L/c})\right). \tag{6.33}$$

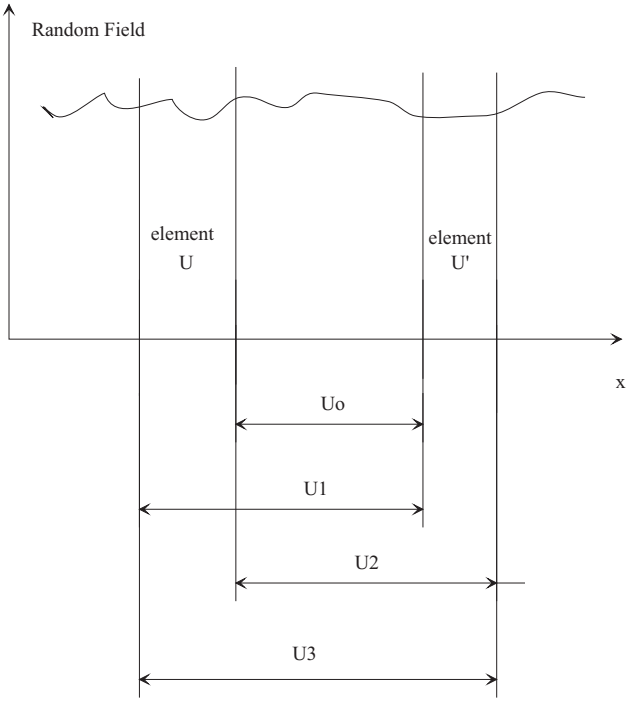

Figure 6.2: Definition of the distances used in the expression of the covariance between local averages in 1-D.

Compared to the midpoint method, the local average method leads to more accurate results, but the accuracy still depends on the mesh refinement. The number of random variables corresponds to the number of elements, so that a fine

mesh requires more computational efforts than a coarse one. According to [40] and Equation (6.28), this method tends to underrepresent the variability within each element, so that bounds can be given for the actual variability using the midpoint and local average methods. When the number of elements increases with respect to the correlation length, both methods converge to the same covariance, which they bracket. In 2-D cases, non-rectangular elements can be used, but they may lead to a non-positive covariance matrix.

The weighted integral method [39, 60, 61] can also be considered as an average discretization method. In this method, the random and finite element meshes have to be identical since the random field is projected onto the space of polynomials involved in the shape function derivative matrices of the elementary structural matrices. The number of random variables is related to the order of these polynomials.

6.2.3 Series Expansion Methods

Series Expansion Methods consist in approximating the random field $X(.)$ by a truncated series involving random variables and deterministic spatial functions:

$$\hat{X}(\mathbf{x}, \xi) = \sum_{i=1}^{N} \zeta_i(\xi)\phi_i(\mathbf{x}), \tag{6.34}$$

where $\phi_i(\mathbf{x})$ are deterministic functions and $\zeta_i(\xi)$ are random variables. The dependence of the variable on ξ explicitly expresses its random characteristic, ξ is a value of the sample space, which is the set of all possible outcomes of a random experiment. The discretization occurs through the truncation of the series and the number of random variables is equal to the order of the expansion, so that it can be much lower than in other methods.

The midpoint and local average methods can also be expressed as series expansion methods:

$$\hat{X}(\mathbf{x}, \xi) = \sum_{i=1}^{N} b_i(\xi)g_i(\mathbf{x}), \tag{6.35}$$

where N is the number of elements and $g_i(\mathbf{x}) = 1$ if $\mathbf{x} \in \Omega_i$ and $g_i(\mathbf{x}) = 0$ if $\mathbf{x} \notin \Omega_i$.

Karhunen-Loeve expansion [58] is based on the spectral decomposition of the

covariance function:

$$\hat{X}(\mathbf{x},\xi) = \bar{X}(\mathbf{x}) + \sum_{k=1}^{N} \sqrt{\lambda_k} f_k(\mathbf{x}) \zeta_k(\xi), \tag{6.36}$$

where $\bar{X}(\mathbf{x})$ is the expected value of the random field, ζ_k are random variables independent of $\mathbf{x}$, λ_k and f_k are the eigenvalues and eigenfunctions of the covariance kernel, respectively, which can be obtained as the solutions of the eigenvalue problem:

$$\int_{\Omega} B_X(\mathbf{x}_1,\mathbf{x}_2) f_k(\mathbf{x}_2) d\mathbf{x}_2 = \lambda_k f_k(\mathbf{x}_1). \tag{6.37}$$

This is an homogeneous Fredholm integral equation of the second kind. The random variables have the following properties:

$$E[\zeta_k] = 0 \quad \text{and} \quad E[\zeta_k \zeta_l] = \delta_{kl}. \tag{6.38}$$

For an exponential covariance kernel, Karhunen-Loeve expansion has analytical solutions for 1-D and 2-D exponential correlation functions. For a 1-D random field defined on a domain of length L, the eigenvalues are given by

$$\lambda_k = \frac{2\sigma^2 a}{1 + a^2 \omega_k}, \tag{6.39}$$

where a is the correlation length, σ is the standard deviation and ω_k is the kth root of the following transcendental functions:

$$f(\omega) = \omega - \frac{\cos(\omega L) - 1}{a \sin(\omega L)} \quad \text{for } k \text{ even} \tag{6.40}$$

and

$$f(\omega) = \omega - \frac{\cos(\omega L) + 1}{a \sin(\omega L)} \quad \text{for } k \text{ odd.} \tag{6.41}$$

Similarly, the eigenfunctions are expressed as functions of ω_k:

$$f_k(x) = \sqrt{\frac{2\omega_k}{\omega_k L - \sin(\omega_k L)}} \sin\left(\omega_k (x - \frac{L}{2})\right) \quad \text{for } k \text{ even} \tag{6.42}$$

and

$$f_k(x) = \sqrt{\frac{2\omega_k}{\omega_k L + \sin(\omega_k L)}} \cos\left(\omega_k (x - \frac{L}{2})\right) \quad \text{for } k \text{ odd.} \tag{6.43}$$

Figure 6.3 shows the first five eigenfunctions of a random field with an exponential correlation function ($a = 5$ and $L = 10$).

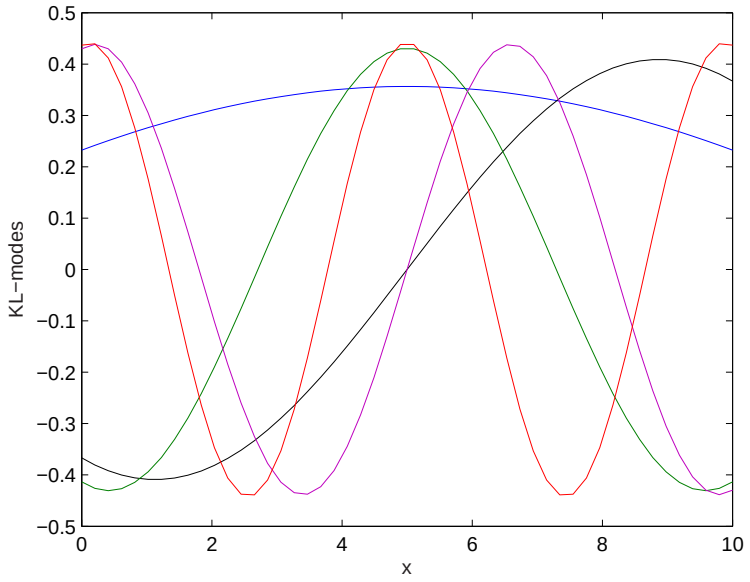

Figure 6.3: First five eigenfunctions of an exponential covariance kernel.

In more general situations, a numerical procedure, such as the finite element method, has to be used to solve the eigenvalue problem (6.37). The resulting basis is not exactly optimal, but may still lead to a sufficiently good approximation $\hat{X}$.

The orthogonal series expansion method [159] avoids solving the eigenvalue problem (6.37) by selecting ab initio a complete set of orthogonal functions, e.g. Legendre polynomials. The orthogonal series expansion approximates the random field by

$$\hat{X}(\mathbf{x},\xi) = \bar{X}(\mathbf{x}) + \sum_{i=1}^{M} h_i(\mathbf{x})\zeta_i(\xi), \tag{6.44}$$

where ζ_i are the components of a zero-mean Gaussian vector, whose covariance matrix component B_{kl} are defined by

$$B_{kl} = \int\int \sigma^2 \rho(\mathbf{x},\mathbf{x}') h_k(\mathbf{x}) h_l(\mathbf{x}') d\mathbf{x} d\mathbf{x}' \tag{6.45}$$

and $h_i(\mathbf{x})$ are orthogonal functions.

The orthogonal series expansion method involves the following steps:

- construct a complete set of orthogonal deterministic functions h_i, for example, this set can be based on the Legendre polynomials [159],

- calculate the covariance matrix according to Equation (6.45) using for example a Gaussian integration procedure.

The Polynomial Chaos expansion [58, 76] is based on the expansion of the random field on the subspace defined by a set of orthogonal polynomials Γ_p not exceeding the order p, called the polynomial chaos of order p, in terms of a set of orthogonal Gaussian random variables $\{\zeta_i\}_i^\infty$:

$$\begin{aligned} X &= a_0\Gamma_0 + \sum_{i_1=1}^{\infty} a_{i_1}\Gamma_1(\zeta_{i_1}) + \sum_{i_1=1}^{\infty}\sum_{i_2=1}^{i_1} a_{i_1 i_2}\Gamma_2(\zeta_{i_1},\zeta_{i_2}) \\ &+ \sum_{i_1=1}^{\infty}\sum_{i_2=1}^{i_1}\sum_{i_3=1}^{i_2} a_{i_1 i_2 i_3}\Gamma_3(\zeta_{i_1},\zeta_{i_2},\zeta_{i_3}) \\ &+ \sum_{i_1=1}^{\infty}\sum_{i_2=1}^{i_1}\sum_{i_3=1}^{i_2}\sum_{i_4=1}^{i_3} a_{i_1 i_2 i_3 i_4}\Gamma_4(\zeta_{i_1},\zeta_{i_2},\zeta_{i_3},\zeta_{i_4}) + \ldots, \end{aligned} \tag{6.46}$$

where Γ_p are successive polynomial chaos and $a_{i_1\ldots i_p}$ are deterministic constants. Truncating after the Jth polynomial, the random field series expansion reads

$$\hat{X} = \sum_{i=1}^{J} \kappa_i \Psi_i[\{\zeta_r\}], \tag{6.47}$$

where κ_i and $\Psi_i[\{\zeta_r\}]$ are identical to $a_{i_1\ldots i_p}$ and $\Gamma_p(\zeta_{i_1},\ldots,\zeta_{i_p})$, respectively.

The spectral decomposition of a random field can also be considered as a series expansion method. Applying the Fast Fourier Transform Method to the generation of a random field gives

$$X(x_j) = \sum_{k=0}^{K} C_k cos(x_j\omega_k + \Phi_k), \tag{6.48}$$

where Φ_k is a random phase angle uniformly distributed on $[0, 2\pi]$ and C_k follows a Rayleigh distribution. Once the upper frequency ω_u is specified, the frequency discretization step is given by $\Delta\omega = \omega_u/K$ and ω_k is equal to $(k - 0.5) * \Delta\omega$.

Shinozuka [133, 135] takes $C_k = \sqrt{2G(\omega_k)\Delta\omega}$ where $G(\omega)$ is the one-sided spectral density function, but this gives an upper bound on X over the space of outcomes of $X \leq \sum_{k=0}^{K}\sqrt{2G(\omega_k)\Delta\omega}$, which may be an unrealistic restriction.

Fenton [48] proposed the following strategy in order to avoid this upper bounding:

1. generate independent, normally distributed realizations of A_k and B_k with a zero mean and a variance given by

$$E[A_k^2] = \begin{cases} 0.5G(\omega_k)\Delta\omega, & \text{if } k = 0 \\ 0.25(G(\omega_k) + G(\omega_{K-k}))\Delta\omega, & \text{if } k = 1, ..., K/2 - 1 \\ G(\omega_k)\Delta\omega, & \text{if } k = K/2 \end{cases} \tag{6.49}$$

and

$$E[B_k^2] = \begin{cases} 0, & \text{if } k = 0 \quad \text{or} \quad K/2 \\ 0.25(G(\omega_k) + G(\omega_{K-k}))\Delta\omega, & \text{if } k = 1, ..., K/2 - 1 \end{cases} \tag{6.50}$$

and set $B_0 = B_{K/2} = 0$. Note that these variances have only to be calculated once,

2. use the symmetry relationships: $A_k = A_{K-k}$ and $B_k = -B_{K-k}$,

3. produce the field realization by fast Fourier transform using $X_j = \sum_{k=0}^{K-1} Z_k e^{i2\pi jk/K}$ where the Fourier coefficient $Z_k = A_k - iB_k$.

The shortcomings of this method are that:

- the covariance function is always symmetric about the midpoint of the field. This can be avoided by modeling twice the size of the physical field.

- the relationship between the spatial and frequency discretization $\Delta\omega$ should be small enough to catch the variation of $G(\omega)$ and the frequency content above $2\pi/\Delta\omega$ should be negligible.

6.2.4 Method Comparison

An efficient method for discretizing a random field requires the smallest number of random variables to describe the field within a given level of accuracy. In order to illustrate the performance of the different methods, a 1-D random field characterized on the domain $[0, 10]$ by an exponential correlation function, a mean of 0, a standard deviation of 1 and a correlation length of 5 is discretized using successively the Midpoint method (MP), Local Average method (LA), Karhunen-Loeve expansion method (KL) and the Orthogonal series expansion method (OSE). For each method, 2000 realizations of the random field are generated and the following analyses are carried out:

- the mean and variance are computed and compared to exact ones,
- the run time is estimated (even if usually the time taken to generate the field is dwarfed by the time taken to subsequently process or analyze the field),
- the upper and lower 90 percents quantiles of estimated mean and variance fields are calculated. Firstly, the mean and variance fields, i.e. the mean and variance of the realizations at each discretization point, are estimated. Then, the upper and lower bounds, such that 5 percents of the field exceeds the bounds above and below, respectively, are found.

Additionally, for series expansion methods, the point-wise error is estimated by

$$\epsilon rr(\mathbf{x}) = \frac{Var\left[X(\mathbf{x}) - \hat{X}(\mathbf{x})\right]}{Var\left[X(\mathbf{x})\right]}. \tag{6.51}$$

For the Midpoint and Local Average methods, a mesh has to be defined and the domain is divided into 50 equal elements (number of elements, $N = 50$). The random fields are generated in three basic steps:

- A random uncorrelated Gaussian vector $\mathbf{Z}$ [size: N] is generated with a zero mean and a variance equal to one, e.g. using randn Matlab function,
- The covariance matrix [size: N x N] is obtained by calculating the correlation function at the middle of every element for the Midpoint method and using Equation (6.27) for the Local Average method.
- The correlated vector $\hat{\mathbf{X}}$ of the random variable which approximate the random field is obtained by one the two following transformations:
  - the Cholesky transformation:

$$\hat{\mathbf{X}} = \bar{\mathbf{X}} + \mathbf{LZ}, \tag{6.52}$$

    where $\mathbf{L}$ is a lower triangular matrix obtained by the Cholesky decomposition of the covariance matrix, which is positive definite,
  - the spectral transformation:

$$\widehat{\mathbf{X}} = \bar{\mathbf{X}} + \mathbf{Zvals}_{0.5}\mathbf{vects}', \tag{6.53}$$

where $\mathbf{vals}_{0.5}$ is a diagonal matrix whose elements are the square root of the eigenvalues of the covariance matrix and **vects** is a matrix whose columns are the eigenvectors of the covariance matrix.

Both methods give the same results. However, the eigensolution transformation is more adequate when the size of the covariance matrix is large. Indeed, for large covariance matrix, only the r first dominant eigensolutions ($r < N$) can be used, while Cholesky decomposition can be very CPU time consuming if the matrix is large.

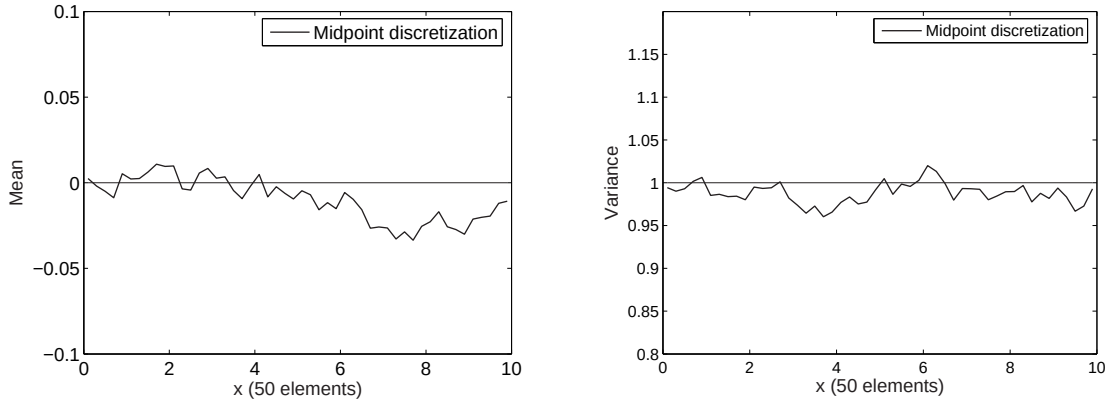

Figure 6.4: Mean and variance fields estimated over 2000 Midpoint realizations.

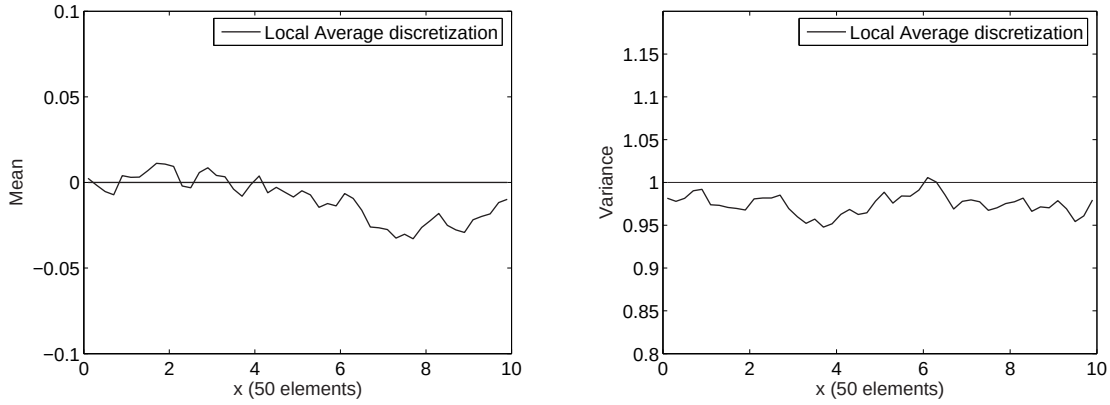

Figure 6.5: Mean and variance fields estimated over 2000 Local Average realizations.

Figures 6.4-6.5 show the mean and variance fields estimated over 2000 realizations for the midpoint and the local average methods, respectively. The mean and variance are close to their target value (0 and 1) for both methods. The variance is slightly lower for the Local Average method than for the Midpoint one in agreement with [40]. Both methods bracket the variance of the 2000 random field samples. If the element size were larger with respect to the correlation length, this underestimation would be larger. The mean seems to diverge in the right part of the domain ($x > 6$), but it is only due to the random set. If the random set were different, the behavior would be different. In order to ensure that the mean has the same behavior all along the field domain, the random set size (i.e. the number of samples) should be increased.

If the spectral transformation (6.53) is used, the random basis can be truncated since only a few modes of the covariance matrix are sufficient to capture the major characteristics of the probabilistic distribution by analogy to modal structural problems. Since the truncation error decreases as the sum of the considered eigenvalues increases (Section 7.8), the highest eigenvalues are employed in contrast to the modal structural problems wherein the lowest eigenvalues are used. Figure 6.6(a) gives the eigenvalues of the covariance matrix for the midpoint method. Only the first six eigenvalues are significantly larger than the other ones. If the relative contribution of the first n eigenvalues to the trace of the covariance matrix is plotted (Figure 6.6(b)), it can be seen that the first eight eigenvalues contribute to 95 % of the covariance trace. Hence, when the first eight eigenmodes instead of all 50 modes are used in Equation (6.53), the generated correlated vectors are characterized by a really good approximation of the first and second probabilistic moments (Figure 6.7). When using an incomplete modal basis, the size of the uncorrelated vector is equal to the size of the modal basis. Hence, the random field is represented with less random variables. Truncating the modal basis becomes advantageous for large size covariance matrices, which are obtained if the number of elements is large. Then, the calculation of all the eigenmodes is no more possible, but an iteration method such as the Lanczos method (Section 4.4) is still able to calculate the highest eigenvalues and the corresponding modes.

For the Karhunen-Loeve (KL) expansion method, the random fields are given by Equation (6.36), where the eigenvalues and eigenfunctions are determined by

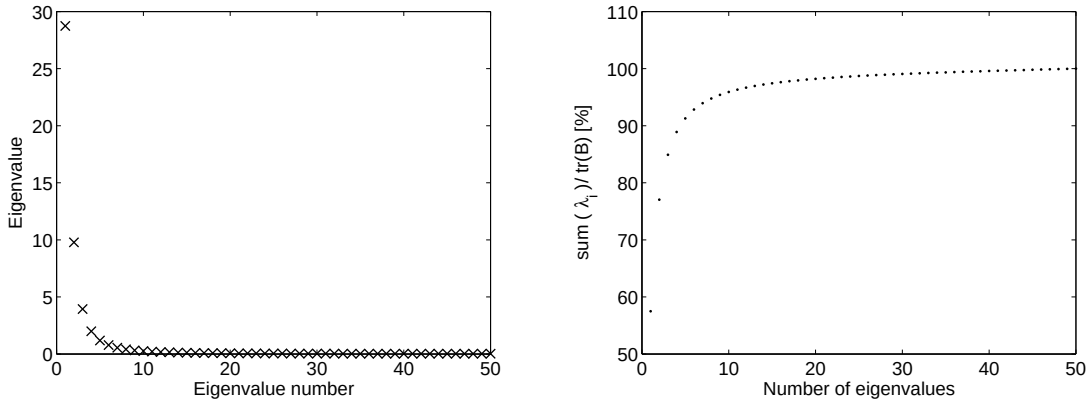

(a) (b)

Figure 6.6: Eigenvalues of the covariance matrix and their contribution to the trace of the covariance matrix (Midpoint method).

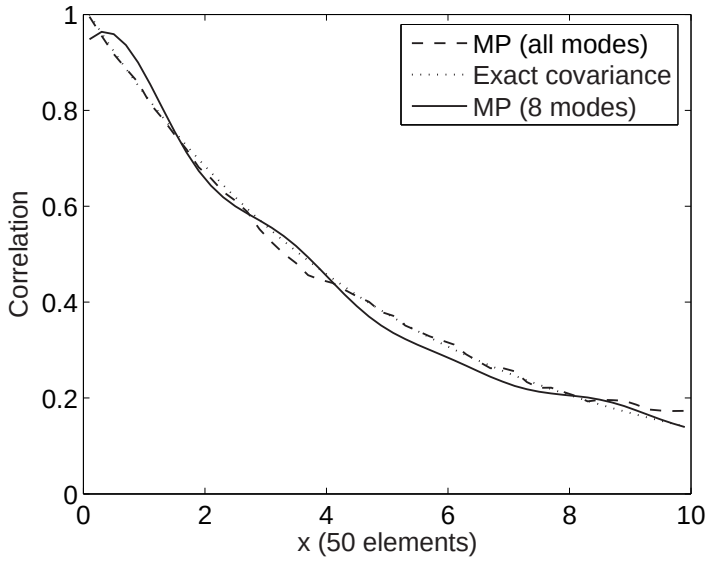

Figure 6.7: Correlation function over 2000 midpoint realizations using only 8 modes to characterize the covariance matrix.

Equations (6.39-6.43). In series expansion methods, the approximation comes from the truncation of the sum at the order r. The error introduced by this truncation decreases when r increases, as illustrated in Figure 6.8. When the order of expansion is larger than eight, the mean of the variance error is less than 5 %.

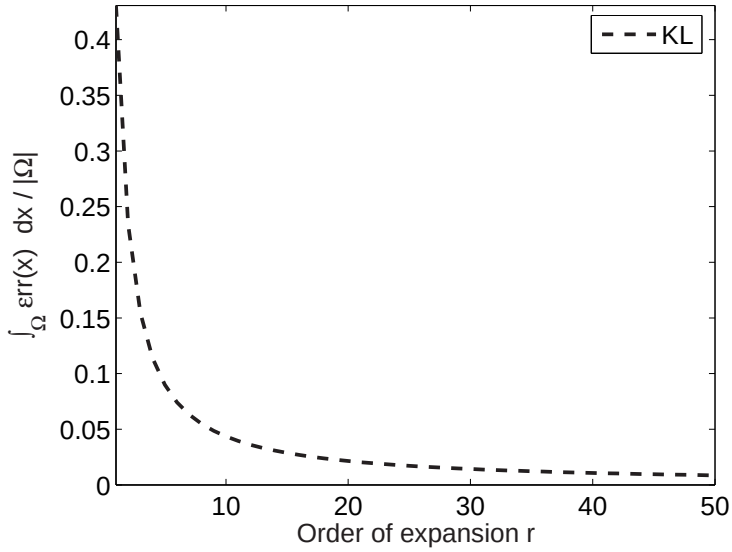

Figure 6.8: Variation of the error on the variance with the order of expansion r.

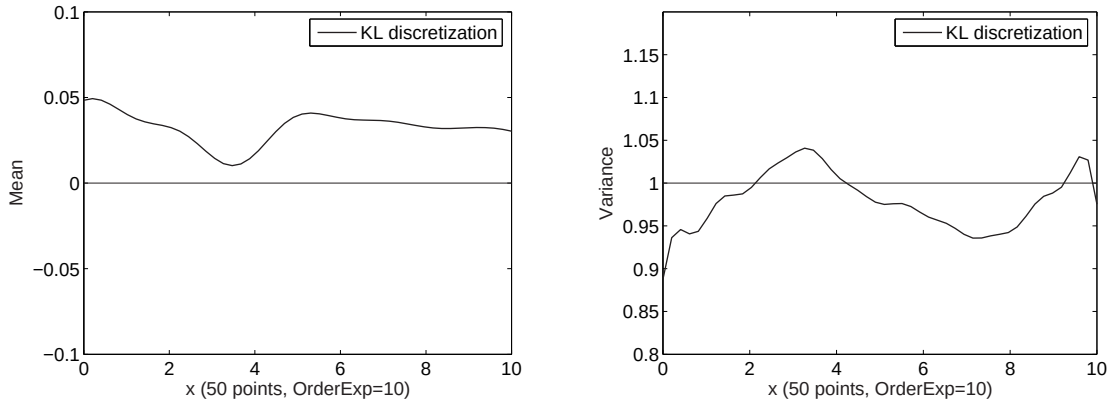

Figure 6.9: Mean and variance fields estimated over 2000 Karhunen-Loeve realizations.

Figure 6.9 presents the mean and variance fields of 2000 KL realizations for an expansion order of 10. Figure 6.10 shows that the point wise variance error is larger on the boundary of the discretization domain, which is also illustrated in Figure 6.9(b). This is a characteristic of truncated series expansion representations.

The Midpoint and Local Average methods can also be considered as series expansion methods when the mesh is regular, i.e. all the elements are the same

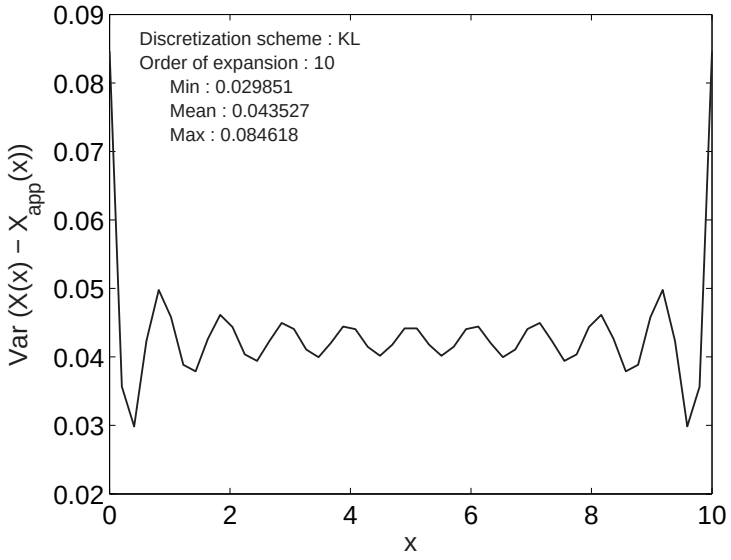

Figure 6.10: Error variance along the discretization domain (OrderExp=10).

[142]. The midpoint and local average methods can be written in the same formalism as the Karhunen-Loeve expansion method (This procedure is exposed in details in Section 7.8). Table 6.1 compares the eigenvalues for the three methods, while Figure 6.11 compares the first eigenfunction. The first eigenfunction is similar for the three methods. The eigenvalues are very close. It can be noticed that the local average method gives larger values than the midpoint ones whose eigenvalues are also higher than the Karhunen-Loeve expansion ones. If the number of elements on the correlation length were smaller, the differences would be larger.

Figure 6.12 represents the mean and variance fields of 2000 realizations using the Orthogonal Series Expansion with an expansion order of 10. As for the Karhunen-Loeve expansion, Figures 6.12(b) and 6.13 show that the error on the variance is larger on the boundaries of the domain. Compared to the Karhunen-Loeve expansion, the error on the variance is larger since the Legendre functions are only approximations, while analytical eigenvalues and eigenfunctions are exact solutions in the Karhunen-Loeve method. This approximation does not affect the mean.

Table 6.2 compares the CPU time and the mean and variance lower and upper 90 percents bounds. The CPU time measure starts at the setting of the

Table 6.1: Comparison between the eigenvalues in the Karhunen-Loeve, Midpoint and Local Average methods.

Mode	λ_{KL}	λ_{MP}	λ_{LA}
1	5.7466	5.7483	5.7491
2	1.9547	1.9564	1.9567
3	0.78525	0.78676	0.78686
4	0.39778	0.39922	0.39927
5	0.23563	0.23703	0.23706
6	0.15466	0.15604	0.15606

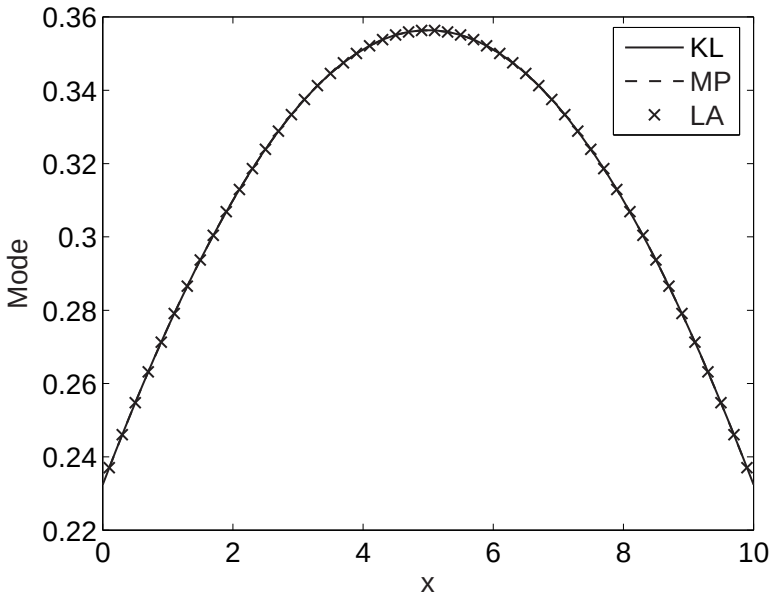

Figure 6.11: Comparison of the first eigenfunction used in the Karhunen-Loeve, Midpoint and Local Average methods.

parameters (mean, standard deviation, correlation type, correlation length,...) and stops after 2000 realizations of the random field.

The CPU times are larger for the series expansion methods than for the midpoint and local average methods. The orthogonal series expansion is the most time consuming method. This is due to the fact that the eigenfunctions are ex-

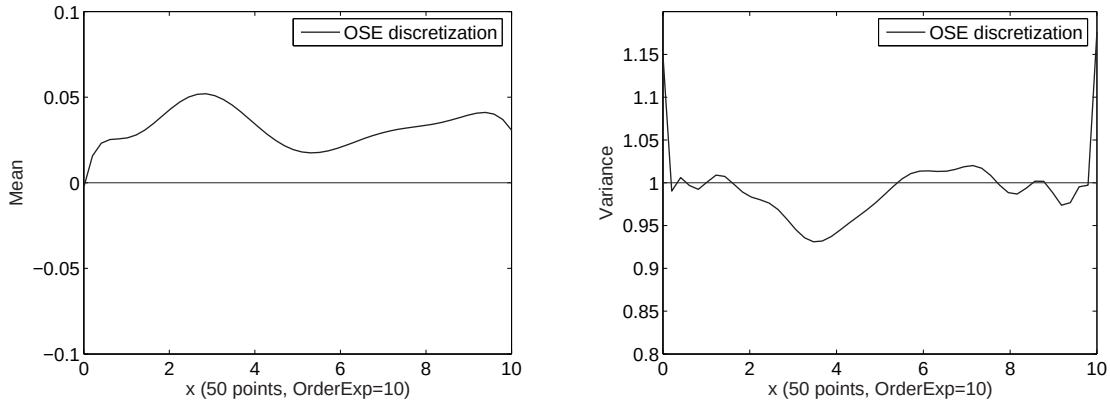

Figure 6.12: Mean and variance fields estimated over 2000 Orthogonal Series Expansion realizations (Expansion order=10).

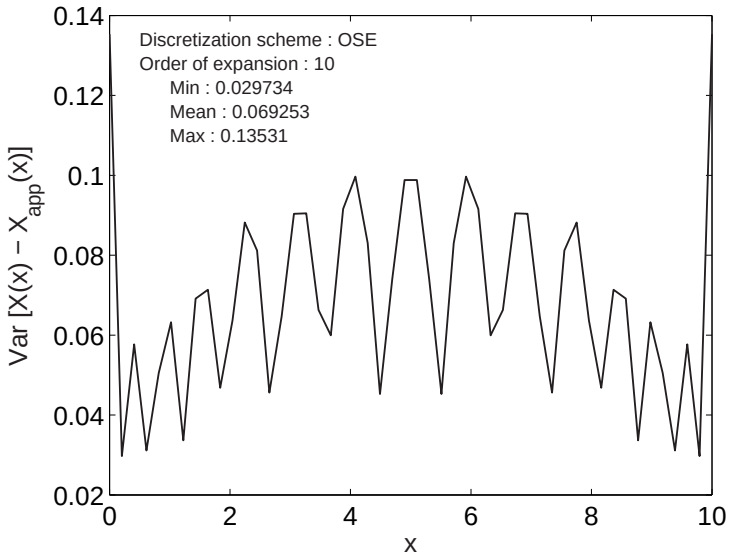

Figure 6.13: Point wise error variance along the discretization domain (Order-Exp=10).

pressed as a sum of orthonormal functions (e.g. based on Legendre polynomials). Hence, the evaluation of the random field requires two successive sums over the order of expansion. Of course, when the order of expansion increases, the CPU time increases.

Table 6.2: CPU time and mean and variance bounds for different methods.

Method	CPU time [s]	Mean bounds	Variance bounds
Midpoint	1.79	(-0.0377, 0.0108)	(0.9630, 1.0144)
Local Average	1.87	(-0.0337, 0.0108)	(0.9361, 1.0146)
KL (OrderExp=5)	20.34	(0.0087, 0.0283)	(0.8157, 0.9366)
KL (OrderExp=10)	37.61	(0.0112, 0.0493)	(0.9357, 1.0384)
OSE (OrderExp=5)	222.51	(0.0048,0.0260)	(0.8047, 1.1274)
OSE (OrderExp=10)	1453.5	(0.0183,0.0479)	(0.9455,1.0168)

The Midpoint and Local Average methods give similar results because the element size is small (25 elements per correlation length). Differences would occur if fewer elements (less than 2 [40]) per correlation length were taken. The Midpoint and Local Average bounds are centered on the exact values (Mean=0 and Variance=1) while the others are close but not centered on it.

Based on these analyses, the most appropriate method(s) of random field discretization in order to study the thermoelastic damping can be selected. Since MEMS are manufactured by thin film processes, their material structure does not exhibit 3-D heterogeneity, but 1-D or 2-D variations are expected in their properties. Therefore, if the correlation function is assumed to be exponential, the Karhunen-Loeve method is the first choice since analytical solutions are then available for the eigenvalue problem. Moreover a series expansion method can be more useful when used in a stochastic finite element method since it takes into account the properties variations inside the finite element formulation and requires less random variables than the midpoint or local average methods. However, in order to study the effects of other correlation functions, the local average method is also considered as analytical expressions are available for the covariance of different correlation function kinds and it is superior to the midpoint method [40]. Moreover, as the local average method has a series expansion expression, it has also the advantage of the reduced number of required variables. For both chosen methods, the CPU time remains relatively small compared to methods such as the Orthogonal Series Expansion. Of course, this criterion is not the most critical one since the time taken to generate the random field is dwarfed by the time

taken to subsequently process or analyze it.

6.3 Stochastic Finite Element Methods

Stochastic finite element methods can be classified with respect to the kind of results they yield. Two main categories can be distinguished. Firstly, reliability methods aim at calculating the failure probability and hence, focus on the tails of the probability density function of the response. Secondly, other methods aim at calculating the probabilistic characterization of the response. In this category, it exists particular methods that determine only the first two statistical moments of the response. This work focuses on these second moment methods, which are briefly reviewed hereafter. For more details, the reader should refer to [97, 128, 129, 137, 142].

6.3.1 Monte-Carlo Simulations

Monte-Carlo simulations have the major advantage that accurate solutions can be obtained for any problem whose deterministic solution is known, since it statistically converges to the correct solution provided that a large number of simulations is employed. Indeed, the basic principles of Direct Monte-Carlo Simulations is to generate a sampling of the input parameters accordingly to their probability distributions and correlations. For each input sample, a deterministic finite element analysis is carried out, giving an output sample. Finally, a response sampling is obtained, from which the mean and the standard deviation of the response can be derived.

The estimator of the response $\bar{y}$ is defined by

$$\bar{y} = \frac{1}{n} \sum_{i=1}^{n} y^{(i)}, \tag{6.54}$$

where n is the number of samples and $y^{(i)}$ is the response corresponding to the ith input sample [127]. The estimator is a random variable whose mean and variance are given by

$$E[\bar{y}] = \mu_y \tag{6.55}$$

and

$$Var(\bar{y}) = E[(\bar{y} - E[\bar{y}])^2] = \frac{\sigma_y^2}{n}, \tag{6.56}$$

where $\mu_y = E[y]$ and $\sigma_y^2 = E[(y - \mu_y)^2]$ denote the unknown mean and variance of the response. Tchebychev's inequality provides a basis for error assessment, i.e.

$$P(|\bar{y} - \mu_y| < \epsilon) \geq 1 - \frac{1}{\epsilon^2}\frac{\sigma_y^2}{n}, \tag{6.57}$$

where ϵ denotes a tolerance. A confidence level $1 - \delta$ can be defined where $\delta = \frac{1}{\epsilon^2}\frac{\sigma_y^2}{n}$. Due to the central limit theorem, the distribution of $\bar{y}$ is normal and the confidence interval corresponding to the confidence level δ is

$$\mu_{y,1-\delta} = [\bar{y} - \Phi^{-1}(1 - \delta/2)\frac{\sigma_y^2}{\sqrt{n}}, \bar{y} + \Phi^{-1}(1 - \delta/2)\frac{\sigma_y^2}{\sqrt{n}}], \tag{6.58}$$

where Φ is the normal cumulative distribution function. This shows that the Direct Monte-Carlo method has an absolute estimation error that decreases as $n^{-1/2}$ when n increases, independently of the dimension of the system. Increasing the number of samples improves the estimation of the mean value at a convergence rate of $n^{-1/2}$.

The disadvantage of the Direct Monte-Carlo method is that it is usually extremely computationally demanding due to the repeated analyses that have to take place. In order to enhance the computational efficiency of the method, different techniques are developed in the literature. The reduction of the size of the problems (e.g. by phase space reduction [129]) and parallel processing [118, 129] appear to be promising for this purpose.

Another way to reduce the CPU time is to increase the efficiency of the generation of the response samples. Since the solutions for different input samples are close to each other, a reference solution is calculated around which the solutions vary. The Neumann expansion technique in static stochastic structural analysis and the solution of random eigenvalue problems in linear stochastic structural dynamics are based on this concept. The Neumann expansion technique [26] allows the repeated inversions of the random stiffness matrix to be avoided and hence, saves a lot of computation time. In modal analyses of large models, the computation of the frequencies and modes uses subspace iteration methods such as Lanczos methods and it is not efficient to independently determine the modal properties for each sample. Taking the eigenvectors of the first calculated sample as start-vector subspace for the other samples allows a significant reduction in the computational time [139].

The convergence rate of the estimator does not only increase by increasing the number of samples but also by decreasing the variance σ_y^2. Variance reduction techniques (VRT) exploit additional a priori information to reduce the necessary sample size n for a specified confidence level. Stratification techniques (e.g. Latin hypercube sampling [103]), which are widely used in practice, use conditional expectations to reduce the variance of the estimator. The Importance Sampling [130] and Controlled Monte-Carlo simulation [121] are designed to increase the sampling density in domain zones of interest, e.g. low probability domain zone in reliability analyses. This is done by modifying the weights associated with the realizations. Controlled Monte-Carlo Simulations differ from Importance Sampling in the way the weights are determined; in Controlled Monte-Carlo Simulations, the weights are modified dynamically in an adaptive manner contrary to Importance Sampling where the weights are specified a priori.

Monte-Carlo simulations deal with random variables as well as random fields. Random fields can be characterized by a finite number of random variables as explained in the previous section so that their sampling generation is similar to the generation of random variable samples. Moreover, Monte-Carlo simulations are applicable to any kind of probability density functions. It should be noted that the distribution law of highly variable parameters has to be chosen carefully since the response variability largely depends on the distribution law [143].

Monte-Carlo simulations can be coupled with other stochastic finite element methods, leading to hybrid stochastic finite element methods. Ghanem [53] couples the spectral stochastic finite element method with Monte-Carlo simulations while Van den Nieuwenhof couples it with the perturbation stochastic finite element method [143]. Mixing two methods allows the advantages and capabilities of each method to be combined and their drawbacks to be circumvented.

6.3.2 Spectral Stochastic Finite Element Method

The Spectral Stochastic Finite Element Method (SSFEM) [55, 57, 58] is based on the spectral discretization along the random dimension. The discretization process occurs at two levels in stochastic problems. The first level concerns the representation of the random field inputs, e.g. the spatial variation of the material properties. The random distribution of these input variables is known a priori and

it is modeled by a Karhunen-Loeve expansion for a Gaussian distribution or by a Polynomial Chaos expansion for a non-Gaussian distribution. The second level concerns the discretization of the response field. As the response distribution is unknown, a generic discretization method such as the Polynomial Chaos has to be used. For linear systems, Neumann expansion can also be used [58] even if numerical applications show that the terms required in the expansion to achieve a certain accuracy are higher for the Neumann procedure.

The main advantages of the Spectral Stochastic Finite Element Method is its easiness to handle large uncertainties and the evaluation of the response statistical moments of order higher than two. However, its performance is somewhat poor for problems with strong nonlinearities and discontinuities where potential divergence in higher order moments may be observed [76].

The Stochastic Spectral Finite Element Method is used to model uncertainty in a variety of problems. Ghanem and Spanos use SSFEM in linear elastic problems in [55, 57, 58]. Ghanem and co-workers apply it to protein labeling reactions [37], transport in random media [53], structural dynamics applications [56] and heat conduction problems [54]. Karniadakis and co-workers apply a generalized polynomial chaos expansion to model uncertainty in diffusion [151], fluid flow applications [153] and transient heat conduction problems [152]. An inverse heat conduction problem using this method is presented in [145]. A variational multiscale stochastic approach to advection-diffusion problems using SSFEM is introduced in [146]. A SSFEM based on a bounding body approach for small deformation elasto-plastic bodies is presented in [12]. SSFEM is used for modeling uncertainty propagation in finite deformation problems in [2].

Ostoja-Starzewski and Woods [116] develop spectral finite elements for vibrating rods and beams with random field properties. They describe the material variabilities by random Fourier series with a typical average characteristic size of inhomogeneity and investigate the relative effects of random noises in all the material parameters on the spectral stiffness matrices.

6.3.3 Perturbation Stochastic Finite Element Method

Basics of the Perturbation Stochastic Finite Element Method (PSFEM) are exposed in [79]. This method consists in a deterministic analysis complemented by

a sensitivity analysis with respect to the random parameters. This permits the development of a Taylor series expansion of the response, from which the mean and variance of the response can be derived knowing the mean, variance and correlation structure of the random parameters. Depending on the expansion order (1 or 2) of the Taylor series expansion, the response statistical moments of the response are first or second order accurate and the method is respectively named first-order second moment (FOSM) and second-order second moment (SOSM) method.

The main advantage of the PSFEM is its simplicity and applicability to a wide range of problems at low cost. For example, it is used in static and dynamic elastic analyses [64, 79], buckling analyses [10], composite ply failure problems [113], inelastic deformation studies [43], linear transient heat transfer problems [65], the analysis of free vibration of composite cantilevers [111], nonlinear dynamics [88] and the study of eigenvalues of structures with uncertain boundary conditions [69].

PSFEM can also be adapted to take into account the spatial variability of parameters. PSFEM is successfully coupled with the midpoint method [49], the shape function [93], the local average method [27, 28, 29, 61], the Kahurnen-Loeve expansion [143] and the weighted integral method [39, 60, 61, 117]. All but the last two methods involve a large number of random variables and induce a high computational cost to calculate the derivative of structural matrices with respect to each random variable. The concept of variability response functions is derived from the coupling of the perturbation stochastic finite element method with the weighted integral representation of the random field, which is also simply called the weighted integral method in the literature. Variability Response Functions allow to determine a spectral-distribution-free upper bound for the response variance [38, 39, 60, 61, 117]. Spectral Stochastic Finite Element Method based on Neumann expansion [58] is in fact a Perturbation Stochastic Finite Element Method coupled with a Karhunen-Loeve or Polynomial Chaos random field discretization method.

Due to the Taylor series expansion, accurate results are expected only in case of small variability of the parameters and for nearly linear problems. The derivatives of the structural matrices have to be calculated with respect to the random variables. This can be done analytically, semi-analytically or by finite

difference. These computations can be time-consuming, particularly when the second order terms are included.

6.4 Method Selection

The selection of the method relies on the kind of analysis that has to be performed. In order to investigate the effects of uncertainty on the thermoelastic quality factor, a stochastic non-symmetric eigenvalue problem has to be solved:

$$\mathcal{A}(\alpha(\mathbf{x},\xi))\mathbf{q}(\mathbf{x},\xi) = \lambda(\xi)\mathcal{B}(\beta(\mathbf{x},\xi))\mathbf{q}(\mathbf{x},\xi), \tag{6.59}$$

where $\mathcal{A}(\alpha(\mathbf{x},\xi))$ and $\mathcal{B}(\alpha(\mathbf{x},\xi))$ are stochastic differential operators defined on the domain Ω; $\mathbf{x} \in \Omega$ denotes a point in the domain; ξ is a value of the sample space; $\alpha(\mathbf{x},\xi)$ and $\beta(\mathbf{x},\xi)$ are second moment random fields describing the coefficients of the stochastic differential operators, $\lambda(\xi)$ and $\mathbf{q}(\mathbf{x},\xi)$ are the random eigenvalues and eigenfunctions, respectively.

The random fields describing the coefficients of the differential operators have to be discretized using techniques that have been reviewed in this chapter. From the method comparison, two discretization methods have been selected: the Local Average method and the Karhunen-Loeve expansion series method. After the discretization of the spatial and random spaces, the stochastic finite element eigenproblem has the form:

$$\left[\mathbf{A}_0 + \sum_{i=1}^{p} b_i(\xi)\mathbf{A}_i\right]\mathbf{x}(\xi) = \lambda(\xi)\left[\mathbf{B}_0 + \sum_{i=1}^{p} b_i(\xi)\mathbf{B}_i\right]\mathbf{x}(\xi), \tag{6.60}$$

where $\mathbf{A}_0$, $\mathbf{A}_i$, $\mathbf{B}_0$ and $\mathbf{B}_i$ are deterministic matrices while $\lambda(\xi)$ and $\mathbf{x}(\xi)$ denote the random eigenvalue and eigenvector, respectively. $b_i(\xi)$ are the random variables representing the random fields.

As reviewed in [97], the first order perturbation method is the most widely used approach for approximating the statistics of eigenparameters. The popularity of this method can be essentially attributed to the ease of its implementation and its computational efficiency. For example, in [163], the first order PSFEM is used with the Local Average and Midpoint methods to study the variability of the eigenvalues of beams. Graham and Deodatis [61] use the first order PSFEM with the Local Average method and the Weighted Integral method to compute the

mean and variance of the eigenvalues of beam and plate structures with stochastic material and geometric properties. The second order method is also used to study the eigenvalue statistics [69, 72, 111]. Since the computation of the higher order perturbation terms can be computationally expensive, first order PSFEM can be modified in order to increase its accuracy. This can be done using a perturbation method based on an optimal point or an asymptotic approximation [5, 6] or using the two terms of the first order perturbation for the eigenvector as basis vectors for Ritz analysis of the governing random eigenvalue problem [105]. However, these methods involve additional computations, i.e. several sensitivity and deterministic analyses have to be carried to find the optimal point [5, 6] or Monte-Carlo simulations for the approximation of the statistical moments [105]. All above analyses assume a symmetric problem without damping. Adhikari [4] proposes a first order PSFEM for symmetrical damped problems, which have complex modes and frequencies, but PSFEM can be extended to non-symmetric damped problems whose eigenvalue sensitivity analyses are studied in the literature [32].

Monte-Carlo approach is adequate for any problem with a deterministic solution procedure; in particular it is commonly used for the prediction of the eigenvalues of structures. Shinozuka and Astill [134] propose Monte-Carlo simulations for calculating the statistical properties of the eigenvalues of a spring supported beam-column whose spring supports and axial force are treated as random variables while material properties are considered as random fields. However, it is a computationally expensive way and procedures to reduce the computational efforts have to be adopted, e.g. a subspace Lanczos iteration scheme with optimally selected start-vectors [122, 139]. Monte-Carlo simulations are also coupled with SSFEM [123].

In this work, the perturbation method is selected since it requires low computational effort and is efficient for treating problems with low variability levels. Since Monte-Carlo simulations are computationally too expensive for large systems, Monte-Carlo results are only calculated for small test cases and are then used as reference solutions due to the absence of inherent assumptions.

6.5 Concluding Remarks

This chapter has focussed on the review of the random field discretization methods and the second moment stochastic finite element methods. Firstly, the concept of uncertainty has been clarified. In this work, uncertainty concerns the probabilistic variation of the model parameters, e.g. material properties or geometric parameters. Moreover, due to the lack of experimental data and for the sake of simplicity, the spatial variation of the parameters is assumed to be isotropic, Gaussian and homogeneous. Based on these restrictions, the most adequate methods for the discretization of random fields have been selected, namely, the Local Average and Karhunen-Loeve expansion methods. Concerning the selection of the stochastic finite element method, it has been decided to extend the Perturbation Stochastic Finite Element Method to the study of non-symmetrically damped eigenproblems since it is efficiently and with low computational effort applied to diverse eigenproblems with low variability level. For small test cases, the Perturbation Stochastic Finite Element Method results will be compared to the Monte-Carlo simulation ones, which will be considered as reference solutions due to the absence of inherent assumptions in Monte-Carlo simulations.

Chapter 7

Perturbation Stochastic Finite Element Method

In this chapter, the perturbation stochastic finite element method is extended to the resolution of non-symmetrically damped eigenproblem. Firstly, the stochastic thermopiezoelectric finite element equations are derived. The first two statistical moments of the quality factor are approximated by a second order perturbation method, which requires the determination of the first and second order sensitivities of the eigenpairs of the problems. Secondly, the connections between the random field discretization methods (i.e. the Local Average method and the Karhunen-Loeve expansion) and the perturbation stochastic finite element method are investigated. Finally, methods to enhance the performance of the perturbation stochastic finite element method are exposed.

7.1 Stochastic Thermopiezoelectric Finite Element Equations

In order to obtain the stochastic thermopiezoelectric equations, the dependence on the uncertainty ξ for each parameter that may exhibit a random variation is

introduced in the weak form of the thermopiezoelectric equations (4.17-4.19):

$$\int_{\Omega(\xi)} \left[\rho(\xi)\ddot{u}_i(\xi)\delta u_i(\xi) + \sigma_{ij}(\xi)\delta\varepsilon_{ij}(\xi)\right] d\Omega = \int_{S^*(\xi)} t_i(\xi)\delta u_i(\xi) dS^*, \quad (7.1)$$

$$\int_{\Omega(\xi)} D_i(\xi)\delta\Phi_{,i}(\xi) d\Omega = \int_{S^*(\xi)} q_e(\xi)\delta\Phi(\xi) dS^*, \quad (7.2)$$

$$\int_{\Omega(\xi)} \left[q_i(\xi)\delta\theta_{,i}(\xi) - \dot{S}(\xi)T_0\delta\theta(\xi)\right] d\Omega = \int_{S^*(\xi)} q_s(\xi)\delta\theta(\xi) dS^*. \quad (7.3)$$

From these equations, the random variables can be divided into two categories:

- the variables that only appear under the integration sign,

- the variables that introduce variability on the integration domains Ω and S^*.

The first category includes the material parameters (e.g. the density, Young's modulus, the thermal conductivity, the electric conductivity,...) and the pseudo-geometric variables, which are geometric variables that due to particular kinematic assumptions are removed from the expression of the integration domain (e.g. the height and width of Euler-Bernoulli beams, the thickness of plane stress or strain structures,...). The second category concerns the shape design variables acting directly on the integration domains Ω and S^*. Both categories are considered in this work.

The stochastic thermopiezoelectric dynamic equation is obtained from Equation (4.36):

$$\begin{pmatrix} \mathbf{M_{uu}}(\xi) & 0 & 0 \\ 0 & 0 & 0 \\ 0 & 0 & 0 \end{pmatrix} \begin{pmatrix} \ddot{\mathbf{u}}_\mathbf{u}(\xi) \\ \ddot{\mathbf{u}}_\mathbf{\Phi}(\xi) \\ \ddot{\mathbf{u}}_\theta(\xi) \end{pmatrix} + \begin{pmatrix} 0 & 0 & 0 \\ 0 & 0 & 0 \\ \mathbf{C}_{\theta\mathbf{u}}(\xi) & \mathbf{C}_{\theta\mathbf{\Phi}}(\xi) & \mathbf{C}_{\theta\theta}(\xi) \end{pmatrix} \begin{pmatrix} \dot{\mathbf{u}}_\mathbf{u}(\xi) \\ \dot{\mathbf{u}}_\mathbf{\Phi}(\xi) \\ \dot{\mathbf{u}}_\theta(\xi) \end{pmatrix}$$
$$+ \begin{pmatrix} \mathbf{K_{uu}}(\xi) & \mathbf{K_{u\Phi}}(\xi) & \mathbf{K_{u\theta}}(\xi) \\ \mathbf{K_{\Phi u}}(\xi) & \mathbf{K_{\Phi\Phi}}(\xi) & \mathbf{K_{\Phi\theta}}(\xi) \\ 0 & 0 & \mathbf{K}_{\theta\theta}(\xi) \end{pmatrix} \begin{pmatrix} \mathbf{u}_\mathbf{u}(\xi) \\ \mathbf{u}_\mathbf{\Phi}(\xi) \\ \mathbf{u}_\theta(\xi) \end{pmatrix} = \begin{pmatrix} \mathbf{F}_\mathbf{u}(\xi) \\ \mathbf{F}_\mathbf{\Phi}(\xi) \\ \mathbf{F}_\theta(\xi) \end{pmatrix} \quad (7.4)$$

Therefore, the stochastic finite element eigenproblem to be solved is obtained introducing the uncertainty dependence in Equation (4.59):

$$\begin{pmatrix} -\mathbf{K}_{uu}(\xi) & -\mathbf{K}_{u\Phi}(\xi) & -\mathbf{K}_{u\theta}(\xi) & 0 \\ -\mathbf{K}_{u\Phi}(\xi)^T & -\mathbf{K}_{\Phi\Phi}(\xi) & -\mathbf{K}_{\Phi\theta}(\xi) & 0 \\ 0 & 0 & -\mathbf{K}_{\theta\theta}(\xi) & 0 \\ 0 & 0 & 0 & \mathbf{I} \end{pmatrix} \begin{pmatrix} \mathbf{x}_u(\xi) \\ \mathbf{x}_\Phi(\xi) \\ \mathbf{x}_\theta(\xi) \\ \dot{\mathbf{x}}_u(\xi) \end{pmatrix} =$$

$$\lambda(\xi) \begin{pmatrix} 0 & 0 & 0 & \mathbf{M}_{uu}(\xi) \\ 0 & 0 & 0 & 0 \\ \mathbf{C}_{\theta u}(\xi) & \mathbf{C}_{\theta\Phi}(\xi) & \mathbf{C}_{\theta\theta}(\xi) & 0 \\ \mathbf{I} & 0 & 0 & 0 \end{pmatrix} \begin{pmatrix} \mathbf{x}_u(\xi) \\ \mathbf{x}_\Phi(\xi) \\ \mathbf{x}_\theta(\xi) \\ \dot{\mathbf{x}}_u(\xi) \end{pmatrix}, \tag{7.5}$$

which is a generalized non-symmetric stochastic finite element eigenproblem:

$$\mathbf{A}(\xi)\mathbf{x}(\xi) = \lambda(\xi)\mathbf{B}(\xi)\mathbf{x}(\xi). \tag{7.6}$$

In practice, the uncertainty is represented by a finite set of random variables:

$$\mathbf{b} = \{b_1, b_2, \ldots, b_n\}, \tag{7.7}$$

so that the dependence on ξ is replaced by the dependence on the vector $\mathbf{b}$. Note that this set includes the random variables resulting from the random field discretization.

The perturbation method considers that the random design variables b_i are perturbed from their expectation $\bar{b_i}$, so that the random variables b_i are written as the sum of a deterministic value $\bar{b_i}$ and a zero mean random variable Δb_i:

$$b_i = \bar{b_i} + \Delta b_i. \tag{7.8}$$

The covariance matrix $\mathbf{B}$ of the random variables b_i is related to the zero mean random variables as follows

$$B_{ij} = Cov(b_i, b_j) \tag{7.9}$$

$$= E[\Delta b_i \Delta b_j]. \tag{7.10}$$

The perturbation method consists in expanding the random quantities in Equations (7.1-7.3) about their expectation via a truncated Taylor series expansion. For instance, the mass density ρ is approximated by

$$\rho(b_1, \ldots, b_n) \approx \rho(\bar{b}_1, \ldots, \bar{b}_n) + \sum_{i=1}^{n} \rho_{,i} \Delta b_i + \frac{1}{2} \sum_{i=1}^{n} \sum_{j=1}^{n} \rho_{,ij} \Delta b_i \Delta b_j, \tag{7.11}$$

where the subscripts $,i$ and $,ij$ respectively denote the first and second order partial derivative with respect to b_i and b_j computed at the nominal value $\bar{\mathbf{b}}$.

Substituting the truncated Taylor series expansion into the finite element formulation leads to the following eigenproblem:

$$\left(\bar{\mathbf{A}}+\sum_{i=1}^{n}\mathbf{A}_{,i}\Delta b_i+\frac{1}{2}\sum_{i=1}^{n}\sum_{j=1}^{n}\mathbf{A}_{,ij}\Delta b_i\Delta b_j\right)\left(\bar{\mathbf{x}}+\sum_{i=1}^{n}\mathbf{x}_{,i}\Delta b_i+\frac{1}{2}\sum_{i=1}^{n}\sum_{j=1}^{n}\mathbf{x}_{,ij}\Delta b_i\Delta b_j\right)=$$
$$\left(\bar{\lambda}+\sum_{i=1}^{n}\lambda_{,i}\Delta b_i+\frac{1}{2}\sum_{i=1}^{n}\sum_{j=1}^{n}\lambda_{,ij}\Delta b_i\Delta b_j\right)\left(\bar{\mathbf{B}}+\sum_{i=1}^{n}\mathbf{B}_{,i}\Delta b_i+\frac{1}{2}\sum_{i=1}^{n}\sum_{j=1}^{n}\mathbf{B}_{,ij}\Delta b_i\Delta b_j\right)$$
$$\left(\bar{\mathbf{x}}+\sum_{i=1}^{n}\mathbf{x}_{,i}\Delta b_i+\frac{1}{2}\sum_{i=1}^{n}\sum_{j=1}^{n}\mathbf{x}_{,ij}\Delta b_i\Delta b_j\right), \tag{7.12}$$

where $\bar{(.)}$ denotes that the quantity $(.)$ is computed at the nominal value $\bar{\mathbf{b}}$.

Grouping the terms of the same order in Δb_i gives the following equations:

- zeroth order:

$$\bar{\mathbf{A}}\bar{\mathbf{x}}=\bar{\lambda}\bar{\mathbf{B}}\bar{\mathbf{x}}, \tag{7.13}$$

- first order $(i=1,\ldots,n)$:

$$\left(\bar{\mathbf{A}}-\bar{\lambda}\bar{\mathbf{B}}\right)\mathbf{x}_{,i}=\left(\bar{\lambda}\mathbf{B}_{,i}+\lambda_{,i}\bar{\mathbf{B}}-\mathbf{A}_{,i}\right)\bar{\mathbf{x}}, \tag{7.14}$$

- second order $(i,j=1,\ldots,n)$:

$$\left(\bar{\mathbf{A}}-\bar{\lambda}\bar{\mathbf{B}}\right)\mathbf{x}_{,ij}=\left(\bar{\lambda}\mathbf{B}_{,ij}+\lambda_{,ij}\bar{\mathbf{B}}+2\lambda_{,i}\mathbf{B}_{,j}-\mathbf{A}_{,ij}\right)\bar{\mathbf{x}}+2\left(\bar{\lambda}\mathbf{B}_{,i}+\lambda_{,i}\bar{\mathbf{B}}-\mathbf{A}_{,i}\right)\mathbf{x}_{,j}. \tag{7.15}$$

The zeroth-order equation is nothing other than the deterministic eigenproblem at the nominal value $\bar{\mathbf{b}}$, so that the zeroth order eigenpairs $\bar{\lambda}$ and $\bar{\mathbf{x}}$ are obtained using the Lanczos method as exposed in Chapter 4. In contrast to the zeroth-order eigenproblem, the solution procedures given by Equations (7.14-7.15) for the first and second derivatives of eigenvalues and eigenvectors with respect to the random variables are not so straightforward. Indeed, these systems are non-homogeneous and the coefficient matrix on the left-hand side, $\bar{\mathbf{A}}-\bar{\lambda}\bar{\mathbf{B}}$, is singular. The first and second order derivatives of the eigenpairs have to be computed by a specific method, which is exposed in Section 7.3.

7.2 Statistical Moments of the Quality Factor

The quality factor corresponding to the rth mode of the eigenproblem (7.5) is a stochastic quantity expressed as

$$Q(\xi) = \frac{1}{2}\left|\frac{\Im(\lambda(\xi))}{\Re(\lambda(\xi))}\right|. \tag{7.16}$$

The second order Taylor expansion about the nominal value $\bar{\mathbf{b}}$ with respect to the random variables b_i is given by

$$Q(\bar{\mathbf{b}}) \approx \bar{Q} + \sum_{i=1}^{n} Q_{,i}\Delta b_i + \frac{1}{2}\sum_{i=1}^{n}\sum_{j=1}^{n} Q_{,ij}\Delta b_i \Delta b_j. \tag{7.17}$$

Since the random variables Δb_i are zero-mean random variables of known covariance, the expectation of the quality factor is

$$\begin{aligned} E\left[Q(\bar{\mathbf{b}})\right] &\approx \bar{Q} + \sum_{i=1}^{n} Q_{,i}E\left[\Delta b_i\right] + \frac{1}{2}\sum_{i=1}^{n}\sum_{j=1}^{n} Q_{,ij}E\left[\Delta b_i \Delta b_j\right] && (7.18)\\ &= \bar{Q} + \frac{1}{2}\sum_{i=1}^{n}\sum_{j=1}^{n} Q_{,ij}Cov(b_i, b_j), && (7.19)\end{aligned}$$

while the variance of the quality factor has the following expression:

$$\begin{aligned} Var\left(Q(\bar{\mathbf{b}})\right) &= E\left[\left(Q(\bar{\mathbf{b}}) - E\left[Q(\bar{\mathbf{b}})\right]\right)^2\right] && (7.20)\\ &\approx \sum_{i=1}^{n}\sum_{j=1}^{n} Q_{,i}Q_{,j}E\left[\Delta b_i \Delta b_j\right] && (7.21)\\ &= \sum_{i=1}^{n}\sum_{j=1}^{n} Q_{,i}Q_{,j}Cov(b_i, b_j). && (7.22)\end{aligned}$$

The mean is second-order accurate, while the variance is first-order accurate since the second-order terms vanish. The first and second order derivatives of the quality factor are expressed in terms of the first and second order derivatives of the eigenvalue:

$$Q_{,i} = sign(\Re(\bar{\lambda}), \Im(\bar{\lambda}))\frac{1}{2}\frac{\Im(\lambda_{,i})\Re(\bar{\lambda}) - \Im(\bar{\lambda})\Re(\lambda_{,i})}{\Re(\bar{\lambda})^2} \tag{7.23}$$

and

$$\begin{aligned} Q_{,ij} &= sign(\Re(\bar{\lambda}), \Im(\bar{\lambda}))\frac{1}{2\Re(\bar{\lambda})^3}(\Im(\lambda_{,ij})\Re(\bar{\lambda})^2 - \Im(\lambda_{,i})\Re(\lambda_{,j})\Re(\bar{\lambda})\\ &- \Im(\lambda_{,j})\Re(\lambda_{,i})\Re(\bar{\lambda}) - \Re(\bar{\lambda})\Re(\lambda_{,ij})\Im(\bar{\lambda}) + 2\Re(\lambda_{,j})\Re(\lambda_{,i})\Im(\bar{\lambda})). \end{aligned} \tag{7.24}$$

If only the first order derivatives of the eigenvalue are known, a pseudo second order approximation of the statistical moment of Q can be carried out by neglecting the second order derivative of λ in Equation (7.24). This pseudo second order approximation is of course less accurate than a second order one, but it is also computationally less demanding.

7.3 First and Second Order Eigenpair Derivatives

The sensitivity of eigensolutions or more precisely the derivative of the eigensolutions with respect to the design parameters has an important role in the studies of design process and the eigensensitivity analysis has been an important research topic over the last past four decades. Different eigensensitivity methods have been developed depending on the characteristics of the eigenproblem (symmetry or asymmetry, real or complex eigenvalues, with or without multiple eigenvalues, standard or generalized eigenproblem...). In the earliest work, Fox and Kapoor [50] give exact expressions for the derivative of eigenvalues and eigenvectors with respect to any design parameter for symmetric real-valued matrices without repeated eigenvalues. For these kind of systems, Nelson [107] proposes an efficient method to calculate the eigenvector derivative, which requires only the eigenvalue and eigenvector under consideration. Ojalvo [112] and Dailey [36] extend Nelson's method to the multiple eigenvalue problem.

The aforementioned methods can be applied to damped systems. However, almost eigensensitivity methods have to use state space equation based on 2N-space to solve problems with damping. These methods require more CPU time and storage capacity because of the larger size of the state-space matrices. In order to overcome these drawbacks, Zimoch [165] presents a direct method for the eigenpair derivatives of damped systems without use of state space equation. However, this method is restricted to discrete systems because the sensitivities are calculated with respect to the components of the structural matrices and not to design parameters. Adhikari [3] also proposes an eigensensitivity method based on N-space. However, it does not give exact solution and is only applicable to small sized damped systems.

Many eigenpair sensitivity methods are restricted to systems whose characteristic matrices are symmetric. However, the thermoelastic damping and stiffness

matrices are asymmetric and the eigenpair sensitivity analysis can not be carried out using the previous methods. Many authors [120, 125, 51] extend the method of Fox and Kapoor to asymmetric matrices. Murthy and Haftka [104] expose an excellent review on the calculation of the eigenpair sensitivity of asymmetric systems. Brandon [23] presents the modal method for asymmetric damped systems. This method solves the problems due to asymmetric matrices by using the left eigenvector. However, it has disadvantages in CPU time and storage capacity because it uses state space form to consider damping of systems and requires a lot of eigenpair information to find eigenpair sensitivity. In [32], a N-space method is exposed where the first order eigenvalue and eigenvector sensitivities are simultaneously obtained from one single equation, which is therefore very efficient in CPU time and storage capacity.

In order to calculate the first order perturbation of the thermoelastic quality factor according to Equation (7.23), only the eigenvalue derivatives are to be calculated. The derivative of the eigenvector are useless. Hence, the method exposed in [32] is computationally too expensive. For first order sensitivities, the state space method is used in order to solve the damped problem and the Fox and Kapoor method is modified in order to take into account the asymmetry of the matrices. The generalized eigenvalue problem for damped systems can be written as follows

$$\left(\lambda^2\mathbf{M} + \lambda\mathbf{C} + \mathbf{K}\right)\mathbf{u} = 0, \tag{7.25}$$

where λ is the eigenvalue, $\mathbf{u}$ is the right eigenvector, $\mathbf{M}$ is the mass matrix, $\mathbf{C}$ is the damping matrix and $\mathbf{K}$ is the stiffness matrix. As the matrices are asymmetric, there is also a left eigenvalue problem:

$$\mathbf{v}^T\left(\lambda^2\mathbf{M} + \lambda\mathbf{C} + \mathbf{K}\right) = 0, \tag{7.26}$$

where $\mathbf{v}$ is the left eigenvector.

In order to determine the eigenvalue sensitivity with respect to a random variable b_i, the derivative of the eigenvalue with respect to b_i is calculated using Equation (7.25). The differentiation of Equation (7.25) with respect to b_i gives

$$\left(\lambda^2\mathbf{M} + \lambda\mathbf{C} + \mathbf{K}\right)\mathbf{u}_{,i} = -(2\lambda\mathbf{M} + \mathbf{C})\mathbf{u}\lambda_{,i} - \left(\lambda^2\mathbf{M}_{,i} + \lambda\mathbf{C}_{,i} + \mathbf{K}_{,i}\right)\mathbf{u}, \tag{7.27}$$

where $(\bullet)_{,i}$ represents the derivative of $(\bullet)$ with respect to the variable b_i. The norm of the left and right eigenvectors are set so that $\mathbf{v}^T(2\lambda\mathbf{M} + \mathbf{C})\mathbf{u} = 1$. Pre-

multiplying Equation (7.27) by $\mathbf{v}^T$ allows the eigenvalue derivative to be expressed as follows

$$\lambda_{,i} = -\mathbf{v}^T \left(\lambda^2\mathbf{M} + \lambda\mathbf{C} + \mathbf{K}\right)\mathbf{u}_{,i} - \mathbf{v}^T \left(\lambda^2\mathbf{M}_{,i} + \lambda\mathbf{C}_{,i} + \mathbf{K}_{,i}\right)\mathbf{u}. \tag{7.28}$$

The use of the left eigenvector allows the dependence in $\mathbf{u}_{,i}$ to be eliminated. The first term of the right hand side of Equation (7.28) is equal to zero as a result of Equation (7.26). Therefore, the eigenvalue sensitivity for asymmetric damped systems is expressed as follows

$$\lambda_{,i} = -\mathbf{v}^T \left(\lambda^2\mathbf{M}_{,i} + \lambda\mathbf{C}_{,i} + \mathbf{K}_{,i}\right)\mathbf{u}. \tag{7.29}$$

As the left and right eigenvectors are both computed when Lanczos analysis is carried out in order to calculate the eigenvalues, the calculation of the eigenvalue sensitivity only requires the computation of the sensitivity matrices.

If a second order perturbation analysis has to be performed, the second order derivative of the eigenvalue has to be computed. Differentiating Equation (7.29) with respect to the variable b_j gives

$$\begin{aligned} \lambda_{,ij} \;=\; & -\mathbf{v}_{,j}^T \left(\lambda^2\mathbf{M}_{,i} + \lambda\mathbf{C}_{,i} + \mathbf{K}_{,i}\right)\mathbf{u} - \mathbf{v}^T \left(\lambda^2\mathbf{M}_{,i} + \lambda\mathbf{C}_{,i} + \mathbf{K}_{,i}\right)\mathbf{u}_{,j} \\ & -\mathbf{v}^T \left(\lambda^2\mathbf{M}_{,ij} + \lambda\mathbf{C}_{,ij} + \mathbf{K}_{,ij}\right)\mathbf{u} - \lambda_{,j}\mathbf{v}^T \left(2\lambda\mathbf{M}_{,i} + \mathbf{C}_{,i}\right)\mathbf{u}, \end{aligned} \tag{7.30}$$

which requires the computation of the sensitivities of the left and right eigenvectors.

In order to avoid the computation of the left and right eigenvector derivatives, Choi's method [32] for the first order eigensensitivity is extended in order to get the second order eigensensitivity. For the first order problem, Choi's method is based on a modified expression of Equation (7.27):

$$\left(\lambda^2\mathbf{M} + \lambda\mathbf{C} + \mathbf{K}\right)\mathbf{u}_{,i} + (2\lambda\mathbf{M} + \mathbf{C})\mathbf{u}\lambda_{,i} = -\left(\lambda^2\mathbf{M}_{,i} + \lambda\mathbf{C}_{,i} + \mathbf{K}_{,i}\right)\mathbf{u}. \tag{7.31}$$

The right eigenvector is normalized as follows

$$\mathbf{u}^T(2\lambda\mathbf{M} + \mathbf{C})\mathbf{u} = 1 \tag{7.32}$$

and differentiating this normalization condition gives

$$\mathbf{u}_{,i}^T(2\lambda\mathbf{M} + \mathbf{C})\mathbf{u} + \mathbf{u}^T(2\lambda\mathbf{M} + \mathbf{C})\mathbf{u}_{,i} + 2\mathbf{u}^T\mathbf{M}\mathbf{u}\lambda_{,i} = -\mathbf{u}^T(2\lambda\mathbf{M}_{,i} + \mathbf{C}_{,i})\mathbf{u}. \tag{7.33}$$

Transposing the first term of the sum in Equation (7.33) gives an equation whose unknowns are $\lambda_{,i}$ and $\mathbf{u}_{,i}$:

$$\mathbf{u}^T(2\lambda\mathbf{M}+\mathbf{C}+2\lambda\mathbf{M}^T+\mathbf{C}^T)\mathbf{u}_{,i}+2\mathbf{u}^T\mathbf{M}\mathbf{u}\lambda_{,i}=-\mathbf{u}^T(2\lambda\mathbf{M}_{,i}+\mathbf{C}_{,i})\mathbf{u}, \tag{7.34}$$

where $\mathbf{M}^T \neq \mathbf{M}$ and $\mathbf{C}^T \neq \mathbf{C}$ due to their asymmetry. Equations (7.31) and (7.34) form a system of two equations with two unknowns, $\lambda_{,i}$ and $\mathbf{u}_{,i}$, which can be expressed as a linear algebraic equation:

$$\begin{bmatrix} \lambda^2\mathbf{M}+\lambda\mathbf{C}+\mathbf{K} & 2\lambda\mathbf{M}+\mathbf{C} \\ \mathbf{u}^T(2\lambda\mathbf{M}+\mathbf{C}+2\lambda\mathbf{M}^T+\mathbf{C}^T) & 2\mathbf{u}^T\mathbf{M}\mathbf{u} \end{bmatrix} \begin{bmatrix} \mathbf{u}_{,i} \\ \lambda_{,i} \end{bmatrix} = - \begin{bmatrix} (\lambda^2\mathbf{M}_{,i}+\lambda\mathbf{C}_{,i}+\mathbf{K}_{,i})\mathbf{u} \\ \mathbf{u}^T(2\lambda\mathbf{M}_{,i}+\mathbf{C}_{,i})\mathbf{u} \end{bmatrix}. \tag{7.35}$$

From the resolution of this equation, the first order sensitivities of the eigenvalue and the right eigenvector are obtained simultaneously without requiring the knowledge of the left eigenvector. This method is thus advantageous in terms of CPU time and storage.

Choi's method has been extended to the computation of second order sensitivities of symmetric damped systems in [31]. In this work, it is further generalized to asymmetric damped systems. Firstly, the following matrices are defined in order to simplify the expression of the equations:

$$\mathbf{F} = \lambda^2\mathbf{M}+\lambda\mathbf{C}+\mathbf{K}, \tag{7.36}$$

$$\mathbf{F}_{,i} = \lambda^2\mathbf{M}_{,i}+\lambda\mathbf{C}_{,i}+\mathbf{K}_{,i}, \tag{7.37}$$

$$\mathbf{F}_{,ij} = \lambda^2\mathbf{M}_{,ij}+\lambda\mathbf{C}_{,ij}+\mathbf{K}_{,ij}, \tag{7.38}$$

$$\mathbf{G} = 2\lambda\mathbf{M}+\mathbf{C}, \tag{7.39}$$

$$\mathbf{G}_{,i} = 2\lambda\mathbf{M}_{,i}+\mathbf{C}_{,i}, \tag{7.40}$$

$$\mathbf{G}_{,ij} = 2\lambda\mathbf{M}_{,ij}+\mathbf{C}_{,ij}. \tag{7.41}$$

The differentiation of Equation (7.31) with respect to variable b_j leads to

$$\begin{aligned} \mathbf{F}\mathbf{u}_{,ij}+\mathbf{G}\mathbf{u}\lambda_{,ij} = & -(\mathbf{F}_{,i}\mathbf{u}_{,j}+\mathbf{F}_{,j}\mathbf{u}_{,i}+\mathbf{G}\mathbf{u}_{,j}\lambda_{,i}+\mathbf{G}\mathbf{u}_{,i}\lambda_{,j} \\ & +\mathbf{G}_{,j}\mathbf{u}\lambda_{,i}+\mathbf{G}_{,i}\mathbf{u}\lambda_{,j}+2\mathbf{M}\mathbf{u}\lambda_{,i}\lambda_{,j}+\mathbf{F}_{,ij}\mathbf{u}). \end{aligned} \tag{7.42}$$

The second order derivative of the normalization condition (Equation (7.33)) with

respect to variables b_i and b_j gives

$$\begin{aligned}\mathbf{u}_{,ij}^T\mathbf{G}\mathbf{u} + \mathbf{u}^T\mathbf{G}\mathbf{u}_{,ij} + 2\mathbf{u}^T\mathbf{M}\mathbf{u}\lambda_{,ij} &= -\mathbf{u}_{,i}^T(\mathbf{G}+\mathbf{G}^T)\mathbf{u}_{,j} - \mathbf{u}^T(\mathbf{G}_{,i}+\mathbf{G}_{,i}^T)\mathbf{u}_{,j} \\ &- 2\mathbf{u}_{,i}^T(\mathbf{M}+\mathbf{M}^T)\mathbf{u}\lambda_{,j} - 2\mathbf{u}_{,j}^T(\mathbf{M}+\mathbf{M}^T)\mathbf{u}\lambda_{,i} \\ &- 2\mathbf{u}^T\mathbf{M}_{,i}\mathbf{u}\lambda_{,j} - 2\mathbf{u}^T\mathbf{M}_{,j}\mathbf{u}\lambda_{,i} - \mathbf{u}^T\mathbf{G}_{,ij}\mathbf{u}.\end{aligned} \tag{7.43}$$

Equations (7.42) and (7.43) can be combined in one linear algebraic equation:

$$\begin{bmatrix} \mathbf{F} & \mathbf{G}\mathbf{u} \\ \mathbf{u}^T(\mathbf{G}^T+\mathbf{G}) & 2\mathbf{u}^T\mathbf{M}\mathbf{u} \end{bmatrix} \begin{bmatrix} \mathbf{u}_{,ij} \\ \lambda_{,ij} \end{bmatrix} = - \begin{bmatrix} \mathbf{F}_{,i}\mathbf{u}_{,j} + \mathbf{F}_{,j}\mathbf{u}_{,i} + \mathbf{G}\mathbf{u}_{,j}\lambda_{,i} \\ +\mathbf{G}\mathbf{u}_{,i}\lambda_{,j} + \mathbf{G}_{,j}\mathbf{u}\lambda_{,i} + \mathbf{G}_{,i}\mathbf{u}\lambda_{,j} \\ +2\mathbf{M}\mathbf{u}\lambda_{,i}\lambda_{,j} + \mathbf{F}_{,ij}\mathbf{u} \\ \\ \mathbf{u}_{,i}^T(\mathbf{G}+\mathbf{G}^T)\mathbf{u}_{,j} \\ +\mathbf{u}^T(\mathbf{G}_{,i}+\mathbf{G}_{,i}^T)\mathbf{u}_{,j} \\ +2\mathbf{u}_{,i}^T(\mathbf{M}+\mathbf{M}^T)\mathbf{u}\lambda_{,j} \\ +2\mathbf{u}_{,j}^T(\mathbf{M}+\mathbf{M}^T)\mathbf{u}\lambda_{,i} \\ +2\mathbf{u}^T\mathbf{M}_{,i}\mathbf{u}\lambda_{,j} + 2\mathbf{u}^T\mathbf{M}_{,j}\mathbf{u}\lambda_{,i} \\ +\mathbf{u}^T\mathbf{G}_{,ij}\mathbf{u} \end{bmatrix}. \tag{7.44}$$

The second order derivatives $\mathbf{u}_{,ij}$ and $\lambda_{,ij}$ are found by solving Equation (7.44), which requires the first-order derivatives $\mathbf{u}_{,i}$, $\mathbf{u}_{,j}$, $\lambda_{,i}$ and $\lambda_{,j}$ obtained by the resolution of Equation (7.35). The coefficient matrix of the left hand side is the same in both Equations (7.35) and (7.44) so that the LU decomposition in the Gaussian elimination has to be done only once. This method allows for the N-space to be maintained without use of the state space equation and requires only corresponding right eigenpair information without use of the left eigenvector information.

Note that the coefficient matrix of the left hand side of Equations (7.35) and (7.44) has to be scaled in order to avoid the decomposition of a badly conditioned matrix and hence, to insure the numerical stability of the procedure.

7.4 Structural Matrix Sensitivity

A numerical procedure can be used in order to determine the sensitivity matrices. In order to obtain the first and second order sensitivities of the structural matrix

$\mathbf{S}$ with respect to the variable b, it has to be calculated for three values of the random variable: its nominal value $\bar{b}$, the upper perturbed value $b_+ = \bar{b} + \epsilon$ and the lower perturbed value $b_- = \bar{b} - \epsilon$, where ϵ is the perturbation. The first and second order derivatives of $\mathbf{S}$ are approximated by finite differences:

$$\frac{\partial \mathbf{S}}{\partial b} \approx \frac{\mathbf{S}(b_+) - \mathbf{S}(b_-)}{2\epsilon} \tag{7.45}$$

and

$$\frac{\partial^2 \mathbf{S}}{\partial b^2} \approx \frac{\mathbf{S}(b_+) - 2\mathbf{S}(\bar{b}) + \mathbf{S}(b_-)}{\epsilon^2}. \tag{7.46}$$

Whenever it is possible to calculate analytically the elementary sensitivity matrices, it would be preferable to use the analytical method instead of the numerical one because of the accuracy dependence on the value of the perturbation ϵ. The method used to analytically compute the elementary sensitivity matrices depends on the nature of the random variable: physical and pseudo-geometric variables and geometric variables. Once the elementary sensitivity matrices are determined, the structural sensitivity matrices are assembled using the same scheme than for structural matrices.

7.4.1 Physical and Pseudo-geometric Variables

If the random variable is a variable of physical or mechanical nature (e.g. Young's modulus, thermal conductivity, density,...) or a pseudo-geometric variable, the elementary sensitivity matrices can be analytically computed and the conventional finite element assembly procedure can be used to obtain the system sensitivity matrices.

For example, the sensitivity with respect to the mass density ρ of the elementary mass matrix is

$$\mathbf{M}^{(e)}_{uu,\rho} = \frac{\partial}{\partial \rho} \int_\Omega {\mathbf{N_u}}^T \rho \mathbf{N_u} d\Omega \tag{7.47}$$

$$= \int_\Omega {\mathbf{N_u}}^T \mathbf{N_u} d\Omega. \tag{7.48}$$

7.4.2 Geometric Variables

For shape design variables, the procedure is different. The thermopiezoelectric elementary matrices (Equations (4.37-4.47)) can be written in a general form:

$$\mathbf{S^{(e)}} = \int_\Omega \mathbf{L}^T \mathbf{A} \mathbf{R} d\Omega, \tag{7.49}$$

where $\mathbf{L}$ and $\mathbf{R}$ are either shape function matrices or shape function derivative matrices, $\mathbf{A}$ is a material constitutive matrix. Considering isoparametric elements, the elementary matrix is given by

$$\mathbf{S^{(e)}} = \int_{\Omega_{ref}} \mathbf{L}^T \mathbf{A} \mathbf{R} \zeta d\Omega_{ref}, \tag{7.50}$$

where $\Omega = \zeta \Omega_{ref}$ with $\zeta = |\mathbf{J}|$ is the Jacobian determinant and $\mathbf{J}$ is the Jacobian matrix of the isomorphism. The differentiation with respect to b yields

$$\frac{\partial \mathbf{S^{(e)}}}{\partial b} = \int_{\Omega_{ref}} \frac{\partial \mathbf{L}^T}{\partial b} \mathbf{A} \mathbf{R} \zeta d\Omega_{ref} + \int_{\Omega_{ref}} \mathbf{L}^T \mathbf{A} \frac{\partial \mathbf{R}}{\partial b} \zeta d\Omega_{ref} + \int_{\Omega_{ref}} \mathbf{L}^T \mathbf{A} \mathbf{R} \frac{\partial \zeta}{\partial b} d\Omega_{ref}. \tag{7.51}$$

If matrices $\mathbf{L}$ and $\mathbf{R}$ and the Jacobian determinant ζ are explicit functions of the nodal coordinates of the element $\mathbf{X}^{(e)}$, their derivative can be calculated as follows

$$\frac{\partial L_{ij}}{\partial b} = \left(\frac{\partial L_{ij}}{\partial \mathbf{X}^{(e)}} \right)^T \frac{\partial \mathbf{X}^{(e)}}{\partial b}, \tag{7.52}$$

$$\frac{\partial R_{ij}}{\partial b} = \left(\frac{\partial R_{ij}}{\partial \mathbf{X}^{(e)}} \right)^T \frac{\partial \mathbf{X}^{(e)}}{\partial b}, \tag{7.53}$$

$$\frac{\partial \zeta}{\partial b} = \left(\frac{\partial \zeta}{\partial \mathbf{X}^{(e)}} \right)^T \frac{\partial \mathbf{X}^{(e)}}{\partial b}, \tag{7.54}$$

where $\frac{\partial \mathbf{X}^{(e)}}{\partial b}$ is the nodal velocity field $\mathbf{V}^{(e)}$ associated to geometric variable b:

$$\mathbf{V}^{(e)} = \mathbf{N}_u^T \mathbf{v}. \tag{7.55}$$

The velocity field $\mathbf{v}$ parameterizes the random geometry by linearly relating the coordinate field of the mean geometry to a realization of the random geometry:

$$\mathbf{x}(b) = \bar{\mathbf{x}} + (b - \bar{b})\mathbf{v}. \tag{7.56}$$

For example, a bar with a random length L is considered. The coordinate $x_{\Delta L}$ of the bar of length $\bar{L} + \Delta L$ can be related to the coordinate x of the nominal bar of length $\bar{L}$ by this relation:

$$x_{\Delta L} = x + \frac{x}{\bar{L}} \Delta L. \tag{7.57}$$

Therefore, the velocity field is $x/\bar{L}$.

7.5 Random Field Discretization

In Chapter 6, two random field discretization methods have been selected: the Local Average method and the Karhunen-Loeve expansion series method. In order to use them in the framework of the perturbation stochastic finite element method, the first and second order derivatives of the structural matrices with respect to the random variables, which model the random field, have to be determined. In this section, the considered random fields represent the spatial variability of material or pseudo-geometric parameters.

7.5.1 Local Average Method

In the Local Average method, the random variables are the mean of the random field over each element of the random mesh, which is in theory not necessarily equivalent to the finite element mesh. In this work, the same mesh is used for the finite element and random field discretizations, so that the random variables are the average of the random field over each finite element. The first and second order derivatives of the elementary matrices with respect to the parameter, which is modeled by the random field, can be calculated analytically as exposed in Section 7.4.1 or numerically by replacing the global structural matrix $\mathbf{S}$ by the elementary one $\mathbf{S}^{(e)}$ in Equations (7.45-7.46). The components of the first order derivative of the global structural matrices with respect to the ith variable are all zero except for those corresponding to the degrees of freedom of the ith element. Analogously, the components of the second order derivative of the global structural matrices with respect to the ith and jth variables are all zero but those corresponding to the degrees of freedom of the ith and jth elements.

If due to the correlation length, the random mesh has to be coarser than the finite element mesh, the random mesh can be constructed so that each random element includes several finite elements and the derivative matrices with respect to the ith variable are calculated considering the components of the elements included into the random element i. If the random mesh has to be finer than the finite element, the finite element mesh has to be refined to match the random mesh and if needed, a multiscale procedure should be applied.

7.5.2 Karhunen-Loeve Expansion Method

The Karhunen-Loeve expansion method (Equation (6.36)) can be used in the framework of the perturbation stochastic finite element method. The first and second order derivatives of the structural matrices with respect to the random variables ζ_k have to be calculated. Generally, material variables ($\rho,\ E,\ k, \ldots$) appear as a first degree multiplicative factor in the expression of the Lagrangian (Equation (4.11)), so that the structural matrices depend linearly on them. Therefore, if the random field X is approximated by its Karhunen-Loeve expansion:

$$\hat{X}(x,\xi) = \bar{X}(x) + \sum_{k=1}^{N} \sqrt{\lambda_k} f_k(x) \zeta_k(\xi), \tag{7.58}$$

the finite element stochastic eigenproblem takes the form:

$$\left[\mathbf{A}_0 + \sum_{i=1}^{n} \zeta_i(\xi)\mathbf{A}_i\right] \mathbf{x}(\xi) = \lambda(\xi) \left[\mathbf{B}_0 + \sum_{i=1}^{n} \zeta_i(\xi)\mathbf{B}_i\right] \mathbf{x}(\xi), \tag{7.59}$$

where $\mathbf{A}_0$, $\mathbf{A}_i$, $\mathbf{B}_0$ and $\mathbf{B}_i$ are deterministic matrices while $\lambda(\xi)$ and $\mathbf{x}(\xi)$ denote the random eigenvalue and eigenvector, respectively. $\zeta_i(\xi)$ are the random variables representing the random fields. The random characteristic is explicitly expressed by the dependence on ξ, which represents a value of the sample space.

Therefore, the first and second order derivatives of matrices $\mathbf{A}$ and $\mathbf{B}$ with respect to the random variables are easily obtained:

$$\mathbf{A}_{,i} = \mathbf{A}_i \quad \text{and} \quad \mathbf{B}_{,i} = \mathbf{B}_i, \tag{7.60}$$

$$\mathbf{A}_{,ij} = \mathbf{0} \quad \text{and} \quad \mathbf{B}_{,ij} = \mathbf{0}. \tag{7.61}$$

In order to illustrate the computation of matrices $\mathbf{A}_i$ and $\mathbf{B}_i$, the mass density ρ is modeled by a random field and the mass matrix $\mathbf{M_{uu}}$ is constructed:

$$\mathbf{M_{uu}} = \int_\Omega \rho \mathbf{N_u}^T \mathbf{N_u} d\Omega \tag{7.62}$$

$$= \int_\Omega \bar{\rho} \mathbf{N_u}^T \mathbf{N_u} d\Omega + \sum_{k=1}^{N} \zeta_k \int_\Omega \sqrt{\lambda_k} f_k(x) \mathbf{N_u}^T \mathbf{N_u} d\Omega \tag{7.63}$$

$$= \bar{\mathbf{M}}_{\mathbf{uu}} + \sum_{k=1}^{N} \zeta_k \mathbf{M_{uu}}_k. \tag{7.64}$$

Since the random variables ζ_k have the following statistic properties (Equation (6.38)):

$$E[\zeta_k] = 0 \ \text{ and } \ E[\zeta_k \zeta_l] = \delta_{kl}, \tag{7.65}$$

the expectation and variance (Equations (7.19) and (7.21)) of the quality factor take a simplified expression:

$$E\left[Q(\bar{\mathbf{b}})\right] \approx \bar{Q} + \frac{1}{2}\sum_{i=1}^{n} Q_{,ii} \tag{7.66}$$

and

$$Var\left(Q(\bar{\mathbf{b}})\right) \approx \sum_{i=1}^{n} Q_{,i}Q_{,i}. \tag{7.67}$$

For random fields which do not appear linearly in the Lagrangian expression, either the Taylor series expansion or the polynomial chaos decomposition scheme can be employed to arrive at a form similar to Equation (7.59) as it is done in the spectral method [58].

7.6 Variability Response Function

In the absence of experimental data on the correlation characteristics of material properties, some assumptions have to be made on the correlation function and arbitrary values have to be used for data like the influence lengths. However, the statistics of the response depend on these correlation characteristics. The variability response function allows the determination of a response variance upper bound, which is independent on the correlation data.

Deodatis and al. [38, 39, 60, 61, 117] introduce the concept of the variability response function (VRF) in order to establish spectral-distribution-free upper bounds of the response variability. The basic idea associated with the VRF is to express the variance of the response (i.e. the quality factor) in the following integral form:

$$Var(Q) = \int_{-\infty}^{+\infty} VRF(\kappa)S(\kappa)d\kappa, \tag{7.68}$$

where $VRF(.)$ is a function depending on the deterministic parameters related to the geometry, boundary conditions, material properties and loading of the nominal (mean) structure, $S(.)$ is the spectral density function of the random field modeling the uncertain properties and κ is the wave number. The response variance is upper-bounded as follows

$$Var(Q) \leq VRF(\kappa_{max})\sigma^2, \tag{7.69}$$

where κ_{max} is the wave number at which the VRF is maximum and σ^2 is the variance of the random field.

Using PSFEM, a first order approximation of the VRF can be determined. In Equation (7.21), the expectation $E[\Delta b_i \Delta b_j]$ is the only unknown quantity, which depends on the correlation function and hence, on the assumptions made on the correlation length and correlation function.

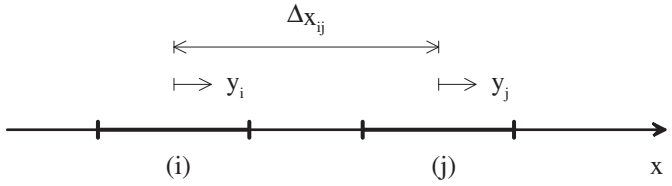

Figure 7.1: Relative positions of elements (i) and (j).

For the local average method in 1-D, the zero mean variable Δb_i is the average of the zero mean random field ΔX on the element i of length L_i:

$$\Delta b_i = \int_0^{L_i} \Delta X(x) dx, \tag{7.70}$$

so that the expectation $E[\Delta b_i \Delta b_j]$ has the following expression:

$$E[\Delta b_i \Delta b_j] = \frac{1}{4} \int_{-1}^{+1} \int_{-1}^{+1} B_{\Delta X} \left(\Delta x_{ij} + \frac{L_j y_j}{2} - \frac{L_i y_i}{2} \right) dy_j dy_i, \tag{7.71}$$

where $B_{\Delta X}$ is the covariance function of the homogeneous random field ΔX, L_i and L_j are the lengths of elements (i) and (j), respectively, and Δx_{ij} is the distance between the center points of elements (i) and (j), as shown in Figure 7.1. Using the Wiener-Khinchine relation [144]:

$$B_{\Delta X}(\tau) = \int_{-\infty}^{+\infty} S_{\Delta X}(\kappa) \cos(\kappa \tau) d\kappa, \tag{7.72}$$

where $S_{\Delta X}(.)$ is the spectral density function of ΔX, the expectation becomes

$$\begin{aligned} E[\Delta b_i \Delta b_j] &= \frac{1}{4} \int_{-1}^{+1} \int_{-1}^{+1} \int_{-\infty}^{+\infty} S_{\Delta X}(\kappa) \cos \left((\Delta x_{ij} + \frac{L_j y_j}{2} - \frac{L_i y_i}{2}) \kappa \right) dy_j dy_i d\kappa \\ &= \frac{1}{4} \int_{-\infty}^{+\infty} S_{\Delta X}(\kappa) \cos(\kappa \Delta x_{ij}) \, Q_i(\kappa) Q_j(\kappa) d\kappa, \end{aligned} \tag{7.73}$$

where

$$Q_i(\kappa) = \frac{4}{\kappa L_i} \sin \left(\frac{\kappa L_i}{2} \right). \tag{7.74}$$

From Equations (7.21), (7.68) and (7.73), the variability response function of the quality factor for a 1-D homogeneous random field discretized via the local average method is expressed as

$$VRF(\kappa) = \frac{1}{4}\sum_{i=1}^{n}\sum_{j=1}^{n}\cos(\kappa\Delta x_{ij})Q_i(\kappa)Q_j(\kappa)Q_{,i}Q_{,j}. \tag{7.75}$$

Note that in the Karhunen-Loeve expansion method, the generation of the random variables depends on the correlation function so that the decomposition of the variance into its deterministic and stochastic parts is not possible.

7.7 Random Variable Decorrelation

Due to the correlation of the random variables, a double summation has to be carried out in order to determine the mean and variance of the quality factor (Equations (7.19) and (7.21)). Moreover, the computation of the mixed second order derivatives $Q_{,ij}$ demands a huge computational effort. Indeed, for n random variables, $n(n+1)/2$ derivatives have to be computed since the mixed partial derivatives commute: $Q_{,ij} = Q_{,ji}$ (Clairaut's theorem). If the number of random variables is large, which is generally the case when random fields are considered, the computation of the statistical moments of Q requires an important computational time due to the correlation of the random variables. A decorrelation procedure can be applied in order to avoid the double summations and hence, the computation of the mixed second order derivatives. Note that the random variables associated to the Karhunen-Loeve expansion method are uncorrelated.

The decorrelation procedure consists in diagonalizing the covariance matrix $\mathbf{B}$. As $\mathbf{B}$ is real and symmetric by construction, it is diagonalized by the following orthogonal transformation:

$$\mathbf{D} = \mathbf{V}^T\mathbf{B}\mathbf{V}, \tag{7.76}$$

where $\mathbf{D}$ is a diagonal matrix whose components are the eigenvalues of $\mathbf{B}$ and $\mathbf{V}$ is the matrix formed by columns from the corresponding eigenvectors. Therefore, the vector $\mathbf{c}$, defined as

$$\mathbf{c} = \mathbf{V}^T\mathbf{b}, \tag{7.77}$$

is the vector of the uncorrelated random variables c_i corresponding to the correlated random variables b_i. The first two statistical moments of $\mathbf{c}$ are related to

those of $\mathbf{b}$:

$$E[\mathbf{c}] = \mathbf{V}^T E[\mathbf{b}] \tag{7.78}$$

and

$$Cov(\mathbf{c}) = \mathbf{V}^T \mathbf{B} \mathbf{V} = \mathbf{D}. \tag{7.79}$$

The mean and variance of the quality factor can be approximated using the uncorrelated variables c_i in the second order perturbation approach:

$$\begin{aligned} E\left[Q(\bar{\mathbf{c}})\right] &\approx \bar{Q} + \frac{1}{2}\sum_{i=1}^{n} Q^*_{,ii} Var(c_i) && (7.80)\\ &= \bar{Q} + \frac{1}{2}\sum_{i=1}^{n} Q^*_{,ii} \mathbf{D}(i,i) && (7.81) \end{aligned}$$

and

$$\begin{aligned} Var\left(Q(\bar{\mathbf{c}})\right) &\approx \sum_{i=1}^{n} Q^{*2}_{,i} Var(c_i) && (7.82)\\ &= \sum_{i=1}^{n} Q^{*2}_{,i} \mathbf{D}(i,i), && (7.83) \end{aligned}$$

where $Q(\bar{\mathbf{c}}) = Q(\bar{\mathbf{b}})$, $Q^*_{,ii} = \partial^2 Q / \partial c_i^2$ and $Q^*_{,i} = \partial Q / \partial c_i$. In order to determine the derivative with respect to the decorrelated variables c_i, the corresponding structural matrix sensitivities have to be computed from the sensitivities with respect to the correlated random variables b_i:

$$\begin{aligned} \frac{\partial \mathbf{S}}{\partial c_i} &= \sum_{j=1}^{n} \frac{\partial b_j}{\partial c_i} \frac{\partial \mathbf{S}}{\partial b_j} && (7.84)\\ &= \sum_{j=1}^{n} \mathbf{V}(j,i) \frac{\partial \mathbf{S}}{\partial b_j} && (7.85) \end{aligned}$$

and

$$\frac{\partial^2 \mathbf{S}}{\partial c_i^2} = \sum_{j=1}^{n}\sum_{k=1}^{n} \mathbf{V}(j,i)\mathbf{V}(k,i) \frac{\partial^2 \mathbf{S}}{\partial b_j \partial b_k}, \tag{7.86}$$

where $\mathbf{S}$ represents any structural matrix.

The drawback of the random variable decorrelation is that one part of the saved CPU time obtained from the transformation of the double summations to simple ones in Equations (7.81) and (7.83) has to be used for the computation

of the structural matrix sensitivities. Moreover, the decorrelation procedure may only be used for random variables characterized by a definite positive correlation matrix. Indeed, a negative eigenvalue of $\mathbf{B}$ would lead to a negative variance in Equation (7.79), which would not make any sense. Therefore, this technique can not be applied in conjunction with the local average discretization based on an irregular mesh.

7.8 Random Basis Truncation

Using the decorrelation procedure described in the previous section, the random field modeled by the local average method can be written as a series expansion starting from Equation (6.35):

$$\hat{X}(x,\xi) = \bar{X}(x) + \sum_{r=1}^{n} \left(\sum_{k=1}^{n} g_k(x) V_{kr} \right) c_r(\xi), \tag{7.87}$$

where n is the number of elements of the random mesh, V_{kr} is the component kr of matrix $\mathbf{V}$ and $g_k(x) = 1$ if $x \in \Omega_i$ and $g_k(x) = 0$ if $x \notin \Omega_i$. In order to have a similar expression to Karhunen-Loeve one, random variable $c_r(\xi)$ and spatial functions $f_r(x) = (\sum_{k=1}^{n} g_k(x) V_{kr})$ have to be orthonormalized, so that $f_r(x) f_k(x) = \delta_{rk}$. The Local Average series expansion expression is then written

$$\hat{X}(x,\theta) = \bar{X}(x) + \sum_{r=1}^{n} \sqrt{\lambda_{LA,r}} f_{LA,r}(x) \zeta_r(\xi), \tag{7.88}$$

where $\zeta_r(\xi) = c_r(\xi)/\sqrt{Var(c_r)}$, $f_{LA,r}(x) = (\sum_{k=1}^{n} g_k(x) V_{kr}) / \sqrt{|\Omega|/n}$ and $\lambda_{LA,r} = Var(c_r)|\Omega|/n$. Note that this orthonormalization is possible only if the mesh elements are identical.

In Equations (7.58) and (7.88), the number of random variables is equal to the expansion order. For the Karhunen-Loeve expansion, the number of random variables should be infinite in order to avoid a truncation error and for the local average method, this number should be equal to the number of elements of the random mesh. For the purpose of decreasing the computational cost, the random basis can be truncated and the expansion order is set to $n^* < n$ giving an approximation $\check{X}(x)$ of $\tilde{X}(x)$, which is the random field modeled by a complete random basis. Note that in the case of the Karhunen-Loeve expansion method

$\tilde{X}(x) = X(x)$, while for the Local Average method, $\tilde{X}(x) = \hat{X}(x)$. The induced truncation error on the variance of the random field can be estimated by

$$\epsilon rr = \frac{Var(\tilde{X}(x) - \check{X}(x))}{Var(\tilde{X}(x))} = 1 - \frac{Var(\check{X}(x))}{Var(\tilde{X}(x))}. \tag{7.89}$$

As $Var(\tilde{X}(x) - \check{X}(x))$ is always positive because of the definition of the variance, the truncation of the random basis always yields a reduction of the variance.

From series expansions (7.58) and (7.88) truncated at order n^*, the variance of $\check{X}(x)$ is expressed

$$Var(\check{X}(x)) = E\left[\sum_{r=1}^{n^*}\sum_{s=1}^{n^*}\sqrt{\lambda_r}\sqrt{\lambda_s}f_r(x)f_s(x)\zeta_r\zeta_s\right]. \tag{7.90}$$

Integrating this equation over the definition domain Ω and using the orthonormality of the random variables ζ_r and of the eigenfunctions $f_r(x)$ gives

$$\int_\Omega Var(\check{X}(x))d\Omega = \sum_{r=1}^{n^*}\lambda_r \tag{7.91}$$

and the mean of the variance error over the domain Ω is equal to

$$\overline{\epsilon rr} = 1 - \frac{\sum_{r=1}^{n^*}\lambda_r}{|\Omega| Var(\tilde{X}(x))}, \tag{7.92}$$

if $\tilde{X}(x)$ has a constant variance over the domain. Therefore, the truncation error can be evaluated by the sum of the eigenvalues considered in the expansion.

Note that this error estimator allows the determination of the variance error on the truncated random field, but not on the response. The number of random variables required for a certain accuracy level is dependent on the characteristic of the random field, especially on the correlation length. This dependence is studied in numerical applications analyzed in Chapter 8.

7.9 Concluding Remarks

This chapter has presented the application of the perturbation stochastic finite element method for the determination of the first two statistical moments of the thermoelastic quality factor. The particularity of this problem is that it requires the determination of the first and second order sensitivities of the eigenpairs of

an asymmetric damped eigenproblem. The structural sensitivity matrices are computed for material variables and pseudo-geometric ones as well as for shape design variables. For material and pseudo-geometric parameters, the concept of random field is used in the framework of the perturbation stochastic finite element method. The number of random variables induced by the discretization of a random field can be high, leading to a high computational cost. In order to improve the efficiency of the method, the decorrelation procedure of the random variables is introduced. Moreover, an estimator of the error induced by the truncation of the random basis is investigated. All these features are illustrated on a test case in Chapter 8. Figure 7.2 sums up the different computational steps involved in the proposed methodology.

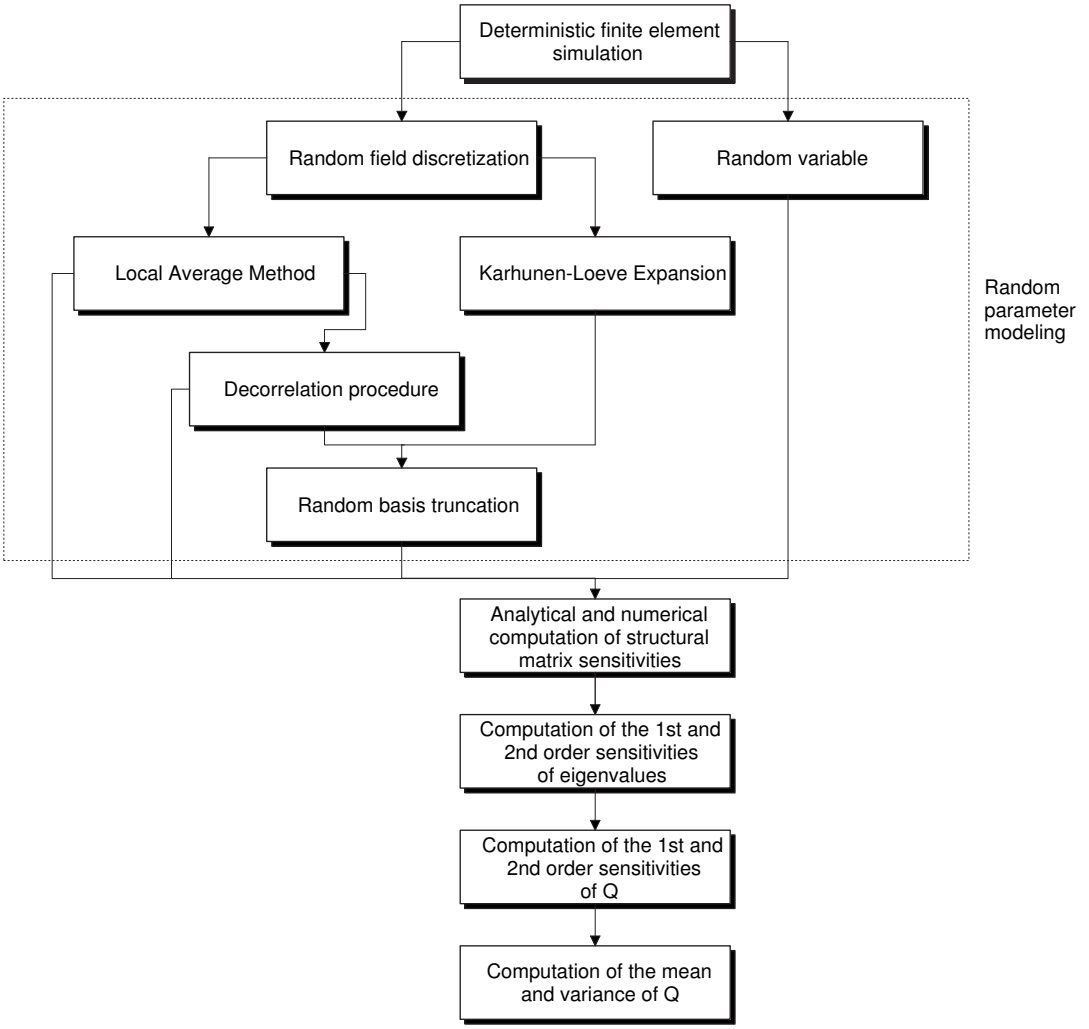

Figure 7.2: Computational steps involved in the second order perturbation stochastic finite element method.

Chapter 8

Application of the PSFEM on Quality Factor Analyses

In this chapter, the methods exposed in Chapter 7 are applied to a simple test case, i.e. the analysis of the thermoelastic quality factor of a clamped-clamped silicon beam modeled using thermoelastic beam finite elements. Firstly, deterministic sensitivity analyses are carried out in order to determine the most interesting material random parameter. This parameter, Young's modulus, is then modeled as a random variable as well as a random field. The results obtained using the perturbation stochastic finite element methods are compared to the Monte-Carlo ones. The influence of the correlation data is also studied. Finally, the variability of the quality factor is studied with respect to a geometric random parameter, i.e. the beam length.

8.1 Clamped-Clamped Silicon Beam

The effect of uncertainty on the quality factor of a clamped-clamped silicon beam is studied. The test case beam has the following dimensions: a length L of 90 μm, a height h of 4.5 μm and a width w of 4.5 μm (Figure 8.1). The thermal and mechanical properties of silicon at $T_o = 298K$ are: $E = 1.5810^{11}\ N/m^2$, $\rho = 2300\ kg/m^3$, $\nu = 0.2$, $c_v = 711\ J/kgK$, $\alpha = 2.510^{-6}\ K^{-1}$ and $k = 170\ Wm^{-1}K^{-1}$. The contribution of the piezoelectric effect is not considered for this example and

the thermoelastic quality factor is determined for the first bending mode in plane OYZ. The structure is modeled using 50 thermoelastic beam finite elements. Note that a stochastic thermopiezoelectric eigenproblem has exactly the same computational specificities and hence, uses the same resolution methodology as a stochastic thermoelastic eigenproblem.

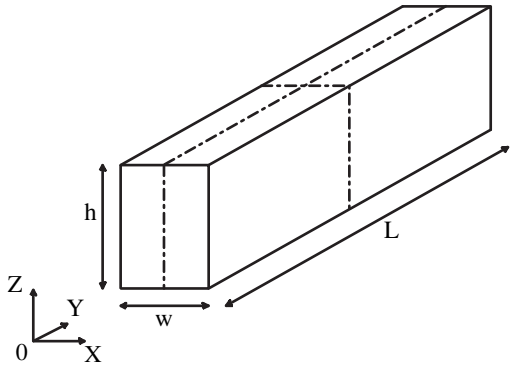

Figure 8.1: Beam geometry.

8.2 Deterministic Sensitivity Analysis

In this section, the sensitivity analysis of the resonant frequency and the quality factor is carried out using the thermoelastic finite element method. The sensitivities with respect to Young's modulus have been computed according to the proposed analytical method and to a forward finite difference method, and the results are compared in Table 8.1. These results correspond to the configuration that has the smaller quality factor, i.e. the height is equal to 5.3 μm. For the finite difference sensitivities, a variation of $\pm 1\%$ of Young's modulus is used. Hence, it is required to solve twice the eigenproblem. The sensitivities are similar for both methods. However, the analytical method is more advantageous computationally than the finite difference method as it requires only one resolution of the eigenproblem.

In order to compare the sensitivities associated with different variables, the normalized sensitivity can be used:

$$Q_{N,\beta} = Q_{,\beta}\frac{\beta}{Q}, \tag{8.1}$$

Table 8.1: Comparison of the analytical and finite difference sensitivities.

Method	Analytical method	Finite Difference
λ [rad/s]	$-1.5540e3 \pm 3.5028e7i$	$-1.5540e3 \pm 3.5028e7i$
$\lambda_{,E}$ [rad/sPa]	$-1.5046e{-}11 \pm 1.1086e{-}7i$	$-1.5099e{-}11 \pm 1.1086e{-}7i$
$Q_{,E}$ [1/Pa]	$-7.3453e{-}11$	$-7.3843e{-}11$

where β is the considered parameter (E, k, ρ,...). Table 8.2 compares the normalized sensitivities for the beam with a 5.3 μm height. The normalized sensitivities are computed with respect to the different material parameters: Young's modulus E, mass density ρ, thermal conductivity k, thermal expansion coefficient α and volumetric heat capacity C_E and two pseudo-geometric parameters: height h and width w. As expected, the beam width does not influence the quality factor and its sensitivity is nearly zero. The parameter for which the sensitivity is the highest is the thermal expansion coefficient. The sensitivities with respect to Young's modulus and volumetric heat capacity are also important.

Table 8.2: Comparison of the normalized sensitivities of the quality factor with respect to different variables (h=5.3 μm).

Variable	Analytical method	Finite Difference
E	-1.0297	-1.0352
ρ	0.0297	0.0292
k	0.0594	0.0578
α	-2.0000	-2.0081
C_E	0.9407	0.9407
w	-4.8154e-5	8.221e-5
h	-0.1756	-0.1861

Table 8.3 compares the sensitivity for different beam heights. The 4.5 μm configuration is on the isothermal side of the peak, while the 6 μm one is on the

adiabatic side of the peak. 5.3 μm is the height for which the thermoelastic losses are maximum. All parameters except the thermal expansion coefficient and beam width influence differently the quality factor depending on the regime.

Table 8.3: Comparison of the normalized sensitivities of the quality factor for different regimes.

Q sensitivity wrt	$h = 4.5\mu m$	$h = 5.3\mu m$	$h = 6\mu m$
E	-1.2487	-1.0299	-0.8505
ρ	0.2487	0.0297	-0.1492
k	0.4973	0.0594	-0.2985
α	-2.0000	-2.0000	-1.9996
C_E	0.5027	0.9407	1.2983
w	3.2617e-6	-4.8154e-5	-1.0123e-4
h	-1.4801	-0.1756	0.8846

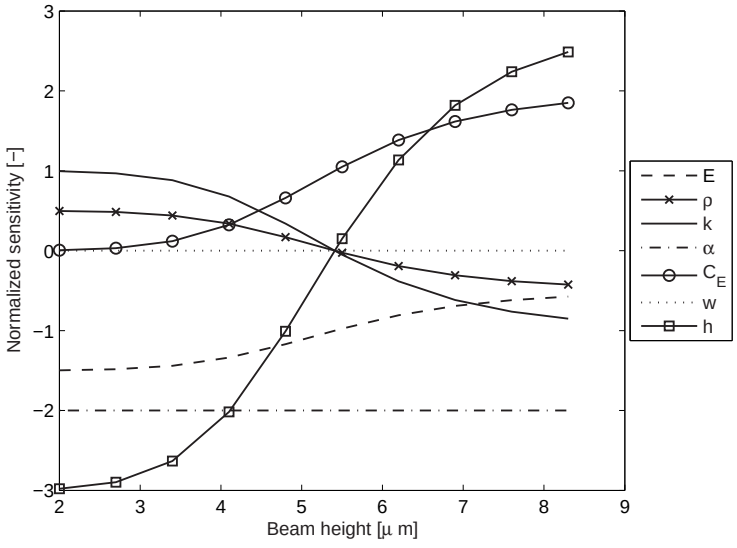

Figure 8.2: Variation of the quality factor sensitivity with the beam height.

Figure 8.2 shows the variation of the quality factor sensitivity with the beam height. When going from the isothermal side to the adiabatic side, sensitivity

changes of sign for the thermal conductivity, mass density and beam thickness. Sensitivities with respect to the thermal expansion coefficient and beam width do not depend on the beam height. On the isothermal side, the quality factor does not depend on the volumetric heat capacity. Whatever the thermoelastic regime, the sensitivity with respect to Young's modulus is always negative which means that an increase in Young's modulus induces a decrease in the quality factor.

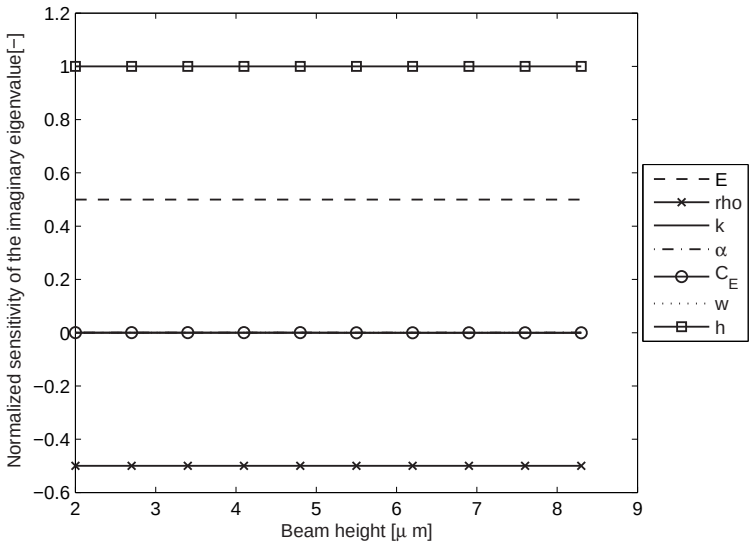

Figure 8.3: Variation of the imaginary eigenvalue sensitivity with the beam height.

The study of the sensitivity of the real and imaginary eigenvalue for the different parameters is also interesting. Indeed, some parameters do not influence the imaginary eigenvalue, i.e. the vibrating pulsation. Figure 8.3 shows that only three parameters, i.e. ρ, E and h, influence the vibrating pulsation and that this influence does not depend on the thermoelastic regime. Note that the pulsation is only sensitive to mechanical parameters. Hence, except for these parameters, the influence on the quality factor is only due to the influence on the real eigenvalue (Figure 8.4).

These analyses show that the quality factor is very sensitive to the beam height except when the thermoelastic losses are maximum. The thermal expansion coefficient is also an important parameter even if usually this parameter do not vary a lot. Young's modulus is a very important parameter as the sensitivity

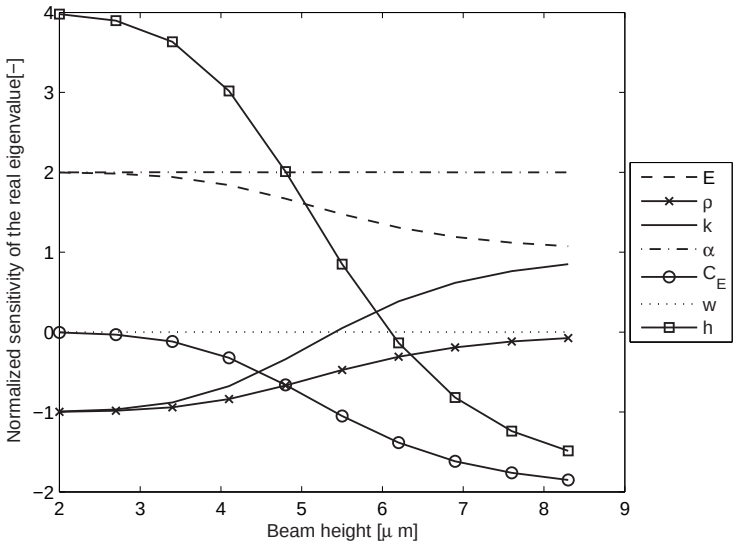

Figure 8.4: Variation of the real eigenvalue sensitivity with the beam height.

of the quality factor but also of the pulsation is never zero whatever the regime. For these reasons, the effect of the variability of Young's modulus on the quality factor is selected to illustrate the performances of the perturbation stochastic finite element method.

8.3 Material Random Variable

Young's modulus is considered as a Gaussian random variable. Its mean is equal to 158 GPa and its coefficient of variation, i.e. the ratio between the standard deviation and the mean, is set to 6 %, which is a typical value encountered in polysilicon [132]. Direct Monte-Carlo simulations are carried out in order to get a reference solution. 2000 samples are generated. Figure 8.5 represents the evolution of the mean and the variance of the quality factor with respect to the number of samples calculated. The mean of the 2000 samples of the quality factor is equal to 13035 and their coefficient of variation is equal to 7.52 %.

Table 8.4 lists the means and standard deviations of the quality factor obtained by different methods. Monte-Carlo results, denoted MC, are considered as reference solutions. First and second order perturbation stochastic finite element methods, denoted PSFEM 1st and PSFEM 2nd, are applied to study the ther-

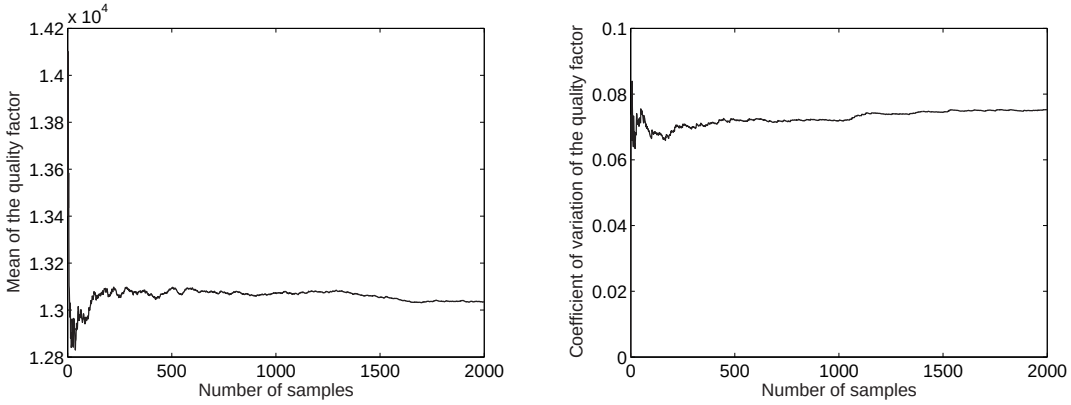

Figure 8.5: Evolution of the mean and coefficient of variation of the quality factor with the number of samples (RV:E).

moelastic quality factor of the test case. Since the determination of the second order derivative of the eigenvalue can be too computationally demanding, a second order PSFEM in terms of the quality factor but only taking into account the first order derivative of the eigenvalue in Equation (7.24), denoted PSFEM p2nd, is also investigated. The CPU times for each method are normalized with respect to the CPU time required for one deterministic finite element resolution and are presented in Table 8.4. MC simulations are a lot more CPU time costly than PSFEM and as the order of PSFEM increases, the CPU time increases. Since the approximation of the standard deviation of the quality factor is first order accurate (Equation (7.21)), the standard deviation has the same value whatever the order of the PSFEM and the relative error with respect to MC standard deviation is less than 1 %. The first order PSFEM gives a mean equal to the deterministic quality factor, i.e. 12967, while MC simulations yield a higher mean. This is due to the fact that the quality factor is a non-linear function of Young's modulus as shown in Figure 8.6(b). Moreover, due to this non-linear variation, the probability density function of the quality factor is not strictly Gaussian as shown in Figure 8.6(a). In this figure, the bars represent the distribution of the output samples obtained by MC simulations and the solid line plots the Gaussian distribution with a mean and a standard deviation equal to the values of the MC samples. The second order PSFEM approximation of the mean is really good (0.02 % relative error) and the pseudo second order PSFEM approximation has

also a good accuracy (0.026 % relative error) at a less computational effort.

Table 8.4: Comparison of mean and standard deviation of the quality factor obtained by different methods.

Method	Mean(Q) [–]	σ(Q) [–]	t^*_{CPU} [–]
MC	13035	980	2005
PSFEM 1st	12967	971	1.02
PSFEM 2nd	13037	971	1.16
PSFEM p2nd	13069	971	1.04

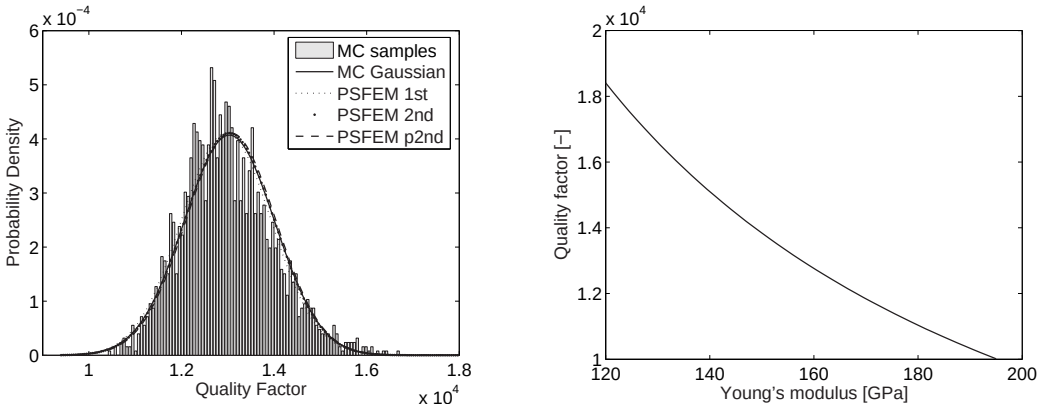

(a) (b)

Figure 8.6: (a) Probability density function of the quality factor (CoV(E)=0.06), (b) Variation of the quality factor with respect to Young's modulus.

Table 8.5 compares the means and standard deviations of the quality factor corresponding to three different coefficients of variation of Young's modulus, i.e. 6 %, 10 % and 20 %. As the coefficient of variation of Young's modulus increases, the approximations of the mean and standard deviation of the quality factor by PSFEM become less accurate. The second order PSFEM is more accurate than the pseudo-second order PSFEM at the price of a considerably larger computational effort. Figure 8.7 shows that as the coefficient of variation of Young's modulus increases, the probability density function drifts away from the Gaussian distribution and PSFEM approximations get worse.

Table 8.5: Variation of the mean and coefficient of variation of the quality factor with respect to the coefficient of variation of Young's modulus.

Method	CoV(E) [%]	Mean(Q) [−]	σ(Q) [−]	CoV(Q) [%]
MC	6	13035	980	7.52
PSFEM 1st	6	12967	971	7.49
PSFEM 2nd	6	13037	971	7.45
PSFEM p2nd	6	13069	971	7.43
MC	10	13 181	1720	13.05
PSFEM 1st	10	12967	1619	12.49
PSFEM 2nd	10	13161	1619	12.30
PSFEM p2nd	10	13250	1619	12.22
MC	20	13895	4313	31.05
PSFEM 1st	20	12967	3238	24.97
PSFEM 2nd	20	13744	3238	23.56
PSFEM p2nd	20	14099	3238	22.97

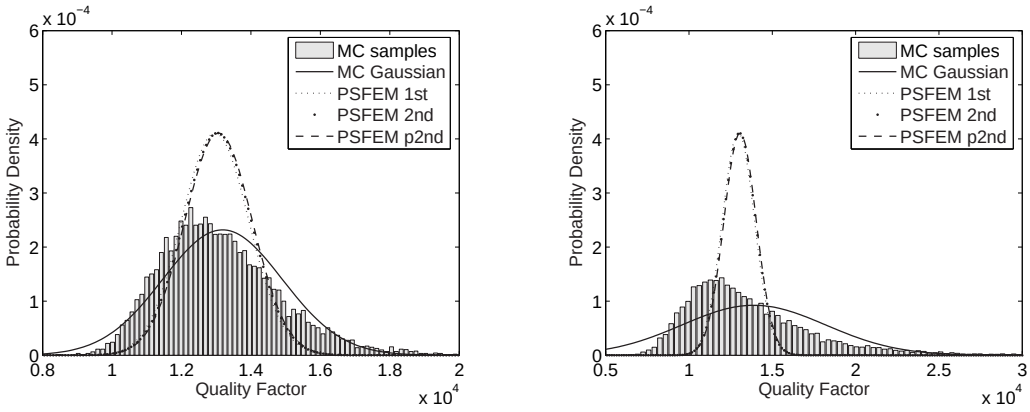

Figure 8.7: Probability density function of the quality factor (CoV(E)=10 % (a) and CoV(E)=20 % (b)).

These analyses show that the perturbation stochastic finite element method is adequate in order to determine the mean and standard deviation of the quality

factor when Young's modulus variation is small (i.e. in this application, a coefficient of variation lower than 10 %). The second order and the pseudo-second order perturbation stochastic finite element methods provide more information than the first order one. Indeed, the first order method does not take into account the variation of the mean due to the non-linear characteristic of the response with respect to the random variable. Moreover, the increase in accuracy from PSFEM p2nd to PSFEM 2nd is not sufficient to justify the increase in computational effort.

8.4 Material Random Field

In this section, the spatial variation of Young's modulus is considered by modeling it as a 1-D isotropic homogeneous Gaussian random field. Its mean and coefficient of variation are set to 158 GPa and 6 %, respectively. The aim of this section is to highlight the influence of the random field discretization method as well as its correlation data on the statistical moments of the quality factor. The correlation function is assumed to be exponential and the correlation length is set to an arbitrary value of 45 μm.

8.4.1 Random Field Discretization Method

Local Average Method

The random mesh is chosen to be the same as the finite element mesh, so that the number of random variables is equal to the number of finite elements, i.e. 50. Firstly, reference solutions are generated using Monte-Carlo simulations, following the computational steps of Figure 8.8. Random field samples $\mathbf{b}$ are generated in two basic steps:

- The covariance matrix $\mathbf{B}$ is generated using Equation (6.27).
- The uncorrelated vectors $\mathbf{c}$ with a variance equal to one, generated by a random number generator, are transformed to correlated vectors $\mathbf{b}$ using the Cholesky factorization of the covariance matrix $\mathbf{B} = \mathbf{L}\mathbf{L}^T$:

$$\mathbf{b} = \mathbf{L}\mathbf{c}. \tag{8.2}$$

Young's modulus value of element i is the ith components of vector $\mathbf{b}$. 10000 random field samples are generated and 10000 deterministic finite element analyses are carried out resulting in 10000 quality factor samples. Figure 8.9 represents the evolution of the mean and the standard deviation of the quality factor with respect to the number of samples calculated. The mean of the 10000 samples of the quality factor is equal to 13022 and their coefficient of variation is equal to 5.47 %.

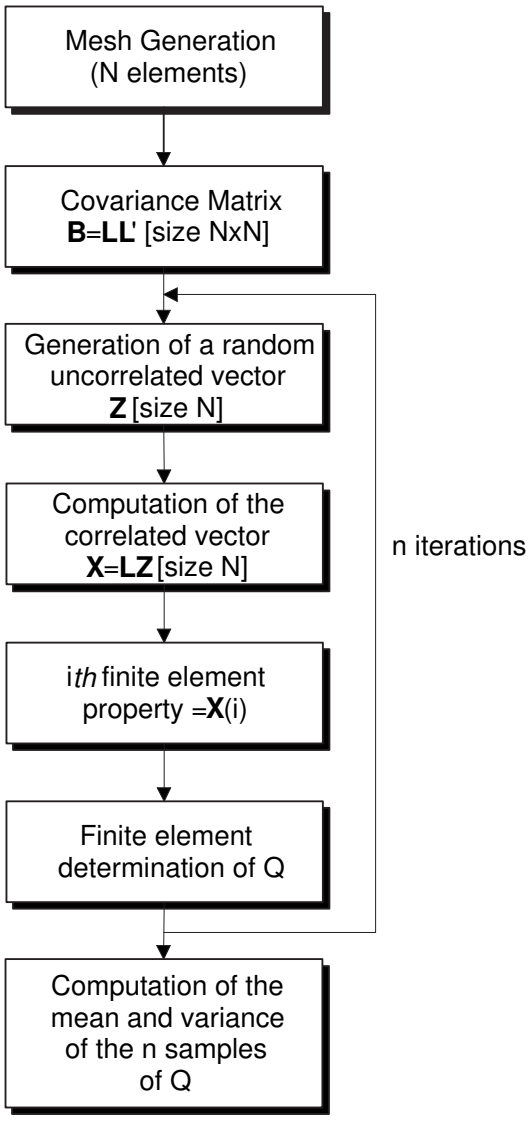

Figure 8.8: Monte-Carlo steps with a Local Average discretization of the random field.

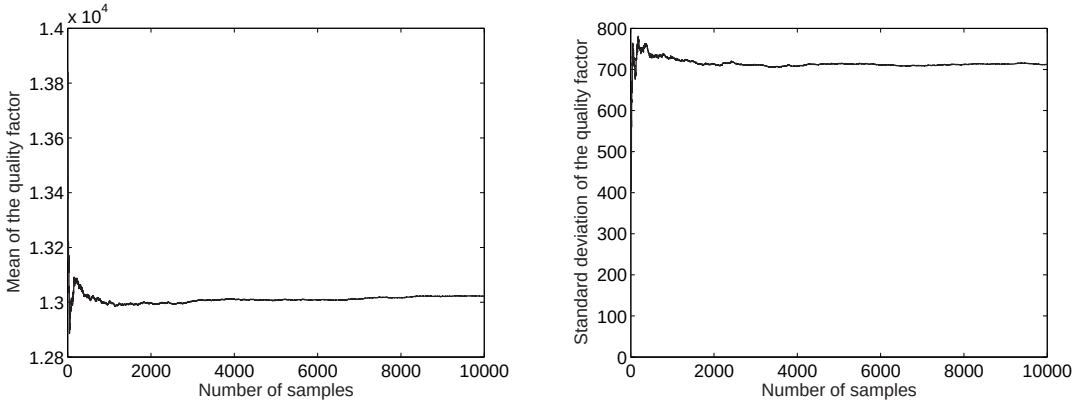

Figure 8.9: Evolution of the mean and standard deviation of the quality factor with the number of samples (RF:E, $\ell_c = 45\ \mu m$, LA Cholesky factorization).

As explained in Section 7.5.1, the perturbation stochastic finite element method can be applied in conjunction with the local average discretization of the random field. Table 8.6 compares Monte-Carlo results with first, pseudo-second and second order PSFEM results. The pseudo-second and second order PSFEM give results close to the MC ones. The CPU times required for each method are also listed in Table 8.6. The CPU times are normalized with respect to the CPU time required for one deterministic finite element resolution. Hence, MC simulations are 10500 times longer than one deterministic finite element resolution, while the most expensive PSFEM is only 20 times longer. Compared to the first order PSFEM, the 2nd order PSFEM is nearly 20 times slower. The increase in CPU time is mainly due to the fact that $n(n+1)/2$ second order derivatives of the eigenvalue $\lambda_{,ij}$ have to be determined ($i = 1, \ldots, 50$ and $j = 1, \ldots, i$). One way to reduce the CPU time is to transform the random variables into uncorrelated variables as explained in Section 7.7. The results obtained using the decorrelation procedure (noted PSFEM d2nd) are the same as for the classic PSFEM but thanks to the decorrelation procedure, the CPU time is reduced by 15 %. Figure 8.10 compares the CPU time with and without decorrelation of the random variables as a function of the number of random variables. As the number of random variables increases, the CPU time becomes larger and the CPU time saved using a decorrelation procedure increases.

Table 8.6: Comparison of mean and standard deviation of the quality factor obtained by different methods (RF:E, $\ell_c = 45\ \mu m$, LA).

Method	Mean(Q) [–]	σ(Q) [–]	t^*_{CPU} [–]
MC LA Chol	13022	712	10500
PSFEM 1st	12967	706	1.25
PSFEM 2nd	13010	706	20.24
PSFEM p2nd	13021	706	1.27
PSFEM d2nd	13010	706	17.54

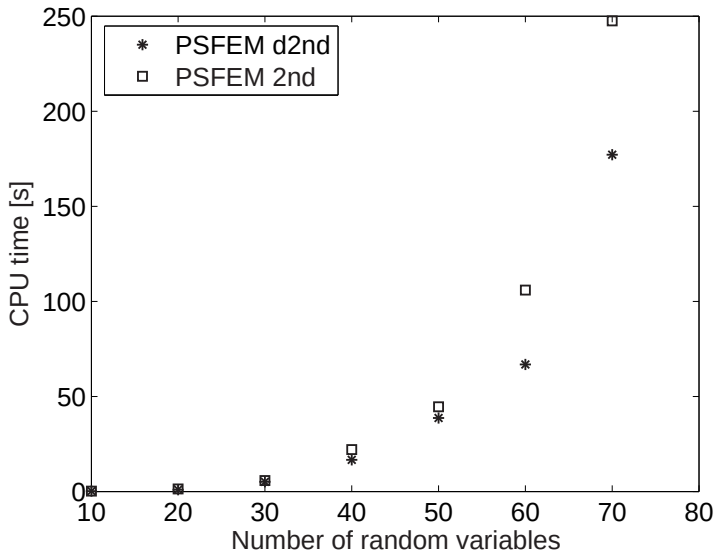

Figure 8.10: Variation of the CPU time for the standard and decorrelated 2nd order PSFEM with respect to the number of random variables.

Karhunen-Loeve Expansion Method

The Karhunen-Loeve expansion method is used to discretize the random field, so that the number of random variables is equal to the expansion order. In order to chose the adequate expansion order, the mean over the domain of the variance point-wise error due to the truncation is plotted as a function of the expansion order (Figure 8.11). The higher the expansion order, the lower the error but

also the larger the number of random variables. A compromise has to be found between the accuracy and the computational cost. An expansion order of 10 is chosen as the corresponding error is relatively small (i.e. less than 5 %) and it is an easily manageable number of random variables.

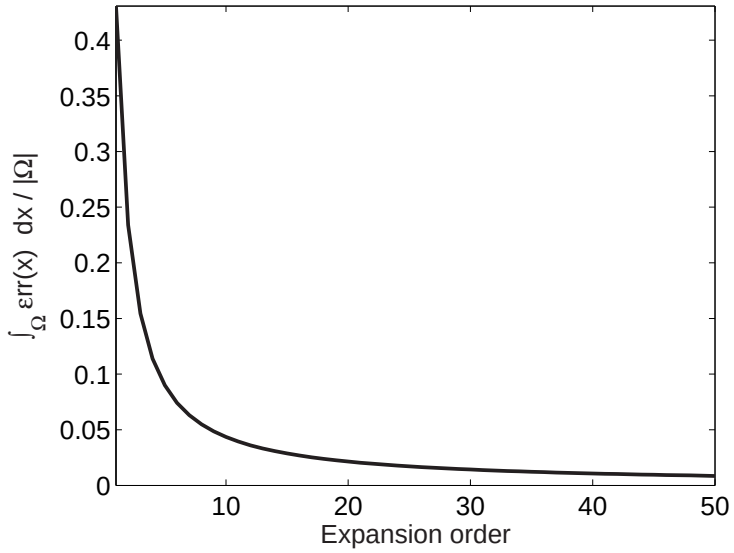

Figure 8.11: Variation of the mean over the domain of the variance point-wise error due to the truncation.

Firstly, Monte-Carlo simulations are carried out, following the computational steps of Figure 8.12. The generated random fields are continuous, so that inside each finite element, Young's modulus varies. However, for the sake of simplicity in the finite element analysis, Young's modulus is considered as constant in each finite element and is set to the value of the random field at the middle point of the element. Figure 8.13 represents the evolution of the mean and the standard deviation of the quality factor with respect to the number of samples calculated. The mean of 10000 samples of the quality factor is equal to 12989 and their standard deviation is equal to 711.

As explained in Section 7.5.2, the perturbation stochastic finite element method can be applied in conjunction with the Karhunen-Loeve expansion of the random field. The sensitivity matrices with respect to the random variables have to be computed as exposed for the mass matrix (Equation (7.62)). Appendix A gives the expression of these matrices for thermoelastic beam finite elements. Ta-

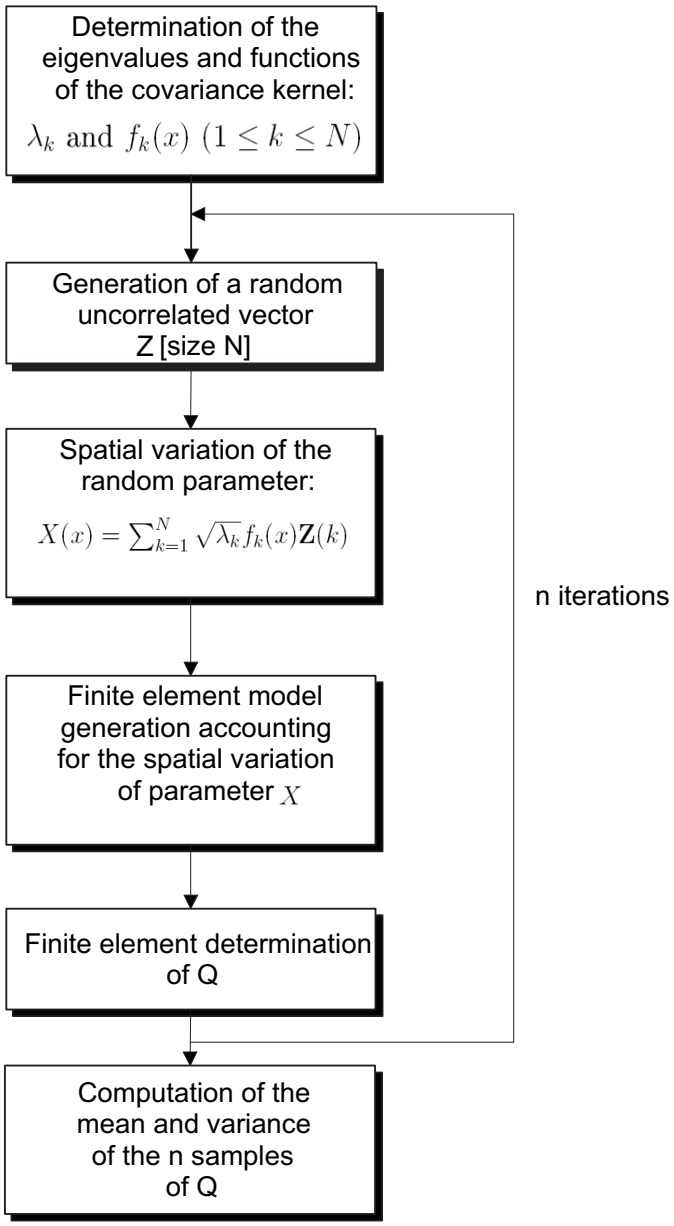

Figure 8.12: Monte-Carlo steps with a Karhunen-Loeve expansion of the random field.

ble 8.7 compares Monte-Carlo results with first, pseudo-second and second order PSFEM results. The results are similar to those obtained using the local average discretization (Table 8.6). However, the CPU time for the second order PSFEM is largely lower when using the Karhunen-Loeve expansion than the local average method. This lower required CPU time can be explained by two advantages of

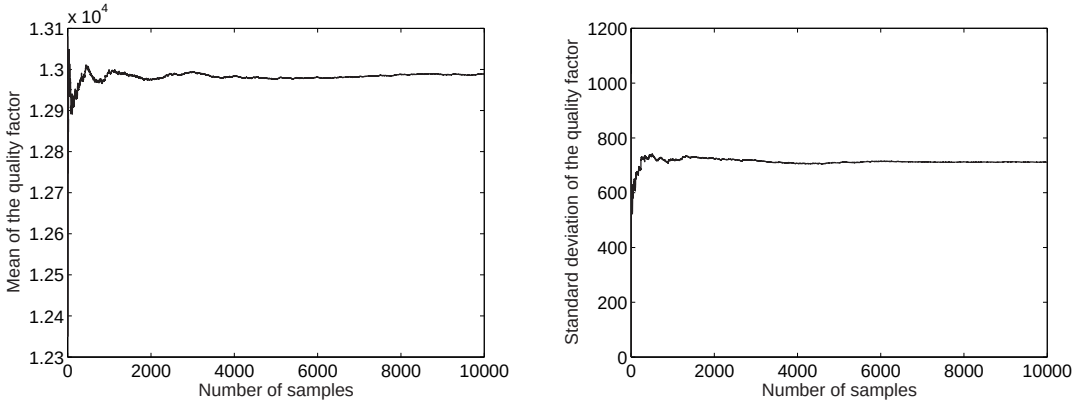

Figure 8.13: Evolution of the mean and standard deviation of the quality factor with the number of samples (RF:E, $\ell_c = 45\ \mu m$, KL).

the Karhunen-Loeve expansion. Firstly, the number of random variables is lower than for the local average method, i.e. in this case, $n_{KL} = 10$ and $n_{LA} = 50$. Secondly, the random variables associated with the Karhunen-Loeve expansion are uncorrelated.

Table 8.7: Comparison of mean and standard deviation of the quality factor obtained by different methods (RF:E, $\ell_c = 45\ \mu m$, KL).

Method	Mean(Q) [−]	σ(Q) [−]	t^*_{CPU} [−]
MC	12989	711	10600
PSFEM 1st	12967	706	1.18
PSFEM 2nd	13008	706	1.44
PSFEM p2nd	13020	706	1.21

8.4.2 Effect of the Correlation Data

In order to investigate the influence of the correlation length of the random field on the response statistics, the pseudo-second order PSFEM is used to calculate the quality factor of structures whose Young's modulus is a random field for different correlation length values. In these simulations, the random field is modeled using

the local average method since it easily allows different correlation functions to be taken into account. Figure 8.14 shows the influence of the correlation length on the mean and variation of the quality factor. As the correlation length decreases, the mean and the variance decrease. For high correlation length, the mean and variance values tend to the values obtained by considering Young's modulus as a random variable, i.e. as being spatially uniform. The reduction of the variance due to the fact that the random parameter is modeled by a random field instead of a random variable is also called the compensation effect on the variability.

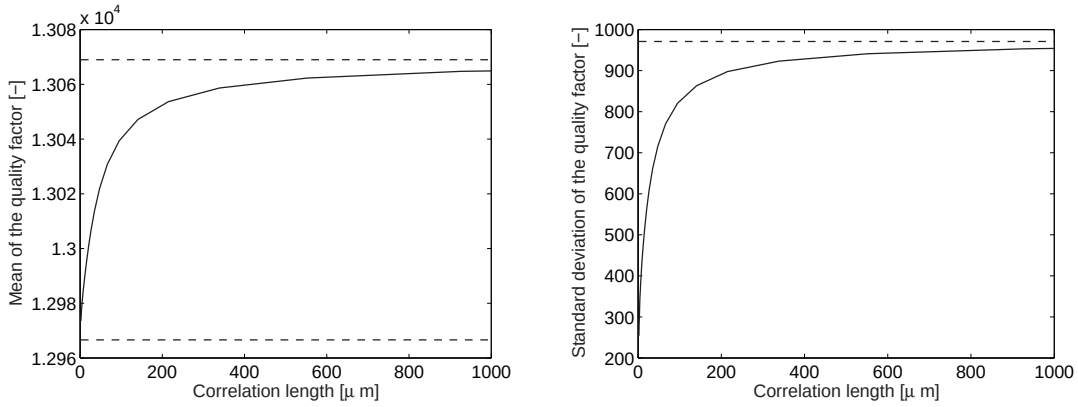

Figure 8.14: Influence of the correlation length on the mean and standard deviation of the quality factor (RF:E, LA PSFEM p2nd).

Figure 8.15 studies the influence of the correlation function on the mean and variance of the quality factor. The exponential, triangular, squared exponential and autoregressive correlation functions are compared. For each of these functions, the statistics of the quality factor is calculated as a function of the fluctuation scale. The relative difference in the variance can reach a value of 10 % depending on the correlation function.

8.4.3 Random Basis Truncation

As exposed in Section 7.8, the random basis can be truncated in order to reduce the computational effort. However, this truncation induces an error. The truncation error on the variance of the random field can be easily estimated using Equation (7.92) but the error induced on the response statistics has to be investigated through numerical applications.

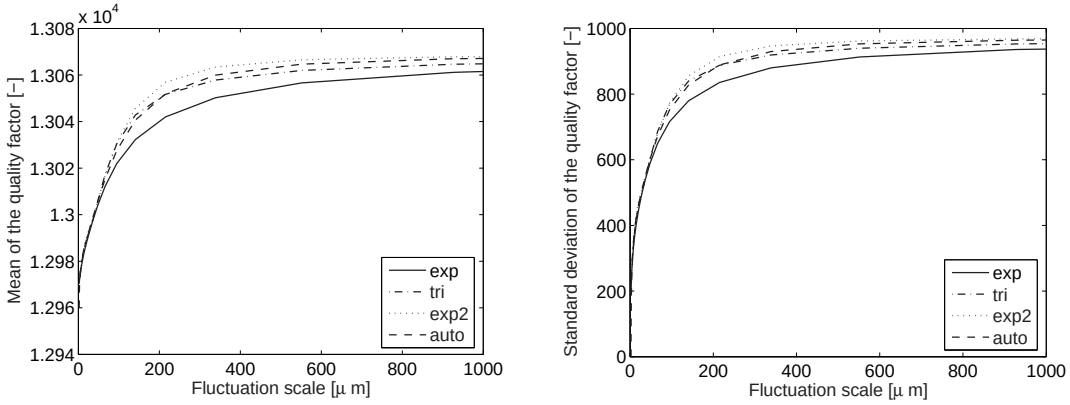

Figure 8.15: Influence of the correlation function type on the mean and standard deviation of the quality factor (RF:E, LA PSFEM p2nd).

Firstly, the statistics of the quality factor are studied using the second order perturbation stochastic finite element method with a Karhunen-Loeve expansion of Young's modulus. Figure 8.16 shows the variation of the mean and standard deviation of the quality factor as the expansion order increases. While the standard deviation is a monotonically increasing function of the expansion order, the mean shows a decreasing behavior when the expansion order goes from 2 to 4. This is due to the contribution of the second order sensitivity of the eigenvalues. Indeed, if a pseudo-second order PSFEM is used, the mean is a monotonically increasing function of the expansion order (Figure 8.17). For the variance and the mean obtained by the pseudo-second order PSFEM, the contribution of expansion terms of order larger than 10 is negligible. However, the terms of order higher than 10 have a noticeable contribution on the mean obtained by a complete second order approximation (Figure 8.16(a)).

Figure 8.18 shows the variation of $\overline{\epsilon rr}$ as a function of the expansion order for different correlation lengths, where $\overline{\epsilon rr}$ is the average over the domain of the random field variance truncation error given by Equation (7.92). As the correlation length decreases, the required expansion order to reach a given level of accuracy increases. This illustrates the so-called spectral convergence phenomenon. For example, the spectral convergence also governs the convergence of the modal expansion in mechanics, where the required number of modes depends on the frequency content of the excitation. Figure 8.19 shows the relative contri-

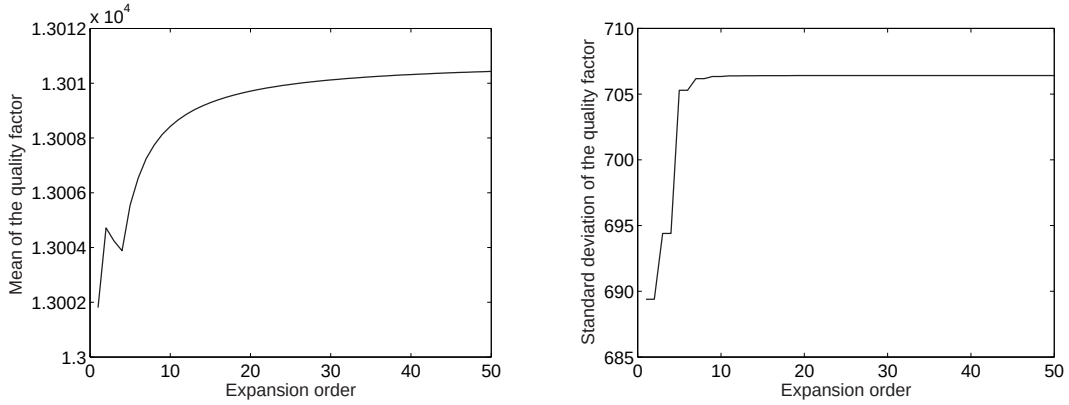

(a) (b)

Figure 8.16: Influence of the expansion order on the mean and standard deviation of the quality factor (RF:E, KL PSFEM 2nd).

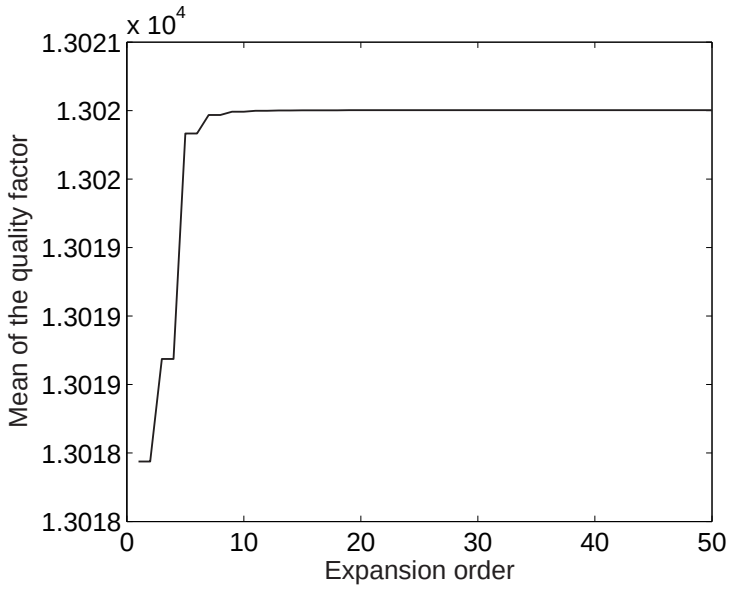

Figure 8.17: Influence of the expansion order on the mean of the quality factor (RF:E, KL PSFEM p2nd).

bution of the first r expansion terms on the first two statistical moments of the quality factor for different correlation lengths. Whatever the correlation length, the standard deviation of Q is a monotonically increasing function of the expansion order and the mean is an increasing function except for expansion orders from 2 to 4. As for the variance of the random field, the required number of

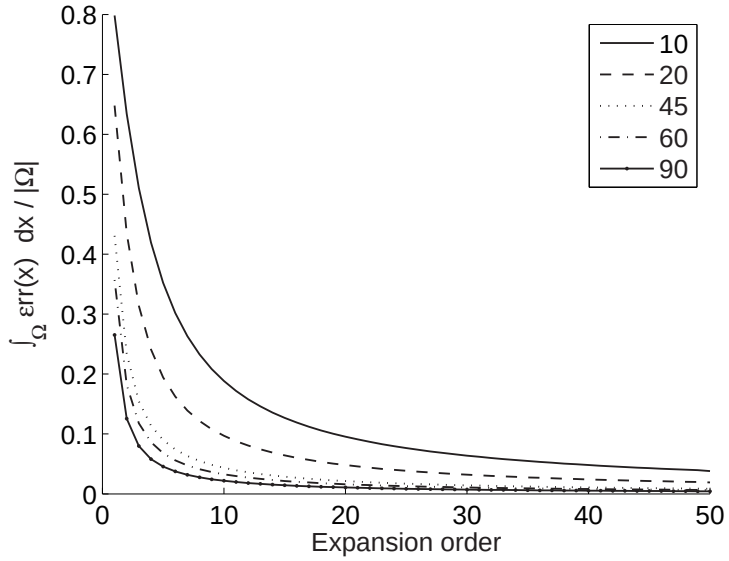

Figure 8.18: Variation of the mean over the domain of the random field variance truncation error for different correlation lengths.

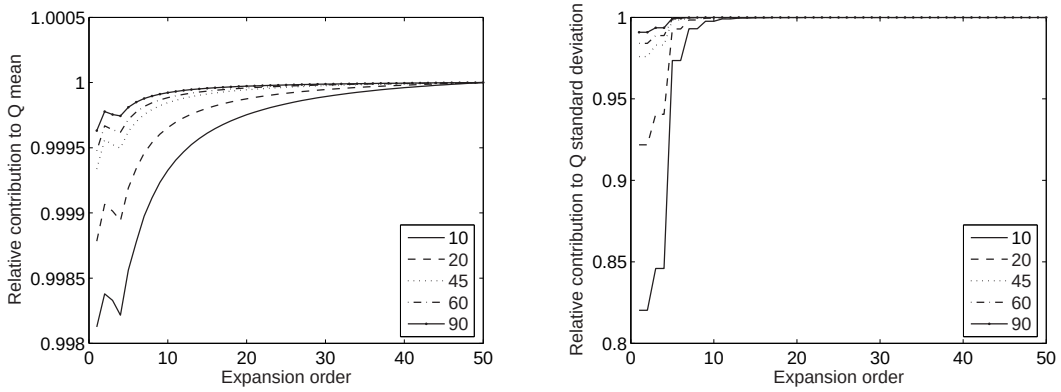

Figure 8.19: Influence of the expansion order on the mean and standard deviation of the quality factor for different correlation length (RF:E, KL PSFEM 2nd).

the expansion terms to reach a given level of accuracy becomes larger when the correlation length is smaller.

Using the decorrelation procedure when the random field is modeled by the local average method allows the expression of the random field as a series expansion, so that the number of random variables can be reduced by truncation. The error due to the truncation of the expansion to order r is directly related

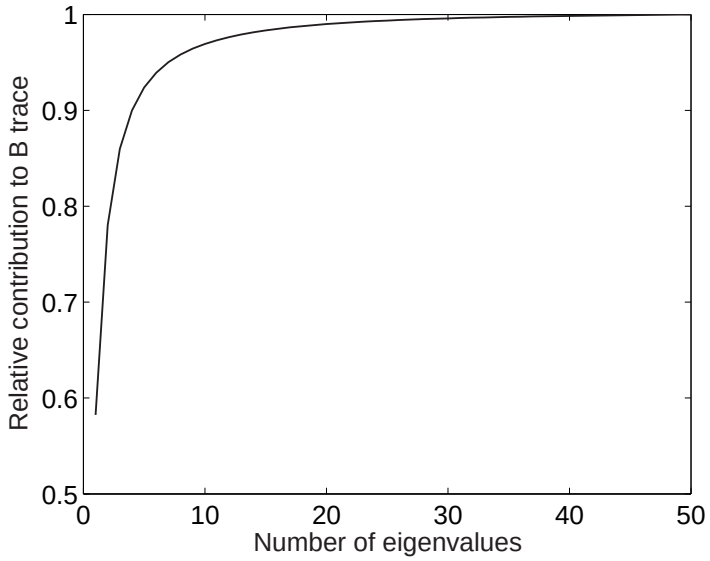

Figure 8.20: Relative contribution of the r first eigenvalues to $\mathbf{B}$ trace (RF:E, LA).

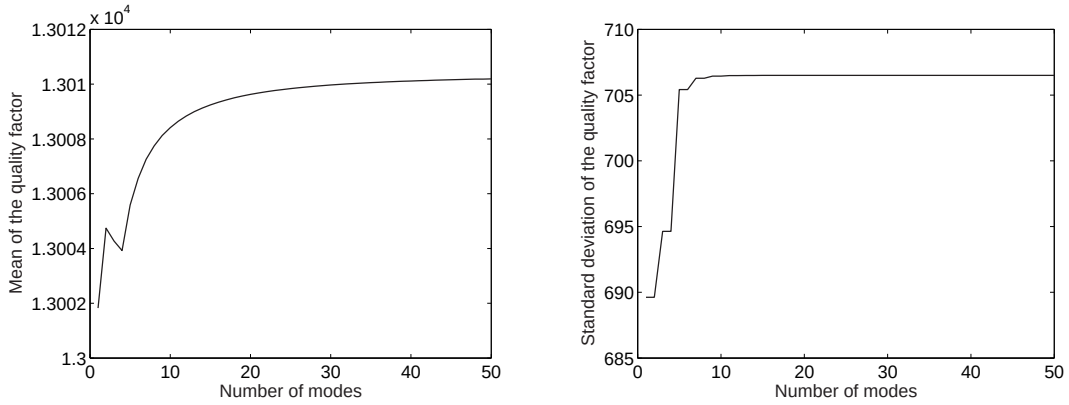

Figure 8.21: Influence of the number of modes on the mean and standard deviation of the quality factor (RF:E, LA PSFEM d2nd).

to the contribution of the first r eigenvalues (sorted in descending order) of the covariance matrix to its trace, see Figure 8.20. Figure 8.21 shows the influence of the expansion order on the mean and standard deviation of the quality factor. The curves are similar to those obtained with the Karhunen-Loeve expansion of the random field (Figure 8.16).

These numerical applications show that the required number of random vari-

ables depends on the correlation length but also on the order of the perturbation stochastic finite element method. Therefore, the expansion order can be based on the study of the random field truncation error but this has to be done carefully since a small error on the random field does not warranty a small error on the response statistic moments. In practice, the number of random variables is chosen after the study of the random field truncation error and this choice is validated by checking that increasing the number of random variables does not significantly influence the response statistics.

8.4.4 Variability Response Function

As observed previously, the correlation characteristics have an influence on the response statistics. In order to get a free-distribution upper bound of the response variance, the variability response function can be calculated. The variability response function is plotted in Figure 8.22. The VRF is a non-negative function of κ possessing the following symmetry:

$$VRF(\kappa) = VRF(-\kappa), \tag{8.3}$$

as given by Equation (7.75). The variability response function behaves similarly to the frequency response function in linear random vibration analyses. For example, knowing the form of the power spectral density function of the exponential correlation function for a given correlation length (Figure 8.23), the analysis of Figure 8.22 allows the explanation of the evolution of the response variance with the expansion order (Figures 8.21(b) and 8.16(b)). Each peak on Figure 8.22 represents an eigenmode of the covariance contributing to the response variance (analogous to resonating mode in mechanical vibrations) and each drop to zero corresponds to an eigenmode that does not contribute to the response variance (analogous to antiresonating mode in mechanical vibrations). Due to the form of the spectral density function, the higher modes have less importance than the lower ones. From the VRF, after a contributing mode, there is always a non-contributing mode. This phenomenon is illustrated in Figures 8.21(b) and 8.16(b), where modes with an even number do not contribute to the response variance while modes with an odd number does. It is also shown on these figures that mode 5 is more significant in the response variance than mode 3 conformingly to the peak height of the VRF. Due to the evolution of the form of the

spectral density function, when the correlation length increases, the importance of higher order modes decreases, so that the lower the correlation length, the higher the number of contributing modes to reach a given level of accuracy. This is in agreement with the curves plotted in Figure 8.19(b).

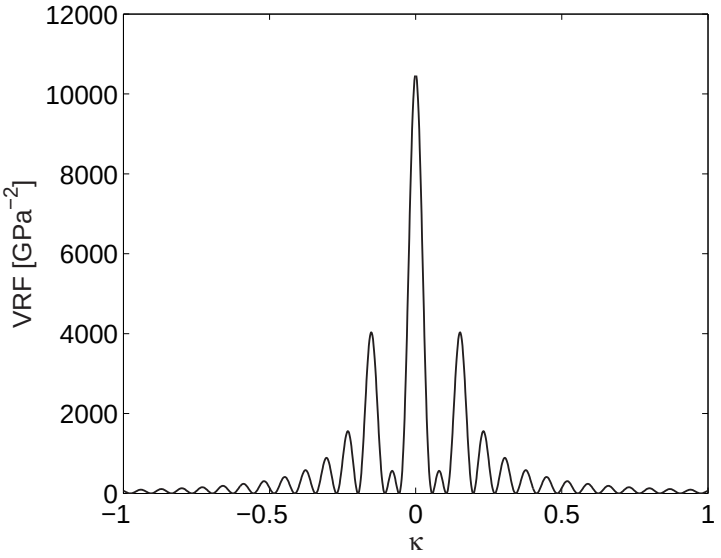

Figure 8.22: Variability response function of the quality factor.

From the maximum value of the VRF (Equation (7.69)), the upper bound of the standard deviation can be obtained, i.e. 969 in this case. Whatever the correlation length and correlation function, this upper bound has the same value. Note that this upper bound is close to the value of the standard variation of the quality factor when Young's modulus is considered as a random variable, i.e. 971.

8.5 Geometric Random Variable

The length, which is the only non-pseudo-geometric variable in this application, is considered as a random variable. It is modeled as a Gaussian random variable with a mean of 90 μm and a coefficient of variation of 5 %. 10000 Monte-Carlo samples are generated, which gives a mean of 13 008 and a standard deviation of 636 for the quality factor (Figure 8.24).

In order to use the perturbation stochastic finite element method, the sensitivity with respect to the length of the structural matrices has to be determined.

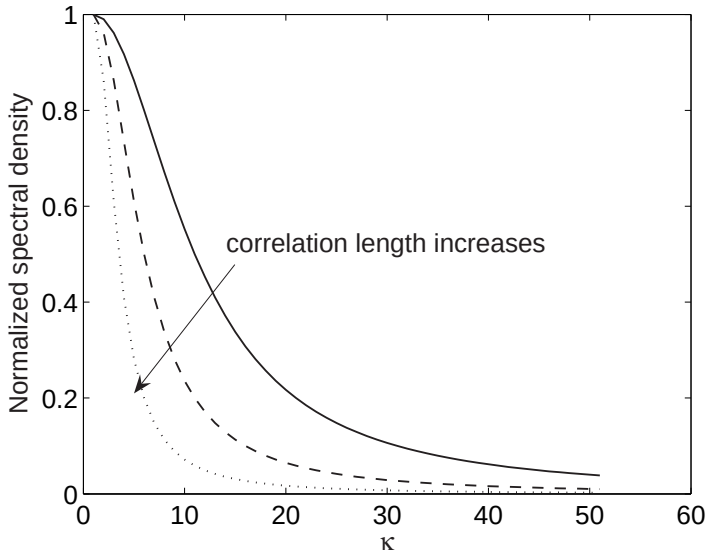

Figure 8.23: Variation of the form of the exponential power spectral density function with the correlation length.

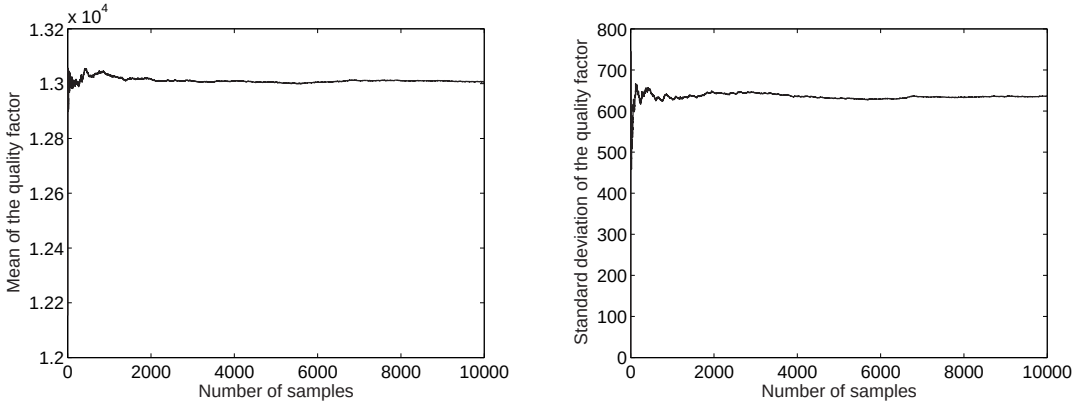

Figure 8.24: Evolution of the mean and standard deviation of the quality factor with the number of samples (RV: length).

The velocity field is easily identified in this case:

$$x_{\Delta L} = x + v_x \Delta L, \tag{8.4}$$

where the velocity v_x is given by $\frac{x}{L}$. The second order PSFEM gives a mean of 13076 and a standard variation of 637 for the quality factor, which is similar to Monte-Carlo results.

8.6 Concluding Remarks

Through the application of the perturbation stochastic finite element method on the determination of the first two statistical moments of the quality factor, it is shown in this chapter that this method is adequate for a low variability of the random parameter, e.g. a coefficient of variance less than 10 % for Young's modulus, which is typically the kind of variation observed in MEMS.

These analyses also show that the pseudo-second order PSFEM gives excellent approximations for a considerable lower CPU time than the second order one. When applying a random basis truncation, it is shown that this procedure does not only affect the random field variance but also the response variance and mean. Indeed, the minimum required random basis for a certain level of accuracy depends on the random field and its influence length as well as on the PSFEM order. In practice, the number of random variables is based on the study of the random field truncation error and this choice is validated by checking that increasing the number of random variables does not significantly influence the response statistics.

Using a random field model for Young's modulus shows the effect of compensation that occurs when a random variable is replaced by a random field. Moreover, the influence of the correlation data (influence length and correlation function) on the response statistics is not negligible, requiring accurate estimations or measurements of these data. Therefore, when no experimental correlation data are available, an upper bound of the response variance can be obtained by modeling the random parameter as a random variable or using the variability response function.

Due to its advantage in terms of CPU time over Monte-Carlo simulations, the perturbation stochastic finite element method is well suited for the study of complex cases such as the Vibrating Inertial Accelerometer developed at ONERA. Carrying out a stochastic finite element analysis allows the prediction of the performance range of the device by providing confidence intervals for its quality factor or its resonant frequency.

Chapter 9

Introduction to a Stochastic Micro-meso-macro Approach

The objective of this chapter is to pave the way to the definition of the stochastic macroscale variation of the structure properties on the basis of material properties at the microscale. It gives an overview rather than a detailed analysis, which is out of the scope of the present work.

9.1 General Methodology

The aim of the micro-meso-macro approach is to characterize the random field properties used in the stochastic macro-model via a stochastic micromechanical model of the continuum as proposed in the work of Ostoja-Starzewski [114, 115] and Huyse [70]. This approach is based on three scales: the microstructure scale d (i.e. the characteristic size of a grain, a fibre, a crystal,...), the mesoscale Lm (i.e. the characteristic length of the finite elements used to discretize the macrostructure) and the macroscale L (i.e. the characteristic length of the macrostructure). The scales satisfy the following relation:

$$d < Lm < L. \tag{9.1}$$

The methodology consists in three main steps:

- the generation of the microstructure model, which is based on the microgeometry of the heterogeneous material,

- the characterization of consistent random field properties at the mesoscale from a stochastic microstructure model using homogenization techniques,

- the determination of the response statistics using the stochastic finite element model of the macrostructure.

When using a microstructure based framework, it is required to estimate the impact of each assumption made at the microlevel on the macro-response:

- The microgeometry of a material is fully described when the shape, size and location of each constituent are defined. These data can be obtained from Transmission Electron Microscope (TEM) or Scanning Electron Microscope (SEM) images. To generate a stochastic microstructure model, the microgeometry data are to be modeled to generate samples from which the statistics of the random field are derived. For example, Voronoi model [15] can be used.

- Stochastic homogenization aims at relating the stochastic characteristics of a homogenized continuum to those of a discrete microstructure. Different homogenization techniques are distinguished according to the boundary conditions on which they rely: essential or natural boundary conditions. Techniques based on essential boundary conditions give upper bounds for the actual property, while using natural boundary conditions provide lower bounds.

Once the microstructure model and homogenization technique are selected, Monte-Carlo simulations of the microstructure, followed by subsequent homogenization allows the estimation of the mean, variance and covariance of the mesoscale properties for a given finite element mesh size. Since the homogenized properties samples can be considered as averages of the microstructure properties over the finite elements, their variance reduces as the size of the finite element increases. This variation of the variance is expressed by the variance reduction function (γ) in the Local Average method (Section 6.2.2) for homogeneous random fields. Therefore, fitting the curve of the variance variation with respect to the finite element size to an analytical expression of the variance reduction function allows the estimation of the correlation function as well as the influence length.

Finally, the required stochastic data are available to carry out a stochastic finite element analysis of the macrostructure.

9.2 1-D Application

In order to illustrate the proposed methodology, a 1-D case is considered in which Young's modulus is a stochastic variable. It aims at determining the characteristics of the random field consistent with a two-phase material microstructure with the following properties:

- the volume fraction of each phase = 50%,
- a contrast level between Young's modulus of both phases equals to $E^{(2)}/E^{(1)} = 130/170$,
- a microscale d of 200 nm.

Figure 9.1 shows a realization of a bi-phase material with a 1-D microgeometry of a total of 100 grains. It illustrates also the macroscale L and mesoscale Lm when five finite elements discretize the bar.

In order to determine the homogenized Young's modulus over a finite element, a spring network is used. The equivalent Young's modulus $E^{(e)}$ is calculated as the equivalent stiffness of a series of springs:

$$\frac{n^{(1)} + n^{(2)}}{E^{(e)}} = \frac{n^{(1)}}{E^{(1)}} + \frac{n^{(2)}}{E^{(2)}}, \tag{9.2}$$

where $n^{(1)}$ and $n^{(2)}$ are respectively the number of springs of stiffness $E^{(1)}$ and $E^{(2)}$ in the finite element.

A bar of length L equal to 90 μm is considered, which means that there are 450 grains along the length. Several mesocales Lm (i.e. lengths of the finite elements) are considered. For each mesoscale, the mean and variance of $E^{(e)}$ are computed from 500 samples of the microstructure.

Figure 9.2 shows the variation of the mean of the equivalent Young's modulus as the size of the finite elements increases. The mean of $E^{(e)}$ depends on the mesoscale for small finite elements but tends rapidly to a constant value when the mesoscale increases. Indeed, for small finite elements, the mesoscale is too

Figure 9.1: A realization of a bi-phase material with a 1-D microgeometry of a total of 100 grains (black: phase (1), $E^{(1)} = 170$ GPa; white: phase (2), $E^{(2)} = 130$ GPa).

close to the microscale so that the mean is affected by the averaging position because of the heterogeneity of the material.

Figure 9.3 shows the variation of the variance of the equivalent Young's as the finite element size increases. The variance reduction function γ can be modeled by [144]

$$\gamma(Lm) = \left(1 + \left(\frac{Lm}{\theta_F}\right)^n\right)^{-1/n}, \tag{9.3}$$

where the model parameters θ_F and n are estimated by fitting γ model (solid line in Figure 9.3) to the data obtained from Monte-Carlo samples (crosses in Figure 9.3). In this case, the model parameters are $\theta_F = 0.3\ \mu m$ and $n = 0.6$.

Therefore, the 1-D microstructure analysis provide the stochastic data required for a stochastic finite element analysis where Young's modulus random

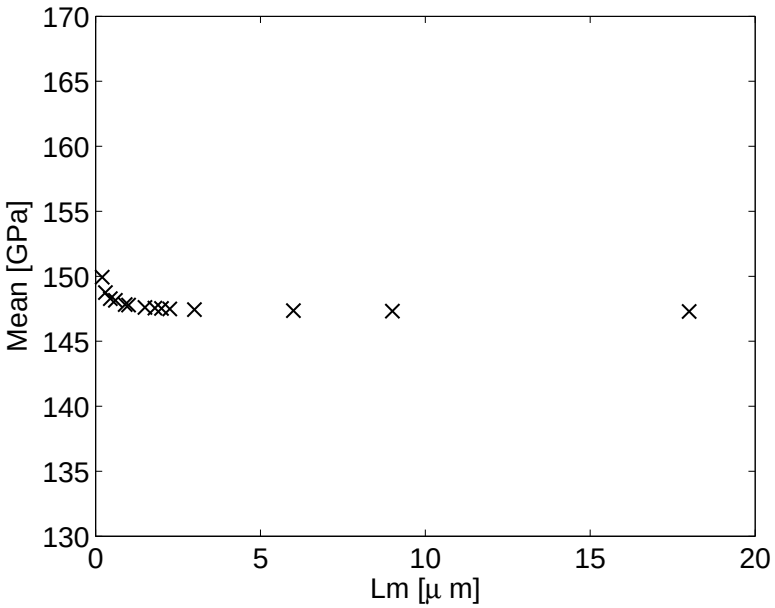

Figure 9.2: Mean of the equivalent Young's modulus as a function of the mesoscale Lm.

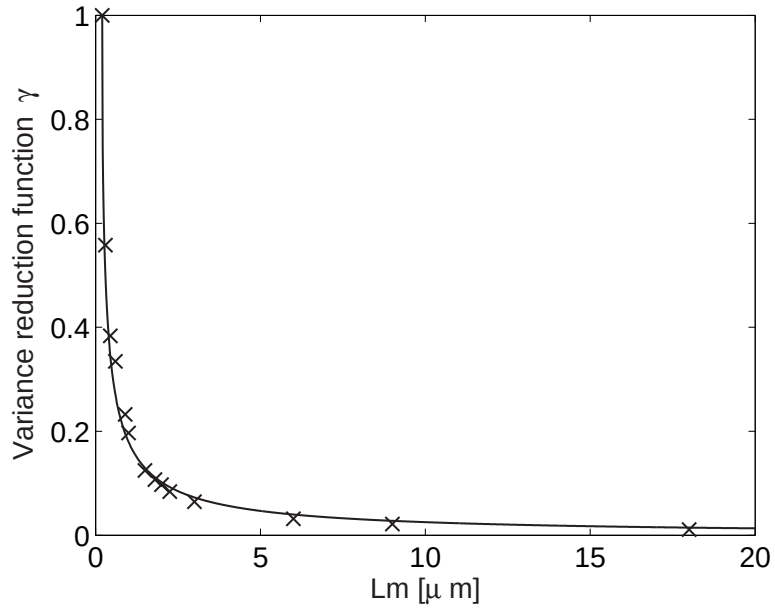

Figure 9.3: Variance reduction function of the equivalent Young's modulus.

field is discretized by the Local Average method:

- a mean of 147 GPa,
- a standard deviation of 20 GPa,
- a variation reduction function γ given by

$$\gamma(Lm) = \left(1 + \left(\frac{Lm}{0.3}\right)^{0.6}\right)^{-1/0.6}, \tag{9.4}$$

  which is used to get the covariance matrix via Equation (6.27).

9.3 Concluding Remarks

This chapter has introduced a multiscale method to model the microstructural disorder, the mesoscale finite elements and the macroscopic response. Using this micro-meso-macro approach, the spatial variation of heterogeneous properties at the mesoscale can be characterized using a microscale model and then, the stochastic finite element method can use these data to compute the macroscale variation of the structure response. The feasibility of this micro-meso-macro approach has been illustrated on a 1-D case.

Conclusion

Due to the importance of the interaction between several physical fields in MEMS design, numerical multiphysic simulations are required. In particular, the **purpose** of this work was to develop a numerical method to analyze the influence of random variations of geometric and material properties on the thermoelastic quality factor of micro-resonators. The dissertation was divided into two main research tasks: the development of a computational framework to determine the thermoelastic quality factor of micro-resonators, and the modeling of uncertainty. The specific conclusions associated with each of these two parts are drawn hereafter.

Thermoelastic Quality Factor Determination

Since existing analytical models are limited to simple cases due to their restrictive assumptions, a numerical method has been developed in order to study real 3-D structures. The development of the computational framework relies on several **strategic choices** and **personal contributions**:

- The finite element method has been chosen to discretize the mechanical, thermal and electric fields. A unified variational principle describing the fundamental equations of thermopiezoelectricity has lead to the *thermopiezoelectric finite element formulation*. Bar and beam finite elements have been developed in order to validate the methodology after comparing finite element and analytical results. 2-D and 3-D finite elements have also been implemented for the purpose of the analysis of real micro-structures.

- The quality factor is determined from the complex frequency obtained by a modal analysis of the thermopiezoelectric system. The discretized dynamic

equilibrium equation governing the thermopiezoelectric problem has been transformed into a *real generalized non-symmetric eigenproblem* using a state-space formulation and eliminating the time derivatives of the electric and thermal degrees of freedom, which are massless artificial variables.

- In order to solve large-scale eigenproblems that are inherent to finite element analyses, an iterative method has to be used. Due to the presence of conjugate eigenvalues, a block Lanczos method has been selected. A *non-symmetric real block Lanczos method* has been developed based on the approximation of the complex eigenvalues and eigenvectors of a real non-symmetric matrix by the complex eigensolutions of the real non-symmetric tridiagonal matrix of the Lanczos coefficients. This extension of the classic Lanczos method is particulary efficient to solve real non-symmetric eigenproblems since using real vectors subspaces, the iterative algebraic operations are real.

The application of the finite element method to different test cases makes possible the determination of the quality factor of these structures, and it allows a better understanding of the phenomena occurring in thermopiezoelectric vibrations. Due to the strong interaction between the thermal, electric and mechanical fields, the influence of a parameter on the multiphysic behavior of a MEMS is not straightforward. The effects of residual stress and non-perfect clamping conditions, which are well known for purely mechanical vibrations, have been studied for thermoelastic vibrations.

All the exposed developments have been implemented in `Oofelie`, an object oriented finite element software commercially available. Thanks to this software integration, the proposed methodology has been successfully applied on complex cases provided by ONERA. In the interesting case of the Vibrating Inertial Accelerometer, finite element analyses have shown the importance of the influence of the gold electrodes on the quality factor and the effect of piezoelectric actuation on the resonant frequency. Therefore, compared to experiments, a thermopiezoelectric finite element analysis taking into account the gold electrodes gives similar results in terms of the quality factor and the resonant frequency, but has also permitted a more *in-depth understanding of the involved phenomena.*

In **conclusion**, thanks to the developed finite element approach, the different factors that influence the behavior of the micro-resonator can be identified, so that the physical phenomena are better understood and the design of the micro-resonator can be modified in order to improve its quality factor and hence, its performances.

Uncertainty Modeling

Micro-resonators are subject to inevitable and inherent uncertainty in geometric and material parameters, that lead to variability in their performances and in particular, in their quality factor. Due to the small dimensions and high feature complexity, manufacturing processes leave substantial variability in the shape and geometry of the device, while the material properties of a component are inherently subject to scattering. The stochastic finite element method has been selected to study the uncertainty effect on the quality factor of micro-structures.

The **originality** of this work is the application of the stochastic finite element method to the analysis of strongly coupled multiphysic phenomena. From existing stochastic finite element methods, the *Perturbation Stochastic Finite Element Method* has been selected as the most adequate method to study the thermoelastic quality factor. This method consists in a deterministic analysis complemented by a sensitivity analysis with respect to the random parameters. **Personal developments** were carried out for its extension to the thermoelastic quality factor study:

- From the second order Taylor series expansion of the *stochastic thermopiezoelectric finite element eigenproblem*, the zeroth, first and second order equations in the eigenpairs are obtained. While the zeroth order equation allows the determination of the eigenpair mean, the first and second order derivatives of the eigenpair cannot be obtained through the resolution of the first and second order equations.

- The second order Taylor series expansion is performed on the *quality factor* expression in order to relate its *mean and variance* to the zeroth, first and second order derivatives of the eigenvalues, and to the mean, variance and correlation structure of the random parameters. Moreover, a pseudo-second

order expression of the quality factor mean and variance has been derived, in which the second order derivatives of the eigenvalues do not appear.

- An efficient method to compute the *first and second order sensitivities of the eigenpair of a non-symmetric damped problem* has been developed based on Choi's method [31].

The *random field* concept has been used to take into account the spatial variability of material and pseudo-geometric parameters. The *Local Average* and *Karhunen-Loeve expansion* methods have been chosen as random field discretization methods. Since the random field discretization involves a quite large number of random variables, a *decorrelation procedure* and a *random basis truncation procedure* have been proposed to enhance the performance of the Perturbation Stochastic Finite Element Method. The Variability Response Function has been introduced in order to get a spectral-distribution-free upper bound when the correlation data are unknown.

From the application of the developed Perturbation Stochastic Finite Element Methodology on the determination of the first two statistical moments of the quality factor, **it can be concluded** that:

- This method is adequate for a *low variability level* of the random parameter, which is typically encountered in MEMS.

- The *pseudo-second order* Perturbation Stochastic Finite Element Method gives excellent approximations for a considerable lower CPU time than the second order Perturbation Stochastic Finite Element Method.

- The *random basis truncation* does not only affect the random field variance but also the response variance and mean. Therefore, the minimum required random basis for a certain level of accuracy depends on the random field and its influence length as well as on the order of the Perturbation Stochastic Finite Element Method.

- A *compensation effect* occurs when a random variable is replaced by a random field.

- The *influence of the correlation data* (i.e. influence length and correlation

function) is not negligible, so that accurate estimations or measurements of these data are required.

- An *upper bound* of the response variance can be obtained by modeling the random parameter as a random variable or using the Variability Response Function.

- The study of the Variability Response Function coupled to the analysis of the spectral density function allows the identification of the influence of the covariance eigenfunctions on the response variance.

The stochastic methodology has been applied to one-dimensional analyses, but it could be easily applied to 2-D and 3-D cases. Therefore, using the proposed Stochastic Finite Element Method, a numerical method is available to quantify the influence of uncertain geometric and material property variations on the thermoelastic quality factor of micro-resonators.

Perspective and Closure

Any stochastic simulation method requires information on the stochastic properties of the input data. In this work, due to the lack of data, roughly estimated values have been used for the correlation of the uncertain parameters. The experimental determination of these stochastic data would require a large and costly measurement campaign. Alternatively, using a *micro-meso-macro approach*, the random field properties of the stochastic macro-model can be characterized via a stochastic micromechanical model of the continuum. Chapter 9 has given a general overview of the feasibility of this micro-meso-macro approach.

The proposed methodology could also find some applications in the quantification of damping in laminated and particulate composite structures. Indeed, several studies show that thermoelastic damping in this kind of composite is important [82, 95] and till now, can only be approximated using restricted analytical models. On top of that, using the stochastic approach, the effects of random imperfections could be quantified.

MEMS technology is rapidly growing. In order to improve MEMS design and performances, complex multiphysic phenomena have to be clearly identified and

understood. Extending modeling techniques available in classical mechanics to multiphysics appears as a fruitful strategy to offer new efficient numerical tools to MEMS designers.

References

[1] R. Abdolvand, G. Ho, A. Erbil, and F. Ayazi. Thermoelastic Damping in Trench-refilled Polysilicon Resonators. In *Transducers'03, the 12th International Conference on Solid State Sensors, Actuators and Microsystems*, pages 324–327, Boston, June 8-12, 2003.

[2] S. Acharjee and N. Zabaras. Uncertainty Propagation in Finite Deformations - A Spectral Stochastic Lagrangian Approach. *Computer Methods in Applied Mechanics and Engineering*, 195:2289–2312, 2006.

[3] S. Adhikari. Calculation of derivative of complex modes using classical normal modes. *Computers and Structures*, 77:625–633, 2000.

[4] S. Adhikari. Complex Modes in Stochastic Systems. *Advances in Vibration Engineering*, 3(1):1–11, 2004.

[5] S. Adhikari and M. I. Friswell. Random Eigenvalue Problems In Structural Dynamics. *45th AIAA/ASME/ASCE/AHS/ASC Structures, Structural Dynamics and Materials Conference, Palm Springs, California, USA*, April 2004.

[6] S. Adhikari and R. S. Langley. Distribution of Eigenvalues of Linear Stochastic Systems. *In A. Der-Kiureghian, Samer Madanat, and Juan M. Pestana, editors, Proceedings of the ninth International Conference on Applications of Statistics and Probability in Civil Engineering (ICASP 9), San Fransisco, California, USA, volume 1 of Applications of Statistics and Probability in Civil Engineering, Rotterdam, Netherlands, Millpress.*, pages 201–207, July 6-9, 2003.

[7] Y. Ahn and H. Guckel. Fabrication Process for High-Q Polysilicon Beam Resonators. *Sensors and Materials*, 12:143–162, 2000.

[8] M. Allen, M. Raulli, K. Maute, and D. Frangopol. Reliability-based Analysis and Design Optimization of Electrostatically Actuated MEMS. *Computers and Structures*, 82:1007–1020, 2004.

[9] G. Altay and M. Dokmeci. Fundamental Variational Equations of Discontinuous Thermopiezoelectric Fields. *International Journal of Engineering Sciences*, 34(7):769–782, 1996.

[10] E. Altus and E.M. Totry. Buckling of Stochastically Heterogeneous Beams, using a Functional Perturbation Method. *International Journal of Solids and Structures*, 40:6547–6565, 2003.

[11] S.P. Anaraki, R. Abdolvand, and F. Ayazi. A 600 kHz Electrically coupled MEMS Bandpass Filter. *IEEE MEMS'03, Kyoto, Japan*, 2003.

[12] M. Anders and M. Hori. Stochastic Finite Element Method for Elasto-plastic Body. *International Journal for Numerical Methods in Engineering*, 46:1897–1916, 1999.

[13] E. Anderson, Z. Bai, C. Bischof, S. Blackford, J. Demmel, J. Dongarra, J. Du Croz, A. Greenbaum, S. Hammarling, A. McKenney, and D. Sorensen. LAPACK User's Guide, Third Edition, SIAM. Philadelphia, 1999.

[14] M. Andrews, I. Harris, and G. Turner. A Comparison of Squeeze-film Theory with Measurements on a Microstructure. *Sensors and Actuators A: Physical*, 36, 1993.

[15] F. Aurenhammer. Voronoi Diagrams - A Survey of a Fundamental Geometric Data Structure. *ACM Computing Surveys*, 23:345–405, 1991.

[16] F. Ayazi and K. Najafi. A HARPSS Polysilicon Vibrating Ring Gyroscope. *Journal of Micromechanical Systems*, pages 169–179, 2001.

[17] Z. Bai, G. Sleijpen, and H. van der Vorst. Quadratic Eigenvalue Problems. In Z. Bai, J. Demmal, J. Dongarra, A. Ruhe, H. van der Vorst, editor,

Templates for the Solution of Algebraic Eigenvalue Problems: A practical Guide, SIAM, Philadelphia, 2000.

[18] M. Bao, H. Yang, Y. Sun, and P.J. French. Modified Reynolds' Equation and Analytical Analysis of Squeeze-film Air Damping of Perforated Structures. *Journal of Micromechanics and Microengineering*, 13:795–800, 2003.

[19] R.D. Biggar and J.M. Parpia. Magnetic Field Effects on Boron-doped Si Oscillators. *Physical Review B*, 56(21), 1997.

[20] D.S. Bindel and S. Govindjee. Elastic PMLs for Resonator Anchor Loss Simulation. *International Journal for Numerical Methods in Engineering*, 64(6):789–818, 2005.

[21] J.E. Bishop and V.K. Kinra. Thermoelastic Damping of a Laminated Beam in Flexure and Extension. *Journal of Reinforced Plastics and Composites*, 12:210–226, February 1993.

[22] F.R. Blom, S. Bouwstra, M. Elwenspoek, and J.H.J. Fluitman. Dependence of the Quality Factor of Micromachined Silicon Beam Resonators on Pressure and Geometry. *Journal of Vacuum Science and Technology B*, 10(1):19–26, 1992.

[23] J.A. Brandon. Second-order Design Sensitivities to Assess the Applicabillity of Sensitivity Analysis. *AIAA Journal*, 29(1):135–139, 1991.

[24] M.G. Burzo, P.L. Komarov, and P.E. Raad. Non-contact Thermal Conductivity Measurements of Gold Covered Natural and Isotopically-Pure Silicon and Their Respective Oxides. *5th International Conference on Thermal, Mechanical and Thermo-mechanical Simulation and Experiments in Microelectronics and Micro-systems (EUROSIME 2004), Brussels, Belgium, May 10-12*, 2004.

[25] R. Candler, M. Hopcroft, C. Low, S. Chandorkar, B. Kim, M. Varghese, A. Duwel, and T. Kenny. Impact of Slot Location on Thermoelastic Dissipation in Micromechanical Resonators. In *Transducers'05, the 13th International Conference on Solid State Sensors, Actuators and Microsystems*, pages 597–600, Seoul, Korea, June 5-9 2005.

[26] S. Chakraborty and B. Bhattacharyya. An Efficient 3D Stochastic Finite Element Method. *International Journal of Solids and Structures*, 39:2465–2475, 2002.

[27] S. Chakraborty and S.S. Dey. Stochastic Finite Element Method for Spatial Distribution of Material Properties and External Loading. *Computers and Structures*, 55(1):41–45, 1995.

[28] S. Chakraborty and S.S. Dey. Stochastic Finite Element Simulation of Random Structure on Uncertain Foundation under Random Loading. *International Journal of Mechanical Sciences*, 38(11):1209–1218, 1996.

[29] S. Chakraborty and S.S. Dey. A Stochastic Finite Element Dynamic Analysis of Structures with Uncertain Parameters. *International Journal of Mechanical Sciences*, 40(11):1071–1087, 1998.

[30] Y.-H. Cho, B.M. Kwak, A.P. Pisano, and R.T. Howe. Slide Film Damping in Laterally Driven Microstructures. *Sensors and Actuators A: Physical*, 1994.

[31] K.M. Choi, S.W. Cho, M.G. Ko, and I.W. Lee. Higher Order Eigensensitivity Analysis of Damped Systems with Repeated Eigenvalues. *Computers and Structures*, 82:63–69, 2004.

[32] K.M. Choi, H.K. Jo, W.H. Kim, and I.W. Lee. Sensitivity Analysis of Non-conservative Eigensystems. *Journal of Sound and Vibration*, 274:997–1011, 2004.

[33] M. Christen. Air and gas damping of quartz tuning forks. *Sensors and Actuators*, 4:555–564, 1983.

[34] J.V. Clark, D. Garmire, M. Last, and J. Demmel. Practical Techniques for Measuring MEMS Properties. *Technical Proceedings of the 2004 NSTI Nanotechnology Conference and Trade Show*, 1, 2001.

[35] A.N. Cleland and M.L. Roukes. Nanostructure-based Mechanical Electrometry. *Nature*, 392(160), 1998.

[36] R.L. Dailey. Eigenvector Derivatives with Repeated Eigenvalues. *AIAA Journal*, 27:486–491, 1989.

[37] B.J. Debusschere, H.N. Najm, A. Matta, O.M. Knio, and R.G. Ghanem. Protein Labeling Reactions in Electrochemical Microchannel Flow: Numerical Simulation and Uncertainty Propagation. *Physics of Fluids*, 15:2238–2250, 2003.

[38] G. Deodatis. Bounds on Response Variability of Stochastic Finite Element Systems: Effect of Statistical Dependence. *Probabilistic Engineering Mechanics*, 5:88–98, 1990.

[39] G. Deodatis and L.L. Graham. The Weighted Integral Method and the Variability Response Function as Part of a SFEM Formulation. In World Scientific, editor, *Uncertainty Modeling in Finite Element, Fatigue and Stability of Systems*, pages 71–116. A. Haldar, A. Guran and B.M. Ayyub, 1997.

[40] A. Der Kiureghian and J.B. Ke. The Stochastic Finite Element Method in Structural Reliability. *Probabilistic Engineering Mechanics*, 3(2):83–91, 1988.

[41] J.N. Ding, Y.G. Meng, and S.Z. Wen. Size Effect on the Mechanical Properties and Reliability Analysis of Microfabricated Polysilicon Thin Films. *IEEE 39th Annual International Reliability Physics Symposium, Orlando, Florida*, pages 108–111, 2001.

[42] J.N. Ding, Y.G. Meng, and S.Z. Wen. Specimen Size Effect on Mechanical Properties of Polysilicon Microcantilever Beams Measured by Deflection using a Nanoindenter. *Materials Science and Engineering B*, 83:42–47, 2001.

[43] I. Doltsinis and Z. Kang. Perturbation-based Stochastic FE Analysis and Robust Design of Inelastic Deformation Processes. *Computer Methods in Applied Mechanics and Engineering*, 195:2231–2251, 2006.

[44] A. Duwel, J. Gorman, M. Weinstein, J. Borenstein, and P. Ward. Quality Factors of MEMS Gyros and the Role of Thermoelastic Damping. In *Proceedings of the 15th International Conference on Microelectromechanical Systems (MEMS)*, pages 214–219, Las Vegas, NV, January 20-25 2002.

[45] A. Duwel, J. Gorman, M. Weinstein, J. Borenstein, and P. Ward. Experimental Study of Thermoelastic Damping in MEMS Gyros. *Sensors and Actuators A*, (103):70–75, 2003.

[46] A. Eringen. *Mechanics of Continua*. John Wiley and Sons, 1967.

[47] C. Fell, I. Hopkin, K. Townsend, and I. Sturland. A Second Generation Silicon Ring Gyroscope. *Proceedings of the DGON Symposium on Gyro Technology, Stuttgart*, 1999.

[48] G.A. Fenton. Error Evaluation of Three Random-Field Generators. *Journal of Engineering Mechanics*, 120(12):2478–2497, Dec. 1994.

[49] J. Fonseca, C. Mares, M.I. Friswell, and J.E. Mottershead. The Propagation of Parameter Uncertainty through Structural Dynamics Models. *21st International Modal Analysis Conference, Orlando, Florida, USA*, February 2003.

[50] R.L. Fox and M.P. Kapoor. Rates of Change of Eigenvalues and Eigenvectors. *AIAA Journal*, 6(12):2426–2429, 1968.

[51] S. Garg. Derivative of Eigensolutions for a General Matrix. *AIAA Journal*, 11(8):1191–1194, 1973.

[52] M. Geradin and D. Rixen. *Mechanical Vibrations - Theory and Application to Structural Dynamics*. John Willey and Sons, 1994.

[53] R. Ghanem. Probabilistic Characterization of Transport in Heterogeneous Porous Media. *Computer Methods in Applied Mechanics and Engineering*, 158:199–220, 1998.

[54] R. Ghanem. Higher Order Sensitivity of Heat Conduction Problems to Random Data using the Spectral Stochastic Finite Element Method. *ASME Journal of Heat Transfer*, 121:290–299, 1999.

[55] R. Ghanem. Ingredients for a General Purpose Stochastic Finite Elements Implementation. *Computer Methods in Applied Mechanics and Engineering*, 168:19–34, 1999.

[56] R. Ghanem and A. Sarkar. Mid-frequency Structural Dynamics with Parameter Uncertainty. *Computer Methods in Applied Mechanics and Engineering*, 191:5499–5513, 2002.

[57] R.G. Ghanem and R.M. Kruger. Numerical Solution of Spectral Stochastic Finite Element Systems. *Computer Methods in Applied Mechanics and Engineering*, 129:289–303, 1996.

[58] R.G. Ghanem and P.D. Spanos. *Stochastic Finite Elements: A Spectral Approach*. Springer, Berlin, 1991.

[59] J.P. Gorman. Finite Element Model of Thermoelastic Damping in MEMS. Master's thesis, Massachusetts Institute of Technology, June 2002.

[60] L.L. Graham and G. Deodatis. Variability Response Functions for Stochastic Plate Bending Problems. *Structural Safety*, 20:167–188, 1998.

[61] L.L. Graham and G. Deodatis. Response and Eigenvalue Analysis of Stochastic Finite Element Systems with Multiple Correlated Material and Geometric Properties. *Probabilistic Engineering Mechanics*, 16:11–29, 2001.

[62] F.L. Guo and G.A. Rogerson. Thermoelastic Coupling Effect on a Micromachined Beam Resonator. *Mechanics Research Communications*, 30:513–518, 2003.

[63] Z. Hao, A. Erbil, and F. Ayazi. An Analytical Model for Support Loss in Micromachined Beam Resonators with In-plane Flexural Vibrations. *Sensors and Actuators A: Physical*, 109:156–164, 2003.

[64] T.D. Hien and M. Kleiber. Finite Element Analysis Based on Stochastic Hamilton Variational Principle. *Computers and Structures*, 37:893–902, 1990.

[65] T.D. Hien and M. Kleiber. Stochastic Finite Element Modelling in Linear Transient Heat Transfer. *Computer Methods in Applied Mechanics and Engineering*, 144:111–124, 1997.

[66] R. Houlihan and M. Kraft. Modelling Squeeze Film Effects in a MEMS Accelerometer with a Levitated Proof Mass. *Journal of Micromechanics and Microengineering*, 15:893–902, 2005.

[67] B. Houston, D. Photiadis, M. Marcus, J. Bucaro, X. Liu, and J. Vignola. Thermoelastic Loss in Microscale Oscillators. *Applied Physics Letter*, 80(7):1300–1302, February 2002.

[68] B. Houston, D. Photiadis, J. Vignola, M. Marcus, X. Liu, D. Czaplewski, L. Sekaric, J. Butler, P. Pehrsson, and J. Bucaro. Loss due to Transverse Thermoelastic Currents in Microscale Resonators. *Materials Science and Engineering A*, (370):407–411, 2004.

[69] B. Huang, Q.S. Li, W.H. Shi, and Z. Wu. Eigenvalues of Structures with Uncertain Elastic Boundary Restraints. *Applied Acoustics, In Press.*

[70] L. Huyse and M. A. Maes. Random Field Modeling of Elastic Properties Using Homogenization. *Journal of engineering mechanics*, pages 27–36, January 2001.

[71] T. Ikeda. *Fundamentals of Piezoelectricity.* Oxford University Press, 1996.

[72] R. Ishida. Stochastic Finite Element Analysis of Beam with Statistical Uncertainties. *AIAA Journal*, 39:2192–2197, 2001.

[73] B.D. Jensen, M.P. de Boer, N.D. Masters, F. Bitsie, and D.A. LaVan. Interferometry of Actuated Microcantilevers to Determine Material Properties and Test Structure Nonidealities in MEMS. *Journal of Microelectromechanical Systems*, 10(3):336–346, 2001.

[74] Y. Jimbo and K. Itao. Energy Loss of a Cantilever Vibrator. *Journal of Horological Institute of Japan*, 47:1–15, 1968.

[75] D. Jones. *Handbook of viscoelastic vibration damping.* John Wiley and Sons Ltd, 2001.

[76] R.V. Field Jr. and M. Grigoriu. On the Accuracy of the Polynomial Chaos Approximation. *Probabilistic Engineering Mechanics*, 19:65–80, 2004.

[77] I. Klapka, A. Cardona, and M. Géradin. An Object-Oriented Implementation of the Finite Element Method for Coupled Problems. *Revue Européenne des Eléments Finis*, August 1998.

[78] I. Klapka, A. Cardona, and M. Géradin. Interpreter OOFELIE for PDEs. In *European Congress on Computational Methods in Applied Sciences and Engineering, ECCOMAS 2000*, Barcelona, 11-14 September 2000.

[79] M. Kleiber and T.D. Hien. *The Stochastic Finite Element Method - Basic Perturbation Technique and Computer Implementation.* John Wiley and sons, 1992.

[80] W. Knabe, J. Przewlocki, and G. Rozynski. Spatial Averages for Linear Elements for two-parameter Random Field. *Probabilistic Engineering Mechanics*, 13(3):147–167, 1998.

[81] J.S. Kong, D.M. Frangopol, M. Raulli, K. Maute, R.A. Saravanan, L.-A. Liew, and R. Raj. A Methodology for Analyzing the Variability in the Performance of a MEMS Actuator Made from a Novel Ceramic. *Sensors and Actuators A*, 116:336–344, 2004.

[82] R.S. Lakes. High Damping Composite Materials: Effect of Structural Hierarchy. *Journal of Composite Materials*, 36:287–297, 2002.

[83] C. Lanczos. An Iteration Method for the Solution of the Eigenvalue Problem of Linear Differential and Integral Operators. *Journal of Research of the National Bureau of Standards*, 45:255–282, 1950.

[84] L.D. Landau and E.M. Lifshitz. *Theory of Elasticity.* Pergamon Press, Oxford, 1959.

[85] B. Le Foulgoc, T. Bourouina, O. Le Traon, A. Bosseboeuf, F. Marty, C. Breluzeau, J.-P. Grandchamp, and S. Masson. Highly Decoupled Single-Crystal Silicon Resonators: an Approach for the Intrinsic Quality Factor. *Journal of Micromechanics and Microengineering*, 16, 2006.

[86] O. Le Traon, D. Janiaud, and S. Muller. Monolithic Accelerometer Transducer. *US Patent n 5,962,786 published: 10/05/1999.*

[87] O. Le Traon, D. Janiaud, S. Muller, and P. Bouniol. The VIA Vibrating Beam Accelerometer: Concept and Performance. In *PLANS'98, Position Location and Navigation Symposium*, Palm Springs, April 20-23 1998.

[88] Z. Lei and C. Qiu. Neumann Dynamic Stochastic Finite Element Method of Vibration for Structures with Stochastic Parameters to Random Excitation. *Computers and Structures*, 77:651–657, 2000.

[89] S. Lepage, O. Le Traon, I. Klapka, S. Masson, and J.-C. Golinval. Thermoelastic Damping in Vibrating Beam Accelerometer: A New Thermoelastic Finite Element Approach. In *Caneus 2006*, Toulouse, France, August 27- September 01 2006.

[90] C.C. Li and A. Der Kiureghiam. Optimal Discretization of Random Fields. *Journal of Engineering Mechanics*, 119(6):1136–1154, Jun. 1993.

[91] R. Lifshitz and M.L. Roukes. Thermoelastic Damping in Micro-and Nanomechanical Systems. *Physical Review B*, 61(8):5600–5609, February 2000.

[92] R. Liu, B. Paden, and K. Turner. MEMS Resonators That Are Robust to Process-induced Feature Width Variations. *Journal of Microelectromechanical Systems*, 11(5):505–511, 2002.

[93] W.K. Liu, T. Belytschko, and A. Mani. Random Field Finite Elements. *International Journal for Numerical Methods in Engineering*, 23(10):1831–1845, Oct. 1986.

[94] J. Lothe. Aspects of the Theories of Dislocation Mobility and Internal Friction. *Physical Review*, 117:704–708, 1960.

[95] M.N. Ludwigsn, R.S. Lakes, and C.C. Swan. Damping and Stiffness of Particulate SiC-InSn Composite. *Journal of Composite Materials*, 36:2245–2254, 2002.

[96] M.J. Madou. *Fundamentals of Microfabrication.* CRC Press, 2d edition, 2002.

[97] C.S. Manohar and R.A. Ibrahim. Progress in Structural Dynamics with Stochastic Parameter Variations 1987-1998. *ASME Applied Mechanics Reviews*, 52(5):177–197, 1999.

[98] S. Masson, D. Janiaud, O. Le Traon, and S. Muller. Design and Performances of two Quartz Monolithic Vibrating Inertial Microsensors. In *Caneus 2006*, France, Toulouse, August 27 - September 01 2006.

[99] H.G. Matthies, C.E. Brenner, C.G. Bucher, and C.G. Soares. Uncertainties in Probabilistic Numerical Analysis of Structures and Solids - Stochastic Finite Elements. *Structural safety*, 19(3):283–336, 1997.

[100] K. Maute and D.M. Frangopol. Reliability-based Design of MEMS Mechanisms by Topology Optimization. *Computers and Structures*, 81:813–824, 2003.

[101] A. Mawardi and R. Pitchumani. Design of Microresonators under Uncertainty. *Journal of Microelectromechanical Systems*, 14(1), 2005.

[102] A. Mawardi and R. Pitchumani. Optimal Design of a Micromachined Force Gauge under Uncertainty. *Journal of Micromechanics and Microengineering*, 15:2353–2365, 2005.

[103] M.D. McKay, R.J. Beckman, and W.J. Conover. A Comparison of three Methods for Selecting Values of Input Variables in the Analysis of Output from a Computer Code. *Technometrics*, 21:239–245, 1979.

[104] D.V. Murthy and R.T. Haftka. Devivatives of Eigenvalues and Eigenvectors for a General Complex Matrix. *International Journal for Numerical Methods in Engineering*, 26:293–311, 1988.

[105] P.B. Nair and A.J. Keane. An Approximation Solution Scheme for the Algebraic Random Eigenvalue Problem. *Journal of Sound and Vibration*, 260:45–65, 2003.

[106] A.H. Nayfeh and M.I. Younis. Modeling and Simulations of Thermoelastic Damping in Microplates. *Journal of Micromechanics and Microengineering*, 14:1711–1717, 2004.

[107] R.B. Nelson. Simplified Calculation of Eigenvector Derivatives. *AIAA Journal*, 14(9):1201–1205, 1976.

[108] C.T.-C. Nguyen. High-Q Micromechanical Oscillators and Filters for Communications. *Proceedings, 1997 IEEE International Symposium on Circuits and Systems, Hong Kong, June 9-12*, pages 2825–2828, 1997.

[109] C.T.-C. Nguyen. Communication Architectures Based on High-Q MEMS Devices. *Workshop Notes, Workshop on Microwave and Photonic Applications of MEMS at the 2000 IEEE MTT-S International Microwave Symposium, Anaheim, California, June 16*, 2000.

[110] W. Nowacki. *Thermoelasticity.* Pergamon Press, Oxford, 1986.

[111] D.H. Oh and L. Librescu. Free Vibration and Reliability of Composite Cantilevers Featuring Uncertain Properties. *Reliability Engineering and System Safety*, 56:265–272, 1997.

[112] I.U. Ojalvo. Efficient Computation of Modal Sensitivities for Systems with Repeated Frequencies. *AIAA Journal*, 26:361–366, 1988.

[113] A.K. Onkar, C.S. Upadhyay, and D. Yadav. Probabilistic Failure of Laminated Composite Plates using the Stochastic Finite Element Method. *Composite and Structures*, 77:79–91, 2007.

[114] M. Ostoja-Starzewski. Microstructural Disorder, Mesoscale Finite Elements and Macroscopic Response. *Proceedings of the Royal Society A: Mathematical, Physical and Engineering Sciences*, 455:3189–3199, 1999.

[115] M. Ostoja-Starzewski and X. Wang. Stochastic Finite Elements as a Bridge Between Random Material Microstructure and Global Response. *Computer Methods in Applied Mechanics and Engineering*, 168:35–49, 1999.

[116] M. Ostoja-Starzewski and A. Woods. Spectral Finite Elements for Vibrating Rods and Beams with Random Field Properties. *Journal of Sound and Vibration*, 268:779–797, 2003.

[117] V. Papadopoulos and G. Deodatis. Response Variability of Stochastic Frame Structures using Evolutionary Field Theory. *Computer Methods in Applied Mechanics and Engineering*, 195:1050–1074, 2006.

[118] M. Papadrakakis and A. Kotsopulos. Parallel Solution Methods for Stochastic Finite Element Analysis using Monte Carlo Simulation. *Computer Methods in Applied Mechanics and Engineering*, 168:305–320, 1999.

[119] F. Parrain. Convention ARC 03/08-298. Technical report, Université de Liège/ IEF-CNRS UMR 8622, 2006.

[120] R.H. Plaut and K. Huseyin. Derivative of Eigenvalues and Eigenvectors in Non-self Adjoint Systems. *AIAA Journal*, 11(2), 1973.

[121] H. J. Pradlwarter and G. I. Schueller. Assessment of Low Probability Events of Dynamical Systems by Controlled Monte Carlo Simulation. *Probabilistic Engineering Mechanics*, 14:213–227, 1999.

[122] H.J. Pradlwarter, G.I. Schueller, and G.S. Szekely. Random Eigenvalue Problems for Large Systems. *Computers and Structures*, 80:2415–2424, 2002.

[123] J.R. Red-Horse and R. Ghanem. Polynomial Chaos Representation of the Random Eigenvalue Problem. In *Prooceedings of the 40th American Institute of Aeronautics and Astraonautics/ASME/ASCE/AHS/ASC Structures, Structural Dynamics, and Materials Conference, St Louis, MO*, 1999.

[124] S. Reh, P. Lethbridge, and D. Ostergaard. Quality Based Design and Design for Reliability of Micro-electro-mechanical Systems (MEMS) using Probabilitic Methods. *Technical proceedings of the 2000 International Conference on Modeling and Simulation of Microsystems*, pages 708–711, 2000.

[125] L.C. Rogers. Derivatives of Eigenvalues and Eigenvectors. *AIAA Journal*, 8(5):943–944, 1970.

[126] R.Srinivasan, M.Jayachandran, and K.Ramachandran. Role of Doping on the Thermal Properties of Porous Silicon. *First International Conference on Diffusion in Solids and Liquids, 6 - 8 July 2005, Aveiro, Portugal*, 2005.

[127] C.A. Schenk and G.I. Schuëller. *Uncertainty Assessment of Large Finite Element Systems*, volume 24 of *Lecture Notes in Applied Computational Mechanics*. Springer, 2005.

[128] G.I. Schueller. A State-of-the-Art Report on Computational Stochastic Mechanics. *Probabilistic Engineering Mechanics*, 12(4):197–321, 1997.

[129] G.I. Schueller. Computational Stochastic Mechanics - Recent Advances. *Computers and Structures*, 79:2225–2234, 2001.

[130] G.I. Schueller and R. Stix. A Critical Appraisal of Methods to Determine Failure Probabilities. *Structural Safety*, 4:293–309, 1987.

[131] S.D. Senturia. *Microsystem Design*. Kluwer Academic Publishers, 2001.

[132] W.N. Jr. Sharpe, K.M. Jackson, K.J. Hemker, and Z. Xie. Effect of Specimen Size on Young's Modulus and Fracture Strength of Polysilicon. *Journal of Microelectromechanical Systems*, 10(3):317–326, 2001.

[133] M. Shinozuka. Monte-Carlo Solution of Structural Dynamics. *Computers and structures*, 2(5-6):855–874, 1972.

[134] M. Shinozuka and J. Astill. Random Eigenvalue Problems in Structural Analysis. *AIAA Journal*, 10(4):456–462, 1972.

[135] M. Shinozuka and C.M. Jan. Digital Simulation of Random Process and its Applications. *Journal of Sound and Vibration*, 35(1):111–128, Nov. 1972.

[136] V. Srikar and S. Senturia. Thermoelastic Damping in Fine-grained Polysilicon Flexural Beam Resonators. *Journal of Microelectromechanical Systems*, 11(5):499–504, 2002.

[137] B. Sudret and A. Der Kiureghian. Stochastic Finite Element Methods and Reliability. Technical report, Department of civil and environmental engineering, University of California, Berkeley, 2000.

[138] S. Sung, J.G. Lee, B. Lee, and T. Kang. Design and Performance Test of an Oscillation Loop for a MEMS Resonant Accelerometer. *Journal of Micromechanics and Microengineering*, 13:246–253, 2003.

[139] G.S. Szekely and G.I. Schueller. Computational Procedure for a Fast Calculation of Eigenvectors and Eigenvalues of Structures with Random Properties. *Computer Methods in Applied Mechanics and Engineering*, 191:799–816, 2001.

[140] H.A. Tilmans, M. Elwespoek, and J.H. Fluitman. Micro Resonant Force Gauges. *Sensors and Actuators A*, 30:35–53, 1992.

[141] M. Turowski, Z. Chen, and A. Przekwas. High-Fidelity and Behavioral Simulation of Air Damping in MEMS. *Technical Proceedings of the 1999 International Conference on Modeling and Simulation of Microsystems.*

[142] B. Van den Nieuwenhof. *Stochastic Finite Elements for Elastodynamics: Random Field and Shape Uncertainty Modelling using Direct and Modal Perturbation-based Approaches.* PhD thesis, Université Catholique de Louvain, 2003.

[143] B. Van den Nieuwenhof and J.P. Coyette. Modal Approaches for the Stochastic Finite Element Analysis of Structures with Material and Geometric Uncertainties. *Computer Methods in Applied Mechanics and Engineering*, 192:3705–3729, 2003.

[144] E. Vanmarcke. *Random Fields. Analysis and Synthesis.* The MIT Press, 1983.

[145] B.N. Velamur Asokan and N. Zabaras. Stochastic Inverse Heat Conduction using a Spectral Approach. *International Journal for Numerical Methods in Engineering*, 60:1569–1593, 2004.

[146] B.N. Velamur Asokan and N. Zabaras. Variational Multiscale Stabilized FEM Formulations for Transport Equations: Stochastic Advection-diffusion and Incompressible Stochastic Navier-Stokes Equations. *Journal of Computational Physics*, 202:94–133, 2005.

[147] S. Vengallatore. Analysis of Thermoelastic Damping in Laminated Composite Micromechanical Beam Resonators. *Journal of Micromechanics and Microengineering*, 15:2398–2404, 2005.

[148] K. Wand, A.C. Wong, and C.T.C. Nguyen. VHF Free-Free Beam High-Q Resonators. *Journal of Microelectromechanical Systems*, 9:347–360, 2000.

[149] S.J. Wong, C.H.J. Fox, and S. McWilliam. Thermoelastic Damping of the In-plane Vibration of Thin Silicon Rings. *Journal of Sound and Vibration*, 293(1).

[150] S.J. Wong, C.H.J. Fox, S. McWilliam, and N. Jaroensawat. A Simple Model for Thermoelastic Damping in Slotted Beams. *MicroMechanics Europe 2005, September 4–6, Goteborg, Sweden.*

[151] D. Xiu and G.E. Karniadakis. Modeling Uncertainty in Steady State Diffusion Problems via Generalized Polynomial Chaos. *Computer Methods in Applied Mechanics and Engineering*, 191:4927–4948, 2002.

[152] D. Xiu and G.E. Karniadakis. A New Stochastic Approach to Transient Heat Conduction Modeling with Uncertainty. *International Journal of Heat and Mass Transfer*, 46:4681–4693, 2003.

[153] D. Xiu and G.E. Karniadakis. Modeling Uncertainty in Flow Simulations via Generalized Polynomial Chaos. *Journal of Computational Physics*, 187:137–167, 2003.

[154] J. Yang, T. Ono, and M. Esashi. Energy Dissipation in Submicrometer Thick Single-crystal Silicon Cantilevers. *Journal of Microelectromechanical Systems*, 11(6):775–783, December 2002.

[155] K.Y. Yasumura, T.D. Stowe, E.M. Chow, T. Pfafman, T.W. Kenny, B.C. Stipe, and D. Rugar. Quality Factors in Micron- and Submicron-thick Cantilevers. *Journal of Microelectromechanical Systems*, 9(1):117–125, March 2000.

[156] M. I. Younis. *Modeling and Simulation of Microelectromechanical Systems in Multi-Physics Fields.* PhD Thesis, Faculty of the Virginia Polytechnic Institute and State University, Blacksburg, Virginia, June 2004.

[157] C. Zener. Internal Friction in Solids. *Physical Review*, 52:230–235, August 1937.

[158] C. Zener. *Elasticity and Anelasticity of Metals.* The University of Chicago Press, 1948.

[159] J. Zhang and B. Ellingwood. Orthogonal Series Expansion of Random Fields in Reliability Analysis. *Journal of Engineering Mechanics, ASCE*, 120(12):2660–2667, 1994.

[160] L. M. Zhang, D. Uttamchandani, B. Culshaw, and P. Dobson. Measurement of Young's Modulus and Internal Stress in Silicon Microresonators using a Resonant Frequency Technique. *Measurement Science and Technology*, 1:1343–1346, 1990.

[161] W. Zhang and K.L. Turner. Thermoelastic Damping in the Longitudinal Vibration: Analysis and Simulation. In *Proceeding of IMECE04, 2004 ASME International Mechanical Engineering Congress and Exposition, November 13–20, Anaheim, California, USA*.

[162] Z. Zhang, P.C. Hammel, M. Midzor, M.L. Roukes, and J.R. Childress. Ferromagnetic Resonance Force Microscopy on Microscopic Cobalt Single Layer Films. *Applied Physics Letters*, 73(2036), 1998.

[163] W.Q. Zhu and W.Q. Wu. A stochastic Finite Element Method for Real Eigenvalue Problems. *Probabilistic Engineering Mechanics*, 6:228–232, 1991.

[164] Y. Zhu, F. Barthelat, P.E. Labossiere, N. Moldovan, and H.D. Espinosa. Nanoscale Displacement and Strain Measurement. *Proceedings of the 2003 SEM Annual Conference and Exposition on Experimental and Applied Mechanics, June 2-4, Charlotte, North Carolina,USA*, 2003.

[165] Z. Zimoch. Sensitivity Analysis of Vibrating Systems. *Journal of Sound and Vibration*, 115:447–458, 1987.

Appendix A

Thermoelastic Beam Finite Elements

A.1 Elementary Structural Matrices

The elementary structural matrices of a thermoelastic beam finite element are obtained using the shape function matrices and their derivatives derived in Section 5.1.3 in Equations (4.37-4.47). The material properties are denoted as follows: Young's modulus E, mass density ρ, thermal conductivity k, thermal expansion coefficient α and volumetric heat capacity C_E.

The mass matrix $\mathbf{M}_{uu}$ is expressed for an element of length ℓ, vibrating height h, width b and inertia $I = bh^3/12$ by

$$\mathbf{M}_{uu} = b\,h\rho\,\ell \begin{bmatrix} \frac{13}{35} & \frac{11}{210}\ell & \frac{9}{70} & -\frac{13}{420}\ell \\ \frac{11}{210}\ell & \frac{1}{105}\ell^2 & \frac{13}{420}\ell & -\frac{1}{140}\ell^2 \\ \frac{9}{70} & \frac{13}{420}\ell & \frac{13}{35} & -\frac{11}{210}\ell \\ -\frac{13}{420}\ell & -\frac{1}{140}\ell^2 & -\frac{11}{210}\ell & \frac{1}{105}\ell^2 \end{bmatrix}. \tag{A.1}$$

Stiffness matrices $\mathbf{K}_{uu}$, $\mathbf{K}_{u\theta}$ and $\mathbf{K}_{\theta\theta}$ are expressed:

$$\mathbf{K}_{uu} = \frac{EI}{\ell^3} \begin{bmatrix} 12 & 6\ell & -12 & 6\ell \\ 6\ell & 4\ell^2 & -6\ell & 2\ell^2 \\ -12 & -6\ell & 12 & -6\ell \\ 6\ell & 2\ell^2 & -6\ell & 4\,\ell^2 \end{bmatrix}, \tag{A.2}$$

$$\mathbf{K}_{u\theta} = \frac{\alpha\, Eb\, h^3}{15\ell} \begin{bmatrix} 0 & -1 & 0 & 1 \\ 0 & -\ell & 0 & 0 \\ 0 & 1 & 0 & -1 \\ 0 & 0 & 0 & \ell \end{bmatrix}, \tag{A.3}$$

and

$$\mathbf{K}_{\theta\theta} = \begin{bmatrix} -\frac{b\,kh}{\ell} & 0 & \frac{b\,kh}{\ell} & 0 \\ 0 & K_{\theta\theta}^{(22)} & 0 & K_{\theta\theta}^{(42)} \\ \frac{b\,kh}{\ell} & 0 & -\frac{b\,kh}{\ell} & 0 \\ 0 & K_{\theta\theta}^{(42)} & 0 & K_{\theta\theta}^{(44)} \end{bmatrix}, \tag{A.4}$$

where

$$\begin{aligned} K_{\theta\theta}^{(22)} &= b\left(-\frac{1}{252}\frac{h^3k}{\ell} + \left(-1/15\,\frac{\ell k}{h^4} + 1/30\,\frac{k}{h^2\ell}\right)h^5\right. \\ &\quad \left. + \left(2/9\,\frac{\ell k}{h^2} - 1/12\,\frac{k}{\ell}\right)h^3 - 1/3\,\ell kh\right), \end{aligned} \tag{A.5}$$

$$\begin{aligned} K_{\theta\theta}^{(42)} &= b\left(\frac{1}{252}\frac{h^3k}{\ell} + \left(-1/30\,\frac{\ell k}{h^4} - 1/30\,\frac{k}{h^2\ell}\right)h^5\right. \\ &+ \quad \left.\left(1/9\,\frac{\ell k}{h^2} + 1/12\,\frac{k}{\ell}\right)h^3 - 1/6\,\ell kh\right), \end{aligned} \tag{A.6}$$

and

$$\begin{aligned} K_{\theta\theta}^{(44)} &= b\left(-\frac{1}{252}\frac{h^3k}{\ell} + \left(-1/15\,\frac{\ell k}{h^4} + 1/30\,\frac{k}{h^2\ell}\right)h^5\right. \\ &\quad \left. + \left(2/9\,\frac{\ell k}{h^2} - 1/12\,\frac{k}{\ell}\right)h^3 - 1/3\,\ell kh\right). \end{aligned} \tag{A.7}$$

Damping matrices $\mathbf{C}_{\theta\theta}$ and $\mathbf{C}_{u\theta}$ are

$$\mathbf{C}_{\theta\theta} = b\,C_E\ell h \begin{bmatrix} -1/3 & 0 & -1/6 & 0 \\ 0 & -\frac{17}{945}\,h^2 & 0 & -\frac{17}{1890}h^2 \\ -1/6 & 0 & -1/3 & 0 \\ 0 & -\frac{17}{1890}\,h^2 & 0 & -\frac{17}{945}\,h^2 \end{bmatrix} \tag{A.8}$$

and

$$\mathbf{C}_{\theta u} = T_0\mathbf{K}_{u\theta}^T, \tag{A.9}$$

where T_0 is the reference temperature.

A.2 Elementary Structural Matrix Derivatives

If Young's modulus is considered as a random field, the derivative of the elementary structural matrices with respect to the corresponding random variables have to be determined and are used in Chapter 8.

A.2.1 Local Average Method

When the Local Average method is used, the derivative of the elementary structural matrices of element i are given by

$$\mathbf{K}_{uu,E_i} = \frac{I}{\ell^3}\begin{bmatrix} 12 & 6\ell & -12 & 6\ell \\ 6\ell & 4\ell^2 & -6\ell & 2\ell^2 \\ -12 & -6\ell & 12 & -6\ell \\ 6\ell & 2\ell^2 & -6\ell & 4\,\ell^2 \end{bmatrix}, \tag{A.10}$$

$$\mathbf{K}_{u\theta,E_i} = \frac{\alpha\, b\, h^3}{15\ell}\begin{bmatrix} 0 & -1 & 0 & 1 \\ 0 & -\ell & 0 & 0 \\ 0 & 1 & 0 & -1 \\ 0 & 0 & 0 & \ell \end{bmatrix} \tag{A.11}$$

and

$$\mathbf{C}_{\theta u,E_i} = T_0 \mathbf{K}^T_{u\theta,E_i}. \tag{A.12}$$

All other elementary structural matrix derivatives are equal to zero.

A.2.2 Karhunen-Loeve Expansion Method

Using Karhunen-Loeve Expansion for the discretization of Young's modulus, E (Equation (7.58)), the expression of $\mathbf{K}_{uu}$ is written

$$\mathbf{K_{uu}} = \int_\Omega E\mathbf{B_u}^T\mathbf{B_u}d\Omega \tag{A.13}$$

$$= \int_\Omega \bar{E}\mathbf{B_u}^T\mathbf{B_u}d\Omega + \sum_{i=1}^{N}\zeta_i\int_\Omega \sqrt{\lambda_i}f_i(x)\mathbf{B_u}^T\mathbf{B_u}d\Omega \tag{A.14}$$

$$= \bar{\mathbf{K}}_{\mathbf{uu}} + \sum_{i=1}^{N}\zeta_i\mathbf{K_{uu}}_i, \tag{A.15}$$

where λ_i and $f_i(x)$ are given for a 1-D exponential correlation function by Equations (6.39), (6.42) and (6.43).

$\mathbf{K_{uu,i}}$, the derivative of $\mathbf{K}_{uu}$ with respect to ζ_i is given by

- for i odd

$$\begin{aligned} K_{uu,i}(k,l) &= \frac{bh^3}{24\ell^{a+2}\omega_i^4}\frac{\sqrt{\lambda_i}}{\sqrt{0.5L+\sin(L\omega_i)}}\left[a_{kl}(\omega_i\ell)^2\sin(f1)+b_{kl}\omega_i\ell\cos(f1)\right. \\ &\left.+c_{kl}\sin(f1)+d_{kl}(\omega_i\ell)^2\sin(f2)+e_{kl}\omega_i\ell\cos(f2)-c_{kl}\sin(f2)\right], \end{aligned}$$

- for i even

$$\begin{aligned} K_{uu,i}(k,l) &= \frac{-bh^3}{24\ell^{a+2}\omega_i^4}\frac{\sqrt{\lambda_i}}{\sqrt{0.5L-\sin(L\omega_i)}}\left[a_{kl}(\omega_i\ell)^2\cos(f1)+b_{kl}\omega_i\ell\sin(f1)\right. \\ &\left.+c_{kl}\cos(f1)+d_{kl}(\omega_i\ell)^2\cos(f2)+e_{kl}\omega_i\ell\sin(f2)-c_{kl}\cos(f2)\right], \end{aligned}$$

where

$$f1 = -\omega_i d_e - \omega_i\ell + \frac{1}{2}\omega_i L, \tag{A.16}$$

$$f2 = -\omega_i d_e + \frac{1}{2}\omega_i L, \tag{A.17}$$

and constants a, a_{kl}, b_{kl}, c_{kl}, d_{kl} and e_{kl} are listed in Table A.1. d_e is the abscise of the first node of the element, ℓ is the length of the element and L is the length of the domain.

Note that since $\mathbf{K}_{uu}$ is symmetric, the derivatives are also symmetric.

The expression of $\mathbf{K}_{u\theta}$ is written

$$\mathbf{K_{u\theta}} = -\int_\Omega E\alpha\mathbf{B_u}^T\mathbf{N}_\theta d\Omega \tag{A.18}$$

$$= -\int_\Omega \bar{E}\alpha\mathbf{B_u}^T\mathbf{N}_\theta d\Omega + \sum_{i=1}^{N}\zeta_i\alpha\int_\Omega\sqrt{\lambda_i}f_i(x)\mathbf{B_u}^T\mathbf{N}_\theta d\Omega \tag{A.19}$$

$$= \bar{\mathbf{K}}_{\mathbf{u}\theta} + \sum_{i=1}^{N}\zeta_i\mathbf{K}_{\mathbf{u}\theta i}. \tag{A.20}$$

$\mathbf{K_{u\theta,i}}$, the derivative of $\mathbf{K}_{u\theta}$ with respect to ζ_i is given by

- for i odd

$$\begin{aligned} K_{u\theta}(k,l) &= \frac{1}{c}\frac{\alpha bh^3}{\ell^b\omega_i^4}\frac{\sqrt{\lambda_i}}{\sqrt{0.5L+\sin(L\omega_i)}}\left[f_{kl}\sin(g1)(\omega_i\ell)^2+g_{kl}\cos(g1)\omega_i\ell\right. \\ &\left.+h_{kl}\sin(g1)+i_{kl}\sin(g2)(\omega_i\ell)^2+j_{kl}\cos(g2)\omega_i\ell-h_{kl}\sin(g2)\right] \end{aligned}$$

Table A.1: Values of a, a_{kl}, b_{kl}, c_{kl}, d_{kl} and e_{kl}.

k	l	a	a_{kl}	b_{kl}	c_{kl}	d_{kl}	e_{kl}
1	1	4	-36	144	288	36	144
1	2	3	12	60	-144	-24	84
1	3	4	-36	-144	288	36	-144
1	4	3	24	84	-144	-12	60
2	2	2	4	24	-72	-16	48
2	3	3	-12	-60	144	24	-84
2	4	2	8	36	-72	-8	36
3	3	4	36	144	-288	-36	144
3	4	3	-24	-84	144	12	-60
4	4	2	16	48	-72	-4	24

- for i even

$$\begin{aligned} K_{u\theta}(k,l) &= -\frac{1}{c}\frac{\alpha b h^3}{\ell^b \omega_i^4}\frac{\sqrt{\lambda_i}}{\sqrt{0.5L-\sin(L\omega_i)}}\left[f_{kl}\cos(g1)\,(\omega_i\ell)^2 - g_{kl}\sin(g1)\,\omega_i\ell\right. \\ &\quad \left. + h_{kl}\cos(g1) + i_{kl}\cos(g2)\,(\omega_i\ell)^2 - j_{kl}\sin(g2)\,\omega_i\ell - h_{kl}\,\cos(g2)\right], \end{aligned}$$

where

$$g1 = \frac{1}{2}\omega_i\,(2d_e + 2\ell - L)\,, \tag{A.21}$$

$$g2 = \frac{1}{2}\omega_i\,(2d_e - L)\,, \tag{A.22}$$

and constants b, f_{kl}, g_{kl}, h_{kl}, i_{kl}, j_{kl} and c are listed in Table A.2.

Note that the derivative of $\mathbf{K}_{u\theta}$ is not symmetric and that the components of its first and third columns are equal to zero. The derivatives of $\mathbf{C}_{\theta u}$ are given by

$$\mathbf{C}_{\theta\mathbf{u},\mathbf{i}} = T_0 \mathbf{K}_{\mathbf{u}\theta,\mathbf{i}}{}^T. \tag{A.23}$$

Table A.2: Values of b, f_{kl}, g_{kl}, h_{kl}, i_{kl}, j_{kl} and c.

k	l	b	f_{kl}	g_{kl}	h_{kl}	i_{kl}	j_{kl}	c
1	2	4	0	-1	4	1	-3	5
1	4	4	1	3	-4	0	1	5
2	2	3	0	-1	6	2	-5	15
2	4	3	1	4	-6	0	2	15
3	2	4	0	-1	4	1	-3	-5
3	4	4	1	3	-4	0	1	-5
4	2	3	0	-2	6	1	-4	15
4	4	3	2	5	-6	0	1	15